

LOW-FIELD NMR STUDIES OF STRUCTURE AND DYNAMICS IN SEMICRYSTALLINE POLYMERS

Dissertation

zur Erlangung des
Doktorgrades der Naturwissenschaften (Dr. rer. nat.)

vorgelegt dem

Institut für Physik
der Naturwissenschaftlichen Fakultät II
der Martin-Luther-Universität Halle-Wittenberg

von

Kerstin Schäler

geboren am 20. April 1983 in Zwenkau



Halle/Saale, den 06. 11. 2012

Gutachter:

1. Prof. Dr. Kay Saalwächter (MLU)
2. Prof. Dr. Mario Beiner (MLU)
3. Prof. Dr. Siegfried Stapf (TU Ilmenau)

Eröffnung des Promotionsverfahrens: 21. November 2012

Öffentliche Verteidigung: 05. März 2013

„Ich will Ihnen das Geheimnis verraten,
das mich zum Ziel geführt hat.
Meine Stärke liegt einzig und allein
in meiner Beharrlichkeit.“

Louis Pasteur (1822 - 1895)

Contents

1. Introduction	1
2. Semicrystalline Polymers	4
3. Low-Field Proton Nuclear Magnetic Resonance	8
3.1. Nuclear Spins and Magnetization	8
3.2. The Free Induction Decay	9
3.3. Dipolar Interactions and their Influence on the NMR Signal	10
4. Low-Field Proton NMR Applications for the Investigation of Semicrystalline Polymers	14
4.1. The Free Induction Decay of Semicrystalline Polymers	14
4.2. The Magic Sandwich Echo	20
4.3. Proton Spin Diffusion in Semicrystalline Polymers	26
4.3.1. The Spin-Diffusion Experiment	27
4.3.2. The Differential Equation for Spin Diffusion	28
4.4. NMR Filter Sequences	30
4.4.1. The MAPE Dipolar Filter Sequence	32
4.4.2. The Double-Quantum Filter Sequence	33
5. Dynamics in Crystallites of Semicrystalline Polymers	39
5.1. Investigation of PCL Crystallite Dynamics on Different Time Scales . . .	39
5.2. Determination of Chain-Flip Rates in PE Crystallites for Two Different Sample Morphologies	51
6. Crystallization of PCL	61
7. Investigation of Spin Diffusion in PCL	70
7.1. Spin-Diffusion Coefficients of Heterogeneous Polymers	70
7.2. Proton Low-Field NMR and SAXS Measurements of Semicrystalline PCL	74
7.3. Simultaneous Fit of Spin-Diffusion and Saturation-Recovery Data	80
7.4. Magnetization Transfer Lags in PCL Spin-Diffusion Experiments	84
7.5. Effects of Corrugated Crystalline-Interphase Boundary Surfaces	90
7.6. Quantitative Results from Fitting PCL Spin-Diffusion Data	93
7.7. Initial Rate Approximation for the Estimation of Domain Sizes in PCL .	97
7.8. Summarizing Remarks	101
8. The Influence of Cyclic Chain Topology on PCL Dynamics and Crystallization	103
8.1. Chain Mobility in the Melt	105
8.2. Crystallinity and Crystallization	110
8.3. Domain Thicknesses	113
8.4. Summarizing Remarks	117
9. Summary	119
A. Experimental Details	123

A.1. Experimental Techniques	123
A.2. Samples	128
B. PCL Degradation Investigations	130
B.1. Degradation of Cyclic PCL Chains	130
B.2. Degradation of Linear PCL Chains	130
C. Quantum-Mechanical Basics of NMR	132
D. Demonstration of the Effect of Diverse Pulse Sequences	140
D.1. Average Hamiltonian Theory for Calculating the Mode of Action of Pulse Sequences	140
D.1.1. The Magic Sandwich Echo	140
D.1.2. The Magic and Polarization Echo	149
D.2. The Double-Quantum Filter	150
E. PCL Densities	155
F. Spin Diffusion	156
F.1. Description of Magnetization Transfer Between Two Spins 1/2	156
F.2. The Simulation Program for Calculating Spin-Diffusion and Saturation-Recovery Curves	157
F.3. Derivation of the Source Domain Size by means of the Initial Rate Approximation	158
F.4. Effects of PCL Domain-Thickness Distributions on Spin Diffusion	161
Bibliography	167

1. Introduction

Many industrially important polymeric materials are semicrystalline. Their macroscopic chemical and mechanical properties are governed by the interplay between the well-ordered crystalline domains and the mobile-amorphous regions, both possessing individual microscopic features, such as domain geometry or size and chain mobility. A multitude of experimental techniques is available for the investigation of such heterogeneous polymer structures, e. g., Small Angle X-Ray and Neutron Scattering (SAXS and SANS), Electron and Atomic Force Microscopy (EM and AFM), Raman and fluorescence spectroscopy or thermal analysis. As Nuclear Magnetic Resonance (NMR) spectroscopy experiments detect spin interactions in and between molecules, they can provide very local information on dynamics and structure and are therefore eminently suited for the investigation of semicrystalline polymers.

The beginnings of NMR trace back to studies of Bloch and Purcell et al. who, independently from each other, detected first NMR signals shortly after the end of the second world war. This discovery was rewarded with the Nobel prize for physics for Bloch and Purcell in 1952. At that time, all fundamental parameters influencing the NMR signal, such as the chemical shift, the dipolar splitting, indirect spin-spin couplings, quadrupolar couplings and molecular dynamics, have already been known and a general NMR theory was on hand [1].

During this early years of NMR the measurements based upon the continuous-wave sweep method yielding frequency spectra directly. Yet, the introduction of pulsed NMR by R. Ernst in 1964 in combination with the Fourier transform to generate analyzable spectra from the directly detected time-domain signals represented an important step forward in the development of NMR spectroscopy, as it brought about a dramatic increase in sensitivity of the method [2]. This progress opened up new fields of research and is the state of the art until today. For his work and his services in two-dimensional NMR Ernst received the Nobel prize for chemistry in 1991 [1, 2].

The shift from high-performance electromagnets to superconducting magnets in the 1960s [3] enabled a significant increase in spectral resolution. Since then lots of advancements of NMR techniques have been made with regard to the diverse fields of applications, e. g., the development of multiple-pulse sequences, Magnetic Resonance Imaging (MRI) or Pulsed Field Gradient (PFG) NMR and the introduction of Magic-Angle Spinning (MAS) or two-dimensional spectroscopy [1]. To achieve higher sensitivity and spectral resolution, magnetic fields of increasing strength are required. Currently, superconducting magnets with proton Larmor frequencies up to 1 GHz are available [4]. Yet, such magnets are heavy, bulky, immobile and expensive in purchase and maintenance. Moreover, the operation of high-field spectrometers is rather complex. Another option for an enhancement of the resolution consists in fast Magic-Angle Spinning of the sample in order to average out spin interactions which lead to broad spectral lines [5]. The largest rotation frequencies attainable at present range at about 80 kHz [6]. Probe heads and rotors suited for this ultrafast rotation, however, are expensive. Nevertheless current trends in solid-state NMR tend toward maximum magnetic field strengths and rotation frequencies [7], leading to highly elaborate, cost-intensive and interference-prone technology.

Yet, robust and cheap low-field proton NMR may provide valuable insights in structure

and dynamics of semicrystalline polymers. Low-field spectrometers are easy to handle since they use permanent magnets and comparably simple technology. Admittedly, due to the weak magnetic field and its rather strong inhomogeneity, chemical resolution cannot be achieved here. Hence, low-field devices are mainly used for standard relaxometry applications in industry. However, beyond that, they offer the opportunity to investigate proton dipolar couplings, the strength of which does not depend on the magnetic field strength. As the proton dipolar coupling strength is an indicator for segmental dynamics in polymers, low-field NMR is a suitable method for the investigation of chain dynamics, e. g., in crystallites and mobile-amorphous domains of semicrystalline polymers or in polymer melts. Moreover, differences in chain mobility between the individual phases of a semicrystalline polymer can be observed by low-field NMR, enabling the detection of crystallinity and domain sizes [8]. Due to the exploitation of an internal mobility contrast, a particular sample pretreatment, such as staining, is not required here as opposed to other methods, e. g., EM.

Besides the demonstration of the versatile capabilities of low-field NMR spectroscopy for the investigation of semicrystalline polymers, the objective of this thesis is the exploration of the relation between polymer chain mobility and the semicrystalline structure. For this purpose, two polymer systems, poly(ϵ -caprolactone) (PCL) and poly(ethylene) (PE) have been investigated by low-field ^1H NMR spectroscopy. Despite of their rather similar chemical structure they seem to differ in crystallite chain mobility. While PE is an α_c -mobile polymer with chains performing helical jump motions within the crystallites, PCL is said to be crystal-fixed. As a start, diverse low-field NMR methods had to be adapted to the application to these polymers, such as

- FID and MSE measurements for the determination of the phase composition,
- spin-diffusion and Saturation-Recovery experiments for the exploration of domain sizes and
- the MSE sequence to study the intermediate-regime chain mobility within the polymer crystallites.

Hence, after a short introduction regarding semicrystalline polymers and the basics of low-field NMR in general in Chapters 2 and 3, these NMR methods, which primarily have been used for the investigations presented here, are explicated in Chapter 4. They have furthermore been utilized to study diverse specific problems of polymer-physical or methodological interest:

- The chain dynamics in PCL and PE crystallites has been investigated with regard to the questions whether PCL in fact can be classified as a crystal-fixed polymer and whether the jump rate of the local chain-flip process in PE crystallites depends on the phase morphology (see Chapter 5).
- The crystallization of PCL has been studied in terms of reproducibility of the crystallization isotherms measured by low-field NMR (see Chapter 6).
- The method of proton spin diffusion has been established for the determination of PCL domain sizes by low-field NMR (see Chapter 7).
- The influence of chain topology on chain mobility and the semicrystalline structure has been explored by comparing linear and macrocyclic PCL with regard to melt mobility, crystal growth, crystallinity and domain sizes (see Chapter 8).

The majority of the investigations have been performed by means of low-field Bruker minispec spectrometers with a permanent magnet (field strength $B_0 \sim 0.5$ T) at a proton Larmor frequency of about 20 MHz. Only for Section 5.1 two high-field NMR techniques have been used exceptionally, in order to extend the time range of the dynamics investigations. Moreover, to corroborate the low-field NMR results, complementary methods of the experimental polymer physics have been applied. Details concerning the experimental techniques, settings and samples are given in Appendix A.

2. Semicrystalline Polymers

Polymers are long chain molecules, mostly hydrocarbons, which consist of many covalently-bonded molecular units, named monomers [9, 10]. They are of particular importance in industry and everyday life, e. g., in the form of molded materials, plastic films and synthetic fibers. As their macroscopic properties, such as tensile strength, rigidity, elasticity, temperature and fatigue resistance, depend on molecular structure and dynamics as well as on the assembly of the chains, investigations of these features are of much interest. Basically, depending on the assembly of the chains, a distinction is made between purely amorphous and semicrystalline polymers. This work focuses on investigations of the latter.

In a polymer melt the chains adopt entangled random-coil conformations with statistically determined backbone bond angles, lacking long-range chain order and thus forming liquid-like amorphous material [9]. If the chains exhibit a sufficiently regular chemical constitution and linear architecture, the material is able to crystallize at temperatures below the melting point by partial disentanglement and stretching of chains. The stretched chain parts take on helical conformations of minimal intramolecular conformational energy and pack parallelly into three-dimensional crystalline arrays so as to minimize the packing energy [10]. Here, a crystalline unit cell can be defined similar to those in anorganic crystals.

The thermodynamic equilibrium state is represented by the extended chain crystal comprising completely stretched chains. However, the stretching of entangled chains poses an entropic barrier to crystallization. Hence, the evolving structure is not the one with minimum free energy but the one, which forms most rapidly [10]. Entanglements and other topological impurities, such as chemical defects, loops, chain ends, crosslinks or short chain branches, which cannot be resolved and stretched during the available time, are rejected from the crystallites and concentrated in amorphous regions between them. Thus a semicrystalline structure is formed, usually consisting of lamellae of highly ordered crystalline material and disordered amorphous domains with almost isotropic chain orientation and high chain mobility in between (see Fig. 2.1) [9, 10]. It is the combination of characteristics of the crystalline and amorphous phase, which induces the rigid but flexible consistency of semicrystalline polymers.

The deformed entanglements within the amorphous phase cause an increase in the free energy as compared to the melt and impose a pressure upon the crystalline lamellae, thus stabilizing them at a certain thickness [11]. This thickness in chain direction is typically low, i. e. in the range of 10 nm, while the lateral lamellar extensions are in the micrometer range [9, 10]. The crystalline lamellae arrange themselves in stacks which form superstructures, such as spherulites [10].

The transition zone between crystalline and amorphous regions was and still is a matter of debate [9, 12–15]. According to Flory the border between the two domains must be less sharp than in monomeric systems, as a portion of the well-ordered chains, which leave the crystallite, have to disperse into the disordered amorphous phase, where the multitude of possible chain conformations results in a larger space requirement of the single chains [13, 16]. Therefore, diffuse interphase regions are formed, with a thickness of a few nanometers, which are characterized by partial order and restricted mobility of the chain segments as compared to the mobile-amorphous phase [9, 17]. In-

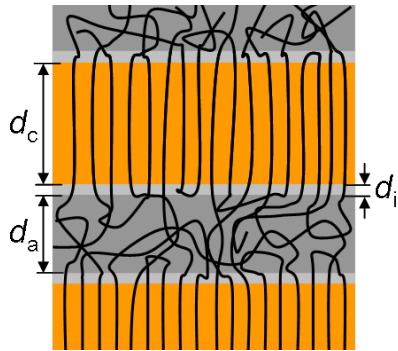


Figure 2.1.: Arrangement of polymer chains in a lamellar semicrystalline structure with domain thicknesses d_c , d_a and d_i of the crystalline lamellae, mobile-amorphous regions and interphase regions, respectively.

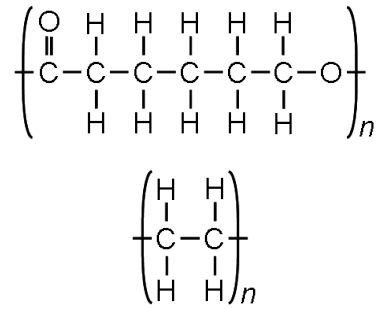


Figure 2.2.: Chemical structure of poly(ϵ -caprolactone) (PCL, upper part) and poly(ethylene) (PE, lower part).

vestigations of semicrystalline polymers using diverse experimental methods, such as (Time-Modulated) Differential Scanning Calorimetry (TM DSC), dielectric and dynamic-mechanical spectroscopy, in fact militate in favor of the existence of a rigid-amorphous interphase [15, 18, 19]. The structure of the interphase is affected, e. g., by the free energy of chain folds, the chain density at the crystallite surface and the space requirement of chain segments in the crystalline and amorphous phase and hence is polymer specific [9, 13].

For creating optimized polymer structures profound knowledge of polymer crystallization is necessary. However, the crystallization process is not clarified completely on a molecular level. It is known, that the crystal growth, proceeding at the lateral faces of the lamellae, is a thermally activated process with a barrier in Gibbs free energy, which has to be overcome in order to attach chain stems to the growth front. However, the nature of the barrier and its reason remain indistinct [10, 20]. Both, enthalpic [21, 22] and entropic [23, 24] barriers are subject of crystallization theories [20]. While the classical model of crystallization kinetics by Hoffman and Lauritzen is based on the assumption of a successive, thermally activated attachment of single chain stems to the crystal growth front, more current multi-stage models presume a pre-arrangement of chains within a mesomorphic phase, before the actual crystallization takes place [23, 25]. Other models propose collective local ordering processes of several polymer chains at once or spinodal-like processes during crystallization [26, 27]. Although certain effects of molecular weight on domain thicknesses have been proven experimentally [9, 28–30], crystallization theories still do not address this topic. Moreover, the influence of chain topology, the structure of the mobile-amorphous phase (and the interphase) as well as the role of entanglements prior to and during crystallization is currently under discussion [11, 31–38].

Besides the phase structure of the polymers also chain dynamics influence the mechanical properties. Molecular motions are typically characterized by a correlation time τ_c , describing an average time required for an orientational change [39], or a motional rate $k \propto 1/\tau_c$. Generally, there is a hierarchy of dynamical processes in polymers, including very fast subsegmental motions, conformational changes of a few neighboring monomers, slower cooperative motions of longer chain segments and even motions of

the whole chain via reptation and free diffusion [10, 40, 41]. The different motional processes are usually named α , β and γ according to the order of their emergence in an experiment, commencing with the process at the highest temperature, i. e. the lowest motional rate and largest correlation time, respectively. However, the denotation does not contain information about the origin of a molecular motion [10, 17, 42].

Compared to a purely amorphous polymer, the dynamical processes in a semicrystalline polymer are much more complex and less uniform as a result of the motional restrictions arising when chains are partially fixed in the crystallites [10, 42]. Local processes, such as side chain motions, take place at high motional rates, i. e. small correlation times. As in purely amorphous polymers, there is often a distribution of rates, e. g., due to the coupling of motions of different side groups [10, 17]. Cooperative segmental motions, which form the basis of the viscoelasticity of polymer melts and lead to the glass transition when freezing in at decreasing temperature, can be found in the amorphous regions of semicrystalline polymers as well. They usually exhibit a distribution of motional rates, too. However, in comparison to purely amorphous polymers, the trapping of entanglements in the mobile-amorphous domains causes changes in the rate of the segmental motions and the temperature dependence of this rate and results in a broadening of the rate distribution [10, 42]. The motional constraints may even induce new relaxation modes [10]. Motions of whole chains at low rates, which require chain disentanglement and are known to occur in polymer melts, are usually suppressed in semicrystalline polymers due to the fixation of the chains in the crystallites [10].

Additional dynamical processes may occur in the polymer crystallites, e. g., microscopic chain diffusion as a result of helical jumps of whole repeat units. Such a motion, a so-called α_c process [43, 44], is thermally activated with a polymer-specific activation energy [42] depending, e. g., on the length of the monomeric unit [45].

The microscopic and macroscopic properties of a semicrystalline polymer depend on the actual structure of and dynamics in the material. There are certain parameters to define the polymer morphology, such as the crystallinity or, more generally, the phase composition, the domain thicknesses and thickness distributions, the extent and structure of the crystalline surfaces and the internal structure of the distinct polymer phases [9]. The term crystallinity describes the portion of crystalline material within a sample. A distinction is made between the volume fraction, as obtained from Small Angle X-ray Scattering (SAXS) or density measurements, and the mass fraction determined by DSC or NMR. Typical crystallinity values of semicrystalline polymers range between a few percent and 90%, depending on the molecular structure and the crystallization conditions. They deviate slightly according to the experimental technique and the underlying physical quantity used for crystallinity determination [9]. Polymer lamellae can be investigated by means of Electron and Atomic Force Microscopy and crystalline and amorphous-domain thicknesses as well as their distributions can be measured, e. g., in SAXS experiments. For studying dynamics within the crystalline and amorphous regions NMR spectroscopy is well-suited.

In this work we investigate poly(ϵ -caprolactone) (PCL) and poly(ethylene) (PE) with molecular weights above the entanglement limit. Both are well-known semicrystalline polymers of industrial importance. Their chemical structure is depicted in Fig. 2.2 and a list of the samples used herein can be found in Appendix A.

PCL is an aliphatic polyester of medium crystallinity, exhibiting a well-manageable DSC

melting point and a glass transition close to 60°C and -60°C, respectively [46]. Because of its biodegradability, non-toxicity and excellent blend compatibility PCL is a candidate for potential biomedical applications, e. g., as drug delivery medium or artificial tissue material [47]. PE is a polyolefin with a melting point close to 130°C and a glass transition at about -120°C [48]. As the chemically simplest polymer it is frequently used as a model system in polymer physics research. It is produced industrially on a large scale and has versatile fields of application in everyday life, e. g., as packaging material or in household articles [46].

PCL and PE resemble each other in chain conformation and geometry of the crystalline unit cell. The chains of both polymers contain CH₂ groups crystallizing in a (more or less) planar all-trans conformation forming orthorhombic unit cells. The cell dimensions of PCL perpendicular to the chain axis ($a = 7.496 \text{ \AA}$ and $b = 4.974 \text{ \AA}$ at 25°C [49]) are similar to those of PE ($a = 7.45 \text{ \AA}$ and $b = 4.93 \text{ \AA}$ at 25°C [50]). By contrast the repeat units of PCL are significantly longer than for PE due to additional ester groups replacing every sixth CH₂ group. This results in an elongation of the PCL unit cell in chain direction ($c = 17.297 \text{ \AA}$ at 25°C [49, 51, 52]) compared to PE ($c = 2.534 \text{ \AA}$ at 25°C [50]).

Depending on the mobility of the polymer chains within the crystallites (see above) a distinction is made between crystal-fixed and α_c -mobile polymers [44]. PE like PEO, POM and iPP, is α_c -mobile with chains performing helical jumps within the crystallites, as it has been proven, e. g., by NMR measurements [44]. This mobility is connected to mechanical polymer properties, such as creep, extrudability and ultradrawability [44]. On the other hand, PCL is said to be crystal-fixed like Nylons, PET and sPP, i. e. the chains do not translate through the crystallites. This classification shall be confirmed in Section 5.1, while the helical chain flips in PE will be investigated in Section 5.2.

3. Low-Field Proton Nuclear Magnetic Resonance

To give an introduction to the application of ^1H low-field time-domain NMR, some NMR basics are summarized here in short. Detailed information can be found in NMR textbooks, such as Refs. [53, 54].

3.1. Nuclear Spins and Magnetization

Nuclear Magnetic Resonance (NMR) spectroscopy relies on the existence of the nuclear spin I . This spin is an intrinsic property of diverse atomic nuclei. Although it exhibits (quantum-mechanical) characteristics of an angular momentum, it does not result from a rotation of the nucleus. Atomic nuclei contain nucleons, i. e. protons and neutrons, which both carry a spin. Depending on the number of nucleons there are different combinations of the nucleon spins to form a net nuclear spin. As the energy differences between the individual combinations are usually large ($\sim 10^{11}$ kJ/mol) compared to the thermal energy (~ 2.5 kJ/mol), it is most likely to find a nucleus in the state of lowest energy. Typically, the nuclear spin quantum number I (see Appendix C), which characterizes the nuclear spin in this ground state, is used to specify the nucleus, e. g., ^1H and ^{13}C nuclei carry spin $1/2$ (i. e. $I = 1/2$), while ^{12}C nuclei do not possess a spin ($I = 0$) and are NMR-inactive. Nuclear-spin quantum numbers between 0 and 7 can be found in nature, however there are no nuclei with $I=2$ [53].

The nuclear spin is related to a magnetic dipole moment μ :

$$\mu = \gamma \cdot I$$

The proportionality factor between both vector quantities is the magnetogyric ratio γ of the respective nucleus, which can take positive or negative values. The magnetic moment of a nucleus arises from the magnetic moments of all nucleons involved as well as the electric currents of the charged nucleons. Summing up all magnetic moments per volume unit yields the macroscopic magnetization M . Due to the isotropic orientational distribution of the magnetic moments, there is no macroscopic magnetization in absence of a magnetic field. However, when a sample is brought into a magnetic field of strength B_0 a torque D will act upon the magnetic moments μ perpendicular to μ and B_0 :

$$D = \mu \times B_0$$

This torque is related to the spin I via the time derivative

$$D = \frac{\partial}{\partial t} I,$$

causing the spin vector I to turn towards D . As a consequence, there is a precession of I about the direction of the magnetic field B_0 . This process is actually of quantum-mechanical origin but it shows the same behavior as known for macroscopic angular momenta. The spin precession takes place at an angular frequency ω_0 , named Larmor frequency:

$$\omega_0 = -\gamma \cdot B_0$$

It adopts values in the megahertz range, e. g., $\omega_0 \approx 2\pi \times 20$ MHz for ^1H nuclei in the low-

field spectrometers used for this thesis with a magnetic field strength of about 0.5 T.

3.2. The Free Induction Decay

Based on the orientation of nuclear magnetic moments in the magnetic field a very small longitudinal magnetization M_z evolves along B_0 . This feature is referred to as nuclear paramagnetism [53]. The build-up of this magnetization is characterized by the spin-lattice relaxation time constant T_1 , which typically ranges between milliseconds and seconds.

NMR does not detect the longitudinal magnetization, but transverse magnetization M_x in the plane perpendicular to the magnetic field B_0 , generated by the action of rf pulses. Such pulses can be described as weak oscillating magnetic fields of strength B_1 which are in resonance with the spin precession [53, 55] and are switched on over a period of time, i. e. the pulse duration. They cause a rotation of the originally longitudinal magnetization about the pulse irradiation axis during the duration of the pulse application. This rotation is actually another precession (see above) performed about the B_1 field. In the special case of a 90° pulse the magnetization is flipped into the transverse plane, where the magnetic moments precess about B_0 , so that the macroscopic transverse magnetization M_x precesses as well.

In order to detect a signal, one exploits the fact that the rotating magnetization generates a time-variable magnetic field, which induces an ac voltage in a coil wound around the sample. This voltage is proportional to the magnetization and can be recorded as a function of acquisition time using a sensitive microwave detector.

Yet, electronic movements, dipolar moments etc. in the environment of the spins induce small local magnetic fields, which vary with the position in the sample and fluctuate due to thermal molecular motions. Thus, the effective local field at the position of a spin, comprising the static magnetic field and the fluctuating field, varies in orientation and intensity. Because of this fluctuation also the precession frequency of the transversal component of the individual magnetic moments vary in space and time, so that the initial phase coherence is lost after a certain time. Hence, the transverse magnetization decays to zero. The signal measured after pulse irradiation is therefore referred to as the Free Induction Decay (FID). The signal decay is characterized by the spin-spin relaxation time constant T_2 . It contains information on molecular dynamics, but is also influenced by the inhomogeneity of the static magnetic field and residual dipolar couplings. After the application of the pulse, moreover, the longitudinal magnetization is built up again with its characteristic time constant T_1 .

The Fourier transformation of the time-domain signal, the NMR spectrum, contains a spectral line at the Larmor frequency ω_0 . The width $\Delta\nu_{1/2}$ of this line correlates with T_2 . Yet, in the largest part of this work we want to investigate time-domain signals after one pulse or a complex series of pulses.

As the nuclear spin is a quantum-mechanical phenomenon the simple macroscopic description does not suffice to explain the effects of complex pulse sequences. A short introduction to the quantum-mechanical basics of NMR is given in Appendix C.

3.3. Dipolar Interactions and their Influence on the NMR Signal

The energy of a nuclear spin system in a magnetic field splits into $2I + 1$ energy levels. This Zeeman effect, resulting from the interaction of the spin system with the magnetic field, dominates the behavior of the system (see Appendix C). However, it does not yield information about the structure of or the dynamics within the material, which both are of scientific interest. Yet, although inducing magnetic fields much smaller than B_0 , the internal interaction contributions within the spin system can afford this task. The spin interactions which are most important for ^1H solid-state NMR are

- the chemical shielding interaction, i. e. the indirect magnetic interaction between the external magnetic field and the nuclear spins via the electronic environment of the spins and
- the direct pairwise dipole-dipole coupling of nuclear spins.

Other interactions, such as the J coupling, are of minor importance in solid-state NMR [53]. The chemical shielding causes a magnetic-field-strength-dependent shift $\Delta\omega_{CS}$ of NMR spectral lines, i. e. the Chemical Shift (CS),

$$\Delta\omega_{CS} = -\delta\gamma B_0 ,$$

where δ ranges between 0 and 10 ppm (parts per million) for protons in polymers. This work is mostly concerned with low-field NMR. In this case, because of the small magnetic field strength $B_0 \approx 0.5$ T and Larmor frequency $\omega_0 \approx 2\pi \cdot 20$ MHz, there is only a small line shift due to chemical shielding interactions up to 200 Hz. At the same time the inhomogeneity of the magnetic field results in an intrinsic spectral line width of the spectrometer of ~ 2 to 4 kHz, precluding a resolution of chemical shifts. For this reason the dipolar coupling, which is independent of B_0 , is the dominating interaction here.

Dipolar couplings. A nuclear magnetic dipole moment μ associated with the nuclear spin I generates a small magnetic field B in its environment at a distance r [56]:

$$B = -\frac{\mu}{r^3} + 3\frac{(\mu \cdot r)r}{r^5}$$

This field acts upon the dipole moments of surrounding spins and vice versa, resulting in a direct dipolar coupling of spins through the space (see Fig. 3.1).

The magnetic interaction energy E_{mag} between two spin-carrying nuclei j and k of the same species is described as follows [56]:

$$E_{\text{mag}} = \mu_j \cdot B_k = -\mu_k \cdot B_j = \hbar^2 \gamma^2 \left(\frac{I_j \cdot I_k}{r^3} - 3 \frac{(I_j \cdot r)(I_k \cdot r)}{r^5} \right)$$

From this expression the dipolar coupling Hamiltonian (see Appendix C) can be derived as a quantum-mechanical analogue of the interaction energy using the correspondence principle [57]. As an approximation for a very strong external static magnetic field compared to the local fields arising from the dipolar couplings (secular approximation, see Appendix C) the strength of the dipolar coupling between two spins of the same

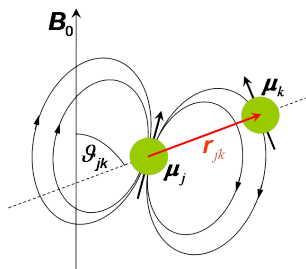


Figure 3.1.: Dipolar interaction between magnetic dipole moments.

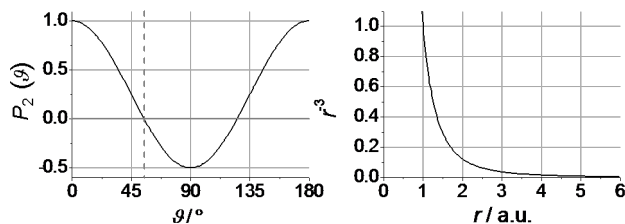


Figure 3.2.: Angular (left picture) and distance (right picture) dependence of the dipolar coupling strength given by Eq. 3.1, with P_2 being the second Legendre polynomial. The dashed line in the left plot marks the Magic Angle, where $P_2 = 0$.

species is given in the form of an angular frequency ω_D (see Appendix C):

$$\omega_D = -\frac{\mu_0 \hbar \gamma^2}{4\pi r^3} \frac{1}{2} (3 \cos^2(\vartheta) - 1) \quad (3.1)$$

The coupling strength depends on the distance r between the nuclei and the angle ϑ of the spin-spin interconnection vector r with respect to the magnetic field B_0 as depicted in Fig. 3.2. The orientational dependence is expressed by the second Legendre polynomial $P_2 = \frac{1}{2}(3 \cos^2(\theta) - 1)$ and the quantity μ_0 represents the magnetic constant.

The NMR signal of dipolarly coupled spins. The dipolar couplings in a sample influence the shape of the NMR signal in time and frequency domain. As described in Appendix C pairs of dipolarly coupled spins produce a doublet of spectral lines at positions

$$\omega = \omega_0 \pm (3/2) \langle \omega_D \rangle_t$$

instead of a single line at $\omega = \omega_0$. Here, the angle brackets represent the time average on the NMR time scale. As a multitude of possible orientations of spin-spin interconnection vectors exists in a rigid powder sample, associated with lots of different coupling strengths ω_D , the outcome is a superposition of spectral lines at different frequencies and finally a dipolarly broadened spectral line [58] with a characteristic shape, the so-called Pake pattern (see Fig. 3.3). Measurements of less ideal, real samples often show broad, rather featureless spectra instead. As an example the Fourier transform of an Abragam function (see Section 4.1) is plotted in the picture at the lower right of Fig. 3.3. In the time domain, the superposition of the different frequency components results in an accelerated decay with a reduced T_2 value as compared to the signal of a non-coupled system (see left column of Fig. 3.3).

Since the dipolar coupling strength varies with $(1/r^3)$, sample regions of higher density exhibit stronger couplings than those with larger average distances of the nuclei. Furthermore, molecular motions within a sample may change the orientation angle ϑ of the spin pairs. As a result, motions may average out the dipolar couplings (see Appendix C), when they are fast enough, i. e. when the correlation time τ_c of the motions is small compared to the inverse coupling strength ω_D^{-1} . In case of coupled proton pairs of CH_2 groups, e. g., this is the case for correlation times $\tau_c \ll 50 \mu\text{s}$ and fluctuation rates

$1/\tau_c \gg 20$ kHz, respectively. NMR is sensitive to the averaged dipolar coupling strength on the NMR time scale only. Hence, due to a partial pre-averaging of the couplings, e. g., very fast anisotropic vibrational motions in the picosecond range induce a lowering of the effective coupling strength detected by NMR, in comparison to the value calculated for the static case [53].

On the grounds of the influence of the dipolar couplings on the NMR signal ^1H low-field solid-state NMR is sensitive to segmental mobility in organic systems, such as polymers. Therefore, it can be applied to study the phase composition in polymers based on heterogeneities in molecular mobility, e. g., for measurements of the crystallinity in semicrystalline polymers or glassy fractions in filled elastomers, as well as for the determination of domain sizes. Moreover, it is also well-suited to study chain mobility in polymer crystallites, amorphous regions and melts or elastomers.

3. Low-Field Proton Nuclear Magnetic Resonance

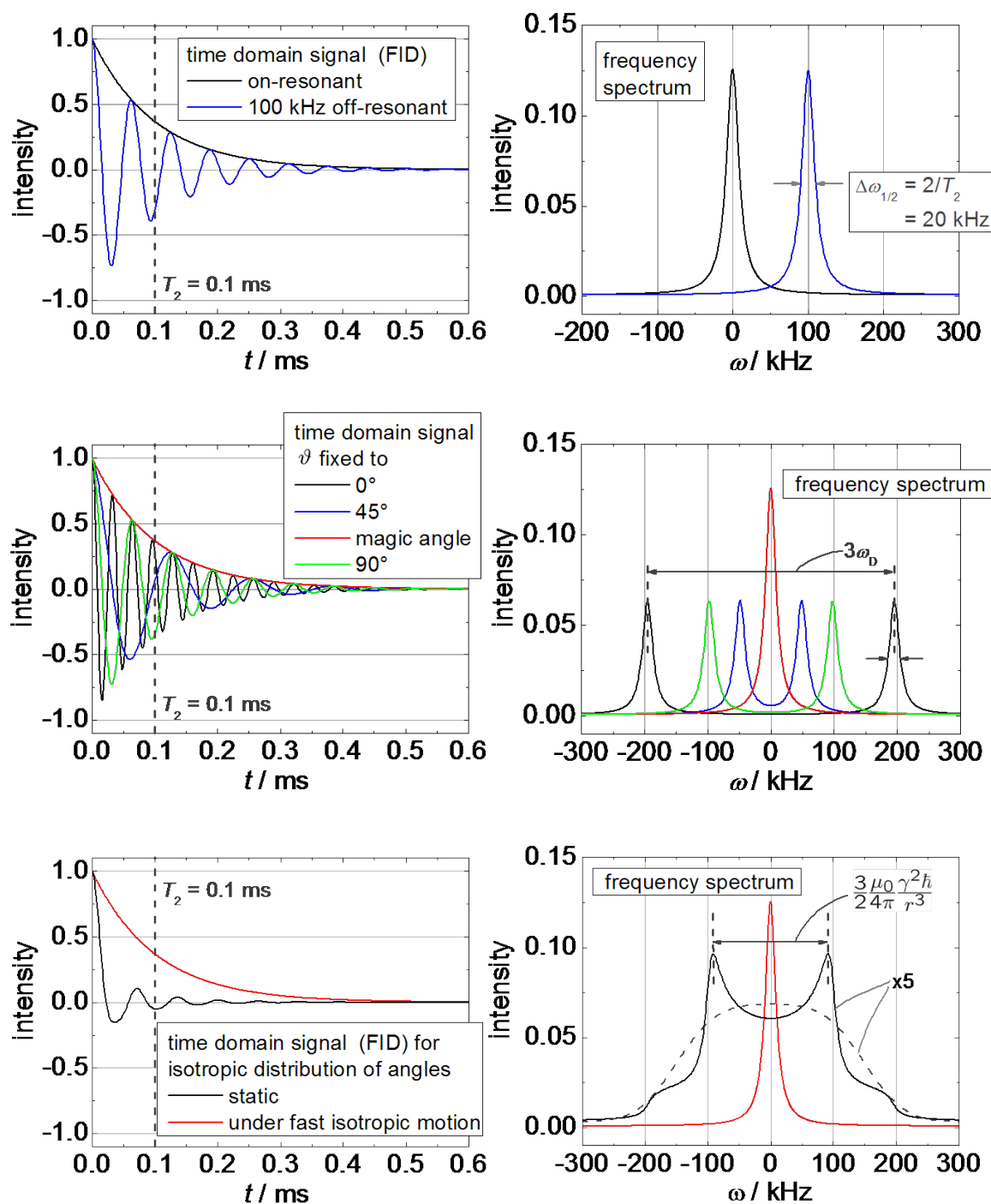


Figure 3.3.: Calculated ^1H NMR time-domain signal (FID, left column) and frequency spectrum (right column) for non-coupled spins for on-resonant and off-resonant measurement [53] (upper line), for dipolarly coupled spin pairs with different, fixed angles ϑ of the spin-spin interconnection vector with respect to the magnetic field (mid line) and for an isotropic distribution of angles ϑ (powder sample) for a rigid system and under fast isothermal motion (lower line). A true T_2 decay due to molecular dynamics was simulated by an exponential decay in the time domain signal with a T_2 time constant of 0.1 ms resulting in a Lorentzian shape of the spectral line with a width at half height of 20 kHz. The curves in the mid and lower line were calculated for the on-resonant conditions of the non-coupled system, using a distance $r = 1.80$ Å between the coupling nuclei. The Magic Angle referred to in the mid left picture is the angle at which P_2 is 0. For the powder a Pake Pattern is found in the frequency domain (lower right picture) which is averaged to a narrow line by fast isothermal motion. The dashed grey curve shows the Fourier transform of an Abragam function for comparison. For further explanations see Appendix C.

4. Low-Field Proton NMR Applications for the Investigation of Semicrystalline Polymers

4.1. The Free Induction Decay of Semicrystalline Polymers

A number of experimental techniques is available for the determination of crystallinities in semicrystalline polymers, such as Small and Wide Angle X-Ray Scattering (SAXS, WAXS), DSC, density and NMR measurements. Yet, they all deal with different measurement quantities. While, e. g., SAXS measurements detect electron density differences to distinguish between crystalline and amorphous material and DSC investigations rely on the changes in heat capacity or latent heat of the polymer during melting or crystallization, in low-field time-domain NMR the mass of immobilized material can be measured, based on differences in dipolar coupling strengths between the polymer phases, influencing the shape of the NMR signal.

In the crystallites the polymer chains are packed regularly and densely, with mean proton distances being slightly smaller than in the mobile-amorphous regions.¹ Due to the ordered arrangement of stems in the crystallites, the chain mobility is largely restricted, enabling only minor orientational changes of the proton spin interconnection vectors. Hence, the protons residing within the crystalline domains are subject to strong dipolar couplings ($\omega_D/2\pi \approx 20$ kHz), inducing a broadened ¹H NMR spectrum and a rapidly decaying time-domain (FID) signal with a short T_2 relaxation time of about 20 μ s, correspondingly (see Section 3 and Appendix C). Partial averaging of the couplings due to very anisotropic molecular motions with correlation times shorter than the inverse coupling strength, as present in the case of α_c -mobile polymers, slightly narrows the spectrum and delays the time-domain signal decay (see Section 5.2).

Far above the glass transition temperature the chains in the amorphous domains of a semicrystalline polymer exhibit fast and almost isotropic mobility, resulting in an averaging of the dipolar couplings on the NMR time scale and leading to a significantly reduced residual coupling strength as opposed to the value of the crystalline regions. Therefore, the NMR spectral line is narrow and the time-domain signal decays slowly with a long T_2 time constant (see below). In contrast to the features of the crystallite signal, here, line width and T_2 depend drastically on temperature, influencing chain mobility and density.

The fact that the crystallite and amorphous-phase signal of a semicrystalline polymer can be distinguished according to their spectral line widths has already been known in the 60s when continuous-wave NMR methods have been well-established [59–61]. Later on, also the decomposition of time-domain signals (FIDs) by means of extrapolation or fit methods was used to derive crystallinity data [62, 63].

Empirical Description of the FID of Semicrystalline Polymers. The shape of the ¹H FID in semicrystalline polymers is governed by the interaction of many proton spins. While there are analytical expressions to describe the FID for systems containing isolated groups of a few interacting spins [64], precise calculations for larger groups are very complex or even impossible [65]. However, it is known that, in case of dominating

¹For example, at 27°C the density of PCL amounts to 1.137 g/cm³ and 1.075 g/cm³ in the crystalline and amorphous domains, respectively (see Appendix E).

dipolar interactions between neighboring spins, Pake patterns arise, which are additionally broadened due to interactions with more distant spins. Yet, strong interactions between more than just next neighbors generally result in broad, rather unresolved spectral lines [66]. Such line shapes may be correlated to time-domain signals exhibiting a characteristic oscillation [66]. This oscillation is detectable in the crystalline-phase signal of PCL and PE at acquisition times between 0.02 ms and 0.05 ms (cf. Fig. 4.1 and Refs. [67, 68]) and is attributed to strong dipolar interactions due to regular interproton distances within the crystallites [66]. From the fact that the oscillation does not disappear near the glass transition temperature T_g (see Fig. 4.2 (a)), it is clear that this feature in fact originates from the packing of structures smaller than the chain segments, e. g. the monomers, as the segmental motions freeze at T_g .

The search for a suitable function for fitting the crystallite signal of PCL and PE was simplified by means of the series expansion of the FID [69] given by

$$f(t) = 1 - M_2 \frac{t^2}{2!} + M_4 \frac{t^4}{4!} - \dots + \dots, \quad (4.1)$$

which relies on the moments of line shape (M_2, M_4, \dots) and bears resemblance to the series expansion of the so-called Abragam function, a superposition of the Fourier transforms of a Gaussian and a box function [57, 70]:

$$f(t) = e^{-0.5(at)^2} \frac{\sin(bt)}{bt} = 1 - \left(a^2 + \frac{b^2}{3}\right) \frac{t^2}{2!} + \left(3a^4 + 2a^2b^2 + \frac{b^4}{5}\right) \frac{t^4}{4!} - \dots + \dots \quad (4.2)$$

In fact, the Abragam function fits the FID data of PCL and PE crystallites well and is known to be suited for the description of signals of other polymers, too [63]. Possibly, the inverse Fourier transform of a Pake pattern could also reproduce the shape of the crystallite signal of the polymers investigated herein. However, no line splitting could be found in the Fourier transforms of the FID signal, meaning that it either does not exist or that it is superimposed by signal arising from more mobile sample parts (see Fig. 4.14 (b)). For reasons of simplicity, the Abragam function is used as a fit function for the crystalline-phase signal contribution herein.

A comparison between the series expansions 4.1 and 4.2 given above shows that the second moment M_2 of the absorption line shape can be calculated from the fit parameters a and b according to

$$M_2 = a^2 + \frac{1}{3}b^2. \quad (4.3)$$

It yields information about the average local dipolar coupling a proton 'feels' within the sample [63] and is sensitive to the proton density and molecular motions, which partially average the dipolar couplings [66]. Hence, it may serve as an indicator for chain motions in polymer crystallites (see Section 5.2).

The time-domain signal of the mobile-amorphous phase decays slowly at temperatures far above T_g . To describe this decay quantitatively, Brereton derived a formula based on theoretical considerations for dynamic polymer chains, whose end-to-end distances obey a Gaussian distribution and for which the motions of the submolecule bond vectors are specified by a single correlation time [71]. As pointed out by Dadayli et al., the appearance of this complex function of Brereton is similar to that of a sum of a stretched exponential and one or two monoexponential functions [72]. However, the Brereton

function does not suffice to characterize the amorphous-phase signal (see Ref. [67]), assumedly because there is a multitude of possible bond vector relaxation times instead of only a single one (see Chapter 2). In case of the low-field measurements described herein, as a further aspect, we have to take into account the rather large inhomogeneity of the magnetic field (see Chapter 3.3), resulting in an additional variation of spin precession frequencies within the sample volume and a dephasing of the magnetization, i. e. an additional contribution to the decay of the amorphous-phase signal. Empirically, the amorphous-phase low-field time-domain signal can be described conveniently by a modified (stretched or compressed) exponential function

$$f(t) = e^{-(t/T_{2a}^*)^{\nu_a}} \quad (4.4)$$

with shape parameters T_{2a}^* and ν_a , as long as the fit interval is suitably restricted to short acquisition times [8, 73].

Often, a third component is necessary to fit the FID of a semicrystalline polymer appropriately (cf. Ref. [67]). This signal contribution is usually ascribed to a rigid-amorphous interphase [8, 68]. Yet, according to the considerations of Hansen et al. and Dadayli et al. it could also be classified as part of the mobile-amorphous-phase signal [67, 72]. Here, we want to follow the first interpretation, as the additional signal contribution usually exhibits a decay time constant ranging between the ones ascribed to the crystallites and the mobile-amorphous phase, thus indicating intermediate dipolar coupling strengths. A rigid-amorphous interphase has been identified before in PCL [68] and PE [12, 14, 74–78] by means of NMR investigations, but hints have also been found for other polymers by comparing crystallinity results from WAXS or density measurements with those from DSC [79]. We specify the interphase signal by a second modified exponential function

$$f(t) = e^{-(t/T_{2i}^*)^{\nu_i}} \quad (4.5)$$

with shape parameters T_{2i}^* and ν_i . However, the signal description using an interphase with fixed shape parameters is a simplification, as there is a gradient of chain mobility when chains pass over from the well-ordered, rather rigid crystallite to the mobile-amorphous phase (see Section 4.4.1).

Determination of the Signal Fractions. In order to evaluate the signal contributions of the three sample phases (see Fig. 4.1 (b)) the initial 200 μs of the FID, detected after a 90° pulse, are fitted using a weighted sum of the three functions 4.2, 4.4 and 4.5:

$$f(t) = g_c e^{-0.5(at)^2} \frac{\sin bt}{bt} + g_i e^{-(t/T_{2i}^*)^{\nu_i}} + g_a e^{-(t/T_{2a}^*)^{\nu_a}} \quad (4.6)$$

with the weighting factors g_c , g_i and g_a and the shape parameters a , b , T_{2i}^* , T_{2a}^* , ν_i and ν_a of the polymer phases. At longer acquisition times the influence of magnetic field inhomogeneities rises and no additional information about structure or dynamics in the sample is available. In comparison, a fit with only two components, neglecting the interphase contribution, has shortcomings in the region of the signal oscillation (see Fig. 4.1 (a)).

To ensure a stable fit with meaningful results, the three weighting factors g_c , g_i and g_a and the six shape parameters a , b , T_{2i}^* , T_{2a}^* , ν_i and ν_a have to be restricted to positive

values. Moreover, the constraint

$$g_c + g_i + g_a = I_{\text{tot},T}(t = 0)$$

has to be fulfilled, where $I_{\text{tot},T}(t = 0)$ is the total signal intensity at the acquisition time $t = 0$.² Due to the well-defined shape of the FID of PCL and PE in the region of the oscillation (see Fig. 4.1), a fit with free shape parameters is usually possible with sufficient fit quality. However, fixing shape parameters to known values obtained, e. g., from filter experiments (see Section 4.4.1) of course stabilizes and accelerates the fitting procedure. In both cases the fit residuals show almost no oscillations and the relative deviation between the fit and the measured data does not exceed 2%. This is well within the range found by Hansen et al. for FID signals of PE fitted by diverse combinations of fit functions [67].

The signal intensities s_p of the three polymer phases p relative to the total signal intensity $I_{\text{tot},T}(t = 0)$ of the (non-filtered) signal can be evaluated from the weighting factors g_c , g_i and g_a by normalization according to

$$s_p = \frac{g_p}{I_{\text{tot},T}(t = 0)},$$

with $p = c, i$ and a denoting the crystalline phase, rigid-amorphous interphase and mobile-amorphous phase, respectively.

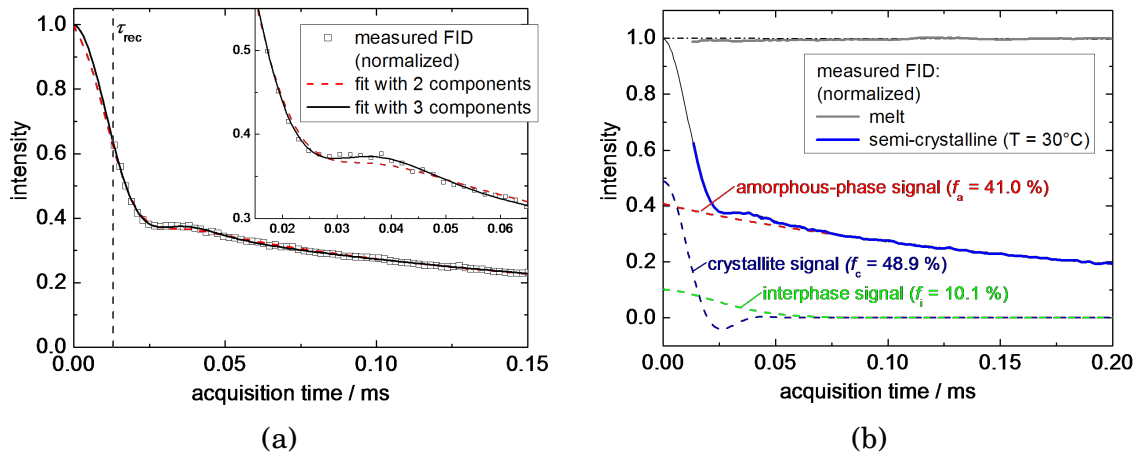


Figure 4.1.: FID of PCL, detected after a 90° pulse at $T = 30^\circ\text{C}$, (a) in comparison to fits with two or three components comprising an Abragam function and one or two modified exponential functions (see text) and (b) in comparison to the Curie-corrected melt curve measured at 90°C (see text). The data in (a) and (b) were normalized to the initial intensity of the melt curve as obtained by extrapolation (dash-dotted line in (b)). The dashed lines and the solid black line represent the phase-specific signal contributions and the complete time-domain signal, respectively, as derived in a three component fit to the FID signal. τ_{rec} designates the receiver dead time.

The proton-mass-averaged signal intensities s_p from the FID signal detected after a 90° pulse correspond to the mass fractions f_p of the sample (see Fig. 4.1 (b)). Uncertainties of the obtained fractions may arise from the measurement statistics ($< 0.5\%$), the

²Note, that a fit to FID signals of PCL and PE with the parameters g_c , g_i and $g_a = I_{\text{tot},T}(t = 0) - g_c - g_i$ produces the same results and is equally stable as a fit with the parameters $g_r = g_c + g_i$, $g_{ri} = g_i/g_r$ and $g_a = I_{\text{tot},T}(t = 0) - g_r$, as used in Ref. [8].

fitting procedure and small temperature deviations during the measurements. From the scatter of the mass fraction data obtained by fits with free shape parameters (see e. g. Fig. 4.2 (b) and Fig. 5.12) we estimate the relative uncertainty of the fractions to be smaller than 5%.

In order to enable a comparison with volume crystallinities obtained, e. g., from SAXS measurements, the mass fractions f_p can be converted to volume fractions $f_{p,V}$ via

$$f_{p,V} = \frac{(f_p/\varrho_{H,p})}{\sum_{j=\{c, i, a\}} (f_j/\varrho_{H,j})}, \quad (4.7)$$

taking into account the proton spin densities $\varrho_{H,p}$ of the phases p , calculated by multiplying the mass density ϱ_p of the individual phase by the weight fraction φ of protons in a polymer chain molecule ($\varphi \approx 0.088$ for PCL):

$$\varrho_{H,p} = \varphi \cdot \varrho_p. \quad (4.8)$$

Due to the rather similar spin densities of the individual polymer phases, mass and volume fractions, e. g., of PCL deviate by only 1% to 2% of the absolute quantities, which is indistinguishable within the uncertainty of the measurement. The mass or volume fraction of the crystalline-phase material is usually referred to as crystallinity.

Each ^1H low-field NMR time-domain signal of PCL and PE originating, e. g., from spin-diffusion or Saturation-Recovery experiments can in principle be analyzed in the way described above. However, the receiver dead time τ_{rec} of the spectrometer, which is required to ensure the complete decay of the pulse intensity and ranges between 11 μs and 15 μs for the low-field devices used here, prevents a detection of the complete FID signal. The initial part of the rapidly decaying signal related to the crystallites is lost, because signal acquisition is not possible during the dead time. Hence, the total intensity $I_{\text{tot},T}(t=0)$ is usually unknown (see Fig. 4.1 (a)). Quantitative data fits are only possible, if $I_{\text{tot},T}(t=0)$ can be estimated based on additional information. For example, in the case of a molten sample, there is no rapid initial signal decay due to the lack of crystallites. Therefore, $I_{\text{tot},T_m}(t=0)$ at the temperature T_m of the melt is obtained easily by an extrapolation of the measured FID data to $t=0$ (see Fig. 4.1 (b)). Furthermore, to account for changes of the signal intensity due to the different measurement temperature, a correction can be made here according to Curie's law [70],

$$I_{\text{tot},T_1}(t=0) = I_{\text{tot},T_2}(t=0) \frac{T_2}{T_1}, \quad (4.9)$$

with T_1 and T_2 being the temperatures of the two FID measurements. Such a Curie correction is necessary in general, to obtain comparable signal intensities from measurements at different temperatures. However, equation 4.9 is applicable only if the recycle delay between the individual signal-acquisition scans is long enough to enable complete T_1 relaxation.

As an example, in Fig. 4.2 (a) the FID signals of PCL at different measurement temperatures between the glass transition and the melting point are shown. The curves are rescaled using Curie's law (Eq. 4.9). Fits according to the explanations above, using free shape parameters, yield the sample fractions given in Fig. 4.2 (b). A significant decrease in crystallinity and increase in the mobile-amorphous fraction is detected when

approaching the melting temperature T_f , due to the onset of melting of the less stable crystallites (pre-melting) [17].

At low temperatures the measured fractions are largely influenced by the glass transition of polymer chains on the NMR time scale. The thermodynamic glass transition as detected by DSC at cooling rates of about 10 K/s happens to be close to the kinetic glass transition measured at frequencies in the range of Hertz, which is based on fluctuations inside the sample with typical correlation times on the order of seconds [10]. Yet, the NMR glass transition is generated by the freezing of motions with correlation times in the range of the inverse dipolar coupling strength, i. e. at about 50 μ s. It occurs at temperatures $T_{g,NMR}$ which are 30°C to 60°C higher than the DSC glass transition temperature $T_{g,DSC}$. When, due to a decrease in temperature, segmental motions in the amorphous phase are slowed down to correlation times higher than some tens of microseconds, i. e. longer than the duration of the measurement, the averaging of dipolar couplings, being responsible for the slow signal decay, is canceled. In this case, the signal of the (now rigid) chains within the amorphous phase cannot be distinguished from interphase (or even crystallite) signal anymore. Hence, with decreasing temperature around and below $T_{g,NMR}$ a rising part of amorphous-phase signal is evaluated as interphase signal. For this reason the rise of the mobile-amorphous-phase fraction in favor of the interphase fraction below $T_{g,NMR}$ (see Fig. 4.2 (b)) is not a true increase of the mass fraction but an artifact arising from the freezing of segmental motions of the polymer chains on the NMR time scale.

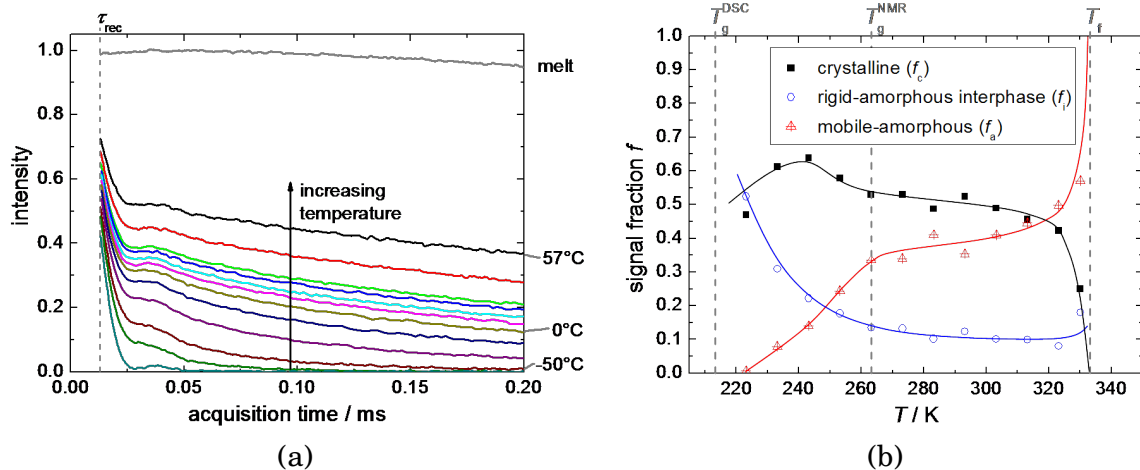


Figure 4.2.: (a) FID signals, detected after a 90° pulse, for PCL at different temperatures between the glass transition and the melting point. The intensities have been corrected according to Eq. 4.9 and normalized to $I_{tot,T}(t=0)$, determined by extrapolation of the melt curve (see text). τ_{rec} denotes the receiver dead time; (b) Signal fractions for PCL, obtained from fits to the FID signals in (a) with free shape parameters and a reference intensity $I_{tot,T}(t=0)$ derived from an extrapolation of the melt curve (see text). Above $T_{g,NMR}$ the signal fractions represent the sample mass fractions f_c , f_a and f_i of crystalline, mobile-amorphous and rigid-amorphous phase, respectively. The solid lines in (b) serve as guides to the eye.

This freezing and unfreezing of chain dynamics is also reflected in the temperature dependence of the shape parameters T_{2a}^* and ν_a of the amorphous-phase time-domain signal (see Fig. 4.3). Starting at $T_{g,DSC}$, at increasing temperatures the onset of the so-called motional narrowing of the NMR spectrum is visible, corresponding to a rise

of the relaxation time constant T_{2a}^* due to increasingly averaged dipolar couplings as a result of growing chain mobility. Moreover, below the NMR glass transition the distribution parameter ν_a of the modified exponential fit function 4.4 takes values below 1 (see Fig. 4.3 (b)), indicating a distribution of signals from different micro-environments with different relaxation time constants, reflecting the strong dynamic heterogeneity of the amorphous regions in the glassy state [73].

Above the NMR glass transition, where all chains within the amorphous regions are mobile, a T_{2a}^* plateau is reached. Despite a further temperature increase, the chain mobility rises only slightly as a result of mobility constraints, such as chain entanglements. Only after the onset of pre-melting a further increase in mobility and T_{2a}^* is detected (see Fig. 4.3 (a)).

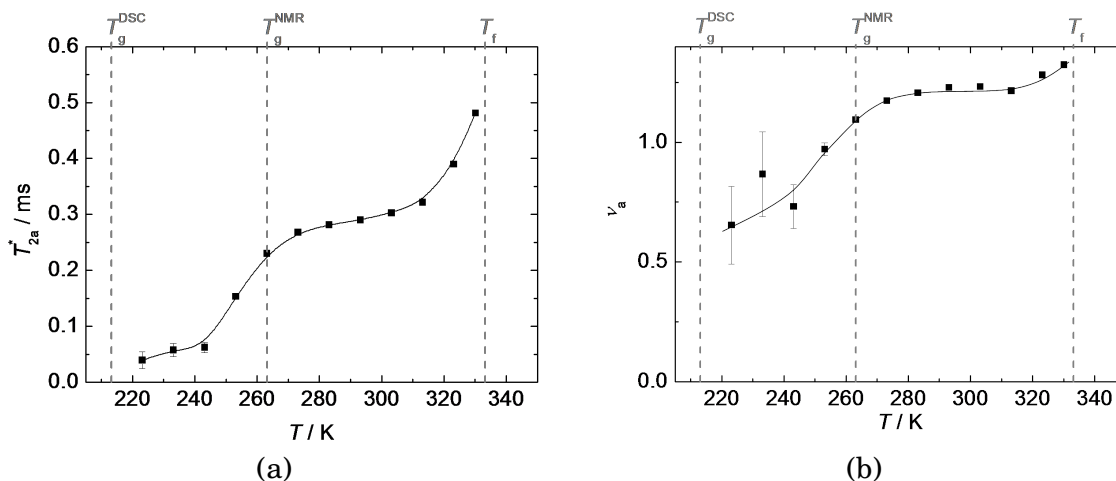


Figure 4.3.: Shape parameters for the mobile-amorphous phase of PCL as a function of temperature obtained from fits to MAPE-filtered FIDs measured at different temperatures. The solid lines are guides to the eye.

In summary, the measurement of 1H low-field NMR FID signals provides the opportunity to determine the crystallinity, or more generally the phase fractions, of semicrystalline polymers and allows the investigation of chain mobility within the amorphous phase to some extent. The measurement relies on mobility differences between the individual polymer phases and can therefore only yield meaningful phase fractions at temperatures far above the DSC glass transition. The experiment itself requires only a short measurement time and the data analysis is usually straightforward and can easily be generalized. However, the fit function has to be adapted for every new sample system. In the case of PCL and PE an interphase fraction has to be assumed to fit the data. A comparison of crystallinities as obtained from NMR, SAXS and DSC measurements will be given in Section 6.

4.2. The Magic Sandwich Echo

The Magic Sandwich Echo (MSE) sequence is a so-called time-reversing pulse sequence [80]. It refocuses rapidly decaying NMR signals, which are governed by the action of strong multiple dipolar couplings between the nuclear spins of the sample, by reversing

the dipolar dephasing [81, 82].

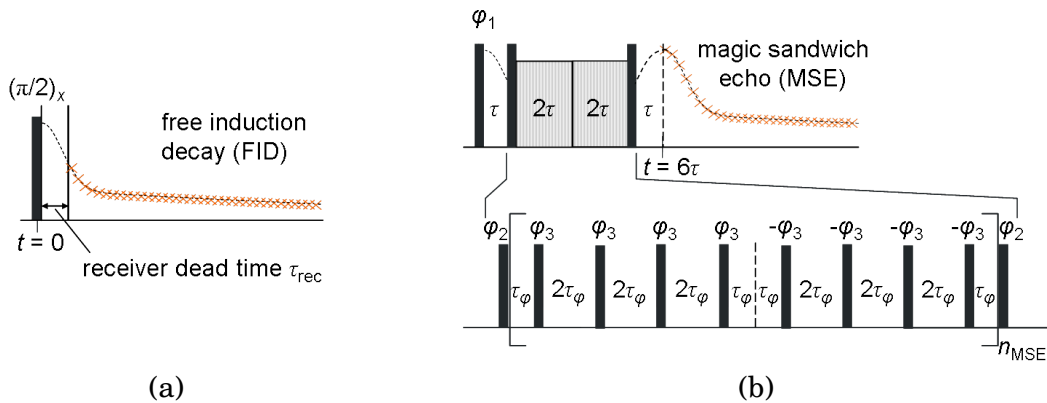


Figure 4.4.: Schematic plot of the 'simple' FID (a) and the Magic Sandwich Echo (MSE) (b) sequence. All pulses are 90° pulses. The signal loss in the FID caused by the receiver dead-time problem is overcome by using the MSE sequence. The waiting time τ in the MSE sequence is calculated as $\tau = (2\tau_{p90} + 4\tau_\varphi)n_{MSE}$, with τ_{p90} , τ_φ and n_{MSE} being the 90° pulse length, the phase-switching time and the number of MSE cycles, respectively. The duration of the MSE sequence is $t_{seq} = 6\tau$. The MSE phase cycle is $\varphi_1 = x \bar{x} x \bar{x} x \bar{x} x \bar{x}$, $\varphi_2 = \bar{y} y \bar{y} y \bar{y} y$, $\varphi_3 = x x x \bar{y} \bar{y} \bar{y} \bar{y}$.

The pulse sequence is depicted in Fig. 4.4 (b). It contains a 90° pulse followed by a delay τ and a so-called sandwich part of duration 4τ , comprising two 90° pulses of the same pulse phase with two pulse blocks, consisting of 4 90° pulses each, in between. The pulses within each block exhibit the same phase and the phases of the second block are inverted compared to the ones of the first block.³ After another delay τ the echo is generated.

Besides the MSE sequence there is a number of other sequences for the refocusing of signal losses due to dipolar dephasing [17, 80, 84]. A main advantage of the sequence used here is that it serves to bridge the receiver dead time τ_{rec} , which causes a signal loss in the FID after a 90° pulse (see Fig. 4.4 (a) and Section 4.1), because the echo appears only at a distinct time τ after the last pulse of the sequence. By choosing τ at least as long as τ_{rec} , a virtually dead-time free time-domain signal can be acquired. Besides, a second echo is generated in the middle of the sequence after 3τ which, however, is not usable, because it appears too soon after the previous pulse. For simplification, in the following FID's detected after a single 90° pulse will be termed 'FID' signals, while FID's detected after the application of the MSE pulse sequence will be referred to as 'MSE' signals.

The mode of action of the MSE sequence can be described as a time reversal of the effects of dipolar couplings on the spin system. It is based on the averaging of dipolar couplings to zero during the sequence, leaving the system at $t = 6\tau$ in a state where dipolar interactions seemingly have never been present before. This refocusing effect can be understood by applying Average Hamiltonian theory to the dipolar Hamiltonian of the sandwich part of the pulse sequence (for further explanations see Appendix D.1).

Two adaptations of the sequence have been made compared to the original version.

³The inversion of the pulse phases in the second block does not serve to refocus the signal but is necessary for the compensation of possible phase imperfections [83].

First, to account for phase-switching times between adjacent pulses which are required by the spectrometer, the long burst pulses suggested in Ref. [80] were substituted by blocks of 90° pulses as described above. Moreover, by inverting the phase of the last pulse compared to the original MSE sequence, in a so-called mixed version we combined the MSE with a Hahn echo, in order to refocus signal losses due to magnetic field inhomogeneities additionally (see Appendix D.1.1) [85, 86].

The refocusing action of the MSE sequence relies on the fulfillment of two conditions:

- $\omega_D = \text{const.}$ during the whole sequence and
- $\omega_D \ll 1/(6\tau)$ [83, 86].

Changes of the dipolar coupling strength ω_D during the sequence hamper a complete averaging of the couplings to zero and cause an inefficient signal refocusing and thus a signal loss compared to the FID (see Fig. 4.5 (a)). This feature provides the opportunity to investigate molecular dynamics on an intermediate time scale, i. e. on the order of tens to hundreds of microseconds, which alter the dipolar couplings during the sequence [83, 86–88]. With increasing sequence length the echo amplitude decays with a relaxation time T_2 characterizing the motion (see Section 5.2).

A complete averaging of couplings during the sequence can be achieved only in case of a short sequence comprising δ pulses. However, pulses of finite lengths with phase-switching times in between as well as pulse imperfections of the pulse phase or the pulse homogeneity cause changes of the mean coupling strength during the different parts of the sequence, which prevent a complete averaging and result in an increasing signal loss at rising sequence length t_{seq} [80]. By introducing a small perturbation into the Average Hamiltonian in a quantum-mechanical calculation, Rhim et al. found that the echo attenuation is a result of a too long sequence compared to the inverse coupling strength (see second condition above) and obeys a t_{seq}^2 dependence (see Appendix D.1.1) [80]. The signal loss due to strong dipolar couplings is demonstrated in Fig. 4.5 (b) for the case of PCL. The indirect dependence of the refocusing efficiency on the inverse coupling strength can be exploited for filter purposes, i. e. to discard signal from strongly coupled spins by tuning the sequence length [89, 90].

Since, compared to the FID, the decay of the echo intensity as a function of the sequence length t_{seq} is usually slow and the corresponding spectrum is narrowed appreciably [91], the MSE sequence is furthermore applied for line-narrowing purposes in Magnetic Resonance Imaging (MRI) [83, 85, 92].

During the MSE measurements for this work, it turned out that the echo position is slightly shifted to shorter times compared to the expected position marked in Fig. 4.4. This shift increases at rising sequence length, induced by an increase of either the phase-switching time τ_φ or the number n_{MSE} of MSE cycles. The latter is demonstrated in Fig. 4.6, presenting a linear dependence of the time difference between measured and expected echo position on n_{MSE} and the sequence length. Yet, the finite pulse lengths can be ruled out as a reason for the shift of the echo position, because an elongation and attenuation of the pulses causes a signal attenuation, but no additional time shift of the echo. Presumably, the shift effect results from imperfect pulse phases, and therefore grows with an increasing number of pulses.

Because a symmetric pulse sequence is favorable for the complete refocusing of signal losses due to off-resonance effects by the hidden Hahn echo within the sequence and for

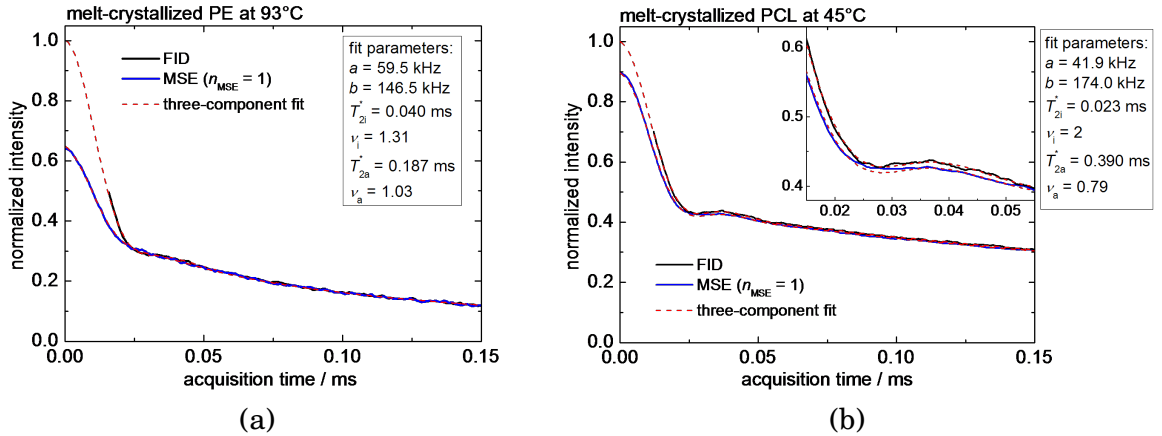


Figure 4.5.: FID detected after a 90° pulse and after the MSE pulse sequence with $n_{\text{MSE}} = 1$ for melt-crystallized PE at 93°C (a) and melt-crystallized PCL at 45°C (b). The dashed red lines represent fits by means of Eq. 4.6 to the 'simple' FID signal with free shape parameters and to the MSE curves with fixed shape parameters obtained from the fit to the FID curves. The signal loss in the MSE compared to the FID curve in (a) is mainly induced by molecular motions whereas in (b) it results from too strong dipolar couplings (see text), as here molecular motions (see Section 5.2) on an intermediate time scale can be excluded (see Section 5.1). The signal curves in (a) and (b) were normalized to the total signal intensity obtained from the extrapolation of the corresponding, Curie-corrected melt curves (see Section 4.1).

the efficiency of the averaging of dipolar couplings [82] (see Appendix D.1.1), it may be reasonable to shorten the interval τ prior to the sandwich part of the MSE sequence in order to compensate for the reduced time between the last sandwich pulse and the detected echo position.

Determination of signal fractions from MSE curves. Like the FID signals also the MSE curves show the typical features of the time-domain signal for semicrystalline polymers. They can be decomposed into three signal contributions and fitted by means of Eq. 4.6.⁴ The fits are defined better than for the FID, as here the complete signal is present starting at the echo top. To take into account the shift of the echo position, before further analysis the MSE curves have to be time-shifted in a way that the echo top is situated at zero time. This is in particular meaningful because fits to non-shifted MSE data using Eq. 4.6 prove to be rather unstable and yield shape parameters and fractions which may differ severely from the values for time-corrected curves. To permit an appropriate time correction, the signal should be acquired directly after the last 'sandwich' pulse and the corresponding receiver dead time. This ensures that the echo top itself is detected in fact.

In the fits to MSE curves occasionally it is beneficial to consider the echo shift directly, by introducing a shift parameter Δt into Eq. 4.6, replacing t by $t + \Delta t$. For the faint echos after long sequences, i. e. in case of large n_{MSE} or τ_φ , Δt should be used as a fixed parameter, determined from a linear extrapolation of Δt as a function of the sequence length t_{seq} for short sequences.

If the time shift is corrected in a suitable way, for short t_{seq} ($n_{\text{MSE}} = 1$ and $\tau_\varphi \leq 2.5 \mu\text{s}$)

⁴A fit with only two contributions, neglecting the interphase, overestimates the initial intensity of the MSE curve.

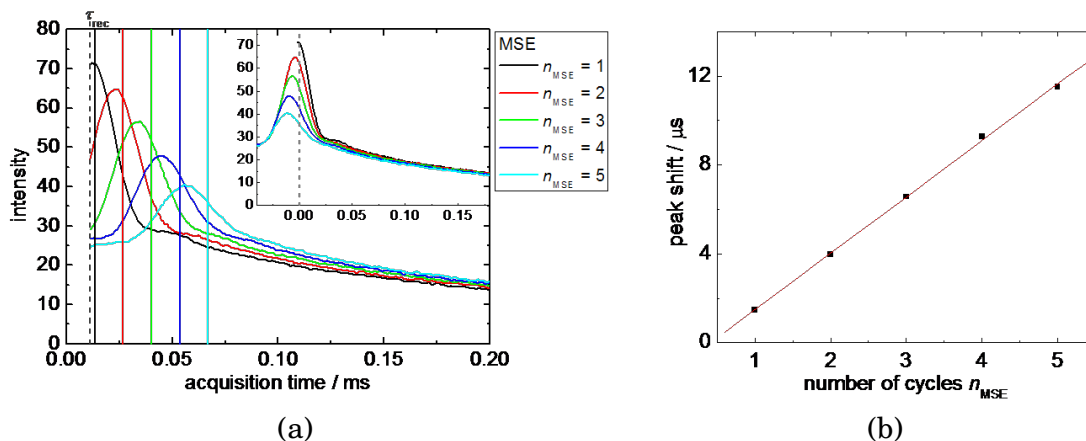


Figure 4.6.: (a) Magic Sandwich Echo (MSE) signals for PCL at 40°C detected directly at the end of the receiver dead time $\tau_{rec} = 11\mu\text{s}$ for different numbers n_{MSE} of MSE cycles. The straight lines mark the expected, theoretical echo positions. In order to illustrate the deviation between expected and measured echo position, in the inset the measured curves are time-shifted in a way that the expected echo positions appear at $t = 0$. In (b) the time difference between expected and measured echo position is depicted as a function of the number n_{MSE} of MSE cycles.

the shape of the MSE signal resembles the one of the FID closely for PCL and PE⁵ (see Fig. 4.5 (b)). This is in agreement with literature results [80, 82].

With increasing sequence length ($\tau_\varphi > 2.5\ \mu\text{s}$) the shape of the crystallite contribution to the MSE signal changes compared to the FID (cf. Ref. [80]). However, when Δt is used as a variable time-shift parameter in the fits, nevertheless the shape parameters a and b can be kept constant with sufficient quality of the fit.

Also for the shortest possible MSE sequence the measurement curves show a phase-specific signal loss when compared to the FID signal as a result of the phase-specific refocusing efficiency, which depends on the respective dipolar coupling strength and the possible occurrence of dynamics on an intermediate time scale. Such effects are known for the Solid Echo sequence as well [8, 76], where they seem to be even stronger. Like the dipolar coupling strength and motional rates, the signal loss depends on temperature.

In Fig. 4.7 the phase-specific MSE signal loss is depicted for PCL as a function of temperature between the glass transition and the melting point in relation to the corresponding mass fractions derived from the FID. For PCL a rather constant portion of MSE crystallite signal is lost over the whole temperature range due to strong dipolar interactions. On the other hand the mobile-amorphous phase hardly exhibits any loss at high temperatures, but a rising deficit at decreasing temperatures around and below the NMR glass transition, resulting from the slow-down of segmental motions to the intermediate time scale and further, accompanied by rising dipolar coupling strengths. The highest loss is found for the PCL interphase, supposedly as a result of dynamics on an intermediate time scale.

To obtain loss-corrected signal fractions, phase-specific correction factors $C_{corr,p}$ can be determined at every measurement temperature by comparing the signal intensities

⁵However, insufficient phase cycling can induce distortions of the signal shape, presumably due to pulse-phase imperfections. For a quick check a comparison of the MSE and the FID signal is reasonable. Here, e. g., MSE intensities being larger than in the corresponding FID give hints to an artifact.

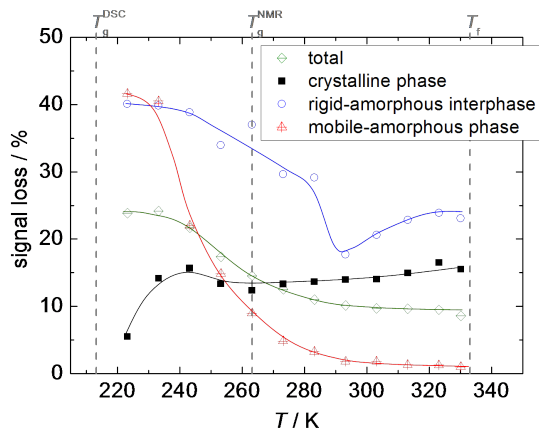


Figure 4.7.: Phase-specific signal loss due to the action of the MSE sequence ($n_{\text{MSE}} = 1$, $\tau_{\varphi} = 2.2 \mu\text{s}$) in PCL as a function of the measurement temperature T , obtained by comparison of the normalized signal intensities s_p from fits to the MSE curves with the mass fractions derived from the corresponding FID signals. The loss values are given relative to the sample mass fraction of the respective phase. The solid lines serve as guides to the eye.

$g_{\text{MSE},p}$ and $g_{\text{FID},p}$ of each phase p , derived from fits using Eq. 4.6 to the MSE and the corresponding FID signal, both measured at the same gain:

$$C_{\text{corr},p} = \frac{g_{\text{FID},p}}{g_{\text{MSE},p}}$$

Once these factors are known for a certain temperature, they can be used to calculate corrected signal fractions also for filtered MSE experiments (see Section 4.3), performed by using the same experimental parameters as for the 'pure' MSE measurement.

The MSE sequence can also be applied to determine the mass fractions of a semicrystalline polymer, if molecular dynamics on the time scale of the sequence length are absent. Here, it is favorable to use the shortest possible sequence⁶ for the measurement, in order to obtain a signal whose shape and intensity resemble the ones of the FID closely. The advantage of using the MSE signal instead of the FID is the better fitting quality and stability in case of the MSE, arising from the fact that there is no missing signal part due to the receiver dead time (see Fig. 4.4). However, here, the signal fractions obtained from the fit have to be converted to mass fractions by correction for MSE signal loss by means of suitable correction factors (see above). These again have to be determined by means of the corresponding FID. The mass fractions obtained from fits to the MSE signal deviate from the FID results by up to 2% on an absolute scale. This is usually within the uncertainty limits.

In summary, the Magic Sandwich Echo sequence serves to overcome the receiver dead time problem of the FID measurement and can be applied to measure sample mass fractions in semicrystalline polymers (see Chapter 8) although corrections of the phase-specific intensity loss due to the MSE sequence are necessary. Yet, the possible applications of the MSE sequence exceed the generation of a virtually dead-time free FID by far. Rather, the MSE sequence can be used as a dipolar mobile-phase filter and allows the investigation of molecular dynamics on an intermediate time scale (see Section 5.2).

⁶The shortest possible sequence is the one where $n_{\text{MSE}} = 1$ and τ_{φ} is as small as possible without violating the condition $\tau = (2\tau_{p90} + 4\tau_{\varphi}) \geq \tau_{\text{rec}}$ (cf. Fig. 4.4 (b)).

4.3. Proton Spin Diffusion in Semicrystalline Polymers

The process of ^1H spin diffusion has been known for many years and is frequently exploited in order to explore microdomain structures and sizes in heterogeneous polymer systems [77, 78, 93–105]. Existing work on NMR spin-diffusion measurements is predominantly concerned with block copolymers [94–96, 104, 106–112], periodic copolymers [113, 114] and semicrystalline polymers [77, 95, 97, 115–119]. However, the experiments are not bound to long-range order or periodic structures. Investigations, e. g., in purely amorphous polymers [102, 120] and blends of them are possible as well [100, 105, 121–125]. Up to now, moreover, there is a number of studies on more 'exotic' materials, such as core-shell latex particles [126–129] and water layers around them [130], polymeric proton exchange membranes [99], hybrid siloxane networks [131], amphiphilic co-networks [132] and membrane proteins [133, 134]. Glassy layers in filled elastomers represent a further potential field of application.

Apart from being non-destructive one main advantage of the method is that it does not necessitate sample modification before measurement, such as staining, deuteration or any other kind of contrast enhancement, as it exploits pre-existing differences in NMR interaction strengths. Length scales of a few up to a few hundred nanometers are accessible by spin-diffusion NMR, as comparable to SAXS measurements [17]. Furthermore spin-diffusion measurements provide information about interphases, which are difficult to obtain by other techniques [103, 111, 126, 127], and using appropriate filter sequences they also serve to gain information about interactions of neighboring proton spins via the investigation of spin dynamics [135].

In semicrystalline polymers spin-diffusion experiments enable the determination of lamellar thicknesses, provided that spin-diffusion coefficients are known. Vice versa, with known domain sizes spin-diffusion coefficients can be obtained. Additionally, information can be gained about the dimensionality of the spin-diffusion process [101] and hence about details of the polymer-phase morphology.

Macroscopic magnetization relies on the magnetic dipole moments of the nuclei in a sample and is coupled to their spin states. The term *spin diffusion* denotes the transfer of magnetization between neighboring spins mediated by dipolar couplings [17]. This transfer is not a true diffusion process involving material transport⁷ but it is based on a quantum-mechanical exchange process which, in a simplified picture, can be visualized as reversible spin flip-flop processes. It occurs, if magnetization is distributed nonuniformly over a sample with the result that these differences will be compensated after a certain time. The effect was named by Bloembergen in 1949, who found drastically accelerated T_1 relaxation in anorganic crystal compounds in the presence of paramagnetic impurities with relaxation times deviating from the theoretical value by a factor of 10^6 [136]. He discovered a magnetization transfer (i. e. spin diffusion) from the surroundings of the rapidly relaxing paramagnetic centers to the more slowly relaxing bulk material to be the reason for this behavior.

Based on a quantum-mechanical calculation (see Appendix F.1) it can easily be demonstrated for a system of isolated pairs of spins $1/2$, that a magnetization transfer in fact takes place under dipolar interaction [17]. The transfer is efficient only if the dipolar

⁷However, the designation *spin diffusion* is well-established because at appropriate length scales the magnetization transfer can be described by Fick's second law for diffusion [17, 116, 136, 137].

coupling strength is larger than the difference between the resonance frequencies of the nuclei involved. In essence, in the NMR spectrum there must be an adequate overlap of the spectral lines of these coupling nuclei [17]. In polymers the density of protons is high and their distances are small, e. g. ~ 0.18 nm between the two protons of a CH_2 group, usually resulting in an efficient proton spin-diffusion process due to strong dipolar couplings (~ 20 kHz) compared to the chemical shift frequency difference amounting, e. g., to up to 4 kHz for a 400 MHz spectrometer ($\delta \sim 1$ ppm to 10 ppm). By contrast, owing to their small natural abundance of 1.1 %, distances between the NMR-active ^{13}C nuclei in polymers are typically larger (~ 0.8 nm) and accordingly the resulting dipolar couplings are considerably weaker (~ 15 Hz) than for protons and low compared to typical chemical shift frequency differences (in the range of kilohertz), so that direct spin diffusion between these nuclei is very inefficient. It proceeds slowly, i. e. with time constants of tens of seconds, and can usually be neglected [17, 138]. Nevertheless there are techniques which allow for the detection of ^{13}C spin diffusion [17].

Contrary to material diffusion, spin diffusion is a coherent process, which can be reversed by inversion of the dipolar interaction. The Magic Sandwich Echo (MSE) sequence is an example for a sequence accomplishing a time reversal (see Section 4.2).

4.3.1. The Spin-Diffusion Experiment

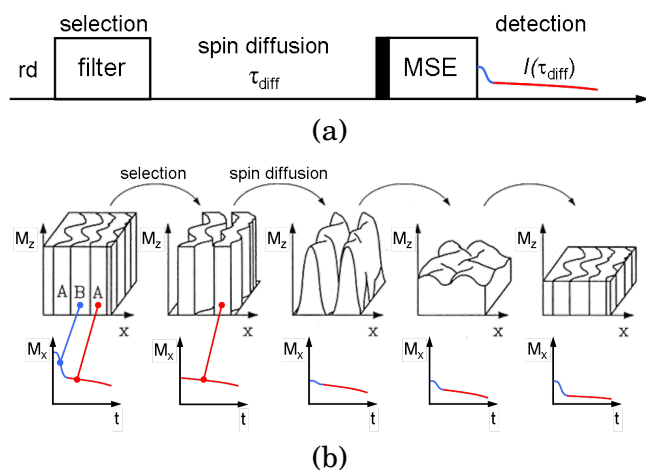


Figure 4.8.: Basic scheme of a ^1H NMR low-field spin-diffusion experiment: (a) generalized pulse sequence, (b) development of the magnetization profile in a two-domain sample system during the experiment [17, 139]; the bottom row depicts the free induction decay (FID) of the transverse magnetization measured at the corresponding points in time, exemplarily for the case of a mobile-phase-selected low-field experiment.

Spin-diffusion experiments in heterogeneous polymer systems allow the observation of magnetization transfer from source to sink domains. For this purpose magnetization in one of the polymer phases (denoted as source) is selected while it is depleted in the rest of the system (referred to as sink) by means of specific filter sequences (see Section 4.4). Thus, spatial gradients of magnetization are generated between source and sink domains within the sample, which induce a magnetization transfer (i. e. spin diffusion) during the subsequent mixing time τ_{diff} towards the initially non-polarized sink phase, until at long τ_{diff} the magnetization is evenly distributed again (see Fig. 4.8). The redistribution of magnetization among the polymer phases can directly be observed in the corresponding signal intensity, provided that phase-selective signal detection is possible. This is the case only if the polymer phases exhibit differences in NMR interactions, such as chemical shift, dipolar coupling strength, relaxation times and so on. In this case the equilibrium intensities of the NMR signals provide information about the

phase composition of the sample.

In the course of the spin-diffusion process the magnetization first reaches structures close to the magnetization source. Therefore information about the local arrangement of the polymer phases can be deduced. Furthermore the speed of the re-equilibration depends on the domain sizes and dipolar coupling strengths within the phases. The uniform magnetization distribution is, e. g., reached rapidly for small domains and strong couplings. Thus, the development of magnetization with increasing mixing time τ_{diff} yields information on domain sizes (and geometry) and on characteristic spin-diffusion coefficients of the phases (see Chapter 7).

The selection of magnetization as the first step of a spin-diffusion experiment is accomplished by a filter sequence (see Section 4.4) on the basis of differences in NMR interaction strengths of the individual polymer phases in the sample. However, because of a lack in chemical shift resolution, in low-field measurements one usually exploits differences in local chain mobility and dipolar coupling strength between the phases for filtering the magnetization as well as for phase-specific detection. Hence, only systems with dynamic heterogeneity on an appropriate length scale are suited for this purpose.

4.3.2. The Differential Equation for Spin Diffusion

Experimental proton spin-diffusion data can be analyzed based on a solution of the differential equation describing the spin-diffusion process. This equation is easily derived under the assumption of a linear arrangement of spins in a row [17]. In this case the development of magnetization M_i in direction of the magnetic field at the site i of one spin, exchanging magnetization with its neighboring spins at $i - 1$ and $i + 1$ with a constant rate R during a time Δt via dipolar couplings, can be described by a Master equation:

$$\frac{\Delta M_i}{\Delta t} = (RM_{i+1} - RM_i) + (RM_{i-1} - RM_i) .$$

Reformulating this equation yields

$$\frac{\Delta M_i}{\Delta t} = D \frac{(M_{i+1} - M_i) - (M_i - M_{i-1})}{(\Delta x)^2} , \quad (4.10)$$

with Δx and $D = R(\Delta x)^2$ being the distance between the spins in the row and the (in this case constant) spin-diffusion coefficient, respectively. For ^1H spin diffusion in polymers, because of the high proton density, it is allowed to transform this discrete equation into a continuous one, i. e. to approach $\Delta t \rightarrow 0$ and $\Delta x \rightarrow 0$. In this limit one finds a continuous differential equation, Fick's second law for one-dimensional magnetization transport, with the spatial coordinate x , the time coordinate t and a constant diffusion coefficient D :

$$\frac{\partial M(x, t)}{\partial t} = D \frac{\partial^2 M(x, t)}{\partial x^2} . \quad (4.11)$$

The general equation for a k -dimensional process and a variable diffusion coefficient D reads:

$$\frac{\partial M(r, t)}{\partial t} = \nabla (D(r, t) \nabla M(r, t)) = \frac{1}{r^{k-1}} \frac{\partial}{\partial r} \left(r^{k-1} D \frac{\partial M(r, t)}{\partial r} \right) . \quad (4.12)$$

Here, r is the spatial coordinate and k the number of orthogonal dimensions along which

a gradient of magnetization exists [102]. Depending on the diffusion scenario the dimension parameter k can adopt the following values [139]:

$$k = \begin{cases} 1 & \text{for a lamellar system,} \\ 2 & \text{for cylinders in a matrix and} \\ 3 & \text{for spheres or cubes in a matrix.} \end{cases}$$

In case of a constant diffusion coefficient D and a lamellar arrangement of domains Eq. 4.12 reduces to Eq. 4.11.

If there are further reasons for changes in magnetization apart from spin diffusion, for instance due to additional magnetization sources or sinks or material transport, corresponding terms have to be incorporated into the diffusion equation. True chain diffusion through the crystallites takes place, e. g., in PE or poly(ethylene oxide) [140]. If spin and chain diffusion occur on a similar time scale, a second diffusion term has to be supplemented to Eq. 4.12. However, this is not necessary for crystal-fixed polymers. Effects of longitudinal relaxation are introduced by means of an additional term $\frac{1}{T_1}(M_0 - M(r, t))$ [141, 142] (cf. Section 7.3), where M_0 denotes the equilibrium magnetization at long times $t \rightarrow \infty$ und T_1 is the longitudinal relaxation time constant.

The spin-diffusion equation 4.12 was solved analytically by many authors for special geometries similar to the situation in heterogeneous polymer systems, i. e. arrangements of two or three polymer phases and distinct dimensionality k of the spin-diffusion process, considering different initial and boundary conditions [89, 95, 97, 101, 102, 116, 139, 142–144]. Solutions for $k > 1$ can be derived by k -fold multiplication of the solution for $k = 1$, if the diffusion process is assumed to be uniform in each of the dimensions [139]. A one-dimensional geometry corresponds, e. g., to the idea of the idealized lamellar arrangement of crystallites in a semicrystalline polymer and will be used for data analysis in Chapter 7.

Regrettably, analytical solutions of Eq. 4.12 are complex and difficult to handle. Furthermore, they cannot be obtained under consideration of T_1 relaxation for the geometries named above. This does not pose a problem for the analysis of spin-diffusion data, if either spin diffusion or T_1 relaxation clearly dominates the time development of magnetization. The former applies for very slow T_1 relaxation compared to the characteristic spin-diffusion time (d^2/D) [141, 145], i. e. $T_1 \gg (d^2/D)$, the latter in the opposite case $T_1 \ll (d^2/D)$. Here, (d^2/D) is the time needed to transfer magnetization through a region of thickness d assuming a constant diffusion coefficient D . However, once spin diffusion and T_1 relaxation take place on the same time scale, $(d^2/D) \approx T_1$, the relaxation has to be taken into account in the analysis, as it influences the development of longitudinal magnetization during the mixing time.⁸ In semicrystalline polymers typical domain sizes d amount to ~ 10 nm and spin-diffusion coefficients range between 0.1 nm²/ms and 1 nm²/ms, resulting in characteristic diffusion times (d^2/D) between 100 ms and 1000 ms. In strong magnetic fields longitudinal relaxation usually proceeds slowly, with typical proton T_1 values at 400 MHz being in the range of seconds. Hence, the magnetization development is dominated by spin diffusion. Yet, at low field strengths T_1 is much smaller, ranging between ~ 50 ms and several hundreds of milliseconds for a 20 MHz

⁸On the other hand, in a Saturation-Recovery experiment for the determination of T_1 , spin diffusion occurring during the waiting period τ_{satr} has to be considered (see Section 5.1).

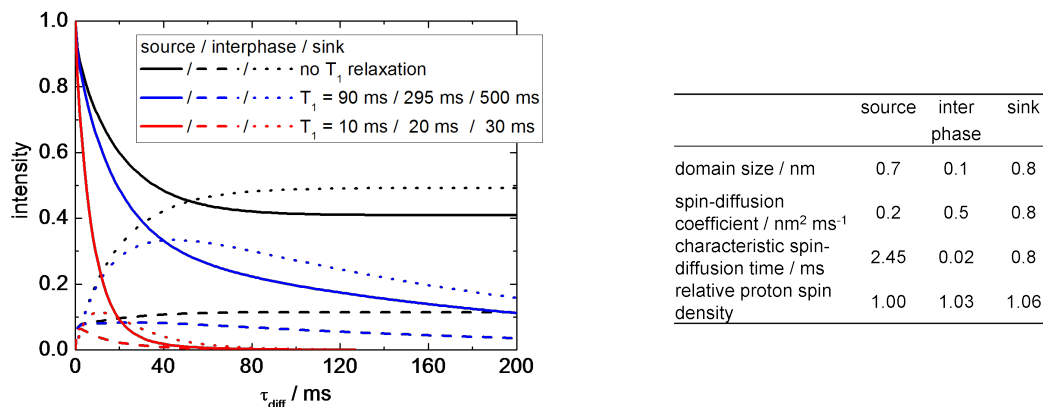


Figure 4.9.: Magnetization development in a simulated spin-diffusion experiment for a one-dimensional three-phase system, i. e. a periodic sequential arrangement of source and sink domains with interphases between them, under the influence of T_1 relaxation for different settings of T_1 . Without the effect of T_1 relaxation, the intensity ratio at long mixing times τ_{diff} represents the mass fractions of the distinct phases in the system. The simulation parameters are given in the table. The simulation is adapted to an experimental setup where longitudinal relaxation causes an intensity decay due to alternating storage of magnetization along and opposite to the direction of the magnetic field in subsequent scans.

spectrometer. Here, T_1 is in the order of the characteristic spin-diffusion time and T_1 relaxation cannot be neglected. Fig. 4.9 shows the effect of T_1 relaxation on the magnetization development in a spin-diffusion experiment simulated for a one-dimensional spin-diffusion scenario.

There are methods for reducing the T_1 influence in spin-diffusion experiments. One option is the alternating storage of magnetization along and opposite to the direction of the magnetic field by a so-called z filter after the selection period in subsequent scans, to partially eliminate relaxation effects from consecutive measurements [17]. This technique works properly only if the magnetization is destroyed after the selection period. Yet, this is not possible in a spin-diffusion experiment, as in this case no magnetization transfer could take place anymore [146]. For magnetization unequal to zero this procedure induces a decay of magnetization (see Fig. 4.9), which can be analyzed more conveniently than a build-up resulting from measurements without z filter. It was therefore used in all spin-diffusion measurements discussed in the following. As an alternative a 180° pulse can be inserted during the mixing time τ_{diff} in a way that T_1 effects before and after the pulse cancel each other out. However, this method operates effectively only in case of a single relaxation time of the whole system [146]. As the different components of a heterogeneous polymer system usually differ in their T_1 time constants, there is no other option up to now than to solve the differential equation 4.12 numerically after introduction of a T_1 relaxation term [8, 108, 109, 141, 147] (see Section 7.3).

4.4. NMR Filter Sequences

A variety of filter sequences usable for low-field spin-diffusion experiments can be found in literature. So-called T_2 filters relying on different T_2 relaxation times of the polymer components serve to select magnetization in mobile polymer phases. Well-known ex-

amples of this type are the *Hahn echo* filter [96, 133, 134, 148] and the *Goldman-Shen* filter [76, 113, 116, 117, 131, 147, 149–151]. Yet, the latter creates signal disturbances, the origin of which still seems to be under discussion [8, 117, 150].⁹ *Dipolar filters* base upon the differences in dipolar coupling strengths between the polymer phases. A part of this filter class including, e. g., the *12-pulse sequence* [94, 98, 106–108, 112, 120, 127, 132, 153], the *Magic Sandwich Echo* (MSE) [89, 95, 110, 144] and the *Magic And Polarization Echo* (MAPE) [8] exploits the incomplete averaging of the dipolar couplings in case of long sequence durations in terms of long cycle times in the Average Hamiltonian sense (see Appendix D.1.1) to achieve a filter action. They allow for the selection of magnetization in mobile polymer components. For selecting rigid-phase magnetization *double-quantum filters* can be employed [78, 97, 101, 103, 144], as originally proposed by Graf et al. [154] for 2D measurements in combination with sample spinning and refined by Ba and Ripmeester [155] for usage in static 1D experiments.

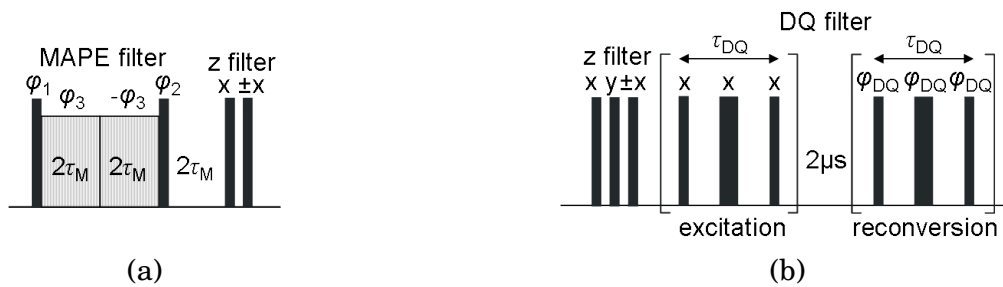


Figure 4.10.: Schematic sketch of the MAPE dipolar filter sequence (a) and the double-quantum filter sequence (b). Both include a z filter for usage in spin-diffusion experiments (see Section 4.3). The narrow bars in the plots denote 90° pulse and the broad ones in (b) represent 180° pulses. The two 'sandwich' pulse blocks of length $2\tau_M$ in the MAPE sequence in (a) are composed of four 90° pulses each, separated by intervals $(2)\tau_\varphi$ as in the case of the MSE sequence (see Figs. 4.4 and D.2). The duration of the MAPE filter amounts to $6\tau_M$ with $\tau_M = 2\tau_{p90} + 4\tau_\varphi$. The MAPE phase cycle is $\varphi_1 = y \bar{y}$, $\varphi_2 = \bar{y} y$ and $\varphi_3 = x \bar{x}$ and the DQ phase cycle is $\varphi_{DQ} = y \bar{x} \bar{y} x$.

For the investigations presented in this thesis, two filter sequences were used, which proved to work well in blockcopolymers [8, 156]:

- the MAPE sequence and
- a double-quantum filter.

Both sequences are depicted schematically in Fig. 4.10. Their adaptation to an application to semicrystalline polymers is demonstrated for the case of PCL in the following subsections. As an example, Fig. 4.11 shows the filtered time-domain signals in comparison to the FID and MSE signal for PCL.

⁹The utilization of T_1 filters in spin-diffusion experiments is unfavorable. In case the difference of the apparent T_1 relaxation times between the polymer components is high enough to be appropriate for filtering, spin diffusion must be very slow, as otherwise it would soon have equilibrated the magnetization discrepancy due to this T_1 difference in a T_1 measurement and only a small apparent T_1 gap would have resulted. Such a slow spin-diffusion process, however, can only transfer magnetization over very short distances precluding a meaningful analysis of the diffusion data [17]. Moreover, $T_{1,q}$ filters, e. g., the Packer sequence for selecting rigid-phase magnetization [141], cause problems inasmuch as spin diffusion already occurs during the filtering process. Thus, the beginning of the spin-diffusion process is not accessible for detection and therefore small domain sizes cannot be measured [17, 152].

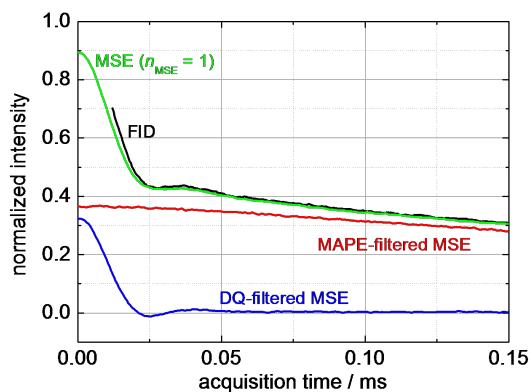


Figure 4.11.: Comparison of a FID and MSE signal for PCL at 45°C with signals from spin-diffusion experiments for a very short mixing time $\tau_{\text{diff}} = 0.21$ ms, using a MAPE ($\tau_{\varphi} = 37$ μs) and a double-quantum filter ($\tau_{\text{DQ}} = 13.8$ μs) as depicted in Fig. 4.10. All signals were normalized with respect to the total FID intensity at $t = 0$, derived from a Curie-corrected FID of the molten sample.

4.4.1. The MAPE Dipolar Filter Sequence

Similar to the MSE sequence the MAPE sequence comprises a ‘sandwich’ part consisting of blocks of 90° pulses between two flanking pulses (see Fig. 4.10 (a)). Moreover, as for the MSE, the mode of action is based on the refocusing of rapidly decaying signal due to strong dipolar interactions (see Appendix D.1.2). In contrast to the MSE sequence, here the ‘sandwich’ pulses are directly applied to longitudinal magnetization (polarization) instead of transverse magnetization. The generated echo is therefore named Magic and Polarization Echo (MAPE) [8]. As the MAPE refocusing efficiency is reduced in case of too strong dipolar couplings (cf. Section 4.2), the MAPE sequence, like the MSE sequence, can be used as a dipolar filter. Omitting the unnecessary generation of transverse magnetization, it is even more direct than the MSE filter.

The MAPE dipolar filter serves to select magnetization in the slowly relaxing mobile-amorphous phase of a semicrystalline polymer due to weak dipolar couplings there. For this purpose the filter length $6\tau_{\text{M}}$ has to be set in a way, that the refocusing condition $6\tau_{\text{M}} \ll 1/\omega_{\text{D}}$ (see Section 4.2) is violated for the rather strongly coupled crystalline and interphase regions, but fulfilled for the weakly coupled mobile-amorphous phase, so that the crystalline-phase and interphase signal is filtered out from the total signal and discarded. The parameter for tuning the filter action is the inter-pulse spacing τ_{φ} .

In Fig. 4.12 (a) MAPE-filtered time-domain signals, detected after application of the MSE sequence, are depicted to demonstrate the effect of the filter length variation. In case of PCL it is not possible to choose a perfect filter duration because a clear criterion to distinguish between the interphase and the mobile-amorphous-phase signal cannot be discerned. The curve shapes are rather unspecific except for the shortest durations. Fitting the data with a modified (stretched or compressed) exponential $I_0 \exp(-t/T_2^*)^{\nu}$, starting with the curves for the longest filter, reveals a continuous change in curve shape as indicated by a continuous decay of T_2^* and ν (see Fig. 4.12 (b)). This finding hints at a gradient of mobility through the rigid-amorphous and mobile-amorphous phase. Such gradients have been found before, e. g., in investigations on segmented poly(urethanes) using a Goldman-Shen filter [151]. When fitting the MAPE-filtered data with a sum of three modified exponentials, starting with the curve for the shortest filter, one of the three fit contributions disappears at an inter-pulse spacing τ_{φ} between 14 μs and 18 μs , and a second one between 36 μs and 38 μs . These vanishing components are interpreted as crystallite and interphase signal component, respectively. Hence, for PCL one MAPE

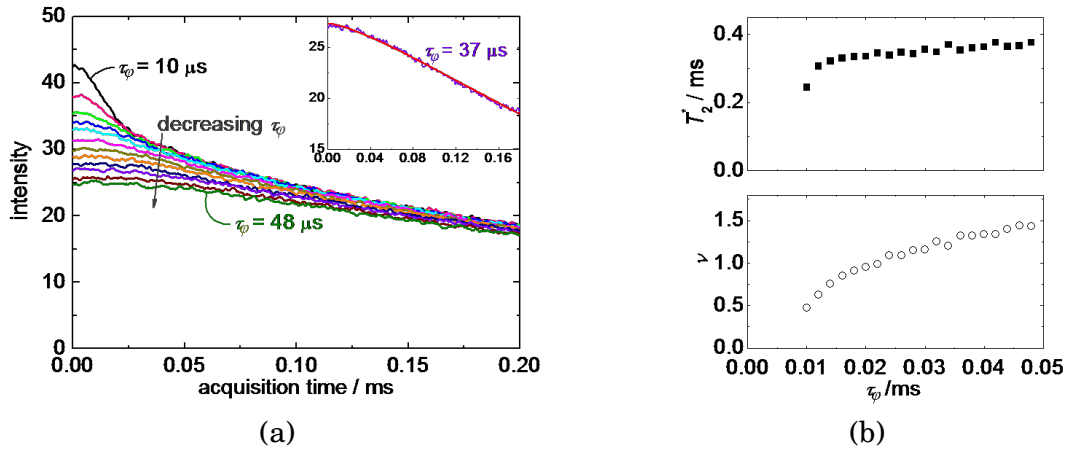


Figure 4.12.: (a) MAPE-filtered MSE curves for PCL at 45°C, detected in spin-diffusion experiments with a short mixing time $\tau_{\text{diff}} = 10 \mu\text{s}$ and different inter-pulse delays τ_ϕ in the MAPE 'sandwich' blocks. The inset shows the curve chosen as the amorphous-phase signal with a corresponding fit using a modified (stretched or compressed) exponential function; (b) Parameters T_2^* and ν from a fit with a single modified exponential function to the data depicted in (a) as a function of the MAPE inter-pulse delay τ_ϕ (see text).

cycle with an inter-pulse delay $\tau_\phi = 37 \mu\text{s}$ was used throughout the measurements to isolate the signal of the mobile-amorphous phase.

Mobile-phase-filtered signals are easily detected by using the spin-diffusion sequence depicted in Fig. 4.8 with the MAPE filter and a very short mixing time to avoid spin diffusion. From these signals the shape parameters T_{2a}^* and ν_a can be determined separately by a fit with a modified exponential function as described in Section 4.1 and used as fixed parameters in fits to FID or MSE signals to stabilize and accelerate the fit. But, as the choice of the MAPE filter length affects the shape of the signal ascribed to the mobile-amorphous phase, it slightly influences the mobile-amorphous fraction, measured in the sample, as well as the shape parameters of the interphase signal and the detected interphase fraction, obtained from a fit to the FID or MSE. The effect cannot be avoided and represents a source of uncertainty in the determination of the phase fractions. It should, in particular, be considered when comparing data sets detected with different MAPE filter lengths. For PCL, an elongation of the MAPE inter-pulse delay by about $8 \mu\text{s}$ (from $\tau_\phi = 38 \mu\text{s}$ to $46 \mu\text{s}$) results in a decrease of the fraction of the mobile-amorphous phase and an increase of the fraction of the rigid-amorphous interphase by up to 2 % each, while the sum of both fraction stays constant. A shortening of the filter length, however, causes stronger deviations.

4.4.2. The Double-Quantum Filter Sequence

Strong dipolar couplings between spins create a complex network of interacting spins in which multi-quantum coherences, involving orientation correlations between interacting spins (see Appendix C) [53], can be excited by certain rf-pulse sequences [54, 155]. For the investigations presented herein, a well-known and simple pulse sequence for excitation of multi-quantum coherences was used as a double-quantum filter for the selection of magnetization in the rigid polymer phase (see Fig. 4.10 (b)) [154, 155, 157].

The mode of action of the sequence is demonstrated for a system of isolated pairs of spins $1/2$ in the Appendix D.2 and shall be described here only briefly. The sequence is divided into a preparation and a reconversion part. The former, comprising two 90° pulses, separated by a short time interval τ_{DQ} , accomplishes the field-independent excitation of double-quantum coherences in the sample.¹⁰ As such a coherence itself cannot be detected directly, it is reconverted into longitudinal magnetization in the second half of the sequence by repeating the first half, however, applying a 4-step phase cycle over the pulse pair (see Appendix D.2). Signal detection is achieved here by means of the MSE sequence for refocusing rapidly decaying crystallite signal. (In practice this is again realized by using the spin-diffusion sequence depicted in Fig. 4.8 with a very short mixing time.) The 180° pulses in the middle of the excitation and reconversion parts eliminate effects due to resonance offsets and magnetic field inhomogeneity during the corresponding period in the sequence [157, 158].

The efficiency of the excitation and reconversion of double-quantum (DQ) coherences, i. e. the portion of originally longitudinal magnetization which is converted into DQ coherence and reconverted back into magnetization, depends on the product of the strength of the dipolar interactions between the spins and the duration of the excitation time τ_{DQ} [54]. The longer the excitation time (within a certain range) or the stronger the couplings, the more magnetization is converted, and the higher is the final signal intensity.¹¹ Using a short, fixed excitation time τ_{DQ} , the sequence excites DQ coherences efficiently only in strongly coupled sample regions, such as the crystallites in semicrystalline polymers. Hence, the measured signal intensity originates from these regions only. This filter effect shall be used here to select crystallite magnetization. As the T_1 relaxation does not affect DQ coherences, it does not influence the filtered signal also for long filter durations [155]. This feature makes the filter suited for spin-diffusion experiments. However, there is a strong signal loss due to the filter, as only a portion of the crystallite signal is converted into DQ coherence and back.

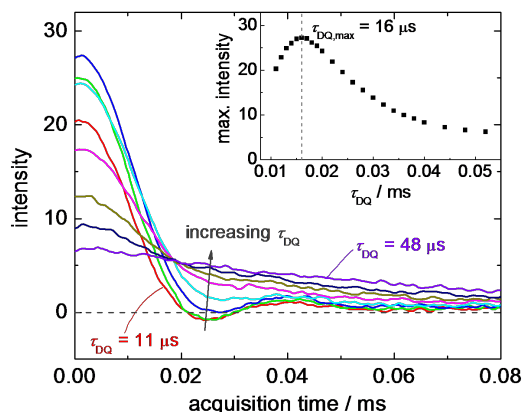


Figure 4.13.: Double-quantum-filtered MSE signals for PCL at 30°C , detected in spin-diffusion experiments with a short mixing time $\tau_{\text{diff}} = 20 \mu\text{s}$, for varying excitation times τ_{DQ} . The inset shows the total signal intensities at $t = 0$ as a function of τ_{DQ} .

By changing the excitation duration τ_{DQ} the filter action can be tuned. In the ideal case, only magnetization from spins in crystalline regions should be selected. In Fig. 4.13 DQ-filtered MSE signals of PCL are depicted for different excitation times. As expected, with

¹⁰Additionally, the sequence also excites higher order coherences, but only to a negligible extent at the short excitation times τ_{DQ} used here [40].

¹¹This provides the opportunity to derive the dipolar coupling strength, e. g., in polymer networks, by measuring the reconverted double-quantum intensity as a function of τ_{DQ} [40].

increasing τ_{DQ} magnetization from more weakly coupled spins in the interphase and the mobile-amorphous phase is increasingly selected, indicated by the rising portion of slowly decaying signal. The total signal intensity is built up until a maximum is reached at $\tau_{DQ,max} \approx 16 \mu\text{s}$. It decays again at higher τ_{DQ} due to molecular motions which change the dipolar coupling strength on the time scale of the sequence length and thus hamper an efficient reconversion of DQ coherences [40].

At every excitation time τ_{DQ} the filtered PCL signal contains a slowly decaying mobile-phase-like component (see Fig. 4.13) which even does not vanish near the DSC glass transition (where it still originates 4% of the total signal intensity at $\tau_{DQ} = 13 \mu\text{s}$). Such a deficit in DQ filter efficiency is known from literature (cf. Ref. [95]) and is present also for a poly(styrene)-poly(butadiene) diblock copolymer (see Fig. 4.15). Actually, fitting the DQ-filtered MSE signals of PCL with an appropriate quality is possible only using a three-component function as given by Eq. 4.6, while a two-component function is less suited to describe the data (see Fig. 4.14 (a)). Accordingly, the frequency spectrum, i. e. the Fourier transform of the filtered MSE signal, shows a superposition of a broad line related to the crystallites and two smaller, more narrow components, which seemingly correspond to interphase and mobile-amorphous phase (see Fig. 4.14 (b)). Moreover, at very short mixing times $\tau_{diff} < 0.1 \text{ ms}$ the signal component associated with the mobile-amorphous phase is enlarged compared to longer mixing times $\tau_{diff} \approx 0.21 \text{ ms}$. This is probably a filter artifact, the reason of which remains unclear. The diffusion of magnetization from crystallites to the interphase sets in already at $\tau_{diff} \approx 0.5 \text{ ms}$, and proceeds to parts of the mobile-amorphous phase during the first 3 ms. This should be considered when selecting the settings for the measurement of crystalline-phase-filtered signals.

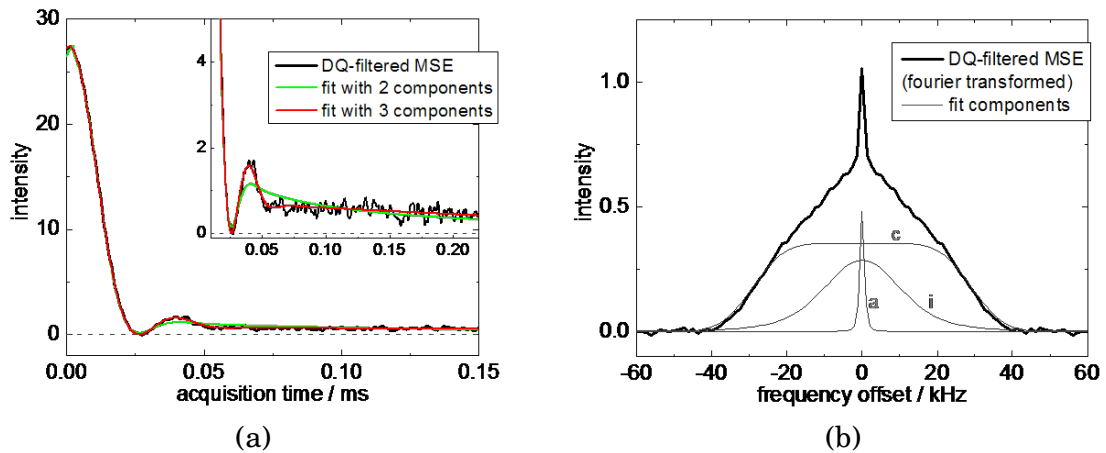


Figure 4.14.: (a) Double-quantum-filtered MSE signal for PCL at 45°C, detected in a spin-diffusion experiment with a short mixing time τ_{diff} for an excitation time $\tau_{DQ} = 16 \mu\text{s}$ compared to fits using two and three components (see text); (b) normalized Fourier transform of the signal in (a) with Fourier transformed fit components from the three-component fit, marked c, i and a, denoting crystalline-phase, interphase and mobile-amorphous-phase signal, respectively.

Powder Averaging. For glassy samples it is known that the magnetization left by the DQ filter is inhomogeneous in its strength throughout the material, because, according to the orientation of the interconnection vectors of dipolarly coupling spins (cf. Sec-

tion 3.3), different chain segments exhibit different coupling strengths. At short excitation times $\tau_{DQ} < \tau_{DQ,max}$, longitudinal magnetization arising from the most strongly coupled spins is selected. It originates from dense sample regions with spin interconnection vectors being oriented preferably in the direction of the magnetic field. In absence of further rf pulses this magnetization is now redistributed within the sample, due to 1H spin diffusion, reaching also more weakly coupled parts of the glass with unfavorable spin pair orientation. After a suitably long mixing time τ_{diff} a re-equilibration of the magnetization is accomplished (cf. [158]). This equilibrating process is called powder averaging and is accompanied by a decrease in the average dipolar coupling strength of the polarized material to an equilibrium value, reached for the uniformly magnetized glass.

The powder averaging is demonstrated in Fig. 4.15 for a poly(styrene)-poly(butadiene) (PS-PB) block copolymer at 45°C with a glassy PS phase and a rubbery phase containing mainly PB [159]. Here, the DQ filter was used to select magnetization from the glassy PS phase. The decrease in the measured, mean coupling strength during the equilibration is reflected by the slow-down of the decay of the DQ-filtered MSE signal and the decrease in the second moment M_2 of the line shape with increasing mixing time τ_{diff} , approaching the equilibrium value derived from an unfiltered MSE signal.

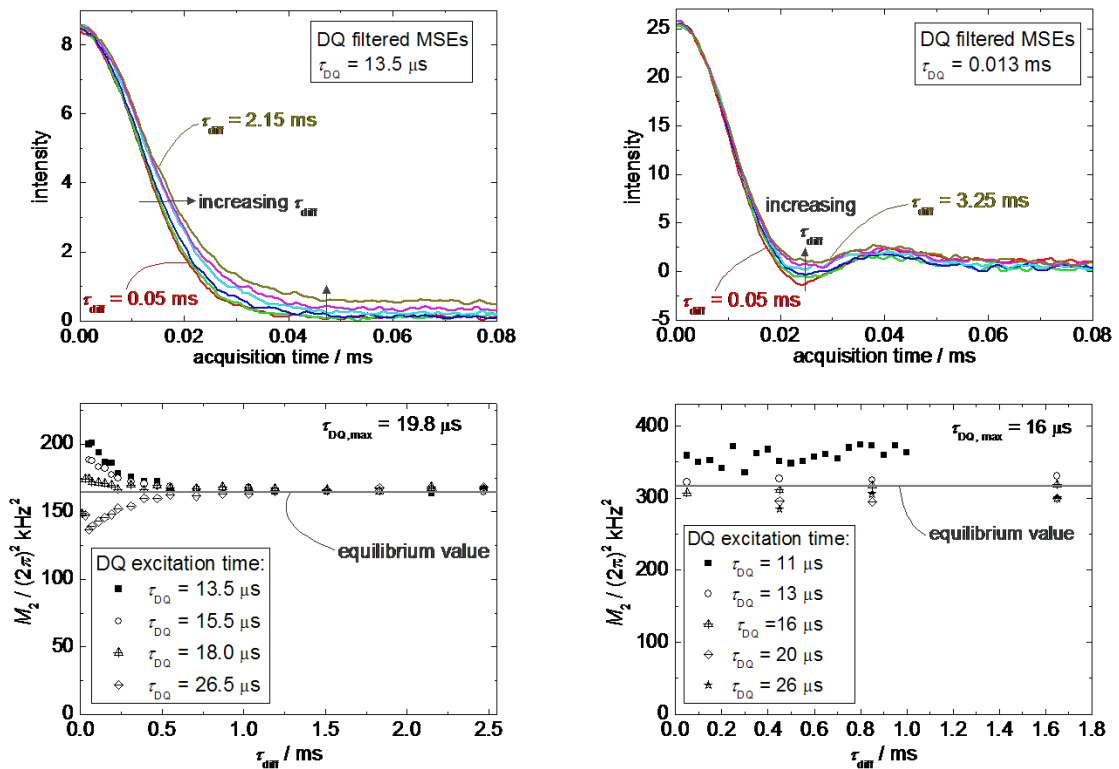


Figure 4.15.: Double-quantum-filtered MSE signals for a PS PB block copolymer at 45°C (upper left) and PCL at 30°C (upper right), detected in spin-diffusion experiments for a short excitation times τ_{DQ} at varying mixing time τ_{diff} as indicated in the plots, and second moment M_2 of the line shape for the same samples and temperatures (lower row; left: PS PB, right: PCL) as a function of the mixing time τ_{diff} for various excitation times τ_{DQ} . The intensity in the upper-row graphs, obtained as spectrometer output data, is given in arbitrary units.

At long excitation times $\tau_{DQ} > \tau_{DQ,max}$ the filter selects magnetization from rather

weakly coupled regions within the glassy phase (and interphase), while it depletes magnetization from the strongly coupled glassy regions. This occurs in analogy to the filter action of the MAPE (and MSE) filter at long filter durations ($\gg \omega_D^{-1}$), due to imperfections of the sequence which cause an insufficient time averaging of the spin interactions¹² [155] inducing a loss of signal from strongly coupled regions.¹³ Here, the re-equilibration is accomplished by a magnetization transfer from more weakly to more strongly coupled spins within the glassy domains, leading to an increase of the average coupling strength of the polarized material and the second moment M_2 with rising mixing time (see Fig. 4.15).

However, the situation is different in semicrystalline polymers, such as PCL. As demonstrated in the right column of Fig. 4.15, indeed M_2 of the crystallites, determined from DQ-filtered MSE signals, decreases with rising excitation time, as a result of the decreasing average coupling strength of the material excited by the filter (see above). At large excitation times $\tau_{\text{DQ}} > \tau_{\text{DQ,max}}$ also values below the equilibrium value for uniformly magnetized crystallites (derived from a non-filtered MSE signal) are reached. However, no equilibration due to a redistribution of magnetization can be seen at rising mixing time. Instead, the second moment M_2 of the line shape and hence the dipolar coupling strength remains constant.

These findings can be explained by considering the phase morphology in PCL. In the crystalline lamellae with their (more or less) all-trans chain conformation, the spin-spin interconnection vectors of the two protons bonded to a carbon atom all have the same direction with respect to the magnetic field (see Fig. 4.16) and hence exhibit the same coupling strength.¹⁴ Moreover, within their stacks the lamellae are arranged parallelly. Thus, after application of the DQ filter magnetization should be distributed uniformly within the crystalline material of a stack of lamellae according to the distinct orientation of the spin pairs and the corresponding coupling strength. Yet, as in a powder sample the stacks are isotropic in their orientational distribution (see Fig. 4.17), different stacks possess different magnetization levels. The measurement results depicted in Fig. 4.15 indicate that missing magnetization in one stack cannot be compensated by spin diffusion from other stacks with a higher magnetization level at short mixing times. The lack in magnetization transfer is presumably caused by a missing direct contact between the lamellae of different stacks, which forces magnetization to pass the amorphous regions first. However, the latter process is slow because of the small diffusion coefficient of the mobile-amorphous phase (see Section 7.1). By contrast, the glassy PS regions in the block copolymer contain chains with different segmental orientations and thus varying dipolar coupling strengths throughout the individual domains, enabling the equilibration at short mixing times.

Because of the missing equilibration of the magnetization distribution within the crystalline phase of PCL, for filtering purposes an excitation time τ_{DQ} should be used, which directly generates the most uniform magnetization distribution in all crystallites. One can easily find an excitation time, where M_2 of the filtered signal agrees well with the

¹²In the case of too long sequences (or too strong couplings, respectively) higher order effects in the Average Hamiltonian become too large to be neglected (see Appendix D.1)

¹³Hence, the DQ filter is in principle also suitable as a mobile-phase filter, when an appropriately long excitation time is used (cf. Ref. [95]).

¹⁴The mean dipolar coupling strength is dominated by the coupling between those geminal protons as a result of their close proximity.

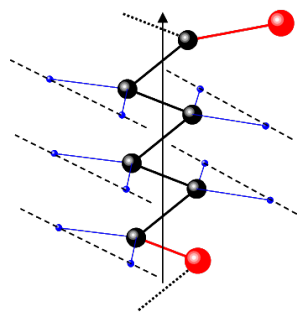


Figure 4.16.: Structure of the PCL monomer within the crystallites [49, 51]. The black, blue and red spheres represent the carbon, hydrogen and oxygen atoms, respectively.

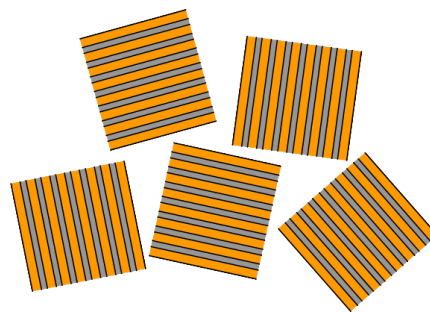


Figure 4.17.: Schematic plot of isotropically oriented stacks of lamellae within a semicrystalline polymer, with crystallites and amorphous regions marked in orange and grey, respectively.

one of the non-filtered MSE. However, at this value the filtered signal comprises a significant interphase portion. Hence, a compromise has to be made, considering the purest possible crystallite signal with the highest possible intensity and the most uniform distribution of magnetization within all crystallites. The purest crystalline-phase signal is attained in PCL for an excitation time $\tau_{\text{DQ}} = 13.8 \mu\text{s}$ and a short mixing time of $\sim 0.2 \text{ ms}$. In this case $\sim 10 \%$ of additional signal (relative to the intensity of the crystalline-phase signal) from the interphase ($\sim 7\%$) and the mobile-amorphous phase ($\sim 3\%$) are detected. However, here, the lamellar stacks are not polarized completely and uniformly. The average coupling strength of the regions in which magnetization is selected by the filter, is slightly higher than in case of a uniform distribution of magnetization, indicated by a slightly higher second moment M_2 . Hence, the values of the shape parameters a and b , derived from a fit to a DQ-filtered MSE and a pure MSE, differ. Nevertheless, for fits to data from DQ-filtered spin-diffusion experiments it seems reasonable to keep a and b fixed at values obtained from fits to the non-filtered MSE signal, in order to ensure a high fitting speed and stability. In doing so, the fitting quality proved to be sufficient.

5. Dynamics in Crystallites of Semicrystalline Polymers

In semicrystalline polymers dynamics take place within the mobile-amorphous domains, but also within crystallites and interphase regions, with correlation times, which may range from picoseconds to seconds and longer. Investigations of the dynamical processes are relevant with regard to material design, as molecular motions in a polymeric material are related to its macroscopic characteristics, such as brittleness, load capacity, mechanic moduli, creep or drawability [17, 43, 44, 160]. According to their time scale relative to the time scale of the inverse interaction frequency, motions are usually classified into fast, intermediate and slow motions (see Fig. 5.1). A number of NMR techniques is available for studying dynamical processes with respect to their characteristic correlation time, amplitude and geometry. Depending on the motional regime, they rely on different effects of the dynamics on the NMR signal [53].

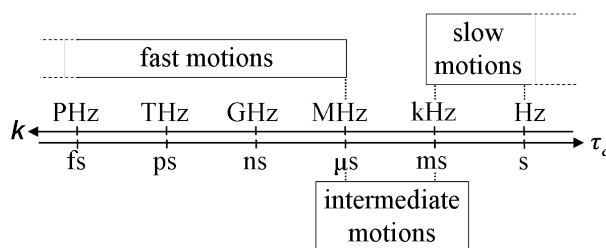


Figure 5.1.: Classification of motions in polymers according to their correlation time τ_c or motional rate $k \propto 1/(\tau_c)$ relative to the time scale of the (inverse) NMR interaction frequency.

In this chapter, chain dynamics within the PCL crystallites shall be examined, using different low-field and high-field NMR techniques. Here, the focus is placed on the investigation of possible intermediate-regime motions, which might give hints to an α_c process, i. e. helical jumps within the crystallites. The presence of such motions in PE crystallites is well-known from literature (see Section 5.2). In the second part of this chapter the time scale of this chain flip motion will be studied quantitatively, by means of the MSE sequence and compared for different sample morphologies and molecular weights.

5.1. Investigation of PCL Crystallite Dynamics on Different Time Scales

As known from literature, the linear aliphatic polyamide Nylon does not exhibit an α_c process [44], because of its long repeat unit and the high energetic barrier for rotational and translational motions of the crystalline chain stems, which would require the breaking of hydrogen bonds between the stems [45]. The molecular structure of PCL is very similar to the one of Nylon and accordingly one would assume that PCL is a crystal-fixed polymer as well. However, from a comparison of simulated spectral line shapes with measured Chemical-Shift Anisotropy (CSA) patterns, Kaji and Horii concluded that jump motions of the methylene groups in the intermediate to slow-motion regime take place in PCL crystallites [161]. Moreover, Ito et al. detected a mechanical α relaxation and a decay of the second moment of the NMR proton line shape in different linear aliphatic polyesters with long repeat units, which also indicates the occurrence of

an α_c process within the crystallites [162].¹ Yet, they did not investigate PCL directly, but samples with even numbers of methylene groups between the COO groups. Still, a consistent overall picture of PCL crystallite dynamics is missing. Hence, here investigations on PCL dynamics were performed by means of ^1H low-field T_1 , FID and MSE measurements as well as ^{13}C high-field DIPSHIFT and CODEX experiments, in order to clarify, which kinds of motions take place in PCL crystallites.

Spin-Lattice Relaxation in PCL. The term spin-lattice relaxation designates the build-up of longitudinal magnetization in a static magnetic field (see Section 3.1) due to the energy exchange of the nuclear spins with their environment, the so-called lattice. This process is induced by fast fluctuations of the local, effective magnetic field strength, mediated by, e. g., the varying dipolar coupling strengths between the spins as a result of molecular dynamics [17, 53]. Motions taking place with rates close to the Larmor frequency ω_0 enable an effective energy transfer between the spins and the lattice and cause a fast relaxation with a short relaxation time constant T_1 . At much higher or lower rates an efficient coupling between the spins and the lattice is not possible, resulting in a slow relaxation with a high value of T_1 [65, 164].

As temperature variations cause changes in the correlation time and the rate of molecular motions, T_1 measurements at different temperatures can give information about the time scale of motions within a sample to a certain extent. In order to determine ^1H T_1 relaxation time constants of PCL, Saturation-Recovery experiments [55] have been performed for an industrially produced PCL sample ($M_n = 42.5$ g/mol) between 27°C and 50°C using the low-field spectrometer ($B_0 = 0.5$ T). Here, the longitudinal magnetization was destroyed by means of a saturation comb of 90° pulses and rebuilt during an incremented waiting period τ_{Satr} . In order to avoid signal loss during the receiver dead time, the MSE sequence was used to detect the rebuilt signal. Fig. 5.2 (a) exemplarily depicts measured signals at 45°C for different values of τ_{Satr} . It demonstrates the build-up of magnetization at increasing waiting time. The signal contributions of the different polymer phases have been evaluated by fitting the measured signals by means of Eq. 4.6. They were corrected for MSE signal loss, according to the explanations in Section 4.2.

As shown in Fig. 5.2 (b) for the mobile-amorphous and the crystalline phase, the magnetization build-up cannot be described by a monoexponentially rising function. The reason for this finding is, beside a possible distribution of T_1 time constants, the occurrence of proton spin diffusion (see Section 4.3) on the time scale of the spin-lattice relaxation, inducing a mixing of information from both processes in the measured data [8, 145, 165]. In the case of PCL, the mobile-amorphous phase, with its fast intrinsic T_1 relaxation and magnetization build-up, acts as a source of magnetization for the more slowly relaxing rigid-amorphous interphase and crystalline phase. Hence, during the relaxation it transfers magnetization into these phases via spin diffusion, thus modifying the shape of the build-up curves of all three phases.

Here, a fit to the total build-up curve of the complete sample, using a sum of monoexponentially rising functions, will neither yield reliable information on the number of individual physical phases within the sample, nor true T_1 relaxation time con-

¹The origin of the mechanical α process is not clarified completely. In PE, e. g., two α processes were found. One of them seems to result from block slips and the other one is said to originate from the diffusive chain motion through the crystallites, which is based on local chain flips, i. e. the α_c process [163].

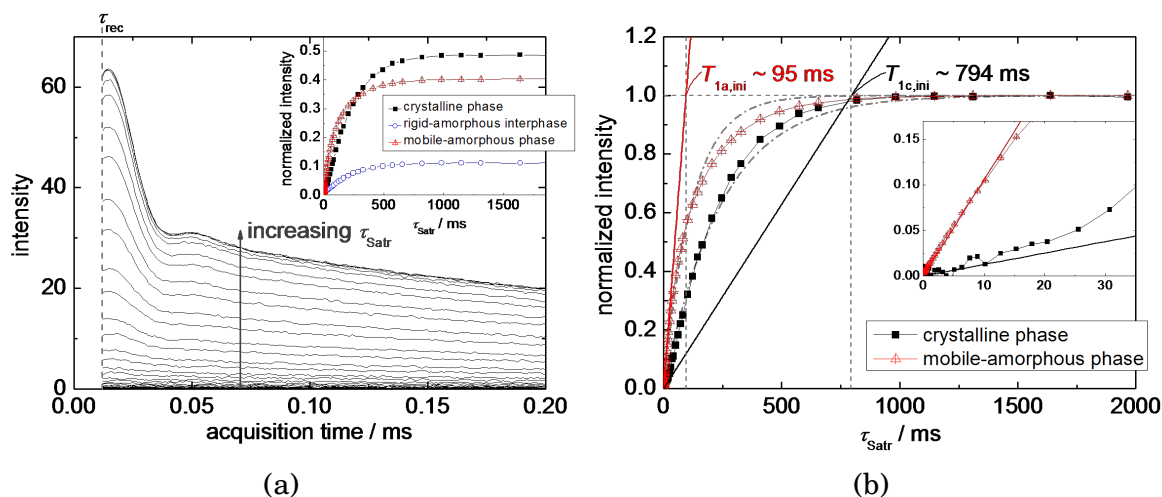


Figure 5.2.: Saturation-Recovery measurement of PCL ($M_n = 42.5$ kg/mol) at 45°C : (a) Measured data for different build-up times τ_{Satr} between 0 and 2000 ms, detected by means of the MSE sequence. The inset shows the normalized and corrected signal intensities s_c , s_a and s_i of crystalline phase, mobile-amorphous phase and interphase, respectively, as a function of τ_{Satr} (see text). The label τ_{rec} designates the receiver dead time; (b) Signal intensities of the mobile-amorphous phase and the crystalline phase, as given in the inset of (a), but normalized to a plateau value of 1. The dash-dotted lines represent fits with monoexponentially rising functions and the solid lines depict linear fits to the initial curve rises with a close-up view given in the inset.

starts [145,147]. Such true time constants can only be obtained by taking into account the spin-diffusion process [142], e. g., by model fits with simulated build-up curves. However, from the Saturation-Recovery build-up curves of the individual phases, time constants $T_{1,\text{ini}}$ can be estimated from the very initial slope by fitting the initial curve rise by means of a linear function and by evaluating the time, at which the fit curve meets the plateau intensity of the build-up curve at long τ_{Satr} (see Fig. 5.2 (b)). In case of a suitably narrow fitting region, the $T_{1,\text{ini}}$ values determined this way are hardly distorted by spin diffusion, because, at the beginning of the build-up process, the magnetization levels of all phases are equal ($M_z = 0$) and a driving force for spin diffusion does not exist [152].

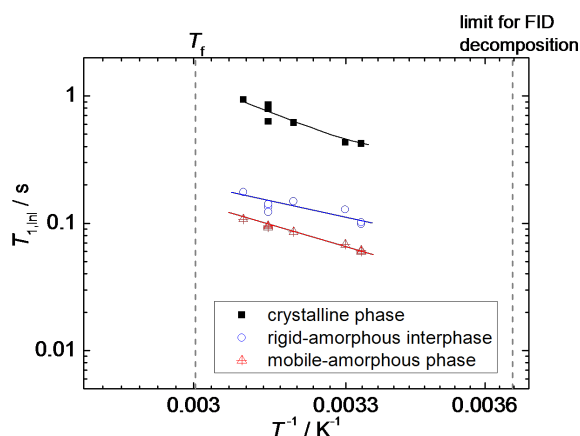


Figure 5.3.: Relaxation time constants $T_{1,\text{ini}}$ of the individual PCL phases as a function of the inverse measurement temperature, derived from Saturation-Recovery measurements of industrially produced PCL ($M_n = 42.5$ kg/mol). The solid lines are guides to the eye. The dashed, straight lines mark the melting temperature T_f and the lower temperature limit, at which chain dynamics within the mobile-amorphous phase start to freeze, so that a time-domain signal decomposition becomes unreliable (see Section 4.1).

By examining these $T_{1,\text{ini}}$ time constants of PCL in the investigated temperature range (see Fig. 5.3), two trends can be found:

- $T_{1,\text{ini}}$ decreases with decreasing temperature for all three polymer phases and
- the time constants of the mobile-amorphous phase are considerably smaller than the ones of the crystalline phase, while the values for the interphase lie in between.

For a Debye process, i. e. a motional process characterized by a single correlation time τ_c and a monoexponential decay of the correlation function, the correlation-time dependence of the T_1 relaxation time constant can be described by an inverse Lorentzian function with a sharp minimum where the motional rate ($1/\tau_c$) equals the angular Larmor frequency ω_0 of the spins [17, 53]. Assuming an Arrhenius dependency of τ_c on the temperature T , the T_1 curve can be represented as a function of temperature (see Fig. 5.4) [17]. In case of the low-field spectrometer used here with a magnetic field strength of 0.5 T, a T_1 minimum would indicate a motion with a correlation time τ_c of about 8 ns. In polymers, however, the situation is usually more complex. Here, different motional processes, characterized by distributions of correlation times, occur on different time scales (see, e. g., Ref. [42]). While the existence of several motional processes with strongly differing correlation times results in the occurrence of several T_1 minima, a distribution of correlation times in a narrow range causes a broadening of the T_1 minimum (see Fig. 5.4).

For PCL no T_1 minimum can be found in the investigated temperature range at the magnetic field strength of 0.5 T. The slow decay at decreasing temperature hints at a broad distribution of correlations times τ_c . The measured temperature trend shows, that the motions which bring about the T_1 relaxation are fast compared to the (angular) Larmor frequency of the proton spins ($\omega_0 \approx 2\pi \times 20$ MHz), i. e. $\tau_c < 8$ ns (cf. Fig. 5.4).

The order of the T_1 relaxation time constants of the different polymer phases

$$T_{1c} > T_{1i} > T_{1a} ,$$

with the labels c,i and a naming the crystalline phase, mobile-amorphous phase and interphase, is already known for the PCL carbon atoms [161], but also for PE [76, 152]. The fact, that each polymer phase exhibits an own, specific T_1 temperature dependence, indicates that the motional processes within the crystallites and the amorphous regions

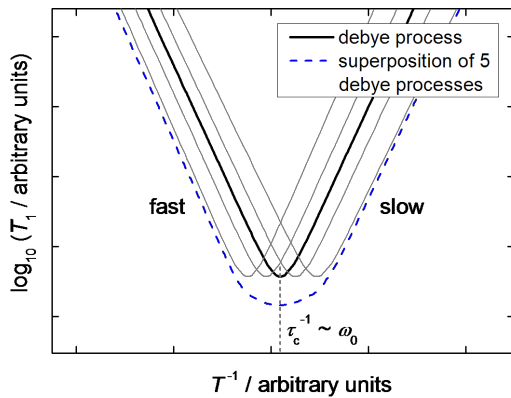


Figure 5.4.: Dependence of T_1 on the inverse temperature for a Debye process with a single correlation time τ_c (see text) and for a superposition of 5 Debye processes with different correlation times. All curves were calculated under the assumption, that $\tau_c(T)$ follows an Arrhenius dependence $\tau_c(T) = \tau_0 \exp(E_A/kT)$. The labels 'fast' and 'slow' refer to a classification of a motional rate compared to the Larmor frequency ω_0 .

are of basically different origin.

Presumably, the T_1 relaxation within the mobile-amorphous domains is induced by fast, cooperative segmental motions or even faster local motions, which are known in the form of the α , β and γ relaxation from dielectric spectroscopy measurements of PCL [166–168] and have been detected in dynamic-mechanical experiments as well [169]. These relaxation processes might exhibit motional rates larger than $\omega_0 \approx 2\pi \times 20$ MHz in the temperature range investigated here. However, a direct determination of the correlation time of these processes by dielectric spectroscopy is not possible, because at such high temperatures the signal is superimposed by the conductivity of free ions and the interfacial polarization [168].

In the fast limit, i. e. for motions being very fast compared to ω_0 , the value of T_1 depends on the strength $\langle B_{\text{flukt}}^2 \rangle$ of the local magnetic field fluctuations arising from the variation of the dipolar couplings between spins due to the molecular motions [53]:

$$T_1 \propto \frac{1}{\langle B_{\text{flukt}}^2 \rangle}$$

Hence, the increased T_1 values of the interphase, compared to the ones of the mobile-amorphous phase, can be explained by the smaller amplitude of motions within the interphase due to the restriction of mobility which follows from the fixation of the chains in the crystallites at one end and reduces the fluctuation strength of the dipolar couplings.

In the crystalline region the enhanced packing density of the chains and their diminished mobility do not permit segmental reorientations. Here, presumably fast vibrations of the methylene groups take place at small amplitudes, which cause small fluctuations of the dipolar couplings and result in large T_1 values.

High-field NMR DIPSHIFT Measurements of PCL. In order to obtain more detailed information on the fast (and intermediate-regime) dynamics within the PCL crystallites, measurements using the so-called DIPSHIFT (Dipolar Chemical Shift Correlation) sequence [170], a high-field NMR technique, have been performed for PCL. The DIPSHIFT experiment is a separated local-field experiment [171, 172], which enables the measurement of heteronuclear dipolar coupling strengths of the different chemical groups within the repeat unit from high-resolution NMR spectra derived under Magic-Angle Spinning (MAS) [170]. As the tensor of the dipolar interaction between ^{13}C and ^1H nuclei is axially symmetric and oriented along the C-H bond, it is a viable probe of dynamic processes, which change the orientation of the C-H bond with respect to the direction of the magnetic field. Thus, DIPSHIFT experiments, probing the strength of this interaction, are well-suited to investigate the mobility of the methylene groups within the crystalline PCL chains. The mode of action of the DIPSHIFT sequence is explained in Refs. [170, 173]. A short description of the sequence as well as information about the experimental settings is given in Appendix A.

DIPSHIFT experiments have been performed at about 25°C and subsequently at 52°C for an industrially produced PCL sample, which before had been crystallized isothermally at 45°C for 4 days. A high-resolution ^{13}C CP spectrum measured at about 25°C is shown in Fig. 5.5 (a). The peak assignment for the different carbon nuclei (see inset in Fig. 5.5 (a)) was adopted from literature [174, 175]. However, the assignment of the

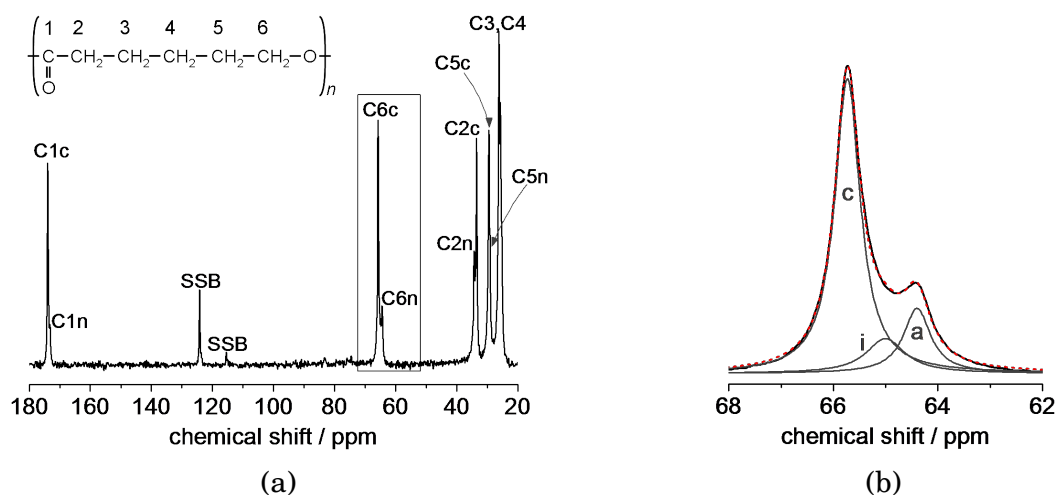


Figure 5.5.: (a) CP spectrum of PCL ($M_n = 42.5$ kg/mol), detected at about 25°C with a 400 MHz spectrometer using a CP contact time of 1500 μ s at a Magic-Angle-Spinning (MAS) frequency of 5 kHz. The chemical shift is given relative to the reference peak position of TMS. The peaks are assigned to the carbon atoms in the PCL repeat unit according to the numbering shown in the upper left. The label appendices c and n designate signal of the crystalline and the non-crystalline phase, respectively, and the label SSB marks spinning side bands. (b) Close-up of the peak region of the carbon nucleus C6, marked by the black rectangle in (a). Additionally, a fit to the signal with a sum of three Lorentzian functions is depicted. The three contributions labeled c, i and a are ascribed to the crystalline-phase, interphase and mobile-amorphous-phase signal, respectively.

carbon nuclei C3 and C4 in the middle of the repeat unit seems to be unclear. Their denotation might be interchanged.² For all peaks in the PCL spectrum a splitting into a crystalline-phase and an amorphous-phase contribution is observed due to the γ -gauche effect [17]. Yet, the overlap of the peaks of the C3 and C4 nucleus complicates the separation of these signals.

The ^{13}C spectra measured in the DIPSHIFT experiments were analyzed by peak deconvolution by means of a fit to each peak region using a sum of two or three Lorentzian functions, with the individual fit contributions representing the signal of crystalline phase, mobile-amorphous phase and, if necessary, the interphase (cf. Fig. 5.5 (b)).

With increasing time t_1 , during which the spin system develops under the action of the heteronuclear ^{13}C - ^1H dipolar coupling in the DIPSHIFT experiment (see Appendix A), the signal intensity varies in a characteristic way, involving information about the strength $\omega_{D,\text{CH}}$ of the ^{13}C - ^1H coupling [170]. In Fig. 5.6 the normalized signal contributions of the individual carbon nuclei in the repeat units of the PCL crystallites are depicted for the measurement at about 25°C. We find the same results qualitatively and quantitatively for the experiment performed at 52°C. As glycine molecules for most practical purposes may be considered to be rigid on the intermediate and slow time scale, for comparison measured data for the methylene carbon nucleus in glycine at 25°C are shown. The strength $\omega_{D,\text{CH}}$ of the heteronuclear coupling is represented by the depth of the dip in the DIPSHIFT curve (see Fig. 5.6). In the presence of slow dynamics with rates $k \propto (1/\tau_c) \ll \omega_{D,\text{CH}}$ the full coupling strength is observed, resulting in a strong

²Hence, in Figs. 5.6, 5.7 and 5.8 question marks were put to the corresponding labels in the legends to highlight this fact.

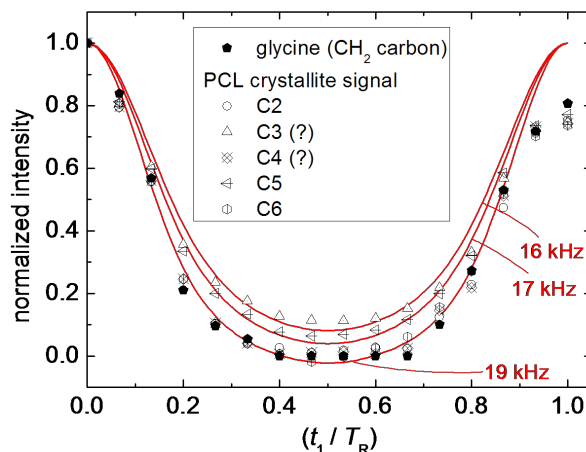


Figure 5.6.: Crystallite signal intensity contributions of the different carbon atoms in the PCL repeat unit as a function of the normalized time t_1/T_R obtained in a DIPSHIFT experiment (see Appendix A for details) of industrially produced PCL ($M_n = 42.5$ k/mol) at about 25°C . T_R designated the rotor period. The numbering of the PCL carbon atoms is given in Fig. 5.5 (a). The intensities are normalized to the one of the first point at $t_1 = 0$. The uncertainties of the intensities, resulting from the peak deconvolution, are in the range of the symbol size. For comparison signal intensities for the carbon nucleus in the glycine CH_2 group and simulated DIPSHIFT curves for different ^{13}C - ^1H dipolar coupling strengths are plotted (see text).

decay with low intensities at times t_1 ranging around half a rotor period $T_R/2$. On the other hand, fast molecular motions with rates $k \gg \omega_{D,\text{CH}}$ cause a partial pre-averaging of the couplings, so that a reduced mean coupling strength is detected and the decay is more slowly and shallow causing higher intensities at times t_1 close to $T_R/2$ [170].

In order to obtain quantitative results for dipolar coupling strengths $\omega_{D,\text{CH}}$, the measured data were compared to simulated DIPSHIFT curves, calculated for a CH_2 group at different coupling strengths (see Fig. 5.6).³ The deviation of the simulated curves from the measured data presumably arises from the superposition of the crystallite peaks in the spectrum with signal from mobile or rigid-amorphous material, which cannot be removed completely by fitting.

For glycine, a coupling strength $\nu_{D,\text{CH}} = \omega_{D,\text{CH}}/(2\pi) = (19 \pm 1)$ kHz was determined (see Fig. 5.6). This value is slightly reduced compared to the static case ($\nu_{D,\text{CH}} \approx 23$ kHz [17]), due to a pre-averaging as a result of fast vibrational motions of the CH_2 group with a rate in the range of terahertz or higher [177, 178]. As the DIPSHIFT curves for the C2, C6 and the C4 (or C3) nucleus are very similar to the one of glycine, the same coupling strength of (19 ± 1) kHz is present here. Hence, there is a similar pre-averaging of couplings due to fast motions of the methylene groups at rates larger than some hundreds of kilohertz for these nuclei. A smaller coupling strength $\nu_{D,\text{CH}} = (17 \pm 1)$ kHz and (16 ± 1) kHz was found for the C5 and the C3 (or C4) nuclei, respectively, which reside more distant from the carboxyl groups. This reduction hints at the pre-averaging of couplings due to fast motions with an enhanced motional amplitude of the corresponding methylene groups compared to the ones close to the carboxyl groups [170].

³The simulated curves represent ^{13}C FID signals for a CH_2 group under the action of heteronuclear dipolar couplings and Magic-Angle Spinning (MAS), considering a powder average. The computation of the curves has been accomplished in analogy to the calculations of the FID under the action of the Chemical-Shift Anisotropy in Ref. [176] and is described in the supporting information of Ref. [173].

The ratio between the experimentally derived coupling strength $\nu_{D,CH}$ and the value for the static case $\nu_{D,CH,stat}$ is referred to as the order parameter S of the motion and can be related to the motional amplitude. Here, we find

$$S = \frac{\nu_{D,CH}}{\nu_{D,CH,stat}} = \frac{\nu_{D,CH}}{21.1 \text{ kHz}} = \begin{cases} 0.90 & \text{for C2, C6 and C4 (or C3),} \\ 0.81 & \text{for C5 and} \\ 0.76 & \text{for C3 (or C4).} \end{cases}$$

The value of $\nu_{D,CH,stat}$ was estimated [53] via

$$\nu_{D,CH,stat} = \frac{1}{2\pi} \left(\frac{\mu_0}{4\pi} \hbar \frac{\gamma_C \gamma_H}{r_{C-H}^3} \right),$$

using the C-H distance r_{C-H} in the methylene groups of PCL, known from X-ray diffraction measurements [49], and the magnetogyric ratios γ_C and γ_H of the carbon and proton spins. If a two-site jump is assumed exemplarily for the fast motions of the methylene groups according to the approach of Kaji and Horii [161], the calculated order parameters for PCL correspond to jump angles of 5° to 10° for the methylene groups close to the carboxyl groups (C2 and C6) and of 15° to 20° for the more distant methylene groups (C5 and C3 or C4) in middle of the repeat unit (cf. Fig. 1 in Ref. [170]).

Hence, from the results of DIPSHIFT measurements one can conclude, that, while the carboxyl groups remain rather rigid (see Ref. [161]), because they are stabilized by the dense chain packing and dipolar interactions between the chain stems within the crystallites, the methylene groups perform fast, presumably vibrational motions. The motional rates k are higher than some hundreds of kilohertz at least. Yet, the amplitude of these fast motions is larger for the CH_2 groups which are more distant from the carboxyl groups. This finding is consistent with the results of ^{13}C T_1 measurements of Kaji and Horii, indicating higher motional amplitudes of the methylene groups in the middle of the repeat units, compared to the positions close to the COO groups, at motional rates in the range of 100 MHz [161]. A similar picture of the fast mobility in the repeat units was found for the crystalline regions of Nylon-66. Here, the methylene groups perform librations at rates around 0.1 THz [179, 180], and the almost rigid amide linkages act as pinning points on the neighboring methylene groups, restricting their mobility [179]. The fact, that the mobility of a chain part may affect the motions of neighboring chain regions, is also known for precisely branched PE, where the rotation of the branches causes twists or rotations of the neighboring methylene groups [181].

In case of very slow or very fast chain dynamics, compared to the strength $\omega_{D,CH}$ of the static heteronuclear dipolar couplings, the DIPSHIFT intensity reaches its initial value at a time $t_1 = T_R$ [170]. However, dynamics on an intermediate time scale, i. e. with rates k on the order of $\omega_{D,CH}$ ($k = 10 - 100$ kHz), cause a decrease of the final intensity at $t_1 = T_R$, as they originate changes of the coupling strength during the MAS rotor period, impeding a complete signal refocusing after a full sample rotation [170]. Although glycine is rigid on an intermediate time scale, a signal decrease at $t_1 = T_R$ was detected for the ^{13}C nucleus in the glycine CH_2 group as a result of imperfections of the pulse sequence [182]. Compared to the DIPSHIFT signal intensity of glycine, the PCL data do not exhibit a significant decrease at $t_1 = T_R$ at 25°C (see Fig. 5.6) and at 52°C . Hence, jump or rotational motions of the methylene groups in crystalline PCL regions on an

intermediate time scale can be excluded in the investigated temperature range.

Low-Field FID and MSE Measurements of PCL. Molecular dynamics in the PCL crystallites on the intermediate time scale, i. e. at rates between kilohertz and megahertz, would also affect proton low-field time-domain NMR signals

- by changing the shape of the FID crystallite signal contribution accompanied by a considerable reduction of the second moment M_2 of the absorption line shape and
- by decreasing the MSE refocusing efficiency, causing an increased MSE signal loss and a change in the shape of the crystallite-signal intensity decay as a function of the MSE sequence length,

compared to the signal of completely rigid crystallites.

Anisotropic chain motions within the crystallites cause a partial averaging of homonuclear dipolar couplings, when the motional rate exceeds the coupling strength of about 20 kHz [183, 184], involving a reduction of the spectral line width and of M_2 compared to the static case. This effect turns M_2 into an indicator for chain motions in crystallites at rate larger than ~ 20 kHz.

Investigating the FID signals of PCL as a function of temperature, the shape parameters a and b , obtained from fits to the signals using Eq. 4.6 (see Section 4.1), proved to depend slightly on temperature. The second moment M_2 , calculated from these parameters via Eq. 4.3, decays slightly and uniformly at increasing temperature (see Fig. 5.13). The reason for this decay is the thermal lattice expansion caused by very fast motions⁴ of small amplitudes at around 10° [185–188], which induce a slight decrease of the dipolar coupling strength due to increasing mean proton distances. By contrast, motions on an intermediate time scale would cause a second, stronger decay of M_2 , as it is visible for PE in Fig. 5.13 discussed in Section 5.2. Ito et al. actually found such a decay for a number of linear aliphatic polyesters with long repeat units and an even number of methylene groups between the carboxyl groups, accompanied by the occurrence of a mechanical α relaxation [162].

As depicted in Fig. 4.7 for a sample of industrially produced PCL ($M_n = 42.5$ kg/mol), the signal loss of crystalline-phase signal due to the MSE sequence is small and almost constant at temperatures above 0°C , where the signal contributions of the three polymer phases can be separated clearly. Thus, the refocusing efficiency is constantly high. The signal loss is not caused by intermediate motions but by technical imperfections in the presence of strong dipolar couplings (see Section 4.2), which is proved by the Gaussian shape of the decay of the crystalline-phase signal intensity as a function of the MSE sequence length (see Fig. 5.15).

Hence, like the results of the ^{13}C DIPSHIFT experiments also the findings from ^1H low-field NMR measurements support the assumption, that there is no dynamics on an intermediate time scale of about 1 kHz to 1000 kHz in PCL crystallites.

High-field NMR CODEX Experiments of PCL. Kaji and Horii have performed two-dimensional switching-angle sample-spinning (2D SASS) ^{13}C NMR measurements of

⁴The correlation time τ_c and the rate k of these motions are in the picosecond and terahertz range, respectively [185–188].

PCL ($M_n = 80$ kg/mol) at 41°C. After comparison of measured and simulated ^{13}C spectra, they concluded that jump motions of the PCL methylene groups take place around the chain axis with rather large amplitudes of about 60° to 90° at rates k between 0.1 kHz and 1 kHz, i. e. on the intermediate to slow time scale [161].⁵ However, as described above, at least motions in the intermediate time regime can be excluded in our PCL sample. Yet, compared to the studies of Kaji and Horii, the methods used here probe motions on the basis of different NMR interactions. While Kaji and Horii investigated changes in the Chemical-Shift Anisotropy (CSA) of ^{13}C nuclei with an interaction strength ω_{CSA} of ~ 1.85 kHz for static methylene groups and ~ 7.5 kHz for static carboxyl groups in the 200 MHz spectrometer used for their measurements [189], the ^{13}C DIPSHIFT and the low-field proton NMR experiments detected the heteronuclear and homonuclear dipolar coupling interaction, respectively, with interaction strengths ($\omega_{D,\text{CH}}/2\pi$) and ($\omega_D/2\pi$) of about 20 kHz each, in static methylene groups. The sensitivity of the individual methods for intermediate motions is different, depending on the ratio of the motional rate and the interaction strength probed by the experiment.⁶ Moreover, the individual interaction tensors are oriented differently with respect to the motional axis, which may also cause different sensitivities, and the response behavior of the methods to motions of a certain amplitude may differ as well.

Hence, in order to check the conclusions of Kaji and Horii concerning the time scale of motions in the PCL crystallites, investigations by means of the CODEX (Centerband-Only Detection of Exchange) sequence [190] have been performed for an industrially produced PCL sample ($M_n = 42.5$ kg/mol). The CODEX experiment is a one-dimensional solid-state NMR exchange experiment, used for the detection and characterization of slow segmental reorientations with rates in the range of hertz to kilohertz. Like the method of Kaji and Horii [161], it probes changes of the CSA of ^{13}C nuclei due to molecular motions. The experiment permits the determination of the correlation function of a motion, the correlation time τ_c and the motional amplitude for each spin position exhibiting a resolved peak in the high-resolution spectrum, obtained by MAS. The reintroduction of the CSA, which is cancelled by sample spinning, is accomplished by a series of rotor-synchronized 180° pulses, applied prior to and after a long mixing time τ_{mix} , during which molecular motion may occur [190–192]. The mode of operation of the CODEX sequence is explained in Refs. [190–192]. A short description as well as information about the experimental settings is given in Appendix A.

In the CODEX experiment slow segmental or molecular reorientations result in a signal decay at increasing mixing time τ_{mix} or increasing number N of 180° pulses in the CSA recoupling periods [190, 192]. With the help of a suitable model for the geometry of a motion, the dependency of the normalized signal intensity I/I_{ref} (see Appendix A) on the length NT_{R} of the recoupling periods, with T_{R} denoting the length of a rotor period, yields information about the amplitude of motion [192]. This NT_{R} dependency was measured for PCL at about 25°C and 50°C after the isothermal crystallization of the sample at 45°C for some days and a storage time at room temperature. From the resulting ^{13}C CODEX exchange and reference spectra (cf. Appendix A) the crystalline-phase signal intensities of the different carbon nuclei in the repeat unit (see Fig. 5.5 (a)) were derived by peak deconvolution as explained for the analysis of the DIPSHIFT measurements. The

⁵They further suggested additional jumps around the C-C bond axis for the carbons C3, C4 and C5 in the middle of the repeat unit.

⁶The closer the value of the ratio is to 1, the more sensitive is the method.

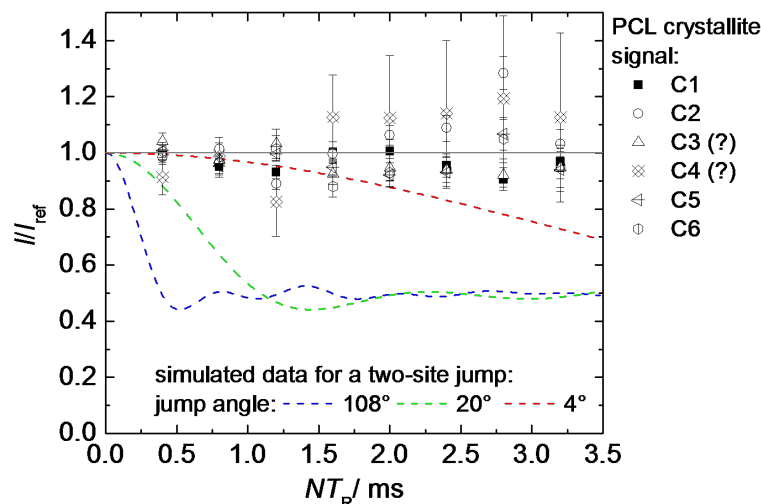


Figure 5.7.: CODEX- NT_R dependency of the exchange intensity I of the crystalline-phase signal contributions of the individual carbon atoms in the PCL repeat unit (cf. Fig. 5.5 (a)). The data were obtained from a CODEX exchange experiment of industrially produced PCL ($M_n = 42.5$ kg/mol) at 50°C ($\tau_{\text{mix}} = 100$ ms, CP contact time = 1500 μs), by peak deconvolution (see text) and normalization with the reference intensity I_{ref} (for details see Appendix A). The plotted uncertainty margins result from the fits for peak deconvolution. For comparison, simulated curves for two-site jumps of CH_3 groups as present in dimethyl sulfone are depicted for different jump angles. They were calculated according to Ref. [193] as FID signals for a spin system developing under MAS and ^{13}C Chemical-Shift Anisotropy (with principal axes values $\sigma_{xx} = 60$ ppm, $\sigma_{yy} = 60$ ppm and $\sigma_{zz} = 6$ ppm), taking into account powder averaging.

CODEX NT_R dependency of the normalized exchange intensities is depicted in Fig. 5.7 for all carbon nuclei in the repeat unit in PCL crystallites exemplarily for the measurement at 50°C . For comparison calculated signal decays are shown for a two-side jump of a methyl group, as it is found, e. g., in dimethyl sulfone, for different jump angles. No signal decay was found for the PCL data at both measurement temperatures and two mixing times (100 ms and 200 ms), indicating that carbon atoms in PCL crystallites do not perform slow jump or rotational dynamics in the regime of milliseconds to seconds. This finding is consistent with the result 2D exchange experiments performed by Kaji and Horii, showing the absence of motions with correlation times between 0.1 seconds and 10 seconds [161].

By means of the CODEX experiment also information about intermediate-regime motions can be derived in principle, as such motions beside other effects, such as signal losses due to the proton decoupling, T_1 relaxation and spin diffusion, cause an intensity decay of the reference signal [192] (cf. Appendix A).

To analyze these signal decays for the PCL measurements described above, the NT_R dependency of the reference intensities I_{ref} of the methylene and carboxyl group carbons is compared in Fig. 5.8 (a). In fact, for the methylene group carbons a slightly faster reference signal decay was observed than for the carbon of the COO group, which seems to be rather rigid on the intermediate time scale (cf. Ref. [161]). However, this cannot be interpreted as a hint to intermediate dynamics, because the carbon nucleus in the carboxyl group is more distant from protons than the methylene carbons, and thus the dipolar coupling interaction mediating the proton decoupling is weaker, result-

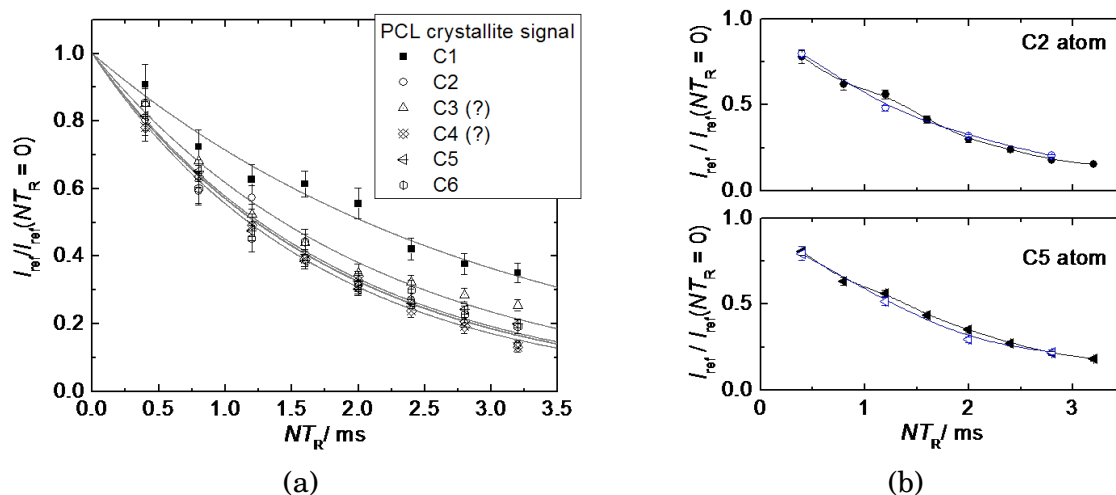


Figure 5.8.: NT_R dependency derived from a CODEX reference experiment of industrially produced PCL ($M_n = 42.5$ kg/mol, $\tau_{mix} = 100$ ms, CP contact time = 200 μ s or 1500 μ s). Signal intensities I_{ref} of the crystallite signal contributions are plotted for the different carbon atoms in the PCL repeat unit for a measurement at 50°C in (a) and for the C2 (upper graph) and C5 (lower graph) atom at about 25°C (open symbols) and 50°C (filled symbols) in (b). The data were normalized to the intensity I_{ref} at $NT_R = 0$, derived from exponential fits to each data set, shown in (a). The uncertainties result from the peak deconvolution and the normalization.

ing in a lower sensitivity for decoupling imperfections, which cause a part of the signal decay [192]. Moreover, the NT_R dependency of the reference signals of the methylene carbons does not vary at differing measurement temperature, as shown exemplarily in Fig. 5.8 (b). Hence, the decay does not originate from a thermally activated, dynamic process.

In contrast to the conclusions of Kaji and Horii from the 2D SASS experiments, the CODEX measurements do not show chain dynamics in PCL crystallites on an intermediate or slow time scale. This finding can be accommodated with those of Kaji and Horii, by assuming that the narrowed CSA patterns measured by them reflect the limit of fast dynamics in the crystallites, for which the line shapes are similar to those shown in their paper (cf. Ref. [161], [194]).

Concluding this section, it can be confirmed that the methylene groups in PCL perform fast, presumably vibrational motions of rather small amplitudes of about 5° to 10°. The motional amplitude is enlarged to 15° to 20° for the groups which reside more distant from the COO groups. The presence of PCL chain dynamics within the crystallites on an intermediate or slow time scale, i. e. at rates between hertz and megahertz and correlation times between microseconds and seconds, can be excluded in the investigated temperature range of about 25°C to 50°C on the basis of the measurements described above. As large-amplitude slow or intermediate-regime jump motions of chain parts do not occur within the crystallites, longer-range chain diffusion through the lamellae and lamellar thickening on cooling, as present in PE of linear topology [10, 195], is not expected for PCL. This expectation is confirmed in Sections 6 and 7.2. Hence, a classification of PCL as a crystal-fixed polymer is justified and PCL can be used as a reference for comparison with the α_c -mobile polymer PE in the following section.

5.2. Determination of Chain-Flip Rates in PE Crystallites for Two Different Sample Morphologies

As PE-containing products are used on a large scale in everyday life, information about the origin of the special mechanical properties of PE is of great industrial importance. It has been known for a long time, that within the crystallites PE chains perform helical jump motions on an intermediate time scale [17,43,44,186]. In particular, the methylene groups flip around the chain axis by 180° and simultaneously move in chain direction by half the length of the repeat unit (see Fig. 5.9, cf. Fig. 2.2). This relocation transfers the chain into an energetically equivalent position with regard to the packing of the CH_2 groups in the crystal lattice [140, 186]. Repeated chain flips enable a longer-range chain diffusion through the crystallites, which causes characteristic macroscopic and technologically relevant features of the material, such as drawability, creep and crystal thickening [42–44, 196].

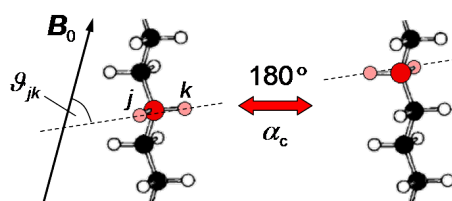


Figure 5.9.: PE chain before and after a local chain flip in a crystallite. The black and white spheres represent carbon and hydrogen atoms, respectively. The flip motion, the so-called α_c process, comprises a 180° rotation of the chain stem and a translational motion along the chain by half the length of a repeat unit (see the methylene group marked in red). All in all, the length of the interconnection vectors of the protons in a chain stem and their orientation with respect to the direction of the magnetic field B_0 does not change due to the jump process.

By investigating PE samples of different morphology by means of ^{13}C high-field NMR exchange experiments under MAS, interestingly, Yao et al. found different diffusion coefficients for the longer-range chain diffusion between amorphous and crystalline domains [197]. In particular, they investigated two chemically identical PE samples, crystallized under different conditions, i. e.

- a melt-crystallized sample of rather switchboard-like structure and almost isotropic chain mobility in the non-crystalline regions and
- a solution-crystallized sample with adjacent-reentry-like morphology and restricted chain mobility in the non-crystalline regions, which mainly consisted of tight chain folds [198].

Intuitively, one would expect easier and faster chain diffusion through the crystallites of the melt-crystallized sample due to the more flexible chains in the non-crystalline regions as opposed to the solution-crystallized analogue. However, the measured diffusion coefficient of the melt-crystallized sample was smaller by a factor of about 20 compared to the solution-crystallized sample [197, 198]. Yao et al. interpreted this finding as a result of the smaller structural difference between the crystalline and non-crystalline regions in the solution-crystallized sample, causing a smaller entropy difference between the phases and facilitating the chain transport between them, compared to the melt-crystallized sample.

Yao's result raises the question, whether this difference in the macroscopic chain-diffusion coefficients is based on a difference in the time scale of the local 180° chain-flip process. This issue is addressed here by the investigation of three PE samples of different morphology:

- a commercial melt-crystallized, high-density (HD) PE sample exhibiting lamellae of the thickness $d_c \approx 13$ nm and disordered fold surfaces, with tight folds as well as loops, entanglements and tie chains in the amorphous regions (see Fig. 5.10 (a)), and
- two ultra-high-molecular-weight (UHMW) PE reactor powder samples [199] of rather adjacent-reentry-like morphology, with lamellar thicknesses of about 8 nm and different molecular weights ($M_w \sim 5000$ kg/mol and 750 kg/mol) (see Fig. 5.10 (b)).

Further information on sample characteristics are given in Appendix A.

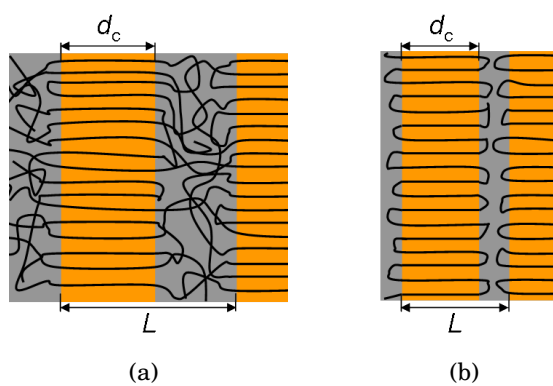


Figure 5.10.: Morphology of the investigated PE samples: (a) melt-crystallized sample with disordered fold surfaces and (b) reactor powder exhibiting an adjacent-reentry-like structure with tight chain folds.

As shown in Section 5.1, NMR spectroscopy is well-suited for the investigation of polymer dynamics over a wide range of correlation times with the help of a variety of measurement techniques. In principle, the local chain-flip process in PE crystallites is also accessible by NMR. However, difficulties arise from the planar all-trans conformation of the chain, because here a 180° chain flip changes the orientation of the H-H and C-H internuclear vectors by 180° , leaving, e. g., the chemical shifts and ^2H quadrupolar interactions unaltered [44, 171]. Also the strong geminal dipolar coupling between two protons j and k bonded to one carbon is invariant under the 180° chain flip, because the parameters governing the interaction strength, i. e. the distance r_{jk} of the protons and the angle ϑ_{jk} of their interconnection vector with respect to the magnetic field (see Section 3.3), are not affected by the jump motion (see Fig. 5.9). Nevertheless, Hu et al. succeeded in proving the 180° chain-flip process in PE [200] by means of time- and cost-intensive NMR investigations, using melt-crystallized high-density (HD) PE labeled with dilute ^{13}C - ^{13}C spin pairs in dipolar-coupling-based stimulated-echo experiments. They exploited the fact, that the echo intensity decay is a measure of the population of ^{13}C - ^{13}C -bond orientations parallel to the initial orientation.

For this thesis chain-flip rates in PE crystallites have been determined by means of the

MSE sequence (see Section 4.2). Here, changes of the average dipolar coupling strength between protons in the crystallites resulting from molecular motions are detected indirectly. This is possible because, as opposed to the couplings of the geminal protons, the weaker, secondary, longer-range couplings between protons of a moving chain and those of the neighboring chains are subject to detectable changes due to the flip process. If the flip motion is fast enough, a mean coupling strength is measured for averaged proton positions, which differs from the one of the static system. In order to determine a jump rate of the chain-flip process, one can exploit the fact, that the MSE refocusing efficiency is reduced systematically, when changes of the mean dipolar coupling strength ω_D within the sample occur on the time scale of the sequence length as a result of molecular dynamics (see Section 4.2). Lengthening of the MSE sequence results in an increasing number of jump motions taking place during the sequence, corresponding to a stronger change of ω_D and a stronger signal loss. The echo intensity as a function of the MSE sequence length t_{seq} can be analyzed in order to derive a jump rate.

For a quantitative investigation of the chain-flip rate, the FID signal and the MSE signals at different sequence lengths have been acquired for the three samples mentioned above at various temperatures below the melting point. The variation of the sequence length t_{seq} was accomplished by increasing the number n_{MSE} of MSE cycles and by correspondingly prolonging the delays τ flanking the MSE 'sandwich' part (see Fig. 4.4 (b)).⁷ In order to enable the normalization of the FID signals to the total signal intensity $I_{\text{tot},T}(t=0)$ as described in Section 4.1, at the end of each sample-specific series of experiments a FID signal was measured at a temperature T_m above the melting point T_f , where the sample was molten completely. All FID and MSE data sets were corrected with regard to the different measurement temperatures by means of Eq. 4.9. In Fig. 5.11 corrected FID and MSE data are depicted exemplarily for the melt-crystallized PE sample at 69°C.

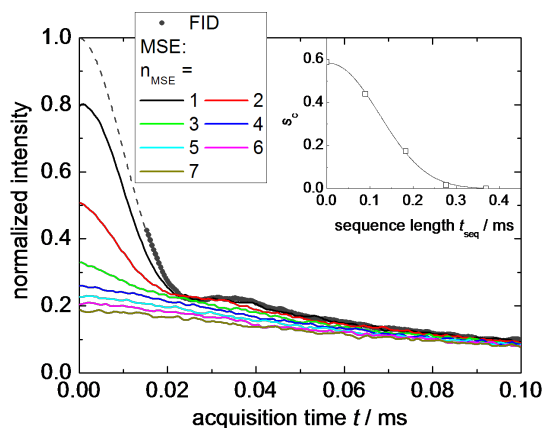


Figure 5.11.: FID signal and MSE signals for different sequence lengths t_{seq} measured for melt-crystallized PE at 69°C. The intensity was normalized to the absolute signal intensity determined from the FID in the melt state as described in Section 4.1. The dashed gray line represents a fit to the FID signal with a three-component function according to Eq. 4.6. In the inset the crystalline-phase signal contribution s_c , obtained from fits to the FID and MSE data shown in the plot (see Sections 4.1 and 4.2), is depicted as a function of the MSE sequence length t_{seq} .

⁷A sequence lengthening is possible also by prolonging the time intervals τ_φ between the pulses of the 'sandwich' blocks. Yet, in case of the spectrometer used here this proceeding generates a faster and more complex signal decay as it is observed when increasing the number n_{MSE} of the basic blocks (cf. Ref. [73]). In principle, smaller increments of the sequence length are available by halving the number of pulses within the basic 'sandwich' blocks. However, compared to the version with four pulses per block, again, at the machine used here, this approach leads to a worse performance, i. e. larger signal loss due to unavoidable problems related to radio-frequency pulse quality.

Crystallinity and Second Moment of Line Shape. The mass fractions of the crystalline, rigid-amorphous and mobile-amorphous sample components obtained from fits to the FID signals (see Section 4.1) are depicted in Fig. 5.12 as a function of the measurement temperature for the melt-crystallized PE and one of the reactor powders. The crystallinity of the melt-crystallized sample ranges at about 60% at ambient temperature and is in good agreement with the DSC crystallinity of 59% (cf. Appendix A). For both samples the onset of the melting process is visible at about 380 K to 400 K, accompanied by a reduction of the crystallinity and an increase of the mobile-amorphous fraction. The distinct differences in the phase composition of the two samples reflect their morphological differences. Contrary to the melt-crystallized sample, a mobile-amorphous fraction could hardly be detected for the reactor powder at temperatures below 400 K, because the tight chain folds at the crystallite surfaces are classified as rigid-amorphous material due to their low mobility.

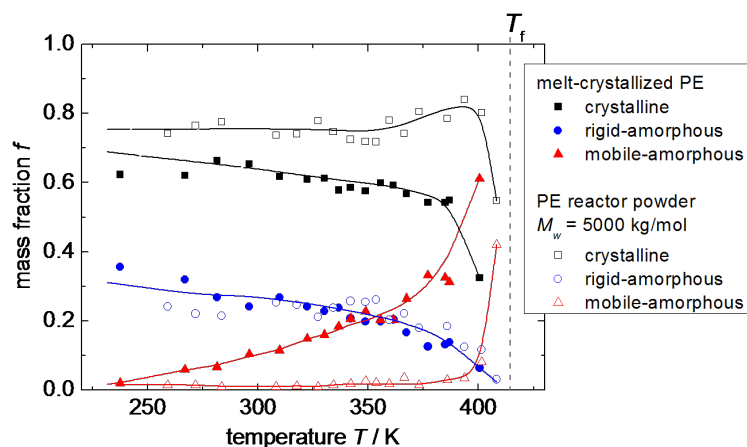


Figure 5.12.: Mass fractions of the crystalline, rigid-amorphous and mobile-amorphous phase as a function of temperature for the melt-crystallized PE sample and one of the reactor powder samples ($M_w = 5000$ kg/mol). The fractions were obtained from fits to the FID signals by means of Eq. 4.6. The continuous lines are guides to the eye and the dashed line depicts the DSC melting temperature T_f . Graph adopted from Ref. [201].

As already mentioned in Section 5.1, the second moment M_2 of the line shape serves as an indicator for chain dynamics at correlation times τ_c below the inverse ^1H - ^1H dipolar coupling strength. The temperature dependence of M_2 as calculated from Eq. 4.3 is depicted in Fig. 5.13 for all three PE samples mentioned above and for an industrially produced PCL sample ($M_n = 42.5$ kg/mol). The M_2 development of the PE samples corresponds well to literature data of Olf and Peterlin [185] for a melt-crystallized PE sample. For both polymers, PCL and PE, a smooth decrease of M_2 can be observed with increasing temperature due to thermal lattice expansion (cf. Section 5.1) [183, 185, 187, 188]. As opposed to PCL, for the PE samples a second, stronger decay was detected above 360 K, arising from the 180° chain-flip process, which starts to average dipolar couplings between the protons at this temperature.

Determination of Jump Rates and Activation Energies. The decay of the crystalline-phase signal contribution $s_c(t_{\text{seq}})$ to the MSE signal at increasing sequence length t_{seq} is depicted in Fig. 5.14 (a) exemplarily for a PE reactor powder ($M_w = 5000$ kg/mol)

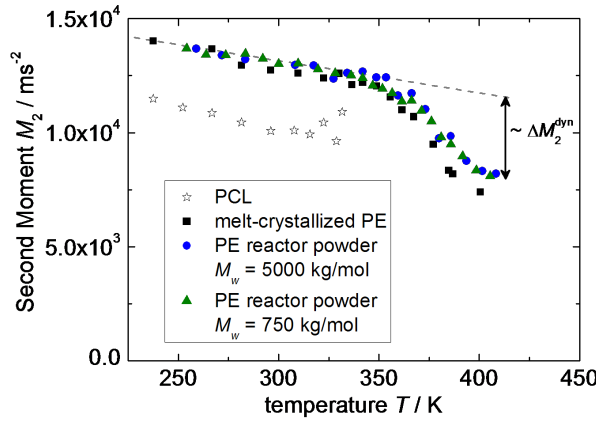


Figure 5.13.: Second moment M_2 of the line shape as calculated from the FID fit parameters a and b according to Eq. 4.3 for an industrially produced PCL reference sample ($M_n = 42.5$ kg/mol) and the three PE samples mentioned in the text. The parameter ΔM_2^{dyn} designates the decay of the second moment due to chain dynamics (see text). Graph adopted from Ref. [201].

and a number of measurement temperatures. The data were normalized to the crystalline mass fraction f_c determined from the corresponding FID signal, which is interpreted as a MSE signal at a sequence length $t_{\text{seq}} = 0$.

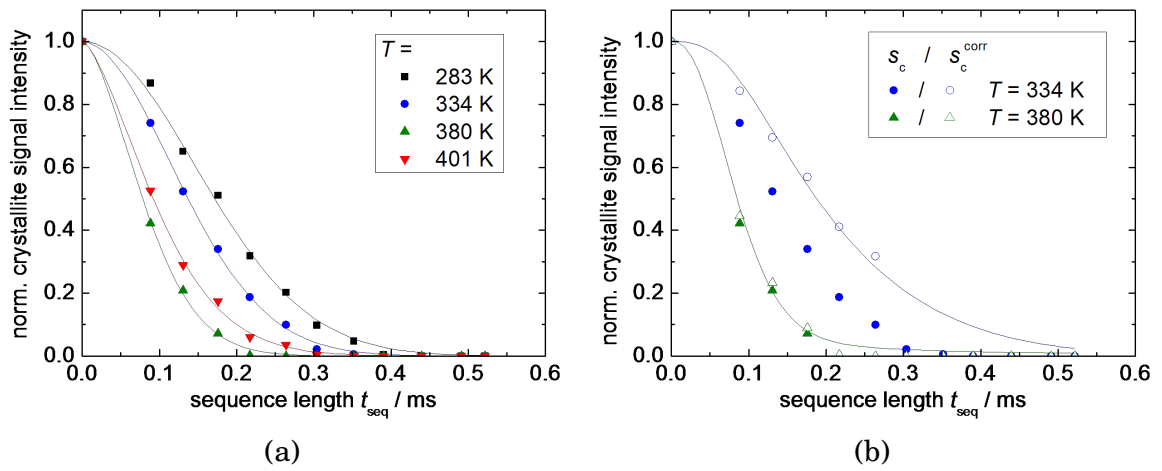


Figure 5.14.: Crystalline-phase signal contribution s_c of a PE reactor powder sample ($M_w = 5000$ kg/mol) as a function of the MSE sequence length t_{seq} at different temperatures. The signal intensities were normalized to the mass crystallinity f_c determined from the FID (a) and corrected additionally with regard to the signal loss following from the reduced MSE refocusing efficiency due to strong static dipolar interactions (b) (see text). The continuous lines are fits to the data using a modified (stretched or compressed) exponential function (a) or Eq. 5.5 (b). Graph adopted from Ref. [201].

As described in Section 4.2, the signal decay is affected by chain dynamics on the one hand and strong static dipolar interactions and technical imperfections on the other hand. However, for a quantitative determination of chain-flip rates the decay $s_c^{\text{corr}}(t_{\text{seq}})$ arising from intermediate-regime chain dynamics had to be isolated. For this purpose apparent T_2 relaxation times were derived from the decay of the normalized crystallite signal contribution ($s_c(t_{\text{seq}})/f_c$) by means of a fit using a modified (stretched or compressed) exponential function (see Fig. 5.14 (a)):

$$f(t_{\text{seq}}) = e^{-(t_{\text{seq}}/T_2^*)^\beta} \quad (5.1)$$

The values of the shape parameters T_2^* and β are displayed in Fig. 5.15. At low temperatures the decay follows the shape of a Gaussian function ($\beta \approx 2$) due to imperfection terms related to strong static dipolar couplings as described in Section 4.2. At higher temperatures (> 360 K) it is additionally affected by intermediate-regime chain dynamics resulting in a value of $\beta < 2$. The characteristic decay time T_2^* passes through a minimum at temperatures, where chain dynamics occur on the time scale of the sequence length t_{seq} (see Fig. 5.15).

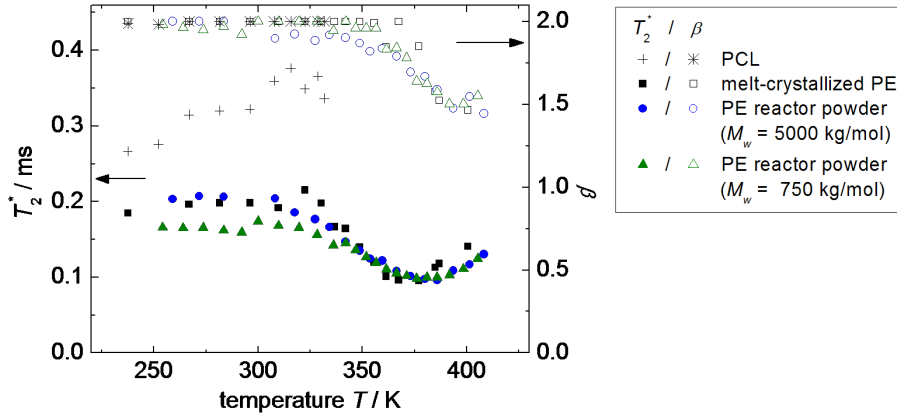


Figure 5.15.: Temperature dependence of the fit parameters T_2^* and β for the PE samples mentioned in the text and the PCL reference sample ($M_n = 42.5$ kg/mol), determined from fits to the normalized crystallite signal intensity ($s_c(t_{\text{seq}})/f_c$) using a modified exponential function. Graph adopted from Ref. [201].

The correction of the normalized crystallite signal contribution ($s_c(t_{\text{seq}})/f_c$) with regard to strong static dipolar interactions was accomplished by multiplication with a Gaussian function

$$s_c^{\text{corr}}(t_{\text{seq}}) = \frac{s_c(t_{\text{seq}})}{f_c} \cdot e^{-(t_{\text{seq}}/T_2^{*\text{corr}})^2}, \quad (5.2)$$

by exploiting the linear correlation

$$T_2^{*\text{corr}}(M_2) = A + B \cdot M_2,$$

which results from the concurrent dependence of M_2 and T_2^* on the dipolar coupling strength and is visible in absence of chain dynamics on an intermediate time scale, i. e. for PE at temperatures below ~ 320 K and for PCL. The parameters A and B were derived from linear fits to T_2^* as a function of M_2 . Here, A was readjusted separately for each sample, in order to ensure the best possible agreement of the fit result for $T_2^{*\text{corr}}$ with the T_2^* data derived from the measurements at low temperatures. Finally, the corrected data curves $s_c^{\text{corr}}(t_{\text{seq}})$ did not exhibit a decay for PCL and PE at low temperatures (data not shown).

In order to obtain the correlation time τ_c of the chain-flip motion, the corrected data sets $s_c^{\text{corr}}(t_{\text{seq}})$ (see Fig. 5.14 (b)) were analyzed by means of the Anderson-Weiss approach [202] as presented by Fechete and co-workers [86]. They assumed a monoexponential correlation function for the description of motions in the range of microseconds and deduced a fit function for the initial part of $s_c^{\text{corr}}(t_{\text{seq}})$. By taking into account higher even moments of the line shape and relating them back to the second moment M_2 under

the assumption of a Gaussian-shaped spectral line, this function could be adapted to the application to a larger range of t_{seq} :

$$S_{\text{MSE}} \left(t_{\text{seq}}, \Delta M_2^{\text{dyn}}, \tau_c \right) = \exp \left[-\Delta M_2^{\text{dyn}} \tau_c^2 \left(e^{-(t_{\text{seq}}/\tau_c)} - 3e^{-(5t_{\text{seq}}/6\tau_c)} + \frac{9}{4}e^{-(2t_{\text{seq}}/3\tau_c)} + 3e^{-(t_{\text{seq}}/6\tau_c)} + \frac{t_{\text{seq}}}{2\tau_c} - \frac{13}{4} \right) \right] \quad (5.3)$$

Here, the parameter ΔM_2^{dyn} represents the decrease of M_2 due to the flip motion (see Fig. 5.13) amounting to about 4000 kHz². Yet, Eq. 5.3 yields a bad description of the development of $s_c^{\text{corr}}(t_{\text{seq}})$. Presumably, this is because Eq. 5.3 is based on the assumption of a chain-flip motion which is characterized by a monoexponential correlation function with a single correlation time. However, a distribution of correlation times seems more probable according to the investigations of Hu et al., who found that the correlation function of the flip process in PE crystallites rather follows a stretched exponential function than a monoexponential one [200]. This finding was considered by introducing a log-normal distribution of correlation times

$$P(\tau_c, \mu, \sigma) = \frac{1}{\sqrt{2\pi\sigma\tau_c}} e^{-\frac{(\ln \tau_c - \mu)^2}{2\sigma^2}} \quad (5.4)$$

into Eq. 5.3, obtaining

$$S_{\text{MSE}}^{\text{distr}} \left(t_{\text{seq}}, \Delta M_2^{\text{dyn}}, \mu, \sigma \right) = \int_0^\infty P(\tau_c, \mu, \sigma) S_{\text{MSE}} \left(t_{\text{seq}}, \Delta M_2^{\text{dyn}}, \tau_c \right) d\tau_c, \quad (5.5)$$

with parameters μ and σ , the latter describing the width of the distribution in decades. The mean of the τ_c distribution

$$\langle \tau_c \rangle = \exp(\mu + \sigma^2/2) \quad (5.6)$$

and the jump rate $1/(2\langle \tau_c \rangle)$ are suitable parameters to characterize the speed of the flip motion.

Fits to the corrected data curves $s_c^{\text{corr}}(t_{\text{seq}})$ using Eq. 5.5, where the integration was performed numerically, were of satisfactory quality for each measurement temperature (cf. Fig. 5.14 (b)), when only the parameter μ was left as a free parameter. Hence, the parameters σ and ΔM_2^{dyn} were fixed in a way, that the temperature dependence of the jump rate in an Arrhenius plot did not exhibit physically unexpected discontinuities or sharp bends. The values of σ and ΔM_2^{dyn} were determined once for one of the reactor powder samples ($M_w = 750$ kg/mol) and adopted for fits to the data of the other two PE samples, which were of inferior data quality.

The jump rates obtained by this procedure are displayed in Fig. 5.16. In the investigated temperature range the jump rates were almost equal for all three PE samples despite the differences in morphology, molecular weight and lamellar thickness. The corresponding correlation times follow an Arrhenius dependence

$$\langle \tau_c \rangle = \tau_0 e^{E_a/(RT)}. \quad (5.7)$$

The jump-rate uncertainties, depicted in Fig. 5.16 were obtained by varying the parameter values of σ and ΔM_2^{dyn} and identifying the ranges for which a straight line persists

in the Arrhenius plot. The activation energy E_a and the prefactor τ_0 were obtained from linear fits to the data in Fig. 5.16 and are summarized in the upper part of Table 5.1. The uncertainties of E_a and $\log_{10}[\tau_0]$ were estimated by determining their maximum and minimum values considering the range of possible jump rates given by the error bars in Fig. 5.16.

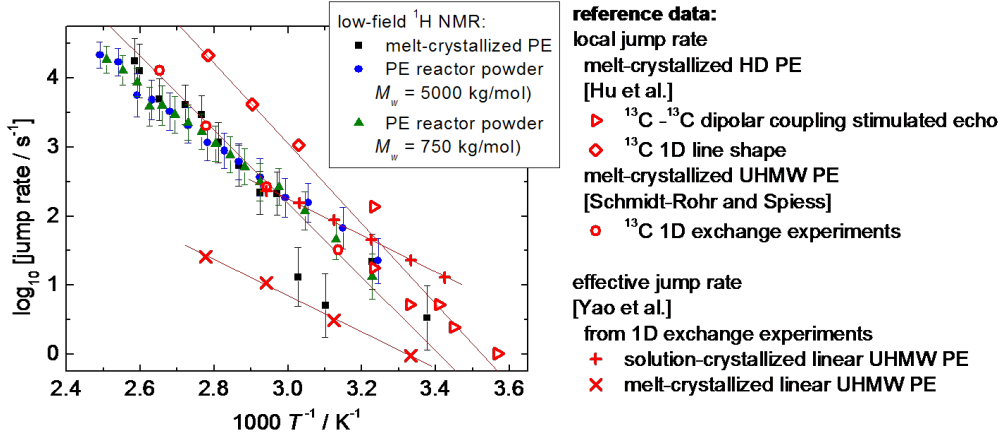


Figure 5.16.: Arrhenius plot of the jump rates obtained by analyzing the normalized and corrected MSE crystallite signal contributions for the different PE samples investigated here. For comparison literature data adopted from Refs. [140, 197, 200] are plotted. Graph adopted from Ref. [201].

Furthermore, for an independent consistency check of the data analysis, an alternative strategy was tested by introducing the Arrhenius dependence observed above directly into the fit function, in order to simplify and accelerate the data analysis. In contrast to the previous approach (referred to as the analysis of $s_c(t_{\text{seq}})|_{T=\text{const.}}$), in which the normalized and corrected crystallite-signal contributions $s_c^{\text{corr}}(t_{\text{seq}})$ to the MSE signals were analyzed separately for each temperature, here the data for all temperatures were fitted simultaneously. For this purpose the parameter μ in Eq. 5.5 was substituted by means of the relation

$$\mu = \ln \tau_0 + \frac{E_a}{RT} - \frac{\sigma^2}{2},$$

obtained from Eqs. 5.6 and 5.7, thus deriving $S_{\text{MSE}}^{\text{distr}}(T, t_{\text{seq}}, \Delta M_2^{\text{dyn}}, E_a, \tau_0, \sigma)$ as a fit function, which depends on the temperature T and contains the MSE sequence length t_{seq} as a fixed parameter [203]. Hence, this fitting method is referred to as the analysis of $s_c(T)|_{t_{\text{seq}}=\text{const.}}$. The new fit function was used to fit the data curves $s_c^{\text{corr}}(T)$ for fixed t_{seq} simultaneously for $n_{\text{MSE}} = 1, 2$ and 3 , thus attaining a single set of values for the free fit parameters ΔM_2^{dyn} , σ , E_a and τ_0 for each sample (see Fig. 5.17). The fit results are given in the lower part of Table 5.1. Due to limited data quality in the case of the melt-crystallized sample, here the parameters ΔM_2^{dyn} and σ had to be fixed in order to stabilize the fit. They were chosen in a way, that the uncertainty of E_a and τ_0 was minimal.

By comparing the results of both fitting methods in Table 5.1 it becomes clear, that the parameters ΔM_2^{dyn} and σ cannot be determined precisely. However, obviously the activation energy E_a of the jump process and the prefactor $\log_{10}[\tau_0]$ depend on these param-

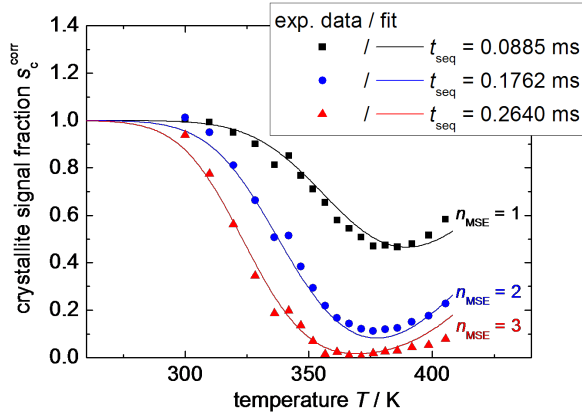


Figure 5.17.: Normalized and corrected crystallite signal fraction s_c^{corr} (see text) of a PE reactor powder sample ($M_w = 750$ kg/mol) as a function of the measurement temperature for three different MSE sequence lengths t_{seq} . The continuous lines represent fits to the data using the function $S_{\text{MSE}}^{\text{distr}}(T, t_{\text{seq}}, \Delta M_2^{\text{dyn}}, E_a, \tau_0, \sigma)$ (see text). Graph adopted from Ref. [201].

eters only slightly. For the two reactor powder samples very similar prefactors τ_0 and activation energies $E_a \approx 76$ kJ/mol were obtained. Although the results for the melt-crystallized sample are influenced by limited data quality, as indicated by the scatter of the data points in Fig. 5.16, the activation energy $E_a \approx 103$ kJ/mol determined for this sample is in very good agreement with the value $E_a \approx 100$ kJ/mol from earlier investigations of melt-crystallized PE reported in literature [140, 200, 204]. Yet, measurements of diffusion coefficients for longer-range translational chain motion between crystalline and amorphous regions by Yao et al. yielded an activation energy $E_a \approx 50$ kJ/mol for a melt-crystallized as well as a solution-crystallized sample [197], which is smaller than all the values determined here for the local jump process within the crystallites.

	melt-cryst. PE	PE reactor powder $M_w = 750$ kg/mol	PE reactor powder $M_w = 5000$ kg/mol
analysis of $s_c(t_{\text{seq}}) _{T=\text{const.}}$			
$\Delta M_2^{\text{dyn}} / \text{kHz}^2$	6700 ± 800	6700 ± 800	6700 ± 800
σ / kHz^2	1.57 ± 0.23	1.57 ± 0.23	1.57 ± 0.23
$E_a / \text{kJ}\cdot\text{mol}^{-1}$	97 ± 45	80 ± 17	72 ± 19
$\log_{10}[\tau_0 / \text{s}]$	-17.6 ± 6.4	-15.0 ± 2.3	-14.0 ± 2.8
analysis of $s_c(T) _{t_{\text{seq}}=\text{const.}}$			
$\Delta M_2^{\text{dyn}} / \text{kHz}^2$	5200	5910 ± 370	7820 ± 550
σ / kHz^2	0.94	1.41 ± 0.12	2.02 ± 0.15
$E_a / \text{kJ}\cdot\text{mol}^{-1}$	109.2 ± 4.2	77.3 ± 2.3	74.5 ± 2.5
$\log_{10}[\tau_0 / \text{s}]$	-19.86 ± 0.61	-14.81 ± 0.29	-13.70 ± 0.33

Table 5.1.: Comparison of results for the local jump process in PE crystallites for the samples mentioned in the text, obtained by means of the two methods of data analysis (see text).

In Fig. 5.16 the jump rates determined as described above for the local chain-flip process are depicted in comparison to literature data for jump rates of the local process and to effective jump rates reported by Yao et al. [197].⁸ These effective rates shall describe the rate of the fraction of chain flips which contribute to the longer-range chain diffusion.

⁸For this comparison, partly, effective jump rates have been calculated from the diffusion coefficients shown in Ref. [197], following the instructions given there.

The results obtained for all PE samples investigated herein match well the largest part of the literature data for jump rates of the local flip process, while the effective jump rates show a different trend.

In conclusion, although the direct investigation of the 180° chain-flip process in PE crystallites by means of NMR techniques is rather difficult, here, jump rates could be determined quantitatively for samples of different morphology, molecular weight and lamellar thickness, using simple and cheap low-field proton NMR methods. In particular the MSE sequence was used, for which the efficiency of the dipolar refocusing depends systematically on intermediate-regime dynamics in the sample. The jump rates obtained here are comparable to those from advanced, complex and time-consuming ¹³C-based high-field NMR experiments. As confirmed here, the mean correlation time of the jump process follows an Arrhenius temperature dependence, which could be implemented into the fit of the data. Although the speed of the longer-range chain diffusion varies between samples of different morphologies, differences in the form of the crystal fold surface (as well as in the molecular weight and the lamellar thickness) of the samples studied here did hardly show any effect on the chain-flip rate within the available correlation-time and temperature window of the method. Yet, the activation energies found for the reactor powder samples appear slightly smaller than those of melt-crystallized PE.

6. Crystallization of PCL

^1H low-field NMR FID or MSE measurements allow the tracking of the crystallinity development during isothermal crystallization of semicrystalline polymers at temperatures far above T_g , provided that the crystal growth process is adequately slow compared to the duration of a single crystallinity measurement of a few minutes. The investigation of crystallization kinetics was tested here for PCL with regard to the effect of nuclei and nucleating agents as well as the influence of temperature changes, in order to derive knowledge about a reasonable sample treatment for reliable and comparable NMR measurements of crystallinity and crystal thickness.

At temperatures above 0°C , where a significant contrast in chain mobility is present between the crystalline and mobile-amorphous domains of PCL, the polymer does not exhibit intermediate-regime dynamics (see Section 5.1). For this reason the MSE refocusing efficiency is high and the sequence is well-suited for crystallinity determination (see Section 4.2).

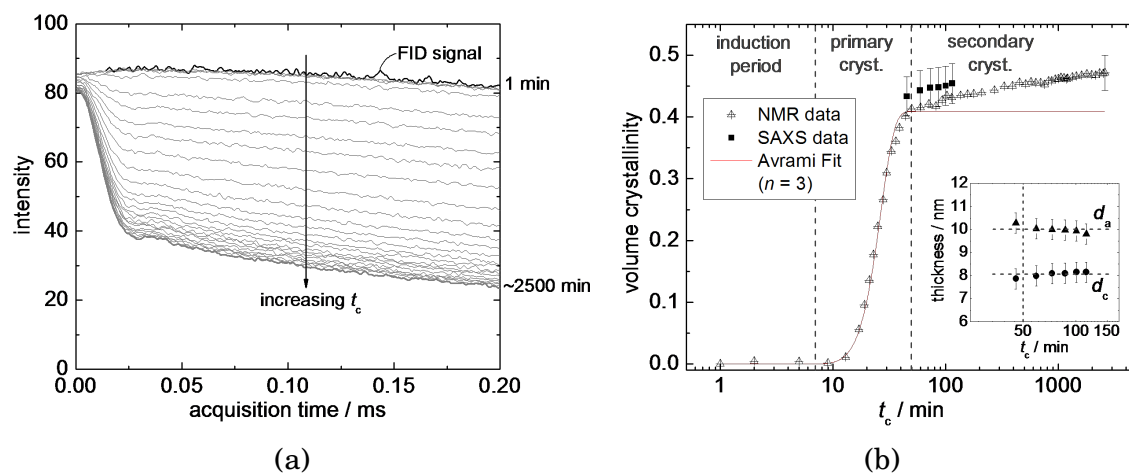


Figure 6.1.: Isothermal crystallization of PCL at 45°C : (a) MSE signals acquired at different crystallization times t_c between 1 and about 2500 minutes. The FID signal of the molten sample is depicted as well; (b) Development of the volume crystallinity as a function of t_c , derived from fits to the data plotted in (a) as described in Sections 4.1 and 4.2. Here, Eq. 4.7 has been used to convert the mass crystallinities to volume crystallinities. The red line represents a fit using the Avrami equation with an Avrami exponent $n = 3$ (see text). For comparison crystallinities from SAXS measurements are plotted additionally and the corresponding thicknesses of crystalline and amorphous domains, d_c and d_a , are shown in the inset. For the sake of clarity the error bar for the NMR data is depicted only for the last data point at long t_c .

In Fig. 6.1 (a) MSE signals of a PCL sample during isothermal crystallization at 45°C are shown exemplarily. At the beginning of the process only mobile, molten material is present, reflected by the slowly and uniformly decaying signal. As PCL crystals start to grow, rapidly decaying crystallite signal emerges, whose extent increases with rising crystallization time t_c . Furthermore, expectedly, the shape of the slowly decaying amorphous-phase signal changes with proceeding crystal growth, following from the increasing restrictions of amorphous-phase chain dynamics posed by the crystallites, which result in stronger residual dipolar couplings and shorter T_2 relaxation times (see Section 3.3). In dielectric investigations of a thin PCL layer during isothermal crystallization Wurm et al. observed an early reduction of the charge carrier mobility on length

scales on the order of the sample thickness, before a crystalline sample fraction could be measured. They interpreted this finding as a hint to structure formation in a pre-phase prior to crystallization [205]. However, in the present NMR measurements and more elaborate investigations of the early stages of PCL crystallization the T_2 relaxation time remained constant until a crystallite signal could be detected, indicating a constant average chain mobility. Thus, no significant pre-ordering affecting a larger part of the sample was found here.

In order to derive volume crystallinity values, the MSE data were fitted using Eq. 4.6. To stabilize the fits, the shape parameters a , b , T_{2i} and ν_i were fixed to values obtained from the fit to the MSE signal, which was detected at the longest crystallization time. The signal fractions were corrected for signal loss according to the considerations in Section 4.2 and converted to volume fractions by means of Eq. 4.7.

The crystallinity development with increasing t_c is depicted in Fig. 6.1 (b). It shows the typical behavior comprising three well-known stages [36, 206, 207]:

1. the introduction period,
2. the primary crystallization period and
3. the secondary crystallization period.

During the introduction period primary nucleation takes place. Here, polymer nuclei are formed at structures within the melt (homogeneous nucleation) or at the surface of particles of low molecular weight or other impurities (heterogeneous nucleation) [10, 36]. The mechanism of the primary nucleation is, however, not clarified completely [207].

The term primary crystallization designates the growth of crystallites from the nuclei formed before. At increasing t_c the crystallinity rises in a characteristic way, following a sigmoidal curve shape [36, 208]. The development of the volume crystallinity $f_{c,V}$ during primary crystallization is often described by means of the Avrami equation [10, 209]

$$f_{c,V} \propto \left(1 - e^{-(kt_c)^n}\right),$$

where k is the crystal growth rate and n denotes the Avrami exponent. Originally, this equation has been developed to describe the filling of a volume by growing objects [10]. It is valid only in case of a radial, isotropic growth of structures from spatially randomly distributed nuclei with a constant growth rate [36, 209, 210]. The PCL crystallinity curve can be fitted by means of the Avrami equation. However, as known from literature [36], at the end of the primary crystallization period the agreement between the measured data and the fit curve worsens (see Fig. 6.1 (b)). Presumably, this discrepancy arises because the crystal growth rate varies in time as a result of the progressive concentration of entanglements within the amorphous regions, counteracting the crystal growth [36].

Literature values of the Avrami exponent n of PCL range between 2 and 4 [29, 30, 210–213]. The PCL data presented in Fig. 6.1 (b) do not permit a definite determination of n from the fit, because of too many adjustable parameters, such as the induction time, the growth rate k and the t_c fitting limits. However, $n = 3$, indicating the growth of spherical structures and a spontaneous nucleation, is within the range of possible values and seems reasonable, as in fact the existence of spherulitic crystalline superstructures has been proven in bulk PCL [213–215]. Anyway, the interpretation of the actual value of n is difficult, because the occurrence of secondary crystallization, the variation of the

crystal growth rate and the nucleation rate, a non-constant crystallite density along the spherulite radius and/or a simultaneous occurrence of instantaneous and spontaneous nucleation affect the Avrami exponent in a complex way [209].

The slight crystallinity increase, which proceeds over many decades in time after the completion of the primary crystallization, is referred to as secondary crystallization [36] and is known to occur in PCL [30, 216] and in many other semicrystalline polymers. In the literature the following reasons of this rise are mentioned [30, 206, 210, 214, 217]:

1. the stabilization of existing lamellae, e. g., by crystal thickening, or
2. the ongoing crystallization within existing superstructures, such as spherulites, e. g., by the growth of less stable subsidiary lamellae in amorphous regions between already existing, primary lamellae (in-filling).

To clarify the reason for secondary crystallization in PCL, results from SAXS measurements, performed during isothermal crystallization at 52.7°C by A. Seidlitz [218] (see Appendix A), are depicted in Fig. 6.1 (b). The time scale of the SAXS data was converted by multiplication with an appropriate factor to account for the different measurement temperature of the NMR data in the plot (see below). In accordance with results from literature, no distinct thickening of the PCL lamellae during secondary crystallization could be detected [218–222]. This is consistent with the findings from Section 5.1, which confirm the classification of PCL as a crystal-fixed polymer, where longer-range chain diffusion through the crystallites are absent and hence crystal thickening is not possible. Thus, the stabilization of lamellae by thickening can be excluded as a reason for secondary crystallization. Also the thickness of the amorphous domains changes only within the uncertainty margin (see Fig. 6.1 (b)). Yet, a slight decay can be supposed, inducing the small gain in crystallinity. Hence, in-filling processes, resulting in a decreasing amorphous-domain thickness at constant lamellar thickness seem possible only to a minor extent.

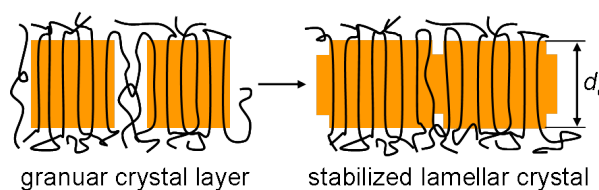


Figure 6.2.: Merging of native crystal blocks into a stabilized lamellar crystal according to Strobl [23].

By reversible heating of a PCL sample during isothermal crystallization in shear spectroscopy measurements, Wurm and Schick showed, that PCL crystallites stabilize during crystallization in a way that the melting point increases with rising crystallization time t_c [223]. Consistently, Kohn and Strobl could prove an enhancement of the inner order of PCL crystallites during isothermal crystallization by WAXS investigations [221]. Moreover, Wurm and Schick provided evidence that, while the crystallinity increase during secondary crystallization is small, the gain in crystal stability is significant. They interpreted their findings on the basis of the multistage model of crystallization by Strobl [23]. It suggests the formation of less stable, native crystal blocks, which merge later on by crystallization of the beforehand non-crystalline material between the blocks, thus creating a stable lamella of unmodified thickness d_c (see Fig. 6.2). As a result of the block merging the crystallinity should increase slightly, while the thick-

ness of the amorphous domains and the crystallites, detected by SAXS measurements, should hardly change. These features can be seen in Fig. 6.1 (b). Hence, secondary crystallization in PCL might be ascribed to the merging of blocks of native crystallites.

The Influence of Nuclei on Crystallization Kinetics. The PCL crystallization kinetics recorded by NMR are reproducible, provided that one and the same sample is investigated. Small time shifts of the crystallization isotherm can be ascribed to small deviations of the measurement temperature (see below). Yet, presumably due to a different density of impurities, measurements with the same settings but for different samples from the same batch may result in significant changes of the curve position (see Fig. 6.3 (a)).

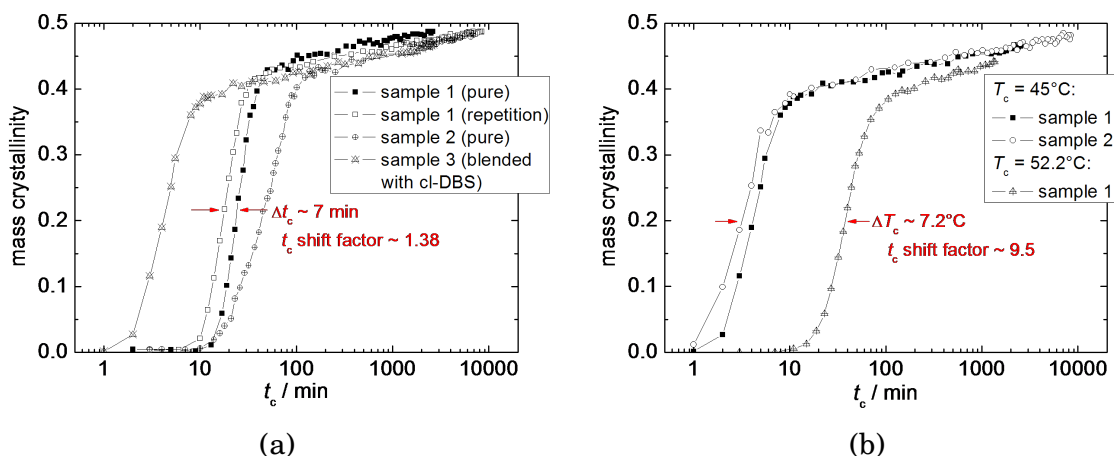


Figure 6.3.: Development of the mass crystallinity of industrially produced PCL ($M_n = 42.5$ kg/mol) during isothermal crystallization, detected by means of NMR MSE measurements: (a) Comparison of the kinetics for two different pure samples and a sample blended with 1.5 wt% of cl-DBS as a nucleating agent (see text), all of them crystallized at 45°C; (b) Comparison of the kinetics for samples blended with cl-DBS and crystallized at 45°C and 52.2°C.

For this reason, the effect of external nuclei on the crystallization kinetics was studied by means of DSC measurements using the temperature protocol depicted in Fig. 6.4 to detect a melt-memory or self-seeding effect [224]. The first 4 steps in the program served to establish a comparable thermal history of the sample. Subsequently, the sample was crystallized non-isothermally in step 5, molten by heating to an incremented self-nucleating temperature T_s and crystallized once more in step 9. A comparison of the onset temperatures T_c of the crystallization in step 5 and 9 yields information about the nucleation within the sample. The results of these measurements are shown in Fig. 6.5 (a) for two industrially produced PCL samples and a filtered and freeze-dried PCL sample, all of them originating from the same sample batch.

Two effects can be seen directly:

1. With increasing T_s , the crystallization temperature T_c , measured in step 9, approaches the equilibrium value T_c^{eq} , which is also found when crystallizing the sample after melting at high temperatures, i. e. in step 5.
2. The equilibrium crystallization temperature T_c^{eq} adopts significantly different values for different samples.

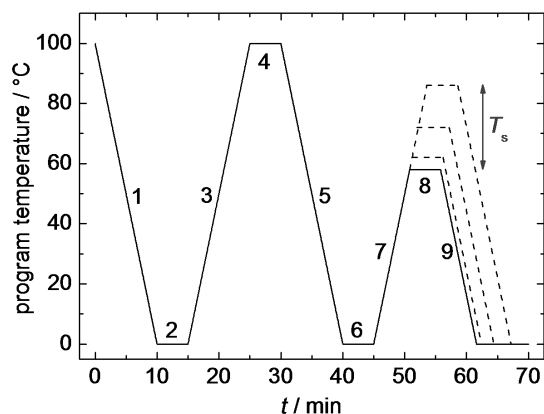


Figure 6.4.: DSC temperature program for studying the self-seeding or melt-memory effect in PCL according to Lorenzo et al. [224] with numbered program steps, including an annealing step at the variable self-nucleating temperature T_s .

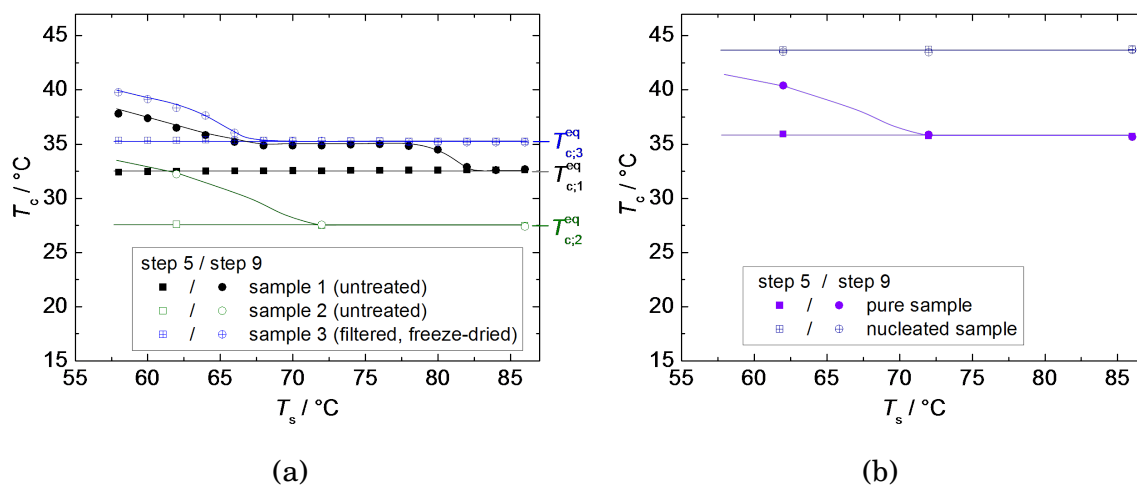


Figure 6.5.: DSC investigations of the non-isothermal crystallization of PCL: Dependence of the onset temperature T_c of crystallization during step 5 and 9 in the temperature program depicted in Fig. 6.4 on the self-nucleating temperature T_s for three different non-nucleated PCL samples of $M_n = 42.5$ kg/mol (a) and for a pure and a nucleated sample ($M_n = 20.1$ kg/mol) in comparison (b). In (a) the equilibrium crystallization temperatures T_c^{eq} are marked.

The first effect arises, because the density of nuclei for crystallization is enhanced, when the crystallites are molten at low temperatures T_s close to the DSC melting point. This leads to an accelerated crystallization during cooling (step 9) and an increased crystallization temperature T_c compared to crystallization from the equilibrium melt (step 5), as nuclei for crystallization do not have to be formed homogeneously in the melt [224]. With rising T_s the density of remaining nuclei approaches the value of the equilibrium melt and hence T_c gradually decreases to T_c^{eq} . Although this effect has been known for a long time [225] and was also found in PCL [224], the reason of the increased density of nuclei is still a matter of debate [226–229]. On the one hand small, stable crystal fragments, so-called self seeds, are under discussion, which survive the heating to T_s and facilitate the formation of active nuclei for crystallization in the subsequent cooling run [228]. On the other hand, compared to the equilibrium melt, the incomplete relaxation of chain segments at the positions of the molten crystallites might leave less entangled regions with enhanced residual order and a lower entropic barrier for a subsequent crystallization, thus accelerating the process (melt-memory ef-

fect) [32, 38, 230, 231]. Whether the self-seeding or the melt-memory effect cause the faster crystallization, could depend on the actual value of the self-nucleating temperature T_s [229]. Anyway, the size of the surviving structures, the self nuclei, must be small, i. e. below the detection limit of well-established measurement techniques, such as microscopy and NMR [227, 228]. Nevertheless, hints to both self-nucleating effects have been found experimentally [224, 225, 228, 229].

The second finding from the DSC measurements of PCL indicates that, also within a single batch, the industrially produced samples contain different amounts of impurities, presumably particles of low molecular weight or dust, which influence the crystallization behavior of the polymers by forming the basis for heterogeneous nucleation. Such external nuclei exhibit larger surface free energies than internal nuclei generated by structures in the melt and thus reduce the undercooling required for crystallization [10]. At low densities of nuclei, an increase in this density results in a faster crystallization with an enhanced temperature T_c . However, at high densities a saturation occurs [232, 233] and T_c remains constant. Obviously the treatment of the third sample, the results of which are depicted in Fig. 6.5 (a), generated an even higher number of external nuclei instead of reducing their density.

Differences in the density of nuclei also explain the deviations of the isothermal crystallization kinetics detected in NMR measurements for different PCL samples shown in Fig. 6.3 (a). Here, nucleating agents help to accomplish defined crystallization conditions with approximately the same number of nuclei in different samples. By adding such agents in a defined amount, the high number of introduced external nuclei causes a harmonization of the nucleation and turns the crystal growth into the rate-determining step of the crystallization process.

In order to compare the growth kinetics of different PCL samples, we used chloro-substituted dibenzylidene sorbitol (1,3:2,4-di(4-Chlorobenzylidene)Sorbitol, cl-DBS), a butterfly-shaped amphiphile derived from D-glucitol as a nucleating agent [233, 234]. Small amounts of cl-DBS dispersed in PCL by solution blending with butanone as a co-solvent self-assemble into a fibrous, crystalline nanoscale framework with average fibril diameters of $\sim 210 \text{ \AA}$, which is destroyed at temperatures above $\sim 130^\circ\text{C}$ [233, 235]. These fibrous structures serve as nuclei for the oriented crystallization of PCL. The dimensions of the PCL lamellae, however, are not influenced by the cl-DBS framework [232, 233, 235, 236].¹ As shown by Wangsoub et al. the fastest possible crystallization of PCL is reached at cl-DBS mass fractions larger than 1.5%. Hence, the measurements presented here have been performed for blends of PCL with 1.5 wt% of cl-DBS.² As opposed to the pure, non-blended samples, the nucleated ones do not show a self-seeding or melt-memory effect, because the influence of the artificially introduced nuclei dominates the behavior, compared to the self-nuclei, remaining within the melt at low T_s (see Fig. 6.5 (b)). Furthermore, due to the given high number of nuclei, in

¹As an organic gelling agent [234], cl-DBS, like pure DBS, causes a physical gelation of the PCL matrix, which has to be considered in practical applications. The blended PCL starts to flow only at high temperatures, where the cl-DBS framework is dissolved. However, at high temperatures there is the danger of polymer degradation (see Appendix B).

²The nucleating agent cl-DBS forms a crystalline network (cf. Ref. [233]) and thus contributes to the crystallinity of the sample. However, at 1.5 wt% of cl-DBS the contribution to the mass crystallinity amounts to 0.8% (absolute), which is within the uncertainty margin of the NMR crystallinity determination and is not considered further, because no quantitative crystallinity information should be derived from the presented data.

a non-isothermal treatment the blended samples crystallize at a significantly reduced undercooling, i. e. enhanced T_c , because of the faster nucleation of PCL at the surface of the cl-DBS framework. The isothermal crystallization is accelerated compared to the pure PCL samples as well (see Fig. 6.3 (a)). After blending with the nucleating agent different samples of the same molecular weight in fact exhibit comparable crystallization kinetics when crystallized isothermally at the same temperature (see Fig. 6.3 (b)). This confirms the suitability of the nucleating agent.

The Influence of Temperature Variations on Isothermal Crystallization. To evaluate the influence of temperature changes on the crystallization kinetics of PCL, an isothermal crystallization of a cl-DBS containing PCL sample was tracked at two different crystallization temperatures T_c (see Fig. 6.3 (b)). The time evolution of the crystal growth is determined by the viscosity of the melt and the thermodynamic driving force in a complex way [10]. Yet, at rather small temperature changes ΔT_c the modification of the crystallization isotherm can be described as a shift of the curve on the logarithmic crystallization time axis [10], characterized by means of a t_c shift factor. In the present case of PCL, a temperature variation ΔT_c of approximately 7.2 K resulted in a scaling of the t_c axis with a factor of about 9.5 (see Fig. 6.3 (b)). Hence, the shift of the crystallization isotherm, achieved by multiplying the time axis with a shift factor of 1.3 to 1.4 as found in Fig. 6.3 (a) for a repeated measurement of the same non-blended PCL sample, may be attributed to a temperature deviation of about 1 K between both experiments, which is within the uncertainty range of the temperature setting and measurement. The comparison of the isotherms of two different cl-DBS containing samples, both crystallized at 45°C, in Fig. 6.3 (b) yields a similar shift factor and a similar possible temperature deviation. Here, however, the different positions of the isotherms might also originate from the t_c measurement during the experiment, which has an accuracy on the order of about one minute.

As it is known from literature, the lamellar thickness depends on the crystallization temperature T_c [10]. Yet, it remains unclear, whether this is the case for the PCL crystallinity as well. The small decrease in crystallinity, which was detected by SAXS and DSC measurements of PCL at increasing T_c after isothermal crystallization [218, 235], can neither be confirmed nor disproved on the basis of the NMR crystallization investigations, as the amount of data points at very long crystallization times does not suffice to solve this issue (see Fig. 6.3 (b)).³

Comparison of Crystallinity Values from NMR, DSC and SAXS Measurements.

At last, the crystallinity values determined from NMR measurements shall be compared to those from DSC and SAXS investigations. Typically, the results derived by different experimental techniques may deviate by some percent, as the rigid-amorphous interphase is evaluated differently. While, e. g., in density and WAXS studies the interphase fraction is included in the crystallinity [79], the opposite is the case for the NMR investigations shown herein.

³Note, that crystallinity measurements at different temperatures T_c but at the same time t_c after the onset of the isothermal crystallization will yield a slightly lower crystallinity at larger T_c , as in this case the secondary crystallization will not have been progressed as far as for the lower crystallization temperature at the same t_c (cf. Fig. 6.3 (b)).

As an example, the DSC crystallinity of a non-blended PCL sample was determined from the heat flow in the heating scan subsequent to an isothermal crystallization step at 48°C of length 20 min and 200 min (see Appendix A). The duration of the crystallization was chosen according to the crystallization kinetics studied by NMR at the same temperature (see Fig. 6.6). The heat of fusion ΔH_m was determined after base-line correction from the area of the melting peak in the heat capacity curves, taking into account the sample mass. In order to estimate the mass crystallinity f_c the heat of fusion was normalized using the theoretical value for the melt of fusion ΔH_m^0 of 100% crystalline PCL. As such a sample does not exist, this value had to be calculated or extrapolated from measurements for samples with different crystallinities. Different values of ΔH_m^0 can be found in literature, ranging between 135 J/g and 148 J/g [161, 237–240]. The latter was calculated as the difference between the temperature dependent enthalpy functions of amorphous and crystalline PCL at 48°C [240, 241]. (The value $\Delta H_m^0 = 157$ J/g stated by Wurm et al. [216] is given for PCL at its equilibrium melting temperature $T_f^0 = 69^\circ\text{C}$.)

The first DSC measurement for $t_c = 20$ min enabled the estimation of a time-axis scaling factor of about 1.3 to match the DSC and NMR crystallinity results (see Fig. 6.6). This shift of the isotherm on the logarithmic time scale corresponds to a temperature deviation of about 1 K between the measurement temperatures of the NMR spectrometer and the DSC equipment. This is again in the order of the experimental uncertainty. The relative uncertainty of the DSC crystallinities settles at 5% to 6% and mainly results from the scattering of the ΔH_m^0 values given in the literature, while the relative uncertainty of the NMR mass crystallinity amounts to about 4%. Very good agreement between the DSC and NMR crystallinities is achieved, using $\Delta H_m^0 = 142.4$ J/g given by Crescenzi et al. [238] as the average of the values listed there (see Fig. 6.6).

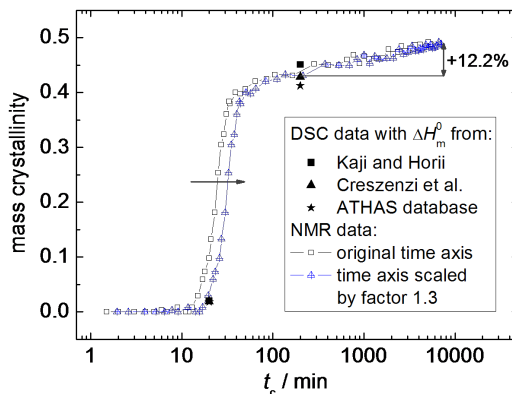


Figure 6.6.: Isothermal crystallization of PCL ($M_n = 42.9$ kg/mol) at 48°C: Comparison of crystallinity data from NMR and DSC measurements of the same sample. The DSC crystallinities were calculated using different values ΔH_m^0 from literature (see Refs. [161, 238, 240]). In order to match the DSC results, the NMR data were time-scaled by multiplication of the time axis with a shift factor of 1.3, corresponding to a temperature deviation between NMR and DSC measurements of about 1 K. (Graph adapted from Ref. [242])

In Fig. 6.1 (b) the volume crystallinities of a PCL sample derived from SAXS measurements during the isothermal crystallization at 52.7°C are compared to the volume crystallinities determined by NMR for a PCL sample of the same molecular weight. The

crystallization time axis of the SAXS data was converted by means of an appropriate time-shift factor to consider the deviating crystallization temperature of the NMR measurements. The SAXS results lie within the uncertainty margin of the NMR crystallinities. However, they exceed the NMR data consistently by 2% on the absolute scale, indicating that a part of the NMR interphase is evaluated as crystalline phase in the SAXS investigations.

In summary, one can state that the crystallization isotherms of PCL can be acquired reproducibly by ^1H low-field NMR measurements at a crystallization temperature, where a suitable mobility contrast is present between chains in crystalline and amorphous regions and where the crystal growth is slow enough to be tracked by MSE measurements. However, for reliable investigations of the crystallization kinetics, prior to crystallization the PCL melt has to be annealed at a sufficiently high temperature to avoid self-seeding or melt-memory effects. Moreover, impurities within the sample change the rate of crystallization in a non-predictable way. Hence, in order to enable a comparison of crystal growth kinetics of different PCL samples, the application of cl-DBS as a nucleating agent is recommended to disable the effect of nucleation as the rate-determining step. By tracking the PCL crystallization isotherm at different crystallization temperatures, the effect of small temperature variations could be estimated in the form of a time-shift factor. The crystallinity values obtained by NMR are in good agreement with the corresponding DSC results, while the SAXS crystallinities slightly exceed the NMR data due to a different evaluation of the interphase fraction.

7. Investigation of Spin Diffusion in PCL

^1H NMR spin-diffusion experiments are frequently used for the determination of domain sizes in heterogeneous polymer systems [76–78, 89, 92, 94–97, 99, 101, 103–107, 109–112, 114, 124, 130–132, 144, 151, 153, 243–245]. The aim of the work reported herein was to establish the low-field spin-diffusion method as a means to determine domain sizes in PCL and to test the usability of this approach. In order to determine lamellar thicknesses, appropriate ^1H spin-diffusion coefficients D of all polymer phases involved have to be known, as they connect length scale and time scale of the magnetization transfer process. For polymers D is typically on the order of $1\text{ nm}^2/\text{ms}$ [17], and there is a multitude of specific values reported in literature, derived on a theoretical or experimental basis. The choice of suitable values of D for the investigated polymer system is essential for the evaluation of reliable domain sizes. Yet, the spin-diffusion coefficient depends on a number of experimental parameters, such as sample-spinning speed, temperature or the length scale of the observed spin-diffusion process, and therefore an appropriate value has to be selected carefully according to the present experimental conditions of the spin-diffusion measurement. In the following an overview about literature work on spin-diffusion coefficients in heterogeneous polymer systems and the difficulties of their determination is given in Section 7.1, before the actual spin-diffusion measurements for PCL and their analysis will be presented.

7.1. Spin-Diffusion Coefficients of Heterogeneous Polymers

A variety of values for ^1H spin-diffusion coefficients D can be found in literature for rigid polymers and polymer phases, i. e. glassy polymers and crystalline polymer domains, ranging from $0.065\text{ nm}^2/\text{ms}$ to $0.83\text{ nm}^2/\text{ms}$ [76, 78, 89, 95, 97, 101, 102, 105, 116, 118, 119, 131, 152, 165, 246]. They originate from measurements on the one hand [102, 111, 139, 152, 165, 246] and theoretical estimations on the other hand [76, 78, 89, 95, 97, 101, 105, 116, 118, 131].

The common experimental approach for the determination of D relies on the analysis of NMR spin-diffusion data with the aid of domain thicknesses derived from external non-NMR measurements, e. g., by SAXS or TEM. In this manner Clauss et al. investigated symmetrical diblock copolymers consisting of two virtually immiscible blocks of glassy poly(styrene) (PS) and glassy poly(methyl methacrylate) (PMMA) using a chemical shift filter, and Magic-Angle Spinning [139]. The resulting value $D = (0.8 \pm 0.2)\text{ nm}^2/\text{ms}$ has so far been largely accepted to be specific not only for glassy polymers but for rigid organic matter in general, because D is not expected to depend much on the chemical nature of the system as long as the ^1H spins are exposed to strong dipolar couplings. Therefore in the past this value was employed not only for glassy PMMA and PS [8, 96, 104, 107–109, 112, 128, 144, 147, 244, 247] but also for other glassy polymers and the crystalline fraction of poly(ethylene) (PE) [94, 132, 151, 245].

The spin-diffusion coefficient D can be calculated analytically or numerically for simple regular lattice structures [137]. For more disordered systems like polymers an exact calculation is much more difficult. However, like spin diffusion, also the width of the spectral line from a static ^1H NMR measurement and the corresponding moments of line shape are governed by the dipolar coupling strength. Therefore D is related to

the line width $\Delta\nu_{1/2}$ [17] and to the second moment M_2 of the line shape for a powder sample. For rigid systems D can be assessed approximately using the expression

$$D = \frac{\sqrt{\pi}}{6} \langle r^2 \rangle \sqrt{M_2}, \quad (7.1)$$

if the spin interactions are purely dipolar [57, 89]. Here, $\langle r^2 \rangle$ is the mean-squared distance between adjacent proton spins [116, 248] and M_2 has to be inserted in units of $(2\pi)^2$. Yet, Meurer and Weill criticize the use of this scaling law [246]. By investigating different glassy polymers with either protonated or deuterated side chains, they showed that spin diffusion is slower (i. e. D is smaller) if the magnetization transfer to neighboring chains via the side chains is disabled due to side chain-deuteration. Furthermore, they found an increase in M_2 when side chains were deuterated. They interpreted this finding as a result of smaller average interproton distances along the chain in absence of side chain protons. From Eq. 7.1 it is clear, that a decrease in D and an increase in M_2 in case of the side-chain deuteration should result in a decrease of $\langle r^2 \rangle$. Meurer and Weill state that $\langle r^2 \rangle$ (in their conception being the mean-squared distance between the protons in the sample in general [246, 249]) is higher for deuterated than for protonated side chains bringing about a failure of Eq. 7.1. However, using the definition given above for $\langle r^2 \rangle$, i. e. considering essentially the mean-squared nearest neighbor distance, makes their argument somewhat questionable because this value should decrease when side chains are deuterated as Meurer and Weill themselves explain in their discussion of the elevated values of M_2 .

Compared to spin-diffusion coefficients of rigid systems those of mobile polymer phases (i. e. amorphous or rubbery phases far above the glass transition temperature) are smaller, because dipolar couplings are partially averaged due to fast and almost isotropic molecular motions [120]. Mobile-phase values of D between $0.02 \text{ nm}^2/\text{ms}$ and $0.5 \text{ nm}^2/\text{ms}$ derived either from measurements [93, 100, 120, 125, 152, 244] or calculations [78, 89, 95, 97, 101, 105, 113, 131, 144, 151] can be found in literature. As temperature variation strongly influences the degree of averaging of the couplings in mobile polymer phases via changes in chain mobility, the mobile-phase spin-diffusion coefficient is known to depend on temperature [120].

In principle, it should be possible to derive D for mobile polymer phases by means of the proton line width from a static NMR measurement. However, for a corresponding pure Lorentzian-shaped spectral line, M_2 used in Eq. 7.1 cannot be calculated analytically. In order to solve this problem the spectra have to be truncated in a way that the spectral intensity is (defined to be) zero for frequencies higher than a cut-off parameter α and lower than $-\alpha$. Now M_2 can be assessed by [70, 89]

$$M_2 = \frac{\alpha \Delta\nu_{1/2}}{\pi}.$$

Hence, for the spin-diffusion coefficient we find

$$D = \frac{1}{6} \langle r^2 \rangle \sqrt{\alpha \Delta\nu_{1/2}} \approx \frac{\sqrt{\pi}}{6} \langle r^2 \rangle \frac{\sqrt{11.2}}{T_2}, \quad (7.2)$$

where the latter term follows from the numerical estimate $M_2 \approx 11.2/T_2^2$, based on the T_2 relaxation time constant and given by Idiyatullin et al. for a Lorentzian-shaped spectral

line.

Yet, some authors advise against the use of the line width $\Delta\nu_{1/2}$ to determine spin-diffusion coefficients according to Eq. 7.2, when anisotropic motions take place in the sample [139, 250], because the distribution of isotropic chemical shifts in the rather complex polymer systems results in an additional line broadening in a static ^1H NMR measurement. Hence, the measured line width is supposed to exceed the one originating from dipolar couplings which is required for the calculation in Eq. 7.2, especially when the couplings are strongly reduced by molecular motions [251]. Therefore Mellinger et al. suggested to determine D for mobile polymers on the basis of the T_2 relaxation time which, similarly to the line width, is governed by dipolar couplings and therefore related to the spin-diffusion coefficient [129, 251]. Moreover, effects of chemical shift distributions on T_2 measurements can be removed by appropriate pulse sequences. To derive a relation between D and T_2 , Mellinger et al. performed static spin-diffusion and T_2 (CPMG) measurements at different temperatures for diblock copolymers consisting of glassy PS and mobile poly(isoprene) (PI) as well as poly(ethylene oxide) (PEO) in a crosslinked matrix. Using the initial rate approximation (IRA, see Section 7.7), domain sizes from SAXS measurements and a spin-diffusion coefficient $D = 0.8 \text{ nm}^2/\text{ms}$ from Ref. [139] for the rigid polymer phases, they obtained a calibration curve $D(T_2)$, which is frequently applied for mobile polymer phases [8, 94, 96, 104, 111, 128, 132, 144].

Spin-diffusion coefficients reported in literature often result from measurements under MAS at different spinning frequencies. Yet, Jia et al. verified that sample spinning influences the spin diffusivity directly via averaging of dipolar couplings but also indirectly as a consequence of temperature changes due to MAS [252]. For crystalline domains in PE they measured a decrease of the diffusion coefficient by a factor of 4 when increasing the spinning frequency from 2 kHz to 16 kHz. Unfortunately they did not perform measurements at frequencies below 2 kHz and for a static setup, so that there is no information about the development of D in these cases. Nevertheless, spin-diffusion coefficients for the analysis of static measurements (as in the case of low-field NMR experiments) should not be adopted injudiciously from experiments under MAS (or spin-lock¹). Based on the findings of Jia et al. it is not surprising that the accepted value $D = (0.8 \pm 0.2) \text{ nm}^2/\text{ms}$ deduced by Clauss et al. for glassy PS from spin-diffusion measurements under MAS (4.5 kHz) [139] is not applicable for static spin-diffusion experiments of a block copolymer containing PS as a glassy component [8, 156]. Here, a significantly lower value of $(0.38 \pm 0.06) \text{ nm}^2/\text{ms}$ was determined [156], suggesting that there is a maximum of D for small MAS frequencies. In line with this re-evaluation of D for the rigid phase also the values for the mobile phase, derived from the calibration curve given by Mellinger et al. [251] (see above), had to be corrected by a factor of (0.76 ± 0.05) , as Mellinger's curve is based on the value of Clauss et al., too. In summary the accepted literature values are too high to be used for the analysis of static measurements. Discrepancies, however, are also known for measurements under MAS [104, 109], possibly due to differences in spinning frequencies.

The necessity to adopt domain sizes from external sources for the estimation of D can be overcome by NMR approaches which use invariant reference lengths within the polymer sample itself instead. Wang and White, e. g., generated a polarization gradient within

¹Apart from MAS, also spin-lock pulses slow down spin diffusion due to changes in dipolar coupling interactions [102].

a poly(isobutylene) (PIB) monomer with the help of a chemical shift filter and a dipolar filter and observed intra-chain proton spin diffusion indirectly via magnetization transfer from protons to proximate ^{13}C nuclei under MAS (4 kHz) [93]. As a reference length for the determination of D they calculated the length of a cylinder inscribing a monomer unit. They obtained a value $D = 0.0044 \text{ nm}^2/\text{ms}$ for spin diffusion through a monomer unit which is very small compared to the one calculated from the width of the static proton spectral line ($D = 0.063 \text{ nm}^2/\text{ms}$). Here, sample spinning could of course be one reason for this significant discrepancy. A similar approach was reported by Jia et al., first for amorphous poly(carbonate) (PC), poly(phenylene oxide) (PPO) and a PS-PMMA diblock copolymer [125] and later for an amorphous blend of PCL und PMMA [100], resulting in spin-diffusion coefficients between $0.42 \text{ nm}^2/\text{ms}$ and $0.69 \text{ nm}^2/\text{ms}$ [125] and $0.11 \text{ nm}^2/\text{ms}$ and $0.21 \text{ nm}^2/\text{ms}$ [100], respectively. However, these approaches yield coefficients for very local magnetization transfer processes and a conversion to a bigger length scale might be problematic as the geometry of the diffusion process may change. In this regard, Chen and Schmidt-Rohr reported that the length scale, at which spin diffusion is monitored, influences the value of the diffusion coefficient. Using a *hole-burning* technique under MAS to detect local spin diffusion on the scale of $\sim 0.5 \text{ nm}$ they measured rigid-phase spin-diffusion coefficients in atactic PS, PE and poly(propylene) (PP) [102]. They found values smaller than $D = 0.8 \text{ nm}^2/\text{ms}$ given by Clauss et al. but increasing from $0.2 \text{ nm}^2/\text{ms}$ to $0.5 \text{ nm}^2/\text{ms}$ with rising diameter of the *hole*, acting as a magnetization sink, and suggested that longer-range spin diffusion might be faster because of more efficient pathways for a magnetization transfer, which open up when the magnetization sink is enlarged, e. g., transfer along the polymer backbone or via side chains to other chains (cf. Ref. [246]).

In order to determine lamellar thicknesses in PCL by means of low-field spin-diffusion experiments, spin-diffusion coefficients for PCL have to be assessed. Up to now, as the only reference for such data, Voda et al. report values of D between $0.14 \text{ nm}^2/\text{ms}$ and $0.25 \text{ nm}^2/\text{ms}$, being calculated from Eq. 7.2 for the case of PCL as a soft segment in thermoplastic polyurethanes [101]. Yet, some more information on the coefficients of PCL might be deduced by considering the values for chemically similar polymers.

PCL resembles PE in the fact that it consists of CH_2 groups. Yet, it contains additional COO groups which induce a significant elongation of the repeat unit and a slight widening of the crystalline unit cell in directions perpendicular to the chain axis compared to PE (see Section 2). Thus, the magnetization transfer along the chain will proceed more slowly than in PE due to a blockage caused by the COO groups, which lack proton spins. Hence, the diffusion coefficients for PCL should be smaller than for PE. Some values can be found for PE crystallites ($D \approx 0.11 \text{ nm}^2/\text{ms}$ to $0.83 \text{ nm}^2/\text{ms}$) and amorphous domains ($D \approx 0.07 \text{ nm}^2/\text{ms}$ to $0.25 \text{ nm}^2/\text{ms}$), which partially result from calculations according to Eqs. 7.1 and 7.2 [78, 105, 116, 118, 250] and partially from static spin-diffusion measurements [76, 152, 165]. Yet, because of the large spread of values, precise information on the spin-diffusion coefficients in PCL cannot be derived here.

Buda et al. however calculated coefficients for Nylon-6 from the static proton NMR line width ($D \approx 0.21 \text{ nm}^2/\text{ms}$ to $0.29 \text{ nm}^2/\text{ms}$ for the crystalline phase and $0.034 \text{ nm}^2/\text{ms}$ to $0.084 \text{ nm}^2/\text{ms}$ for the amorphous phase) [95, 97]. As Nylon-6 exhibits a very similar chemical structure as PCL (the oxygen atoms in the backbone of PCL are substituted by NH groups in Nylon-6) similar values of D can be expected. The additional proton spin

per monomeric unit in Nylon-6 might enable a slightly faster spin diffusion compared to PCL. However, the values for the amorphous phase deviate from those calculated for mobile PCL chains by Voda et al. (see above).

As seemingly neither theoretically nor experimentally spin-diffusion coefficients for the three PCL phases (crystalline, amorphous and interphase) have been determined up to now, it was necessary to catch up on this and to ascertain them by means of static proton low-field spin-diffusion measurements of PCL which will be described in the next section.

7.2. Proton Low-Field NMR and SAXS Measurements of Semicrystalline PCL

In order to quantitatively determine spin-diffusion coefficients for the crystalline, interphase and mobile-amorphous component in PCL, in addition to ^1H low-field spin-diffusion NMR data, information on T_1 relaxation and on the PCL long period is required. The former was obtained here by performing ^1H NMR Saturation-Recovery experiments, while the latter was derived from SAXS measurements. In this section details on the measurement program are discussed as well as changes in crystallinity, domain sizes and the progression of spin diffusion during the measurements.

The investigations were performed using an industrially produced PCL sample ($M_n = 42.5$ kg/mol), the crystallization behavior of which had been studied before intensively under isothermal conditions in the temperature range used here (see Chapter 6). For the NMR measurements the sample was first molten and kept at 90°C for approximately half an hour in order to completely melt all crystallites and to remove a possible melt memory (see Chapter 6) before the sample was crystallized isothermally at $T_c = 45^\circ\text{C}$ for about 4 days. This crystallization temperature T_c was chosen in order to ensure crystallization to be fast enough to attain a practicable measurement program on the one hand. On the other hand the supercooling below the zero growth temperature of about 77°C [253] should be small enough to ensure that slight temperature deviations (< 0.5 K) during crystallization affected the progression of crystallization and the lamellar thickness only sparsely.²

Apart from the quantitative determination of spin-diffusion coefficients the effect of secondary crystallization and temperature changes on the spin-diffusion coefficients should be investigated. Therefore the following temperature program was used for the NMR and SAXS measurements of the PCL sample (see Fig. 7.1):

- A) measurement at the crystallization temperature $T_c = 45^\circ\text{C}$ after 4 days of isothermal crystallization to ensure the existence of well-ordered, stable crystallites of preferably uniform structure,
- B) repetition of the measurement after two days of storage at T_c ,

²At $T_c = 45^\circ\text{C}$ primary crystallization of the sample took 2 to 3 hours, but crystallinity increased further by about $\Delta f_c = 3\%$ to 4.5% on an absolute scale during the next 5 to 6 days. After 4 days of isothermal treatment, the absolute changes in crystallinity during one day ranged between 0.3% and 0.4% . This difference is significantly below the uncertainty level of the crystallinity measurement by NMR ($\Delta f_c = 1\%$ to 2%), so that at this point in time changes occurring during the measurement of a full set of NMR data (see below for an estimation of the duration) could be neglected.

- C) cooling the sample to 27°C and measurement after temperature equilibration,³
- D) repetition of the measurement after two days of storage at 27°C and
- E) heating the sample to T_c and repetition of the measurement after temperature equilibration.

At every step in this program the following data were acquired:

- the long period L from a SAXS measurement,
- the crystallinity f_c from ^1H NMR FID and MSE signals,
- ^1H NMR T_2 relaxation data,
- spin-diffusion data from ^1H NMR mobile- and crystalline-phase-selected experiments and
- ^1H NMR Saturation-Recovery data.

All NMR experiments were performed in low magnetic field using the settings described in Appendix A. The measurement of a whole set of NMR experiments took ~ 12 hours, the main part of which (~ 7 hours) was caused by the DQ-filtered spin-diffusion experiment.

The SAXS measurements and data analyses were performed by M. Sc. A. Seidlitz for a PCL sample analogous to the one used for the NMR experiments under the same temperature conditions. Information about the SAXS apparatus, the experimental settings and the data analysis are given in Appendix A. The temperature setting of the NMR spectrometer and the SAXS sample holder was adjusted prior to the measurements by comparing the readout of one temperature sensor in both devices.

Determination of Domain Sizes and Crystallinity. To track possible changes in crystallinity, NMR FID and MSE signals were acquired before and after the spin-diffusion measurements in steps A to E. The crystalline, mobile-amorphous and rigid-amorphous interphase volume fractions of the sample were calculated corresponding to the procedure discussed in Sections 4.2 and 4.1. However, to obtain the total signal intensity $I_{\text{tot},T}(t = 0)$, the FID of the molten sample was needed. In order to not destroy the sample morphology formed under isothermal crystallization by melting, this intensity was obtained by melting a second PCL sample of the same molecular weight (from the same batch) and with similar sample volume and filling level in the NMR tube, which served as a reference sample.

In contrast to the low-field NMR techniques, SAXS experiments are sensitive to electron density differences, i. e. to the structure of the sample. The analysis of the measured SAXS data is based on a model assuming a one-dimensional stack of crystalline lamellae [254] and a two-phase morphology, i. e. a periodic arrangement of crystalline and amorphous domains, without separating rigid-amorphous interphase domains in between. The evaluation of the scattering data yielded the long period L , average thicknesses of the crystalline and amorphous domains, d_c and d_a , and the widths of the distribution of these thicknesses, σ_c and σ_a , respectively. The uncertainty of the long period amounts to 0.3 nm resulting from the resolution of the measured scattering data, while

³This temperature was chosen for practical reasons, as it is the lowest temperature attainable in the spectrometer without using a cooling unit.

the uncertainty of d_c and d_a is given as ± 0.44 nm [218]. Presuming the one-dimensional arrangement of domains referred to above, the crystalline-phase and amorphous-phase volume fraction of the sample (labeled by the subscript 'V') can be calculated from the thicknesses via $f_{p,V} = d_p/L$, where the index p indicates the corresponding polymer phase.

Importantly, the SAXS results show a slight, reversible decrease of the long period and of the average thicknesses d_c and d_a on cooling from 45°C to 27°C (see Fig. 7.1 (a)). The effect emerged mainly in the thickness of the amorphous domains which fell from 7.9 nm by 0.5 nm to 7.4 nm, whereas the change in crystal thickness was less pronounced. It amounted to ~ 0.3 nm, being below the uncertainty of d_c . Yet, all thickness variations were smaller than the length of a monomer unit in the crystallites $d_{\text{mon}} \approx 0.865$ nm [49, 51]. The very small but systematic decrease in the thickness of the amorphous domains at 45°C by about 0.2 nm, which was detected within the 9 days of measurements, is considered to be a result of secondary crystallization (see Section 5.1).

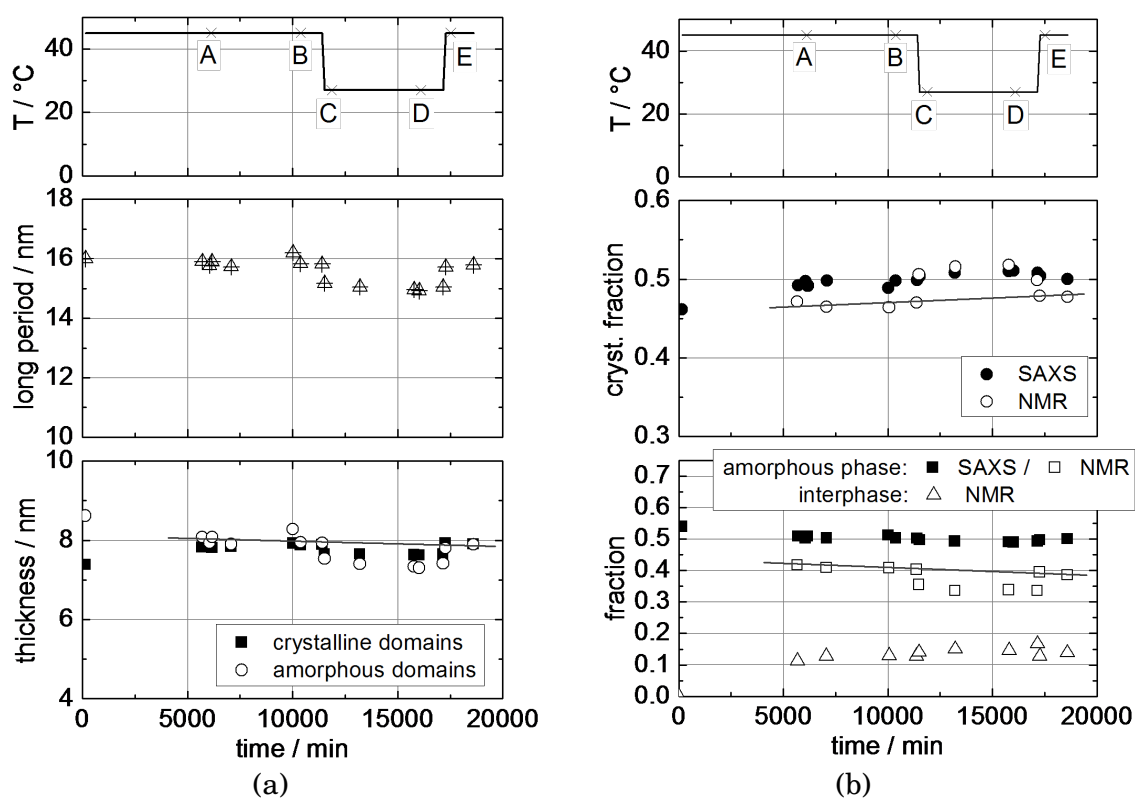


Figure 7.1.: SAXS and NMR results of PCL ($M_n = 42.5$ kg/mol) as a function of time in the measurement program. The starting point $t = 0$ marks the beginning of the isothermal crystallization. The temperature program is shown in the upper parts of (a) and (b). The marks A to E designate the points in time at which NMR spin-diffusion measurements were performed. The solid, grey lines are guides to the eye to indicate the progression of secondary crystallization. (a) Average thicknesses obtained from SAXS measurements; (b) Sample fractions as obtained from NMR MSE and FID signals and calculated from SAXS domain thicknesses.

The absolute sample fractions derived from SAXS and NMR measurements deviate (see Fig. 7.1 (b)) because data analysis is based on different morphological models for the two methods. At 45°C about 80% of the interphase detected by NMR is evaluated as belonging to the amorphous phase in the SAXS measurements, whereas the residual

20% are included in the crystalline phase. At 27°C the proportions shift in a way that the whole NMR interphase is interpreted as amorphous phase in the SAXS measurements (see Fig. 7.2).

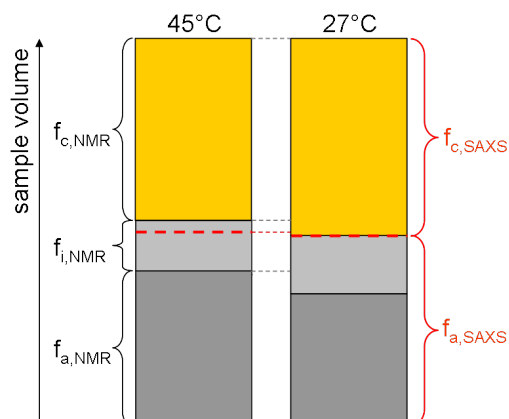


Figure 7.2.: Volume fractions of the PCL sample as obtained from NMR and SAXS measurements at 45°C and 27°C. The crystalline phase, mobile-amorphous phase and interphase, observed by NMR, are depicted as orange, light grey and dark grey rectangles, respectively, with the corresponding areas indicating the fractions $f_{c,NMR}$, $f_{i,NMR}$, $f_{a,NMR}$. The SAXS fractions $f_{c,SAXS}$ and $f_{a,SAXS}$ are marked by the dotted red lines.

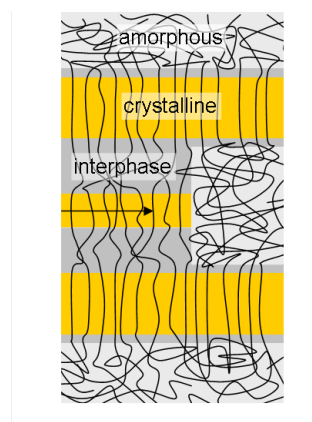


Figure 7.3.: Schematic drawing of the insertion of a lamella after cooling of the sample. Due to the growth of a new, thinner lamella, the interphase fraction detected by NMR is increased excessively due to the augmented immobilization of polymer chains between the growing lamella and the older ones.

Nevertheless, sample fractions from both NMR and SAXS experiments follow consistent and reversible trends upon cooling and heating of the sample. Yet, while the crystallinity $f_{c,V}$ obtained by SAXS grew only minimally upon cooling from 50% to 51% and fell again upon heating, this trend was more pronounced in the NMR results (see Fig. 7.1 (b)). Here $f_{c,V}$ increased reversibly by about 4% from 47% to 51%, while at the same time the mobile-amorphous volume fraction $f_{a,V}$ fell from 40% to 34% and the interphase volume fraction rose from 13% to 15%. The crystallinity changes detected by SAXS were too small to be significant compared to the absolute uncertainty of 3.6% to 3.9% resulting from measurement and analysis uncertainties. Yet, the NMR fractions could be determined with an absolute uncertainty of $\pm 2\%$. It is therefore confirmed that the effect of temperature changes on the sample fractions is no artifact. The temperature effect is superimposed by a slight decrease of $f_{a,V}$ by $\sim 2\%$ and an increase in crystallinity $f_{c,V}$ by $\sim 1\%$ during the 9 days of measurements, resulting from secondary crystallization. In the SAXS results this trend is hardly visible (see Fig. 7.1 (b)).

According to Strobl [10] the results from the domain-size and crystallinity measurements can be interpreted in terms of the *insertion mode* model as follows:

- During crystallization at 45°C crystalline lamellae of thickness $d_{c,45^\circ\text{C}}$ are formed by stretching parts of the chains. All non-crystallizable material such as entanglements or chain ends meanwhile are transported to the edges of the crystallites.

In the crystal-fixed polymer PCL (see Section 5.1) these non-stretchable units are than trapped in amorphous regions between the crystallites as a reorganization by chain transport through the crystallites is not possible.

- The crystalline lamellae and the concentrated non-crystallizable material near the crystallite surfaces form zones with thickness $L_{\min,45^\circ\text{C}}$ in which no other lamella can grow. Thus, stacks of lamellae are built with long periods ranging between $L_{\min,45^\circ\text{C}}$ and $2L_{\min,45^\circ\text{C}}$, as for distances larger than that further lamellae of size $d_{c,45^\circ\text{C}}$ could form in between the others.
- The lamellar thickness d_c depends on the crystallization temperature T_c according to $d_c^{-1} = C_c(T_c^\infty - T)$, where C_c and T_c^∞ denote a specific constant and temperature [10]. Hence, after cooling to 27°C growth of thinner lamellae is preferred which push aside less non-crystallizable material and therefore are surrounded by thinner uncrystallizable zones: $d_{c,27^\circ\text{C}} < d_{c,45^\circ\text{C}}$ and $L_{\min,27^\circ\text{C}} < L_{\min,45^\circ\text{C}}$. Such thinner lamellae can enter amorphous regions in the primary stacks of crystallites where enough space is left, i. e. where the local thickness $d_{a,45^\circ\text{C}}$ of the amorphous layer between the already existing crystallites is larger than $L_{\min,27^\circ\text{C}}$.

Thus, the average thicknesses of amorphous and crystalline domains in the sample decrease, but the effect is stronger for the amorphous phase because a part of the amorphous domains is divided into much smaller regions due to the insertion of crystallites. The crystallinity f_c increases as the amount of amorphous material is reduced more strongly than the rest. By contrast, for an α_c -mobile polymer, where chains are able to move through the crystallites, crystal thickening occurs upon cooling, resulting in a reduced value of d_a but increased values of d_c and f_c . Thus, the results on domain thicknesses and crystallinity indirectly confirm the absence of any transport of chain parts through the PCL crystallites.

Using SAXS measurements, structural information is obtained in terms of differences in electron density between crystallites and amorphous material. NMR experiments in contrast are sensitive to chain mobility. Due to the insertion of lamellae the mobile-amorphous material between old and new lamellae is partially immobilized and therefore augmentedly interpreted as interphase (see Fig. 7.3), while a part of the former interphase at lower temperature is construed as rigid-like material in NMR measurements. Therefore, no fixed ratio between the volume crystallinities from SAXS and NMR measurements exists for the two measurement temperatures (see Fig. 7.2).

Spin-Diffusion Experiments for the Investigation of the Magnetization Transfer Between the Domains. The spin-diffusion experiments were carried out according to the scheme in Fig. 4.8 by incrementing the mixing time τ_{diff} logarithmically between 0.01 ms and about 614 ms. The MSE sequence was used for detection to refocus the crystalline-phase signal (see Section 4.2). For selecting the magnetization in the mobile-amorphous and crystalline regions a MAPE filter and a short double-quantum filter were applied, respectively, with filter parameters chosen according to the considerations in Sections 4.4.1 and 4.4.2.⁴

⁴ As the choice of the MAPE filter length affects the signal fractions ascribed to the mobile-amorphous phase and interphase, the thicknesses of the corresponding domains derived from the analysis of the spin-diffusion curves slightly depend on this filter length and are coupled to each other. Furthermore, also for short spin-diffusion times it was not possible to evenly select magnetization in all crystalline

The MSE signals detected in the spin-diffusion experiments were analyzed phase-specifically by means of fits using Eq. 4.6. The shape parameters a , b , T_{2i}^* , T_{2a}^* , ν_i and ν_a were kept fixed at values gained from the fit to an unfiltered MSE signal. The signal intensities of the three polymer phases were corrected for signal loss during the MSE sequence (see Section 4.2), re-using the correction factors assessed for crystallinity determination, and scaled with a normalization factor in a way that the sum intensity of all three phases at $\tau_{\text{diff}} = 0$ and $t = 0$ is equal to 1. The normalized intensities s_c , s_i and s_a as a function of the mixing time τ_{diff} were analyzed further. In the following they will be referred to as *spin-diffusion curves*. A set of such curves from a MAPE-filtered and DQ-filtered spin-diffusion experiment is shown in Fig. 7.4 (a).

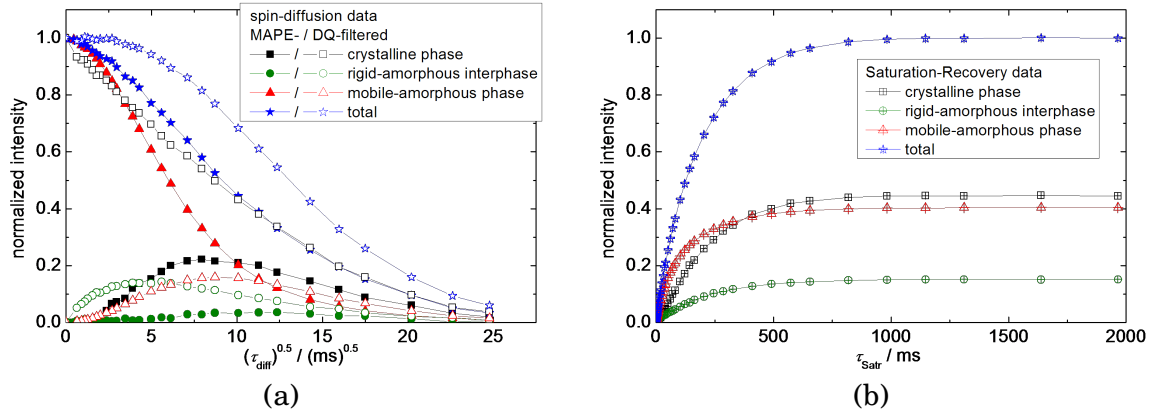


Figure 7.4.: Phase-resolved spin-diffusion curves (a) and Saturation-Recovery curves (b) measured for PCL at 45°C (measurement step A).

By comparing the spin-diffusion curves from all MAPE-filtered experiments, an accelerated intensity rise of the rigid phase signal $s_{\text{rig}}(\tau_{\text{diff}}) = s_c(\tau_{\text{diff}}) + s_i(\tau_{\text{diff}})$ is visible at lower temperature (see Fig. 7.5 (a)), hinting at diminishing mobile-amorphous domain sizes when temperature is reduced. This observation is consistent with the thickness information obtained from the SAXS measurements. Yet, the complementary curves of the mobile-amorphous-phase signal in the DQ-filtered experiments do not show a rise-time change at varying temperature (see Fig. 7.5 (b)), indicating a widely stable thickness of the rigid domains consisting of crystalline lamellae and the flanking interphase regions.

Saturation-Recovery experiments with a MSE sequence prior to detection were performed to allow a phase-resolved determination of T_1 relaxation times. The waiting time τ_{Satr} was incremented logarithmically between 0 ms and 2000 ms in order to cover the whole time period necessary for the magnetization rebuild. Again, the phase-specific signal intensities were obtained by fits using Eq. 4.6 and a subsequent correction for signal loss due to the MSE sequence (see Sections 4.1 and 4.2). Here, the normalization was performed in a way that the sum intensity of all three phases at $\tau_{\text{Satr}} \rightarrow \infty$ and $t = 0$ was equal to 1. The corrected and normalized signal fractions as a function of τ_{Satr} will henceforth be referred to as *Saturation-Recovery curves*. A detailed, quantitative analysis of the spin-diffusion and Saturation-Recovery data conducted by numerically

regions or to prevent excitation of small amounts of interphase and amorphous-phase magnetization (see Section 4.4.2), but the analysis of the spin-diffusion data was not derogated significantly by this fact.

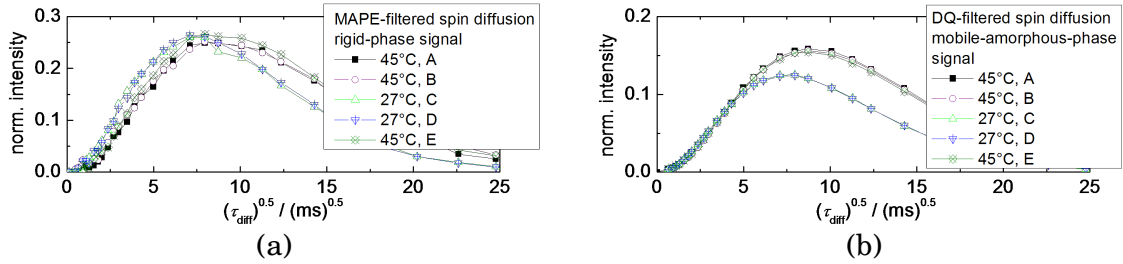


Figure 7.5.: Spin-diffusion curves of the magnetization sink for PCL from (a) MAPE- and (b) DQ-filtered experiments performed at each of the measurement steps A to E. In (a) data from crystalline phase and interphase are subsumed to generate a rigid-phase signal curve.

solving the spin-diffusion differential equation and taking into account T_1 relaxation will be discussed in Section 7.3.

7.3. Simultaneous Fit of Spin-Diffusion and Saturation-Recovery Data

Model Geometry for Simulation of Spin-Diffusion and Saturation-Recovery Curves.

In order to obtain quantitative information on spin-diffusion coefficients, spin-diffusion and Saturation-Recovery data were compared to numerically simulated curves generated by means of a PC program developed by Prof. H. Schneider, which is described in Ref. [8]. It is based on the numerical solution of the one-dimensional spin-diffusion equation 4.11 in consideration of T_1 relaxation. The main features of the simulation program are given in Appendix F.2. In principle the program allows calculations for different model geometries. When magnetization is depleted in either the crystalline lamellae or the mobile-amorphous regions of a semicrystalline polymer, spin diffusion proceeds approximately one-dimensional via the interfaces between crystallites and amorphous regions (see Fig. 7.6 (a)). Therefore, for the simulation a one-dimensional periodic lamellar arrangement of repeat units was assumed and the dimension parameter k in Eq. 4.12 could be set to 1. The repeat unit contained two or three different domains. In the three-phase (3P) model it consisted of three independent polymer phases (see Fig. 7.6 (b)). This model reflects the common idea of the structure in a semicrystalline polymer comprising crystalline, mobile-amorphous and rigid-amorphous interphase domains (see Fig. 7.6 (a) and Section 2). The two-phase (2P) model on the other hand deals with two distinct polymer phases only. It can be applied to PCL by combining crystalline phase and interphase into a rigid phase as suggested by Mauri et al. [8]. This simplification of the situation is, e. g., necessary to implement the Initial Rate Approximation (see Section 7.7).

In order to simulate phase-specific spin-diffusion and Saturation-Recovery curves for comparison with measured data, the partial differential spin-diffusion equation 4.12 for $k = 1$ had to be solved separately for every polymer phase, taking into account the T_1 relaxation. To this end the spin-diffusion coefficients D_p and relaxation times T_{1p} of the individual phases p were considered as constants (cf. Ref. [141]). This represents a simplification, as instead of sharp changes at the phase boundaries a gradual development of these parameters is expected. Furthermore, the value of the diffusion coefficient depends on the orientation of the spin interconnection vectors in the magnetic field, which may vary locally within each phase p . However, as the aim here was to seek effective average values of D_p and T_{1p} the simplification seems feasible.

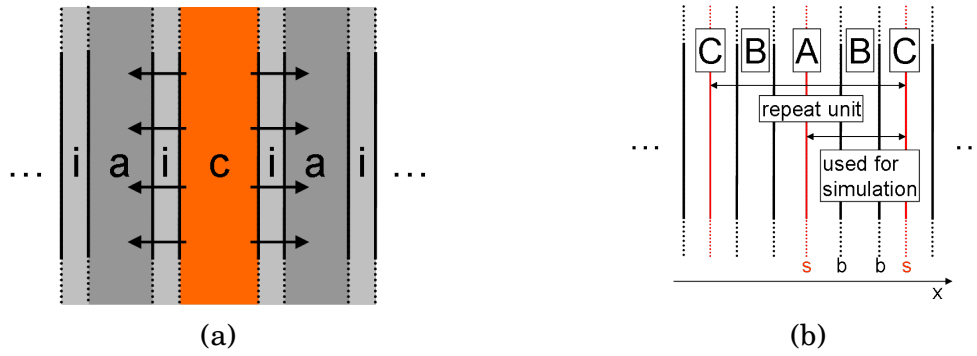


Figure 7.6.: (a) Schematic sketch of the three-phase morphology in PCL with crystalline, interphase and mobile-amorphous domains denoted c , i and a , respectively. The one-dimensional spin diffusion from the crystalline region via the interphases into the amorphous domains is depicted by arrows. (b) Representation of the three-phase (3P) model system (see text) used for simulating spin-diffusion and Saturation-Recovery data. The model phases are denominated as A , B and C with B designating the interphase. Boundary and symmetry planes are named b and s , respectively. The space coordinate is designated as x .

Fitting of Experimental Spin-Diffusion and Saturation-Recovery Curves. The simulation program provides a simultaneous fit of simulated data to experimental data sets from MAPE-filtered and DQ-filtered spin-diffusion and Saturation-Recovery experiments either separately or in arbitrary combinations with spin-diffusion coefficients, T_1 time constants and domain thicknesses of all polymer phases as fit parameters, using an iterative non-linear least-square fitting routine (Levenberg-Marquardt method [165]).

The spin-diffusion process is scale-invariant (as demonstrated by the factor $D_p/(\Delta x)^2$ in Eq. F.1), i. e. the characteristic spin-diffusion time (d^2/D) remains unchanged, when a domain size is increased by a factor a and the corresponding spin-diffusion coefficient by a factor a^2 : $(a \cdot d)^2/(a^2 D) = (d^2/D)$. In this case also the spin-diffusion curves do not vary. Hence, for an unambiguous determination of parameters in the fit either D or d has to be known. Here, thickness information from SAXS measurements was used to obtain quantitative information on spin-diffusion coefficients in PCL. Previous investigations mainly focussed on the 2P model [8], while here they were extended to the 3P model (see above and Fig. 7.6 (a)).

The proton spin densities $\rho_{H,p}$ and the thicknesses d_p of the phases p were chosen to be fixed fit parameters. PCL spin densities were obtained based on mass densities from literature [238] (see Appendix E). All densities used are given in Table E.1. The spin densities were used as input parameters to the fit in the form of relative spin densities, normalized to the mobile-amorphous-phase spin densities.

Because of the different morphological models used for analyzing the SAXS and NMR data (see Section 7.2), the thicknesses of crystalline and amorphous domains derived from SAXS could not directly be adopted for fitting the NMR spin-diffusion data. The long period L however should be a unique quantity for both methods, being independent from segmentation into the individual phases. Therefore in the fit the thicknesses d_p of the phases p were fixed to values calculated by means of

$$d_p = \frac{(f_p/\rho_{H,p})}{\sum_k (f_k/\rho_{H,k})} L, \quad (7.3)$$

valid for a lamellar sample structure. In the sum, the quotients are added up for all phases. Long periods L and sample fractions f_p present at the time points of the spin-diffusion measurements were estimated from the data shown in Fig. 7.1 (a) and (b) and are summarized in Table 7.1.⁵ Following from the uncertainties of the input quantities L , f_p and $\varrho_{H,p}$ of the phases p , the relative uncertainties of the thicknesses d_p amount to $\sim 6\%$ for crystalline, mobile-amorphous and rigid domains and $\sim 13\%$ for the interphase domains.

The longitudinal relaxation times T_{1p} and spin-diffusion coefficients D_p of the phases p were free fit parameters. The T_1 starting values for the simulation and fit program were obtained from linear fits to the initial rise of the Saturation-Recovery curves (see Section 5.1). Spin-diffusion coefficients for Nylon-6 [95, 97] were supposed to represent appropriate initial D_p values (see Section 7.1).

Simultaneous fits to data for all phases from either DQ-filtered spin-diffusion or Saturation-Recovery experiments separately worked acceptably well for both the 2P and 3P model. Inaccuracies were larger but still tolerable when fitting simulated curves for the 2P model to data sets from MAPE-filtered spin-diffusion experiments. However, significant discrepancies occurred here for fits with the 3P model. Due to its delayed rise, the interphase signal could not be described by the simulated curve.

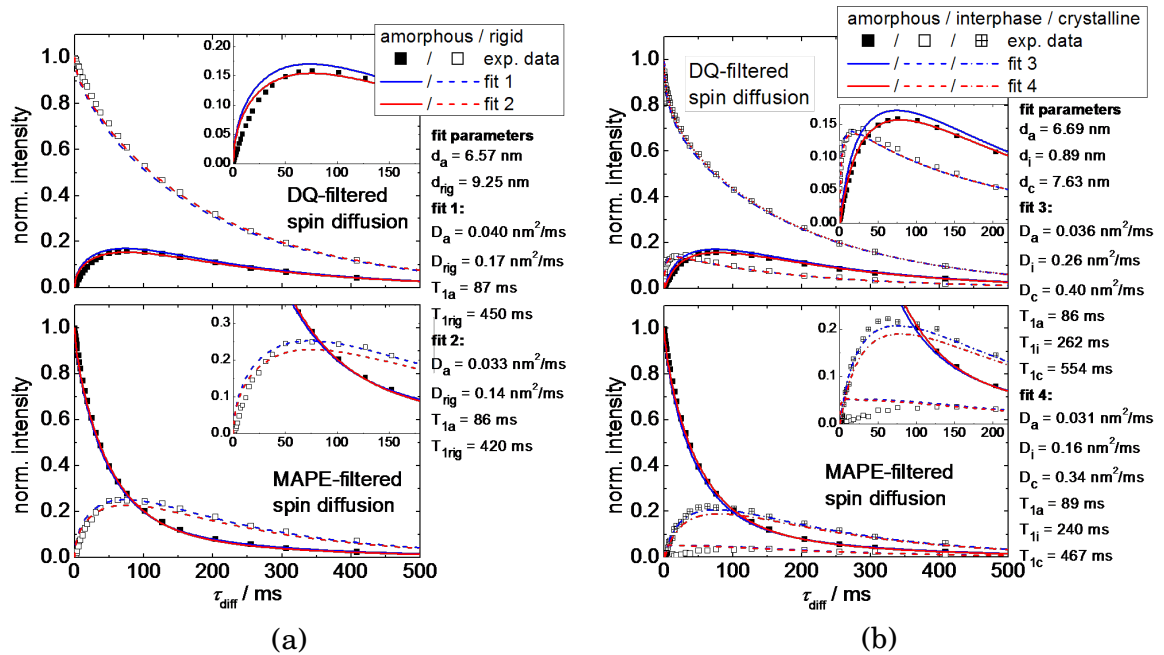


Figure 7.7.: Simultaneous fit to the combination of Saturation-Recovery curves and spin-diffusion curves from either DQ-filtered (fit 2 and 4) or MAPE-filtered (fit 1 and 3) experiments for PCL at 45°C for the 2P (a) and the 3P (b) model. In the upper parts of (a) and (b) the fit curves are compared to spin-diffusion data from a DQ-filtered experiment, the lower parts show comparisons to data from MAPE-filtered measurements. The fit parameters are given in the plots. The simulations were done using relative spin densities $\varrho_{H,a} = 1$, $\varrho_{H,i} = 1.034$, $\varrho_{H,c} = 1.067$, $\varrho_{H,rig} = 1.067$ of the amorphous, interphase, crystalline and rigid domains, respectively.

⁵As in the 3P model the interphase domains flank the crystalline (or mobile-amorphous) domains, they occur twice in each repeat unit (cf. Fig. 7.6 (b)). The interphase domain thickness calculated via Eq. 7.3 refers to the whole interphase content in the repeat unit and therefore has to be halved for application in the fit.

All in all, single data sets derived from either a Saturation-Recovery or a MAPE-filtered spin-diffusion or a DQ-filtered spin-diffusion experiment were too unspecific to permit a reliable simultaneous fit for all phases with 4 (2P) or 6 (3P) free parameters, i. e. the individual sets of simulated data were too insensitive to changes of distinct parameters or allowed large variations of the parameter values in the fit. In particular, the Saturation-Recovery curves depended only slightly on the values of D_p impeding the determination of reliable information about these parameters from these data curves alone. Yet, fits to spin-diffusion and Saturation-Recovery curves at the same time were expected to yield more reliable results for T_{1p} and D_p . However, here partly considerable discrepancies arose between measured and simulated data which may provide further information on the sample morphology:

- 1.) Compared to the simulated curves for the 2P model in DQ-filtered and MAPE-filtered spin-diffusion experiments the measured magnetization of sink and source domain showed a delayed rise and decay, respectively (see Fig. 7.7 (a)).
- 2.) In the DQ-filtered experiments the interphase signal grew before the mobile-amorphous phase signal, as it is expected for one-dimensional stacks of lamellae with planar interfaces between the domains. Furthermore, the intensities reached matched well the 3P fit data, while shape and rise time of the interphase signal in the MAPE-filtered experiments did not comply with the simulated curves (see Fig. 7.7 (b)). Here, signal of interphase and crystalline phase increased almost simultaneously or the crystalline signal even grew first as demonstrated in Fig. 7.8, contrary to the expected development of the magnetization. This finding is not an artifact due to poor measurement statistics. It could be reproduced in a later measurement of the same sample with a much higher number of scans (~ 1400) and was found for a PS-PB block copolymer as well [159].
- 3.) Neither in the 2P nor in the 3P model, spin-diffusion curves from MAPE-filtered and DQ-filtered experiments could be described by the same set of spin-diffusion coefficients D_p . Either the maximum sink magnetization in the DQ-filtered measurements was too low or the one in the MAPE-filtered experiments was too high to match simulated curves for the same D_p values to both data sets simultaneously (see insets in Fig. 7.7). Compared to spin diffusion from the crystallites to the mobile-amorphous phase via the interphase, the magnetization transfer in the opposite direction seemed to be more intense and a larger value of D_a was required to fit the data in the latter case.

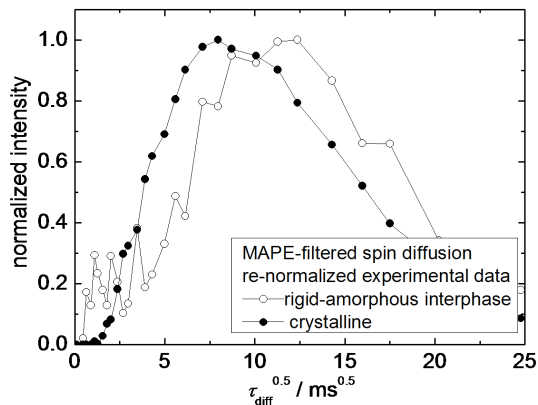


Figure 7.8.: MAPE-filtered spin-diffusion data of crystallites and rigid-amorphous interphase measured for PCL at 45°C. For comparability of the rise time, both curves are normalized in a way that the maximum intensity is equal to 1. The behavior deviates from the one expected for one-dimensional stacks of lamellae with planar interfaces between the domains, where the interphase signal should grow clearly before the crystalline phase signal.

This last point rendered a simultaneous fit of all three data sets (Saturation Recovery and MAPE-filtered and DQ-filtered spin diffusion) impractical.

For the lamellar scenario the ratio of thicknesses (d_{p1}/d_{p2}) of two phases $p1$ and $p2$ is represented by the ratio ($M_{0,p1}/M_{0,p2}$) of magnetizations at large waiting times τ_{Satr} in a Saturation-Recovery experiment:

$$\frac{d_{p1}}{d_{p2}} = \frac{M_{0,p1} \varrho_{H,p2}}{M_{0,p2} \varrho_{H,p1}} = \frac{f_{p1} \varrho_{H,p2}}{f_{p2} \varrho_{H,p1}}. \quad (7.4)$$

Hence, the fit to Saturation-Recovery data is strongly recommended to obtain reliable thicknesses.⁶ Information about spin-diffusion coefficients on the other hand is contained in the spin-diffusion curves. Summarizing the above, mainly the data from MAPE-filtered spin diffusion are believed to be problematic because fits using the 3P model could not be matched here, whereas these fits work well for data from DQ-filtered experiments.

Before outlining quantitative results concerning fit parameters for the individual measurement steps A to E, the general and characteristic deviations between simulated fit curves and data curves shall be discussed more elaborately in the following sections. Possible reasons for these differences are, e. g.,

- magnetization transfer lags according to Mauri et al. [8] (see Section 7.4) and
- a rough crystalline-interphase boundary surface (see Section 7.5).

7.4. Magnetization Transfer Lags in PCL Spin-Diffusion Experiments

As described in the previous section the spin-diffusion curves of source and sink from MAPE-filtered and DQ-filtered experiments show a delayed decay and rise, respectively, when compared to fit data for the 2P model (see Fig. 7.7 (a)). Such a sigmoidal development of magnetization is known from literature [8, 89, 95, 106, 113, 139, 153, 250] as the result of interphase regions between source and sink domains, which are not polarized directly after the selection period in a spin-diffusion experiment, but the signal of which is evaluated as source magnetization. Since the magnetization from the initially polarized source core regions has to pass through these interphase regions before reaching the sink domains, the decay of the complete source signal (originating from the actual core source and the interphase) and the rise of the sink signal occur later, i. e. the magnetization transfer is delayed, compared to a situation where no interphase of this kind exists.

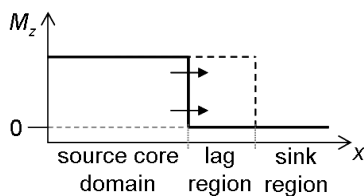


Figure 7.9.: Schematic sketch of the magnetization distribution after filter application for a lag-phase scenario. The lag region is evaluated as a part of the source but does not possess initial magnetization.

⁶In principle, this thickness ratio is also found at large mixing times τ_{diff} in a spin-diffusion experiment (see Fig. 4.9). However, in low-field measurements the magnetization development is superimposed by T_1 relaxation and hence this information is lost.

Applying the same pulse sequences as used here, Mauri et al. [8] found such magnetization transfer lags in PS-PB block copolymers in both, rigid-phase and mobile-phase selected spin-diffusion experiments. The interphase between hard and soft domains, being part of the rigid phase in the 2P model, caused a delayed magnetization transfer to the mobile phase in a DQ-filtered spin-diffusion experiment, as it was not polarized by the DQ filter. On the other hand, as a reason for the mobile-phase lag Mauri et al. suggested the existence of a portion of polymer material within or close to the mobile phase which loses magnetization during the MAPE filter.

The impact of the spin-diffusion curve shape variations due to magnetization transfer lags on the fit parameters D_p and T_{1p} was not investigated by Mauri et al. Hence, this point shall be made up for here. Furthermore, investigations of the measured data in the 3P model might yield additional information about the origin of transfer lags.

For a quantitative investigation on possible lag-causing interphases in PCL, the development of magnetization in spin-diffusion and Saturation-Recovery experiments was simulated using the program described in Section 7.3 and Appendix F.2 under the assumption of an additional lag phase, forming domains between source and sink regions. The same spin-diffusion coefficient, T_1 time constant and spin density as for the source domains was attributed to these interphase domains. Yet, they lacked any initial magnetization (pseudo 2P model). This way the magnetization profile after the selection period in the simulated spin-diffusion experiment was defined to be rectangular (see Fig. 7.9).⁷ For the simulation authentic parameter values for PCL were chosen on the basis of those obtained from simultaneous fits to experimental data for 45°C. Spin-diffusion curves were calculated for varying lag phase thickness between 0 und 16 Å and 0 and 5 Å for a lag phase within the rigid phase and the mobile-amorphous phase, respectively. The source-domain thickness was accordingly reduced by twice the lag-phase thickness.

Expectedly, a lag phase only affects the magnetization development when the initial magnetization in source and lag phase differs. In this case, the increase of the lag-phase thickness causes a shift of the initial rise and the maximum of the spin-diffusion sink curve to longer mixing times τ_{diff} , while the source curve decay is increasingly delayed (see Fig. 7.10). The presence of a lag phase further involves an intensity decrease of the sink curve when T_1 relaxation is fast in the source and lag regions because, due to the delayed transfer of magnetization, a larger portion of magnetization is lost from the combined source and lag domains by T_1 relaxation before the migration into the sink domains starts. Therefore less magnetization can be transported into the sink phase and the maximum sink signal intensity is reduced compared to a situation without lag phase. Obviously this effect is significant only for the mobile-phase selected experiments here due to the short T_1 relaxation time constant of the mobile-amorphous PCL phase (cf. Fig. 7.10(a) and (b)).

When fitting simulated spin-diffusion data for a system with magnetization transfer lags by means of a 2P fit model which does not consider such lags, the curve features described above affect the resulting fit parameters in a characteristic way. Assuming fixed

⁷To consider such a magnetization profile seems feasible, as it was confirmed by Mauri et al. and in a further simulation test series here, that varying the form of the initial magnetization profile within the lag phase hardly influences the shape of the spin-diffusion curves as long as the lag-phase fraction stays constant.

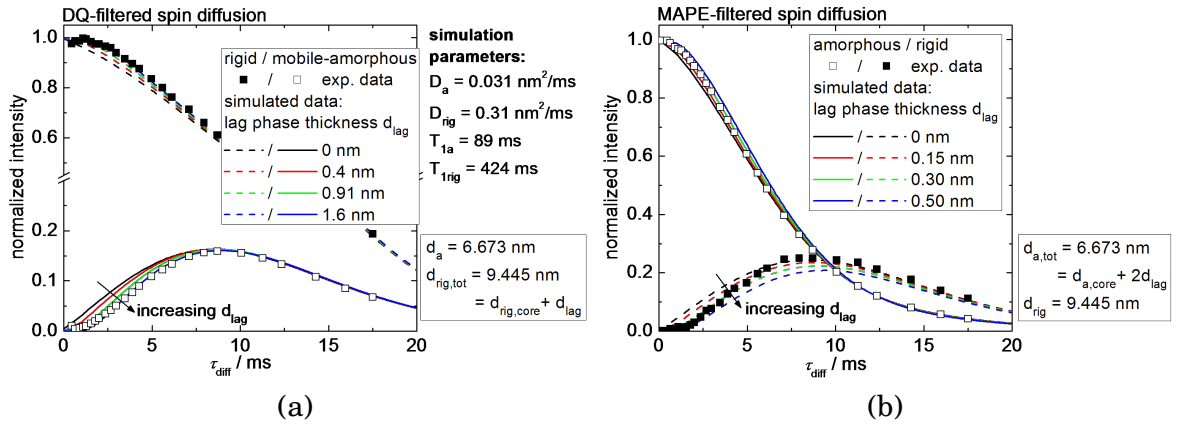


Figure 7.10.: Comparison of experimental data for PCL from (a) a DQ-filtered and (b) a MAPE-filtered spin-diffusion experiment with simulated data for a pseudo 2P model which considers a rigid (a) or mobile (b) lag phase of varying domain thickness d_{lag} flanking the respective source region (see text). With increasing lag-phase thickness the thickness of the actual source domains (denoted by the subscript core) was reduced accordingly, in order to keep the total domain thickness of the combined source and lag phase (denoted by the subscript tot) constant. The same parameter set was used for simulations in (a) and (b) with values given in the plots and relative spin densities $\varrho_{H,a} = 1$ and $\varrho_{H,rig} = 1.067$.

domain thicknesses in the fit, the curves give the impression of reduced spin diffusion from source to sink domains. The fit therefore yields a reduced spin-diffusion coefficient D_{source} of the source compared to the actual value. On the other hand the corresponding value D_{sink} of the sink domains is increased. Here, smaller values of D_{source} require larger values of D_{sink} and vice versa (see Fig. 7.11). Despite the adaption of the spin-diffusion coefficients, the fit curves do not match well the simulated measurement data for small mixing times τ_{diff} , as the delayed curve rise and decay cannot be reproduced by the fit for the 2P model (see Fig. 7.11).

Magnetization Transfer Lags in Rigid PCL Domains. An estimated spin-diffusion coefficient D_{rig} of the rigid phase can be determined by calculating the average of D_c and D_i , obtained from simultaneous fits to curves from Saturation-Recovery and DQ-filtered spin-diffusion experiments using the 3P model, weighted by the corresponding mass fractions f_c and f_i :

$$D_{rig} = \frac{f_c D_c + f_i D_i}{f_c + f_i} \quad (7.5)$$

For PCL at 45°C this estimate amounts to $D_{rig} \approx 0.31 \text{ nm}^2/\text{ms}$ (as used for the simulations described above). However, the fit to the experimental DQ-filtered spin-diffusion data using the 2P model yields much smaller values of D_{rig} between $0.08 \text{ nm}^2/\text{ms}$ and $0.15 \text{ nm}^2/\text{ms}$. Following from the findings above, these small parameter values seemingly are fitting artifacts arising when one tries to fit the delayed curve decay and rise of the source and sink curve with fixed domain thicknesses. Taking into account lag regions of $\sim 16 \text{ \AA}$ thickness at the edges of the rigid domains, the data measured at 45°C can be reproduced well by simulations for the 2P model, assuming spin-diffusion coefficients $D_a = 0.031 \text{ nm}^2/\text{ms}$ and $D_{rig} = 0.31 \text{ nm}^2/\text{ms}$ (see Fig. 7.10 (a)). This corresponds to 34% of initially non-polarized rigid-phase material in the DQ-filtered experiment.

If the magnetization transfer lags were caused by the rigid-amorphous interphase only,

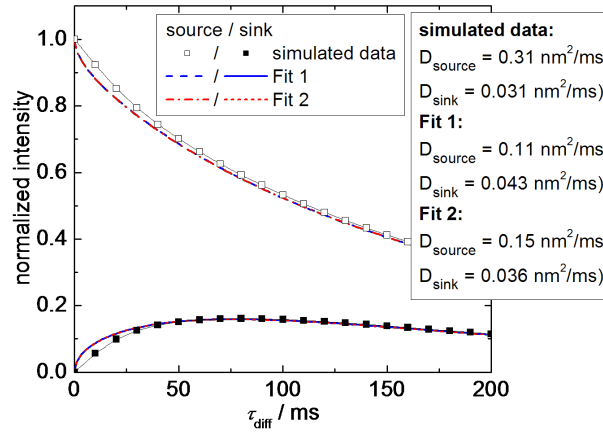


Figure 7.11.: Simulated spin-diffusion curves for a pseudo 2P model which considers lag regions flanking the source domains (see text) and fits to these simulated data in the framework of the 2P model, i. e. disregarding the lag phase. The simulation was performed using the parameters given in Fig. 7.10 (a) and a lag-phase thickness of 1.6 nm. In the fits, domain sizes and spin densities were fixed to values used in the simulation. Two different sets of fitting curves for different spin-diffusion coefficients are shown in the graph. For both sets the T_1 time constants equal those used in the simulation.

no delay of curve decays or rises should be detected compared to data from a fit using the 3P model, as here this interphase is evaluated as a separate phase, the signal of which can be distinguished from the rest. In fact, no delay is visible for interphase and crystallite signal and only a slight retardation for the mobile-amorphous-phase signal (see Fig. 7.7). However, with an interphase fraction of $\sim 12\%$ and a rigid fraction of $\sim 61\%$ in the sample at 45°C (known from the MSE and FID component analysis) the portion of rigid-amorphous interphase in the rigid phase amounts to $\sim 20\%$ only. This value is significantly lower than the lag phase fraction of $\sim 34\%$ estimated above, hinting at one or more additional reasons for curve-shape variations in the 2P representation.

A possible reason is the insufficient efficiency of the DQ filter. In the ideal case after the application of the filter the magnetization level is equal for all lamellae and the magnetization is evenly distributed within a lamella, while interphase and amorphous regions are left unpolarized. In this case, the magnetization profile of every lamella is rectangular (see upper row in Fig. 7.12). However, as shown in Section 4.4.2 for the short DQ excitation times used here, there is an incomplete excitation of magnetization in the crystallites due to the DQ filter. At least two different scenarios are imaginable for this situation (see Fig. 7.12):

- 1.) an unequal distribution of initial magnetization within each crystalline lamella represented by curved magnetization profiles or
- 2.) different magnetization levels of the individual lamellae (or rather stacks of lamellae).

As presumably near the edges of the crystallites chain mobility is slightly higher and dipolar couplings are slightly weaker than in the crystallite core, it seems possible that for short excitation times some protons near these edges are not polarized, so that curved magnetization profiles are generated (see Fig. 7.12). In this situation, due to the large spin-diffusion coefficient of the crystalline phase, spin diffusion would first start to balance the magnetization within the crystallites before magnetization would

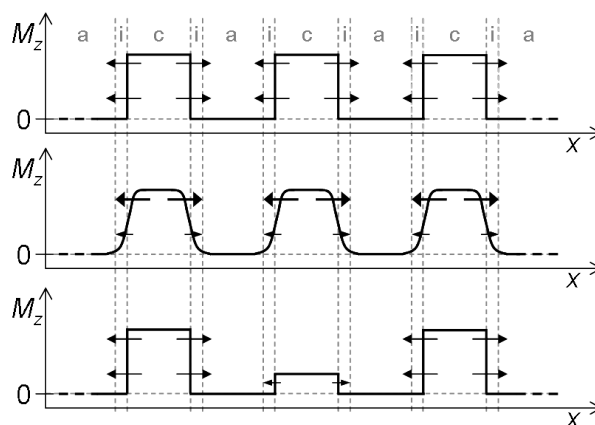


Figure 7.12.: Schematic drawing of possible initial magnetization profiles after application of a DQ filter to semicrystalline PCL. Crystalline, interphase and amorphous domains are labeled c, i and a, respectively. The rectangular profiles in the upper part represent the ideal situation. Filter ineffectiveness might lead to curved profiles (central picture) or unequal magnetization levels in individual lamellae (lower part). The sketch in the lower part represents a much simplified situation, as in reality the magnetization level will rather deviate between whole stacks of lamellae than between the lamellae within one stack (see Section 4.4.2). The arrows depict the spin-diffusion process locally differing in strength for the different scenarios.

be transferred further into the interphase and mobile-amorphous phase. Hence, initially non-polarized outer regions of the lamellae should act as a crystalline lag phase, inducing a delayed decay of the crystallite signal and a retarded rise of the interphase and mobile-amorphous phase signal compared to a scenario without lag phase. However, the fit curves for the 3P model match well the experimental data of interphase and crystalline phase and a delay is not observed. Furthermore, as discussed in Section 4.4.2 the magnetization does not equilibrate within the crystallites as it should in accordance with the argumentation given above. Therefore, either effects of such curved initial magnetization profiles within the lamellae are very small or superimposed by other effects.

The simulation model assumes that all lamellae initially exhibit the same level of magnetization. Yet, as explicated in Section 4.4.2, the initial magnetization level rather varies from stack to stack. Hence, interphase and mobile-amorphous regions close to less polarized lamellae will initially obtain less magnetization via spin diffusion than such near more strongly polarized lamellae and compared to a system with equal initial magnetization of each lamella, changes in the shape of the spin-diffusion curves are expected. Whether this effect can induce curve shapes similar to those discussed above for the 2P model remains to be clarified by simulations of the scenario.

Magnetization Transfer Lags in Mobile-Amorphous PCL Domains. The delayed initial rise and decay of sink and source signal from MAPE-filtered spin-diffusion measurements is expectedly reproduced well by simulations for the 2P model under consideration of a mobile lag phase (see Fig. 7.13).

The MAPE filter action is based on the fact, that signal of protons cannot be refocused when the filter duration largely exceeds the inverse dipolar coupling strength between them, i. e. when the couplings are too strong. As there is a gradient of chain mobilities

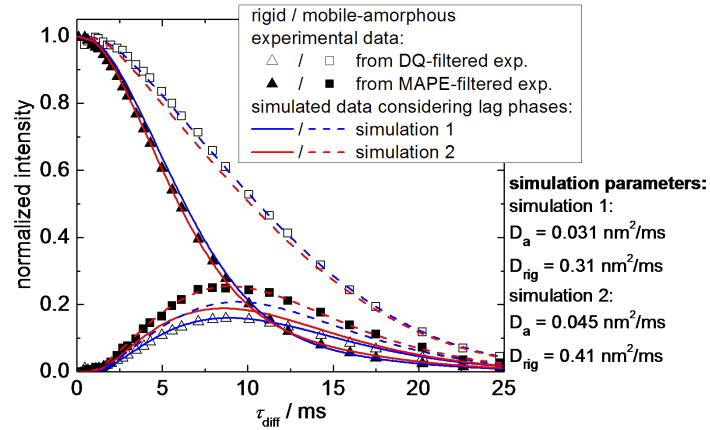


Figure 7.13.: Comparison of experimental spin-diffusion data with simulations using the pseudo 2P model, considering lag-phase regions flanking the source domains, for two different sets of spin-diffusion coefficients. The simulations were performed using the total thickness, T_1 and spin-density parameters given in Fig. 7.10 and assuming a magnetization lag phase of 34% and 15% of the total rigid phase and mobile-amorphous phase, respectively.

and dipolar coupling strengths within the mobile-amorphous phase (see Section 4.4.1), ranging from strong couplings near the interphase to weak couplings in the middle of the domains, a too long filter in fact screens magnetization from protons at the edges of the amorphous domains. A similar effect is known for the Goldman-Shen filter sequence [113, 117, 151]. Furthermore, also technical imperfections and molecular motions on the time scale of the sequence length may induce signal loss.

The fraction of mobile-amorphous-phase signal which is lost due to the filter can be estimated by comparing the corresponding signal intensities from an unfiltered and a MAPE-filtered MSE experiment. In the measurements for PCL at 45°C the loss amounted to 7% of the total mobile-amorphous-phase signal. Signals arising from this non-polarized fraction are not distinguishable from the rest of the mobile-amorphous-phase signal due to very similar signal-shape parameters. Therefore, this loss fraction acts as a typical magnetization lag phase (cf. Ref. [8]). Yet, a good agreement between measured and simulated spin-diffusion data was only reached for 15% of lag-phase content within the mobile-amorphous phase (see Fig. 7.13).

Summarizing the above, the shift in initial rise and decay of the experimental spin-diffusion curves compared to simulated ones for the 2P model can quantitatively be explained by the existence of a rigid and a mobile-amorphous magnetization lag phase. However, in both cases the estimated lag-phase fractions are significantly larger than the directly evident reasons suggest. In presence of such lag phases the spin-diffusion coefficients determined from fitting the data using the 2P model deviate from the true ones. Furthermore, the discrepancy between the sets of spin-diffusion coefficients required to describe the experimental curves from DQ-filtered and MAPE-filtered experiments does not vanish when lag phases are considered. Still the description of MAPE-filtered spin-diffusion data requires higher values of D_a and D_{rig} than necessary to characterize the corresponding DQ-filtered spin-diffusion data (see Fig. 7.13).

7.5. Effects of Corrugated Crystalline-Interphase Boundary Surfaces

Even when taking into account possible lag phase effects (and domain-size distributions, see Appendix F.4) in PCL, discrepancies persist between the measured spin-diffusion data and the fit curves which still could not be interpreted (see Sections 7.3 and 7.4). In this section, a model of corrugated crystallite surfaces will be discussed qualitatively, which may yield a conceivable explanation of these mismatches.

As shown in Fig. 7.6 the 3P model for fitting the spin-diffusion data assumes planar interfaces between the three polymer domains. However, in literature also rough crystallite surfaces have been debated [20, 228, 255–257] or morphologies where rigid-amorphous and mobile-amorphous domains both have direct contact with crystalline material [119]. In the scenario discussed here, crystalline lamellae form protuberances towards the mobile-amorphous phase at their edges, as shown in Fig. 7.14.⁸



Figure 7.14.: Schematic representation of the domain morphology of a semicrystalline polymers consisting of crystalline lamellae, mobile-amorphous regions and rigid-amorphous interphase domains in between, denoted *c*, *a* and *i*, respectively: (a) model with planar boundary surfaces and (b) model with corrugated crystallite surface.

In this scenario, polymer chains in the dents between such crystalline protuberances and on the top of them are subject to mobility restrictions because they are fixed in the crystallite at one end. They would therefore be evaluated as rigid-amorphous interphase material in NMR time-domain measurements. At a certain distance from the crystallite surface the chain mobility is largely isotropic, so that the corresponding material can be referred to as mobile-amorphous. Compared to the model with planar interfaces, in this scenario the crystallite surface is enlarged and the minimum distance between crystallite surface and the boundary of the mobile-amorphous domains is reduced (see Fig. 7.14), causing distinct changes in the magnetization development in a spin-diffusion experiment, which are addressed in the following.

Consequences of Corrugated Crystallite Surfaces on Crystalline-Phase-Selected Spin-Diffusion Experiments. The shape of the contact area between the polymer domains enters the spin-diffusion equation in form of the dimension parameter k . As known from literature, changes of this parameter may affect the spin-diffusion curves [89, 101, 250]. Due to the corrugated crystallite surface the geometry of the spin-diffusion process in a crystalline-phase-selected experiment is fractal with a dimension parameter k ranging between 1 and 2 instead of $k = 1$ for the scenario with planar interfaces. Following from Eq. 4.12, magnetization is transferred slightly faster from the crystallites to the interphase via the enlarged boundary surface, resulting in

⁸Of course, also other forms of rough crystallite surfaces can be imagined.

a somewhat earlier decay and rise of the crystalline and interphase signal, respectively, compared to the curves obtained for a model with planar interfaces.

By contrast with the data from a fit using the 3P model, there is no accelerated intensity rise or decay of the measured crystalline-phase and interphase signal, although such a magnetization development could not be compensated by the fit. However, in Section 7.4 ineffective DQ-filter action in the crystallites was discussed as a possible reason for a further magnetization transfer lag inducing a retarded decay and rise of the crystalline and interphase signal, respectively. Also this effect was not visible in the experimental data, although it probably exists. Possibly, here both influences cancel each other, leaving the rise or decay times of the measured data in fair agreement with those from the fits. For a final clarification of the issue simulations for a scenario taking into account corrugated crystallite surfaces and a lack in filter efficiency are required.

Consequences of Corrugated Crystallite Surfaces on Amorphous-Phase-Selected Spin-Diffusion Experiments. The presumed effects of a corrugated crystallite surface are complex in case of spin diffusion starting from the mobile-amorphous phase. They are demonstrated in Fig. 7.15. Here, magnetization flows to the interphase first, enabling a slight and early rise of the interphase signal intensity. However, at spots where the interphase is thin magnetization is preferably and rapidly transferred further to the crystalline domains with its efficient spin diffusion due to the strong dipolar couplings. Therefore, the crystalline-phase and interphase signal grow almost simultaneously. The magnetization also disperses within the interphase albeit less efficiently than in the crystallites. The interphase signal therefore increases further, but with a smaller slope than present for the crystalline-phase signal. When magnetization has 'filled up' the crystalline protuberances, it seems possible that it is transferred back to still non-polarized interphase material, resulting in a stronger second rise of the interphase signal. Due to their strong dipolar couplings the crystalline protuberances can remove more magnetization from the crystalline-interphase boundary and distribute it within the crystallites than the interphase could do at the same place in case of planar surface boundaries. This suction action of the crystalline phase on magnetization assumedly enables a higher crystalline-phase intensity at short mixing times than calculated for planar boundary surfaces, but at the expense of the interphase signal intensity.⁹ All these effects described here have actually been detected in the experimental PCL data (see Figs. 7.7 (b) and 7.8).

Resulting from the strongly delayed and reduced rise of the interphase signal, being a part of the rigid-phase signal, a retarded increase of the latter is conceivable in the 2P model compared to the scenario with planar interfaces. This effect could constitute the additional magnetization transfer lag needed to finally explain the spin-diffusion data from the MAPE-filtered experiment for the 2P model.

Importantly, the discrepancy between the signal intensities of the sink curves from DQ-filtered and MAPE-filtered spin-diffusion experiments can finally be elucidated by tak-

⁹By contrast, the decreased minimum distance between crystalline and mobile-amorphous domains is not expected to accelerate the rise of the mobile-amorphous-phase signal in a crystalline-phase-selected experiment significantly because magnetization is transported less efficiently within the mobile-amorphous phase than within the interphase with its higher coupling strength and diffusion coefficient.

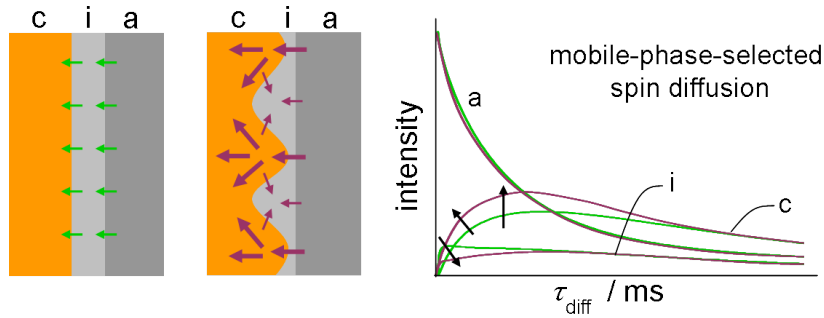


Figure 7.15.: Demonstration of the effects of corrugated crystallite surfaces on the spin-diffusion curves from a mobile-amorphous-phase-selected experiment. Direction and strength of the spin-diffusion process are indicated by green and claret arrows for scenarios with planar interfaces (left) and corrugated crystallite surface (middle), respectively. Expected spin-diffusion curves for both scenarios are sketched on the right using the same colour code.

ing into account corrugated crystallite surfaces and T_1 relaxation. Because of rather fast T_1 relaxation in the mobile-amorphous phase and the interphase and the slow relaxation in the crystallites, a faster magnetization transfer from the mobile phase into the crystalline phase, as described above, partly prevents magnetization from being lost due to relaxation. Therefore the maximum signal intensity of the crystalline phase grows additionally compared to the situation for planar interphases and the total increase exceeds the signal loss in the interphase due to the simple redistribution of magnetization (see above). Thus, also the maximum intensity of the rigid-phase signal exceeds the value reached in a simulation for a 2P model with planar surface boundaries.

Ignoring corrugated crystallite surfaces, enlarged intensities from a mobile-amorphous-phase-selected experiment are evaluated as resulting from enhanced spin diffusion compared to crystalline-phase-selected measurements where no such increase in sink intensity is expected.¹⁰ Hence, fitting such spin-diffusion data using the program described in Section 7.3 with fixed domain-thickness parameters is not possible with one set of spin-diffusion coefficients for both sets of data. To reproduce the enlarged sink intensity in the mobile-phase-selected experiment the fit yields a higher value of D_a (and possibly also of D_{rig}) than for the crystalline-phase-selected experiment, and in the 3P model an increased value of D_i or D_c is needed to additionally compensate the elevated simulated interphase signal intensity arising from the raise in D_a .

In summary, the discrepancies between measured and simulated spin-diffusion data can be explained qualitatively by the existence of corrugated crystallite surfaces in PCL. For a final clarification, however, a comparison of the individual scenarios by numerical simulations is necessary. First tests indicate, that a simultaneous rise of crystalline and interphase signal can be explained by a corrugated interface in fact [159].

¹⁰As the slow T_1 relaxation in the crystalline phase does not cause much signal loss within the first tens of milliseconds of spin diffusion, the faster magnetization transfer due to the corrugated boundary in a crystalline-phase-selected experiment is not expected to affect the intensity of the interphase and mobile-amorphous-phase signal curves compared to the scenario with planar boundary surfaces.

7.6. Quantitative Results from Fitting PCL Spin-Diffusion Data

Despite the described discrepancies between measured and simulated spin-diffusion curves, the measured data were analyzed in order to obtain spin-diffusion coefficients for PCL, which shall later on be used to derive realistic PCL domain sizes from spin-diffusion experiments in practice (see Chapter 8).

The considerations in Section 7.5 confirmed that mainly data from MAPE-filtered experiments pose a problem to the analysis, when using a fit model for three polymer phases with planar interfaces between them (3P model). Therefore the quantitative evaluation has been restricted to data from DQ-filtered spin-diffusion and Saturation-Recovery experiments. Information about the implementation of the fit is given in Section 7.3. The fit quality was fairly good in general (see Fig. 7.16). However, slight systematic deviations between measured data and the fit curves persisted, assumedly as a consequence of domain thickness distributions (see Appendix F.4).

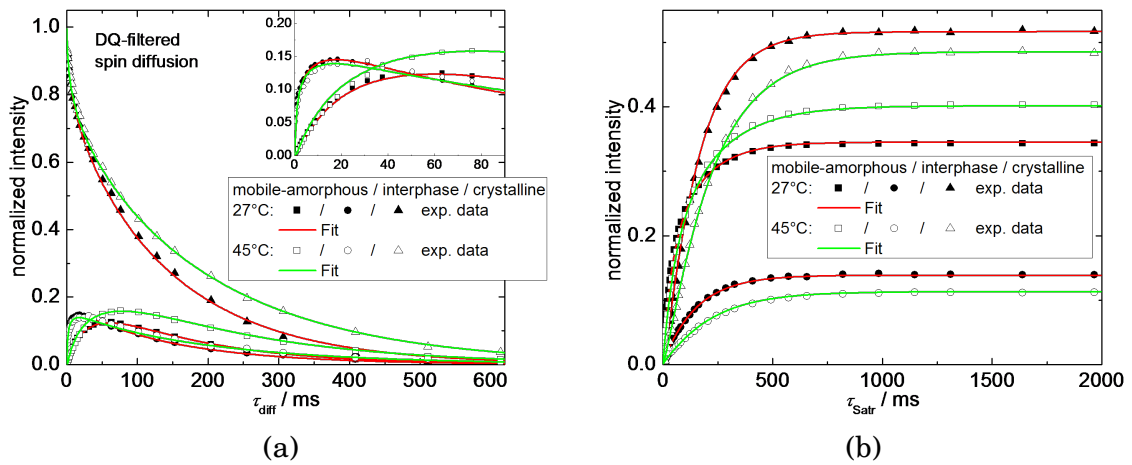


Figure 7.16.: DQ-filtered spin-diffusion data (a) and Saturation-Recovery data (b) in comparison to curves obtained from a simultaneous fit to both sets of data. Exemplarily, data from step C (at 27°C) and A (at 45°C) in the measurement program are plotted.

As it turned out that the fit results partially depend on the initial parameter values, three fits have been performed to data from each of the steps A to E in the measurement program with different initial values. In principle, in the fits the spin-diffusion coefficient D_i of the interphase could have been fixed to the average of the coefficients of crystalline and mobile-amorphous phase because the spin-diffusion curves do not respond sensitively to changes of D_i (see also Ref. [95]). Nonetheless, in order to test the possible parameter variations, D_i was kept as a free parameter, here. During the fitting runs the parameter values possibly had to be reset, if physically unlikely combinations of values arose as a result of domain-size distributions (see Appendix F.4). At the end of each fitting run the domain sizes were allowed to adjust freely in order to optimize the fit quality. The thickness values obtained this way ranged within the margin of uncertainty of the thicknesses calculated from the SAXS long period L in each case. The parameter values derived from the fits are summarized in Table 7.1.

	step A 45°C	step B 45°C	step C 27°C	step D 27°C	step E 45°C
f_a	0.403±0.010	0.393±0.010	0.343±0.010	0.326±0.010	0.381±0.010
f_i	0.112±0.010	0.129±0.010	0.139±0.010	0.144±0.010	0.127±0.010
f_c	0.485±0.010	0.478±0.010	0.518±0.010	0.530±0.010	0.492±0.010
$L_{\text{SAXS}}/ \text{nm}$	15.83 ± 0.30	15.80 ± 0.30	15.13 ± 0.30	14.99 ± 0.30	15.78 ± 0.30
$d_{a,\text{SAXS}}/ \text{nm}$	6.57 ± 0.42	6.40 ± 0.42	5.38 ± 0.35	5.07 ± 0.33	6.20 ± 0.40
$d_{i,\text{SAXS}}/ \text{nm}$	0.89 ± 0.12	1.02 ± 0.13	1.06 ± 0.14	1.08 ± 0.14	1.00 ± 0.13
$d_{c,\text{SAXS}}/ \text{nm}$	7.48 ± 0.45	7.34 ± 0.44	7.65 ± 0.46	7.77 ± 0.47	7.55 ± 0.45
$\sigma_{\text{rel},c}$	0.10	0.10	0.13	0.13	0.10
$\sigma_{\text{rel},a}$	0.51	0.51	0.48	0.48	0.50
$d_{a,\text{NMR}}/ \text{nm}$	6.59 ± 0.01	6.43 ± 0.01	5.36 ± 0.01	5.10 ± 0.04	6.22 ± 0.02
$d_{i,\text{NMR}}/ \text{nm}$	0.90 ± 0.01	1.02 ± 0.01	1.06 ± 0.01	1.09 ± 0.01	1.01 ± 0.01
$d_{c,\text{NMR}}/ \text{nm}$	7.53 ± 0.02	7.32 ± 0.02	7.66 ± 0.01	7.76 ± 0.01	7.56 ± 0.01
T_{1a}/ ms	89 ± 2	93 ± 2	62 ± 1	54 ± 2	88 ± 3
T_{1i}/ ms	214 ± 100	132 ± 10	87 ± 10	120 ± 20	134 ± 10
T_{1c}/ ms	595 ± 160	683 ± 20	423 ± 35	484 ± 30	753 ± 120
$D_a/ \text{nm}^2\text{ms}^{-1}$	0.031±0.001	0.029±0.001	0.032±0.002	0.0344±0.0003	0.030±0.001
$D_i/ \text{nm}^2\text{ms}^{-1}$	0.179±0.016	0.209±0.062	0.160±0.035	0.210±0.024	0.206±0.031
$D_c/ \text{nm}^2\text{ms}^{-1}$	0.308±0.055	0.375±0.058	0.330±0.076	0.279±0.028	0.358±0.054

Table 7.1.: Summary of results from NMR and SAXS measurements for all 5 steps in the temperature program (see Fig. 7.1): Sample fractions f from NMR MSE measurements, long periods L from SAXS, mean domain thicknesses d_{SAXS} calculated from L via Eq. 7.3 using proton spin densities from Table E.1, relative distribution widths $\sigma_{\text{rel}} = \sigma/d_{\text{SAXS}}$ of domain sizes from SAXS (see Appendix F.4) and domain thicknesses d_{NMR} , T_1 relaxation time constants and spin-diffusion coefficients D from fitting the NMR spin-diffusion data (see text). The subscripts a , i and c denote the mobile-amorphous phase, interphase and crystalline phase, respectively.

Spin-Diffusion Coefficient of the Mobile-Amorphous Phase. The spin-diffusion coefficient D_a could be determined from the fits with little scatter.¹¹ No effect of secondary crystallization was seen, but expectedly D_a increased slightly and reversibly with falling temperature because of increasing chain mobility and hence rising strength of the residual dipolar couplings which mediate spin diffusion (see Fig. 7.17 (a)). The absolute change of D_a from $(0.030 \pm 0.003) \text{ nm}^2/\text{ms}$ at 45°C to $(0.033 \pm 0.003) \text{ nm}^2/\text{ms}$ at 27°C was low, however, compared to variations in the order of $\sim 0.012 \text{ nm}^2/\text{ms}$ determined for PB by Spiegel et al. for an equivalent temperature change [120]. In the temperature range between 27°C and 45°C the value of D_a is found by a linear fit yielding $D_a = ((-1.7 \pm 3.0) \cdot 10^{-4} T[\text{°C}] + (0.0375 \pm 0.012)) \text{ nm}^2/\text{ms}$.

For PCL similar, yet slightly smaller spin-diffusion coefficients are expected than for Nylon-6 (see Section 7.1) amounting to $0.034 \text{ nm}^2/\text{ms}$ to $0.084 \text{ nm}^2/\text{ms}$ as calculated from the NMR proton line width at room temperature by Buda et al. [95, 97]. In fact, this expectation is confirmed here. Literature data for D_a in PE ($0.07 \text{ nm}^2/\text{ms}$ to $0.25 \text{ nm}^2/\text{ms}$) are larger than those obtained here for PCL. Furthermore, the values given for

¹¹Due to domain-thickness distributions within the sample the magnetization transfer is presumably stronger locally than determined in the fits. At 45°C instead of $D_a \approx 0.030 \text{ nm}^2/\text{ms}$ it rather amounts to a true value of $\sim 0.045 \text{ nm}^2/\text{ms}$ (see Appendix F.4).

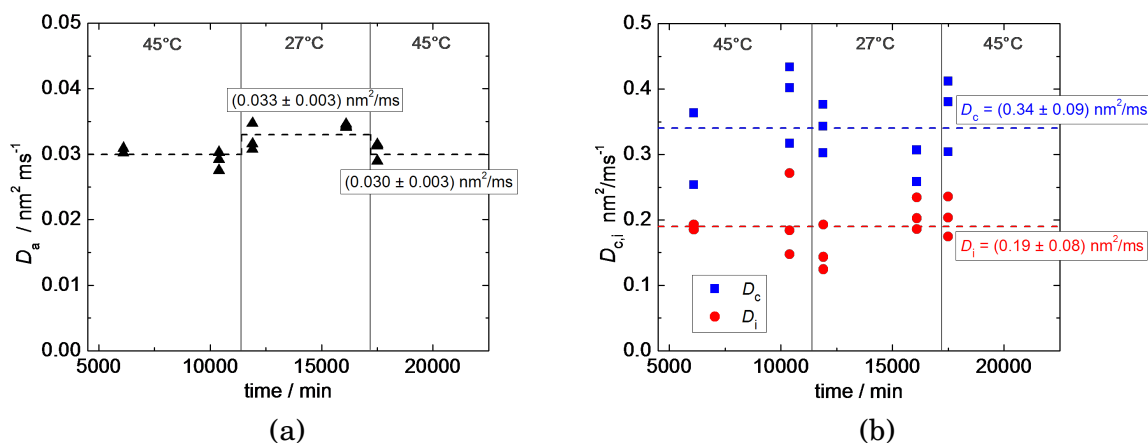


Figure 7.17.: Spin-diffusion coefficients D_a , D_c and D_i of the mobile-amorphous phase (a) and the crystalline phase and interphase (b), obtained from simultaneous fits to Saturation-Recovery curves and spin-diffusion curves from DQ-filtered experiments for PCL, as a function of the time in the measurement program (see Section 7.2). Results from fits with different initial parameters are plotted for every measurement step.

mobile-amorphous PCL at room temperature by Voda et al. [101] ($D_a = 0.14$ nm²/ms to 0.25 nm²/ms) exceed the results presented herein by a factor of 4 to 7, whereas investigations on local spin diffusion within the mobile-amorphous PCL phase at 45°C, using a hole-burning technique, yielded only half the value obtained here [258], supposedly because at this very local scale (~ 1 nm) the geometry of the process is different compared to the scenario assumed for the low-field measurements (see Section 7.1).

The trend of rising dipolar coupling strength with falling temperature is visible in the development of the T_2 relaxation time constant as expected.¹² However, the absolute values of D_a calculated by help of T_2 exceed the ones derived from the fit significantly (see Table 7.2). The calibration of Mellinger et al. [251] yields values which are approximately 10 times larger than D_a from the fit. Anyway, this calibration cannot be used here, because it is based on a reference value obtained from NMR measurements under MAS (see Section 7.1). Yet, after scaling down the values derived from this calibration by a factor of (0.76 ± 0.05) to adapt them to results from static NMR measurements as suggested in Ref. [156], they are still too large by a factor of 8 to 9. Also by computing D_a from the T_2 relaxation time constant via Eq. 7.2, a factor of 4 to 5 persists.¹³ These findings indicate, that the stated relations of T_2 and D_a do not hold true in general for mobile polymer phases. Compared to soft PI or PB blocks in block copolymers the amorphous PCL phase exhibits considerably reduced spin diffusion [156, 251]. A possible reason could be an effective obstruction of the magnetization transfer in direction of the chain backbone due to the COO group in the PCL repeat unit.

Spin-Diffusion Coefficients of Crystalline Phase and Interphase. The spin-diffusion coefficients of crystalline phase, interphase and rigid phase derived from the fit

¹² T_2 relaxation time constants were measured using the CPMG and Hahn-echo sequence. The results of both kinds of experiments were in good agreement.

¹³However, the value used here for the mean-squared distance $\langle r^2 \rangle$ between the nearest spins might be inappropriate as it was calculated by Voda et al. for PCL as a soft segment of a thermoplastic polyurethane [101].

	step A 45°C	step B 45°C	step C 27°C	step D 27°C	step E 45°C
T_{2a} / ms	0.68	0.63	0.48	0.46	0.60
$D_{a,\text{calc}} / \text{nm}^2 \text{ms}^{-1}$	0.326 ^a	0.331 ^a	0.353 ^a	0.357 ^a	0.334 ^a
	0.248 ^b	0.252 ^b	0.268 ^b	0.271 ^b	0.254 ^b
	0.123 ^c	0.133 ^c	0.173 ^c	0.181 ^c	0.139 ^c
$D_{a,\text{fit}} / \text{nm}^2 \text{ms}^{-1}$	0.031±0.001	0.029±0.001	0.032±0.002	0.0344±0.0003	0.030±0.001
$M_2 / (2\pi)^2 \text{kHz}^2$	290	291	303	301	292
$D_{c,\text{calc}} / \text{nm}^2 \text{ms}^{-1}$	0.423 ^d	0.424 ^d	0.432 ^d	0.431 ^d	0.425 ^d
$D_{c,\text{fit}} / \text{nm}^2 \text{ms}^{-1}$	0.308±0.055	0.375±0.058	0.330±0.076	0.279±0.028	0.358±0.054

^a calculated using the calibration of Mellinger et al. [251];

^b as ^a but scaled down by a factor of 0.76 as suggested in Ref. [156];

^c calculated via Eq. 7.2 with $\langle r^2 \rangle = (0.29)^2 \text{nm}^2$, adopted from Ref. [101];

^d calculated from the second moment M_2 of the line shape of the crystalline-phase signal via Eq. 7.1.

Table 7.2.: Comparison of calculated spin-diffusion coefficients (subscript calc) of the mobile-amorphous (subscript a) and crystalline (subscript c) phase of PCL and the corresponding values derived in the fit (subscript fit) for all steps in the measurement program.

amount to $D_c = (0.34 \pm 0.09) \text{nm}^2/\text{ms}$, $D_i = (0.19 \pm 0.08) \text{nm}^2/\text{ms}$ and $D_{\text{rig}} = (0.31 \pm 0.09) \text{nm}^2/\text{ms}$, the latter being calculated as a weighted average of D_c and D_i according to Eq. 7.5. Following from these results, the spin-diffusion coefficient of the rigid-amorphous interphase can be fixed in the fits to the average of D_c and D_a without hesitation. Values of D_c for Nylon-6 [95, 97] ($0.21 \text{nm}^2/\text{ms}$ to $0.29 \text{nm}^2/\text{ms}$) are at the lower limit of the uncertainty range of values obtained from the fit, while those computed from the second moment M_2 of the line shape of the crystalline-phase signal¹⁴ via Eq. 7.1 are at or above the upper limit (see Table 7.2). Due to the slight temperature dependence of M_2 (see Section 5.1) a decrease of D_c by about $0.008 \text{nm}^2/\text{ms}$ was expected for a temperature change from 45°C to 27°C . However, the fit results scatter by up to $0.09 \text{nm}^2/\text{ms}$ (see Fig. 7.17 (b)) rendering such a small deviation undetectable.

The widely accepted value of the spin-diffusion coefficient in glassy PS reported by Clauss et al. ($(0.8 \pm 0.2) \text{nm}^2/\text{ms}$) [139], which is frequently considered to be specific for rigid organic matter but was determined from measurements under MAS, significantly exceeds the value obtained here for PCL crystallites. Yet, the corresponding value from static low-field experiments ($(0.38 \pm 0.06) \text{nm}^2/\text{ms}$ [156]) matches the PCL value within the uncertainty range. Furthermore, the parameter value determined here lies within the wide range of literature values for the crystalline phase of PE ($0.11 \text{nm}^2/\text{ms}$ to $0.83 \text{nm}^2/\text{ms}$, see Section 7.1). Expectedly, as already reported for the amorphous PCL phase, investigations on local spin diffusion yielded a much smaller spin-diffusion coefficient in the crystallites ($(0.08 \pm 0.02) \text{nm}^2/\text{ms}$) than found here (see above and Section 7.1).

Results on T_1 Relaxation Time Constants. The fits yield stable and well-defined T_1 values only for the mobile-amorphous phase, where the longitudinal relaxation proceeds

¹⁴The second moment M_2 of the line shape for the PCL crystallites was deduced from fits to the MSE data (see Section 4.1).

much faster than the spin diffusion: $T_{1a} \ll d_a^2/D_a \approx 1370$ ms. The T_{1a} values are in good agreement with those from a linear fit to the initial rise of the corresponding Saturation-Recovery curves (see Section 5.1) and thus are supposed to be close to the true values.

The relaxation time constants T_{1c} and T_{1i} of the crystalline phase and interphase are larger than T_{1a} (see Table 7.1). Here the ratio between the T_1 relaxation time and the characteristic spin-diffusion time d^2/D is in the range of 15 to 25 for the interphase and 3 to 4 for the crystalline phase. Thus, spin diffusion dominates within these phases. Supposedly due to domain-size distributions in the sample, the fits allow a multitude of different combinations of values for T_{1c} and T_{1i} (see Appendix F.4). The actual fit values depend on the initial T_1 parameter setting. True T_1 values of these phases therefore cannot be given.¹⁵ As already described in Section 5.1 all three T_1 times decrease with falling temperature. Yet, no change due to proceeding secondary crystallization can be seen i. e. the very fast local dynamics in the sample are not influenced appreciably due to this process.

In summary by means of simultaneously fitting data from DQ-filtered spin-diffusion and Saturation-Recovery experiments the effective spin-diffusion coefficient and the T_1 time of the mobile-amorphous phase could be determined with high accuracy. The corresponding values of the other two phases scatter strongly. Nevertheless average values were obtained for the parameters of these phases as well. While expectedly a temperature trend for the spin-diffusion coefficient of the mobile-amorphous was found, such a tendency could not be confirmed for the coefficients of the interphase, crystalline phase and rigid phase owing to the large scatter of these parameters. The value of the amorphous-phase spin-diffusion coefficient of PCL is in agreement with those known from literature for Nylon-6 but is significantly lower than those calculated from proton T_2 relaxation times or line widths and the spin-diffusion coefficient of the crystalline PCL phase lies within the range of literature values for rigid polymer phases from static low-field experiments.

7.7. Initial Rate Approximation for the Estimation of Domain Sizes in PCL

As an alternative to complex computations the Initial Rate Approximation (IRA) provides a simple, fast and widely used approach to estimate domain sizes in heterogeneous polymer systems from spin-diffusion curves without requiring exact knowledge of the structure of the system (i. e. the dimensionality of the magnetization transfer) [17, 93, 94, 96, 99, 104, 105, 110–112, 127, 128, 130, 139, 251]. Basically, the approach relies on the idea that in a spin-diffusion experiment only a small layer around the interface between magnetization source and sink is affected by the magnetization transfer at short mixing times τ_{diff} . Because the sink region is much larger than this layer, as a short-time approximation one can assume a scenario of a finite source region, from which magnetization is transferred into an infinite sink region [143]. For this situation an analytical solution of the spin-diffusion equation exists, from which an expression for

¹⁵The T_1 data shown in Table 7.1 were obtained using characteristic time constants from a linear fit to the initial rise of the Saturation-Recovery curves as initial values for the simultaneous fit of spin-diffusion and Saturation-Recovery data.

the source domain size can be deduced:

$$d_{\text{source}} = 2r_0 = \frac{4}{\sqrt{\pi}} \frac{\sqrt{D_A} \sqrt{D_B}}{\left(\frac{\rho_{\text{H,A}}}{\rho_{\text{H,B}}} \sqrt{D_A} + \sqrt{D_B} \right)} \sqrt{t_0} \quad (7.6)$$

Here, r_0 denotes the position of the interface between source and sink domain and the subscripts A and B designate the source and sink domain, respectively (see Fig. 7.18 (a)). In case the dimensionality of the spin-diffusion process differs from $k = 1$, a factor $4k$ instead of 4 is used in Eq. 7.6. A derivation of this equation according to the considerations of Clauss et al. [139] is given in Appendix F.3, for a one-dimensional periodic structure of alternating rigid and mobile-amorphous regions (2P model, see Section 7.3) of, e. g., a semicrystalline polymer.

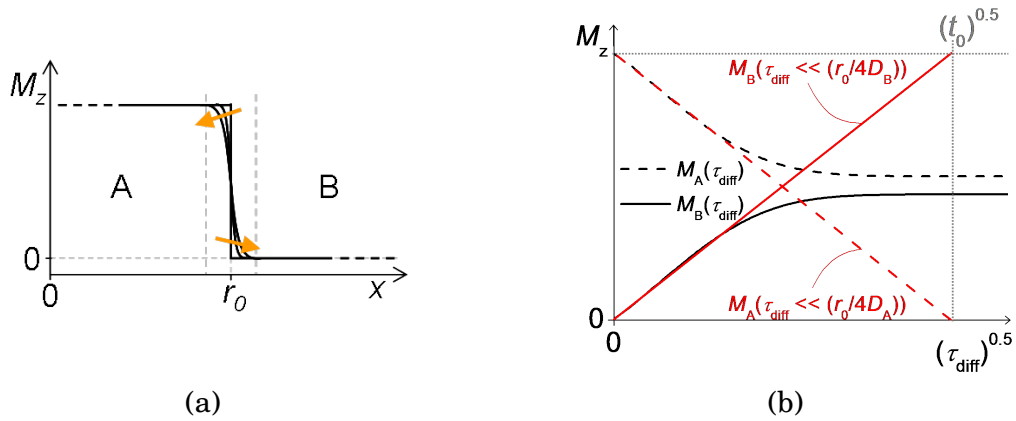


Figure 7.18.: Initial Rate approximation: (a) Magnetization profiles for the initial stages of spin diffusion from a magnetization source A at $x < r_0$ to an infinite sink region B at $x > r_0$. The arrows depict the evolution of the spin-diffusion process. The profile changes only in a small region around r_0 . (b) Spin-diffusion curves of source A and sink B in absence of T_1 relaxation as a function of the square-root of the mixing time τ_{diff} . At the initial stage of spin diffusion the curves can be approached by linear functions of $\sqrt{\tau_{\text{diff}}}$. The characteristic value $\sqrt{t_0}$ can be used to estimate r_0 (see Eq. 7.6).

The parameter $\sqrt{t_0}$ yields specific information about the speed of the spin-diffusion process from the source to the sink domain. It is easily accessible from the spin-diffusion curves in a $\sqrt{\tau_{\text{diff}}}$ representation by performing a linear fit to the initial rise or decay of the sink or source curve, respectively (see Fig. 7.18 (b)). From the source domain size d_{source} the thickness d_{sink} of the sink domain can be found with the help of the mass fractions and proton spin densities of the two phases as described by Eq. 7.4 for a one-dimensional spin-diffusion process. Due to the restriction of the considerations to the magnetization development at only one interface (see Appendix F.3) the IRA cannot be applied directly to a 3P model, where two different kinds of interface exist. Yet, by subdividing one of the two phases in the 2P model, the calculation of domain sizes of the sub-phases from d_{source} or d_{sink} is also possible using Eq. 7.4.

Eq. 7.6 was derived neglecting T_1 relaxation. Thus, before it can be applied, data from spin-diffusion measurements at low magnetic field, which are substantially influenced by T_1 relaxation effects, have to be corrected correspondingly, e. g., by multiplication by an exponential factor e^{t/T_1} [17]. But, as relaxation processes within source and sink phase both affect the shape of the spin-diffusion curves, a correction with the T_1 value

of only one of the phases is inadequate. Here, the corrections of the experimental data have been performed by multiplying them by $e^{t/T_{1,\text{ave,ini}}}$, with $T_{1,\text{ave,ini}}$ being a weighted average of the $T_{1,\text{ini}}$ time constants of all three phases in the sample, obtained from linear fits to the initial rise of the corresponding Saturation-Recovery curves: $T_{1,\text{ave,ini}} = f_c T_{1c,\text{ini}} + f_i T_{1i,\text{ini}} + f_a T_{1a,\text{ini}}$. This parameter was chosen because the T_1 relaxation in all PCL phases affects the experimental spin-diffusion data to a certain extent, presumably depending on the corresponding phase fraction. $T_{1,\text{ave,ini}}$ amounted to about 240 ms to 360 ms at 45°C and ~ 140 ms at 27°C.

According to Mauri et al. the spin-diffusion sink curve is better suited for the initial rate approach than the source curve, as seemingly its shape depends less on the actual T_1 value chosen for correction, the fit region and the experimental uncertainties [8]. Following this suggestion, linear fits to the initial rise of the normalized and T_1 corrected sink curves (as a function of $\sqrt{\tau_{\text{diff}}}$) from the spin-diffusion experiments for PCL and the 2P model have been performed for all steps in the measurement program. An example is displayed in Fig. 7.19. Actually the sink curve shape is sigmoidal at very short mixing times τ_{diff} due to magnetization transfer lags discussed in Section 7.4. Therefore the fit range was adapted to cover only the region of the linear curve rise as recommended by Mauri et al. [8]. The values of the parameter $\sqrt{t_0}$ obtained here are summarized in Table 7.3. The uncertainties reported were determined by slightly varying the interval boundaries for the linear fit.

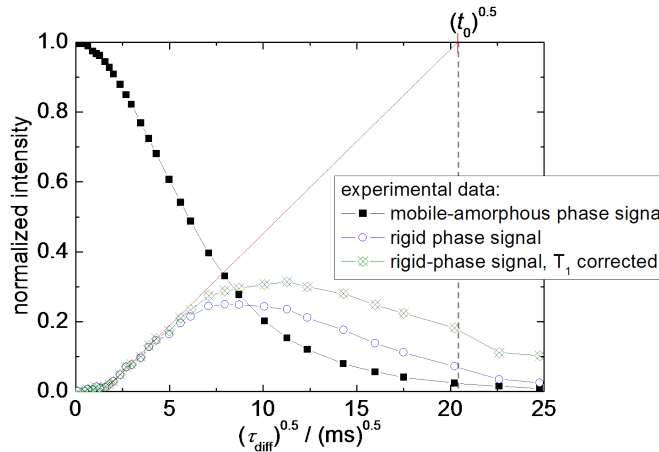


Figure 7.19.: Experimental spin-diffusion curves for PCL at 45°C from a MAPE-filtered experiment and Initial Rate Approximation after T_1 correction as described in the text.

Domain sizes were calculated for the one-dimensional spin-diffusion scenario from $\sqrt{t_0}$ via Eq. 7.6 for the source domain and via Eq. 7.4 for the sink domain, using relative proton spin densities given in Table E.1. The values of the spin-diffusion coefficients required for the calculation were adopted from the simultaneous fits to the experimental data described in Sections 7.3 and 7.6. Here, for each step in the measurement program at least three triples of values (D_a, D_i, D_c) were used, for which a good fit of the spin-diffusion and Saturation-recovery data had been obtained. The diffusion coefficient of the rigid phase was estimated as a weighted average via Eq. 7.5. The domain sizes resulting from the IRA are summarized in Table 7.3. The uncertainties given in the table arise from the uncertainties of $\sqrt{t_0}$ and the scatter of the spin-diffusion coefficients.

	step A 45°C	step B 45°C	step C 27°C	step D 27°C	step E 45°C
results from MAPE-filtered spin diffusion					
$\sqrt{t_0}/\sqrt{ms}$	20.4 ± 1.0	22.3 ± 1.0	15.3 ± 1.8	16.7 ± 1.4	18.4 ± 1.0
d_a/nm	6.2 ± 0.4	6.7 ± 0.5	4.7 ± 0.7	5.2 ± 0.5	5.6 ± 0.4
d_{rig}/nm	8.7 ± 0.6	9.8 ± 0.7	8.5 ± 1.4	10.3 ± 0.9	8.7 ± 0.7
results from DQ-filtered spin diffusion					
$\sqrt{t_0}/\sqrt{ms}$	33.0 ± 0.8	33.8 ± 0.6	33.6 ± 0.5	34.1 ± 0.5	23.8 ± 0.6
d_a/nm	6.7 ± 0.3	6.6 ± 0.3	5.4 ± 0.3	5.2 ± 0.1	6.4 ± 0.3
d_{rig}/nm	9.5 ± 0.4	9.6 ± 0.5	9.8 ± 0.5	10.1 ± 0.2	9.8 ± 0.4
results from SAXS					
d_a/nm	6.6 ± 0.4	6.4 ± 0.4	5.4 ± 0.4	5.1 ± 0.3	6.2 ± 0.4
d_{rig}/nm	9.3 ± 0.6	9.4 ± 0.6	9.8 ± 0.6	9.9 ± 0.6	9.6 ± 0.6

Table 7.3.: Results from Initial Rate Approximation performed for data from MAPE-filtered and DQ-filtered spin-diffusion experiments of PCL compared to domain sizes calculated from SAXS long periods via Eq. 7.3 using proton spin densities from Table E.1. The subscripts *a* and *rig* denote the mobile-amorphous and rigid phase, respectively.

Comparing the calculated values with *true* domain sizes derived from SAXS long periods, the best agreement is found for thicknesses obtained from DQ-filtered spin-diffusion experiments. Here the values from the IRA are slightly larger than the true ones by 2% to 3% and the temperature trend is readily reproduced. As already pointed out in Section 7.5 data from the MAPE-filtered experiments cannot be described by a model with planar interfaces between the polymer domains. Consequently problems were also expected when performing the IRA. In fact, the thickness results obtained from MAPE-filtered experiments are in worse agreement with the true values than those from the DQ-filtered measurements (see Table 7.3). Yet, the temperature trend of the mobile-amorphous-phase domain size is visible here as well.

Importantly, no agreement could be found between thicknesses derived from the SAXS long period and those estimated via Eq. 7.6 using spin-diffusion coefficients of the mobile-amorphous phase which were calculated from proton T_2 relaxation time constants or line widths. Here, the domain sizes obtained from IRA are too large by a factor of about 2.

In summary, the Initial Rate Approximation yields domain sizes for PCL which match well the real values derived from SAXS long periods under the condition that

- only data from DQ-filtered experiments is analysed by IRA,
- the weighted average of $T_{1,ini}$ values of all three polymer phases, obtained from linear fits to the initial rise of the corresponding Saturation-Recovery curves, is used for T_1 correction and
- the calculation of the average source domain size via Eq. 7.6 is accomplished with the help of the spin-diffusion coefficient values given in Section 7.6 for measurement temperatures in the range of about 27°C to 45°C.

7.8. Summarizing Remarks

Generally solid-state ^1H NMR spin-diffusion measurements are well-suited for the determination of domain sizes in semicrystalline polymers. In comparison to other techniques used for this purpose, in principle, they do not require any sample pretreatment, such as staining, as here differences in chain mobility between crystallites and amorphous phase are exploited. Importantly, domain sizes in systems with about 50% crystallinity, which may pose problems to SAXS measurements due to overlying peaks, are accessible by the help of spin-diffusion investigations.

However, difficulties arise in the case of low-field NMR due to phase-specific T_1 relaxation affecting the shape of the spin-diffusion curves in a complex way. In this work, this effect was accounted for in a numerical approach for solving the spin-diffusion equation for two or three-phase morphologies using a simulation and fit program.

Furthermore a lack of knowledge about correct spin-diffusion coefficients in a distinct sample system complicates the determination of domain sizes. As information on spin-diffusion coefficients in PCL, the polymer system of choice here, has been rare, the aim was to perform spin-diffusion experiments to identify these coefficients with the help of domain thicknesses derived from SAXS measurements. By interpreting the spin-diffusion data interesting insights were gained:

- By examination of spin-diffusion data for PCL as a two-phase system, containing rigid and mobile-amorphous domains, magnetization transfer lags became evident which partly result from the initially unpolarized interphase and signal loss due to the MAPE filter. To prevent the former it is recommended to treat the interphase as a separate phase using a three-phase model. Incomplete excitation of magnetization within the crystalline phase by the DQ filter is a further possible reason for a magnetization transfer lag.
- Non-planar, corrugated crystallite boundary surfaces can qualitatively offer explanations for
 - 1.) the deviating shape of the spin-diffusion curves of the interphase measured in MAPE-filtered experiments as compared to simulated data and
 - 2.) the fact that stronger spin diffusion is detected from the mobile-amorphous phase to the crystallites via the interphase than vice versa.

Such non-planar interfaces may represent another reason for retarded magnetization transfer, detected for the 2P model. The quantitative clarification of this matter by means of model simulations is the subject of ongoing work.

In order to determine spin-diffusion coefficients for PCL which are useable in practice, solely DQ-filtered spin-diffusion and Saturation-Recovery data of crystalline phase, mobile-amorphous phase and interphase were simultaneously fitted. MAPE-filtered data have been excluded from the analysis because of the considerable discrepancies between the measured and simulated curves. The resulting coefficients amount to

- $D_a = ((-1.7 \pm 3.0) \cdot 10^{-4} T[^\circ\text{C}] + (0.0375 \pm 0.0120)) \text{ nm}^2/\text{ms}$,
- $D_i = (0.19 \pm 0.08) \text{ nm}^2/\text{ms}$,
- $D_c = (0.34 \pm 0.09) \text{ nm}^2/\text{ms}$ and
- $D_{\text{rig}} = (0.31 \pm 0.09) \text{ nm}^2/\text{ms}$,

for temperatures of about 27°C to 45°C. Within the limits of uncertainty the coefficient D_c of the crystalline phase is in good agreement with literature data obtained from static low-field NMR measurements. Yet, the coefficient D_a of the mobile-amorphous phase is significantly smaller than values calculated from line widths or T_2 relaxation times, possibly due to COO groups in the PCL repeat units, obstructing an efficient magnetization transfer along the chain backbone.

The domain sizes derived from SAXS long periods can be reproduced well by analyzing spin-diffusion data from DQ-filtered experiments by means of the Initial Rate Approximation, when T_1 correction is realized by means of a weighted average of the T_1 time constants of all three polymer phases, obtained from linear fits to the initial rise of the corresponding Saturation-Recovery curves.

8. The Influence of Cyclic Chain Topology on PCL Dynamics and Crystallization

In order to synthesize semicrystalline polymers which are adapted to particular purposes, it is necessary to obtain comprehensive knowledge about the effects of all parameters influencing the developing semicrystalline structure. Yet, until now certain aspects of the polymer crystallization have remained indistinct, such as the influence of chain topology and molecular weight as well as the role of the entanglements prior to and during crystallization [31–38, 226, 229, 231].

In this context, the effect of chain topology on polymer crystallization and the forming semicrystalline structure shall be elucidated here, by comparing cyclic polymer chains and their linear analogues with the same number of repeat units with regard to chain mobility in the melt, crystal growth, crystallinity and crystal thickness. For this purpose the crystal-fixed polymer PCL was chosen as a model system, because mechanisms for the synthesis of linear, cyclic and other PCL topologies are well-known [259–262] and the crystallization of the linear form has already been investigated intensively (see Section 6 and Refs. [68, 221, 253, 263, 264]).

Cyclic polymers are supposed to adopt more compact conformations than linear chains [265–273]. They comprise double-folded loops and may be percolated by loops of neighboring chains [274, 275]. Often ring polymers are depicted in a 'lattice-animal' representation, describing single rings moving in a lattice of immobile topological obstacles which are formed by the neighboring chains [273]. Their specific topology turns cyclic polymers into attractive model systems for the exploration of, e. g., effects of highly mobile chain ends on chain dynamics and the physical properties of the material [275–279], reptation processes which seem to be unavailable for rings [275], percolation [280] or chain-folding phenomena [281, 282].

So far, theoretical investigations of cyclic chains have mostly been concerned with the conformation and the dynamics of rings in solution or in the melt [266, 267, 270–273, 283–286]. A number of cyclic polymers have also been characterized experimentally up to now, such as cyclic PS and PB [275, 277, 278] and, in particular, cyclic PDMS for which comprehensive investigations have been performed by Semlyen and coworkers since the 1960s [279, 287–294]. However, studies on macromolecular self-organization processes, e. g. the crystallization of cyclic polymers, are rare. Besides some DSC characteristics of cyclic systems of high molecular weight [237, 261, 292], investigations of monodisperse cyclic alkanes and poly(ethylene oxide)s of low and medium molecular weights have been reported [281, 282]. Yet, such systems exhibit almost perfect crystal structures with closely packed and integer-folded chains and reach crystallinities close to 100%. Hence, they are not representative for highly entangled semicrystalline polymers.

Reports on PCL of different topologies mostly concentrated on polymer synthesis and the determination of crystallization temperatures in DSC experiments [259, 261, 262]. In general they seem to indicate a reduction of the crystallization tendency with decreasing large-scale chain mobility and increasing steric hindrance of the individual polymer chains [260, 295]. Only recently new synthesis strategies enabled first attempts to a more detailed comparison of the crystallization behavior of linear and cyclic PCL of low [296] and high [297] molecular weights by DSC, optical microscopy and SAXS.

Remarks on the Investigated Samples. In this chapter, the semicrystalline structure of linear and comparable cyclic PCL chains at molecular weights M_n between 28 kg/mol and 43 kg/mol, i. e. above the entanglement molecular weight M_e of about 3 kg/mol [298–300], and polydispersities between 1.6 and 2.1 as determined by Gel Permeation Chromatography (GPC, see Appendix A and Table 8.1) is surveyed. The cyclic PCL chains were prepared by Dipl.-Chem. E. Ostas by insertion polymerization according to procedures reported by Kricheldorf et al. [301]. For the ring opening polymerization of ϵ -caprolactone, an Sn-based cyclic initiator was used which did not allow for the concatenation of rings. The linear polymers were obtained from the respective cyclic PCLs directly, by cleavage of the Sn-O bond generated by the initiator. They were free of tin and exhibited the same number of monomers as their cyclic counterparts. More detailed comments and details on sample synthesis are given in Appendix A.

GPC measurements (see Appendix A) revealed higher retention volumes and thus lower apparent molecular weights for the cyclic PCLs as compared to their linear analogues (see Fig. 8.1), although equal molecular weights were to be expected.¹ The reason for this difference lies in the fact that GPC detects the hydrodynamic radius of the polymer chains. This radius is lower for a cyclic chain in comparison to its linear counterpart with the same number of monomers, because linking both ends of a linear chain reduces the overall dimensions of the chain [302]. Hence, the GPC results confirm the successful synthesis of rings.

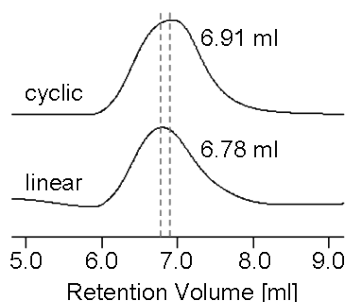


Figure 8.1.: GPC traces for a pair of linear and corresponding cyclic PCL with indicated retention volume. The apparent molecular weights resulting from a calibration with PS standards and the converted PCL molecular weights amount to 63.4 kg/mol and 35.4 kg/mol for the linear PCL and 57.4 kg/mol and 32.1 kg/mol for the cyclic PCL, respectively (see Appendix A, plot adopted from Ref. [242]).

Furthermore, results from GPC studies indicated a fast degradation of cyclic PCL in a humid environment. Therefore, all measurements described here have been performed under the exclusion of air and moisture and the samples have been stored under vacuum. However, also linear chains decomposed when stored at high temperatures for a longer time. Details concerning the investigation of sample degradation are given in Appendix B.

In order to elucidate the connection between chain mobility and the semicrystalline structure formed by the linear and cyclic PCL chains, first, results on chain mobility in the melt are presented as obtained from ^1H low-field NMR Hahn-echo and multiple-quantum experiments and supported by findings from rheological measurements. Moreover a comparison is drawn between crystallinities, lamellar thicknesses and crystallization kinetics of the linear chains and their cyclic analogues as detected by ^1H low-field NMR and DSC.

¹The molecular weight of the initiator (233 g/mol), which was eliminated during the formation of linear chains from the cyclics, is within the GPC uncertainty.

8.1. Chain Mobility in the Melt

^1H Low-Field NMR Hahn Echoes. In polymer melts a variety of molecular dynamics takes place spanning a wide range of correlation times (see Chapter 2). Fast, random and almost isotropic segmental motions (Rouse modes) at motional rates far above the proton dipolar coupling strength of about 20 kHz average the couplings to a large extent (see Section 3.3). Thus, in the ideal case these motions hardly cause any decay of the transverse magnetization, measured by means of the Hahn-echo sequence [148]. Moreover, chain motions on the time scale of the Hahn-echo sequence, i. e. in the range of some milliseconds, hamper the signal refocusing and cause a slow decay of the transverse magnetization with a rather long corresponding T_2 relaxation time constant [71,303].

However, for long polymer chains, with molecular weights above the entanglement limit M_e , topological restrictions, posed by chain entanglements or other packing constraints, induce an anisotropy of the fast chain motions on the NMR time scale and a semi-local residual order of the chains. Thus, dipolar couplings are not averaged out completely [40,71] and the residual static dipolar couplings cause an additional (coherent) dephasing of the transverse magnetization detected in a Hahn-echo measurement [303]. Hence, the investigation of the T_2 relaxation of the transverse magnetization at temperatures far above T_g can yield information about the density of topological constraints (e. g. entanglements) and/or the time scale of large-scale chain motion [40].

In order to compare the T_2 relaxation behavior of the linear and cyclic PCL chains in the melt (under exclusion of disturbing effects due to the inhomogeneity of the magnetic field), Hahn-echo decay curves have been measured at 80°C for samples which had been kept at 90°C for approximately 30 minutes to avoid melt-memory or self-seeding effects (see Chapter 6) and were then transferred into the pre-heated spectrometer directly. The Hahn-echo decay curves are displayed in Fig. 8.2 for a pair of samples of linear and corresponding cyclic chains with a molecular weight $M_{n,\text{lin}} = 35.4$ kg/mol of the linear form.

The initial non-exponential shape of the decay curves (see Fig. 8.2) implies dominating effects of the residual dipolar couplings as expected for melts of polymers with a molecular weight above M_e [71,304]. An apparent T_2 time constant was derived for every investigated sample as the time at which the Hahn-echo intensity had decayed to

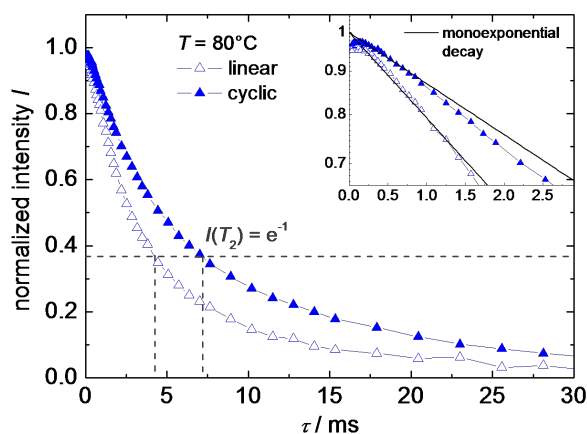


Figure 8.2.: Relaxation curves of transverse magnetization for a pair of samples of linear and corresponding cyclic PCL with $M_{n,\text{lin}} = 35.4$ kg/mol in the melt at 80°C, measured by low-field ^1H NMR Hahn-echo experiments. The inset highlights the non-exponential initial shape of the decay curves (graph adopted from Ref. [242]).

a fraction of $(1/e)$ of the initial intensity (see Fig. 8.2). The corresponding values are summarized in Table 8.1.

As visible in Fig. 8.2 and Table 8.1, the T_2 relaxation is faster for the linear PCL chains than for the cyclic ones. This difference indicates a stronger motional anisotropy in the samples containing linear PCL as compared to the cyclic analogues. This stronger anisotropy may result from stronger or more frequent restrictions to the fast mobility of the linear chains due to more or enhanced chain entanglements or a higher number of packing constraints caused by neighboring chains compared to the cyclics.² Yet, also a longer time required for isotropic large-scale motions of the linear chains could be the reason for this finding.

¹H Low-Field Multiple-Quantum NMR. From Hahn-echo decay curves the information about the dephasing due to residual static dipolar couplings and about spin relaxation induced by thermal motions on the time scale of the sequence length can hardly be separated [40,305]. Therefore, additionally ¹H NMR multiple-quantum (MQ) experiments have been performed here for three sample pairs of linear and cyclic PCLs with molecular weights M_n between 28.3 kg/mol and 42.9 kg/mol to study the chain mobility in the molten state.

Typically, MQ NMR sequences are used for the determination of weak residual dipolar couplings in polymeric systems such as polymer melts and elastomers [40]. Details on the theoretical background and the applicability of the method as well as on the experimental implementation and the data analysis are summarized elsewhere [40,41,306,307]. Here, a pulse sequence of variable duration τ_{DQ} (an advanced version of an early MQ experiment of Baum and Pines [40]) was used to obtain a normalized double-quantum build-up curve $I_{\text{nDQ}}(\tau_{\text{DQ}})$, whose initial increase is related to the residual dipolar coupling strength D_{res} as well as to the semi-local order in the sample and is independent of the time scale of segmental fluctuations.

As can be seen in Fig. 8.3 (a), build-up curves $I_{\text{nDQ}}(\tau_{\text{DQ}})$ were received for linear and cyclic PCL, confirming again that residual local order is present in the samples.³ However, the initial slope and intensity of the curves is larger for the linear chains compared to the cyclic ones. (In the region of the steepest increase at $\tau_{\text{DQ}} \approx 1$ ms the intensity ratio amounts to about 2.5.) In agreement with the conclusions from the Hahn-echo measurements, this observation indicates stronger motional anisotropy and higher residual local order in the samples consisting of linear PCL chains due to more or stronger hindrances to fast chain mobility.

As longer chains tend to form more entanglements and induce a higher degree of motional anisotropy, the build-up intensity exhibits a slight increase with rising molecular weight for the linear chains. Yet, the effect is weak for the narrow range of molecular weights studied here, where polydispersities larger than 1.6 cause a considerable overlap of the molecular weight distributions. No molecular weight trend could be found for the Hahn-echo relaxation curves. Presumably, it was masked there by dynamic effects

²From the polymer theoretical point of view, cyclics adopt collapsed conformations rather than forming entanglements in the conventional sense [283,285]. Hence the term ‘packing constraint’ seems more reasonable here.

³The intensities presented here are smaller than shown in Refs. [40,41] because a tail subtraction as described in these references has not been possible due to the polydispersity of the samples.

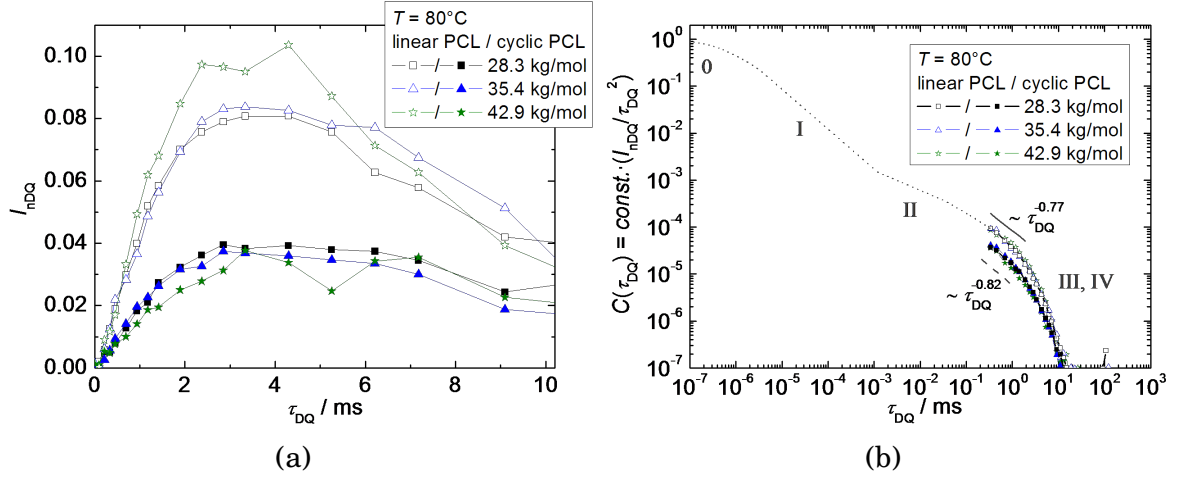


Figure 8.3.: Results from ^1H low-field multi-quantum NMR experiments at 80°C for samples of linear and corresponding cyclic PCL chains of different molecular weights given in the legend for the linear PCL. (a) Normalized intensities I_{nDQ} as a function of the excitation time τ_{DQ} , (b) orientational autocorrelation function $C(\tau_{DQ})$ of the second Legendre polynomial (in arbitrary units), calculated from the data in (a). The dotted line represents a constructed autocorrelation function for $Z = 11$ (see text) based on experimental data for PB, PI and PDMS from Ref. [41] with corresponding Doi-Edwards tube-model regimes indicated by Roman numerals. The label 0 designates subsegmental dynamics (graphs adopted from Ref. [242]).

due to motions of the dipolar coupling tensor [307]. The cyclic PCL chains do not exhibit a molecular weight effect neither in the MQ measurements nor in the Hahn-echo experiments. Assumedly this is due to contaminations of the samples with small but differing amounts of linear chains (see below).

In the region of the initial curve rise the normalized intensity I_{nDQ} is directly related to the orientation autocorrelation function $C(t)$ of the second Legendre polynomial P_2 :

$$C(t) = \langle P_2(\cos\theta(t)) \cdot P_2(\cos\theta(0)) \rangle ,$$

describing the loss of orientational memory of the chain segments, with θ being the angle of the segmental orientation relative to the external magnetic field [306]:

$$\frac{I_{nDQ}}{\tau_{DQ}^2} \propto C(\tau_{DQ}) \propto D_{\text{res}}^2 .$$

In Fig. 8.3 (b) the autocorrelation functions $C(\tau_{DQ})$ of the investigated samples are depicted. For the linear PCL chains no significant deviations of the initial curve decays of the three samples have been found, hinting at a distribution of residual dipolar coupling strengths D_{res} , probably as a consequence of polydispersity. The same can be concluded directly from the rather linear initial rise of the build-up curves in Fig. 8.3 (a). By contrast, for a single residual dipolar coupling strength an inverted Gaussian shape is expected.

According to the Doi-Edwards tube model, the autocorrelation function $C(\tau_{DQ})$ obeys a power law with specific scaling exponents for the different time regimes of polymer dynamics, ranging from free Rouse modes (regime I) at short correlation times in the range of nanoseconds via constrained Rouse dynamics (regime II) and chain reptation

(regime III) to free chain diffusion (regime IV) at correlation times between milliseconds and days [41, 307]. As it is known from literature for a melt of linear chains, the scaling exponent adopts a value of -0.85 in regime I, which increases when passing over to entangled dynamics at the entanglement time τ_e [41, 308]. In the constrained-Rouse regime II the scaling exponent depends on the molecular weight of the polymer. For the investigated PCL samples with an average number Z of entanglements per chain between 6 and 14 ($Z = M_{n,\text{lin}}/M_e$ with M_e ranging between 3 kg/mol and 5 kg/mol [298–300]) the regime-II exponent adopts values between -0.44 and -0.48 (cf. Ref. [41]). The correlation function decay steepens in regime III before passing over to regime IV (see Fig. 8.3 (b)), with the corresponding scaling exponent changing from -0.5 near the Rouse time τ_R to -1.5 being reached at the disentanglement time τ_d [41].

For the linear PCL chains investigated herein the relaxation power law exponent extracted from the autocorrelation function $C(\tau_{\text{DQ}})$ amounts to -0.77 ± 0.15 (see Fig. 8.3 (b)), the large uncertainty being caused by bad statistics for the small signal intensities. The slope for the cyclics is slightly steeper, yet, the exponent (-0.82 ± 0.20) is similar to the one of the linear chains within the limits of uncertainty. The entanglement time τ_e of the linear PCL chains at 80°C can be estimated to be on the order of 10^{-3} ms using the relation $\tau_e \simeq 4\tau_\alpha N_e^2$ found for PB in Ref. [41], with τ_α being the α -relaxation time constant at the measurement temperature and N_e naming the number of Kuhn segments between two entanglements. The time constant τ_α was extrapolated from the results of dielectric measurements [167, 168] and N_e was estimated⁴ to range between 30 and 50 with the help of the entanglement molecular weight M_e (see above) and the Kuhn segment length of PCL of 7 Å [309]. As the time range of our measurements is far beyond τ_e (see Fig. 8.3 (b)), the scaling exponent of -0.77 is related to the Doi-Edwards regime III, revealing the presence of reptation-like dynamics of the linear PCL chains at 80°C.

As the autocorrelation function $C(t)$ is proportional to the time-dependent shear modulus $G(t)$, the multi-quantum NMR data can be compared to rheology data from literature directly. Conducting shear measurements of a melt of polystyrene rings of high molecular weight (Z between 8 and 11, $M_e \approx 17.5$ kg/mol), in contrast to linear-chain stress relaxation via reptation, Kapnistos et al. [275] found additional, faster relaxation modes following a power law behavior. This finding has been confirmed recently by molecular dynamics simulations of Halverson et al. [285]. The stronger relaxation of the cyclics due to these additional modes is expressed in a lower stress-relaxation modulus of the cyclic PS as compared to corresponding linear chains at times larger than the entanglement relaxation time τ_e . In accordance with this finding the autocorrelation functions of the cyclic PCLs are placed beneath the ones of the linear chains (see Fig. 8.3 (b)). However, according to theoretical and experimental results reported in literature the autocorrelation function should decay much faster for the melt of rings than for the linear analogues [273, 275]. The similar scaling exponents obtained here again hint at a contamination of the melt of rings with linear chains (see below).

Rheological Investigations. The differences in the mechanical relaxation spectrum of PCL rings and linear chains are reflected in the frequency-dependent shear storage and loss moduli G' and G'' measured in rheological experiments (see Appendix A) in

⁴The estimated value is large as compared to the value $N_{e,\text{PB}} \simeq 15$ found for PB [41] with a similar M_e , but still it is in the same range.

the melt. As depicted in Fig. 8.4 (a) for a pair of PCL samples ($M_{n,\text{lin}} = 35.4$ kg/mol) at 60°C, the moduli of the cyclic polymer both are significantly lower than those of the corresponding linear analogue. The coinciding log-log slopes of the shear moduli of both samples are consistent with the very similar power law exponents of their orientation autocorrelation functions (see above).

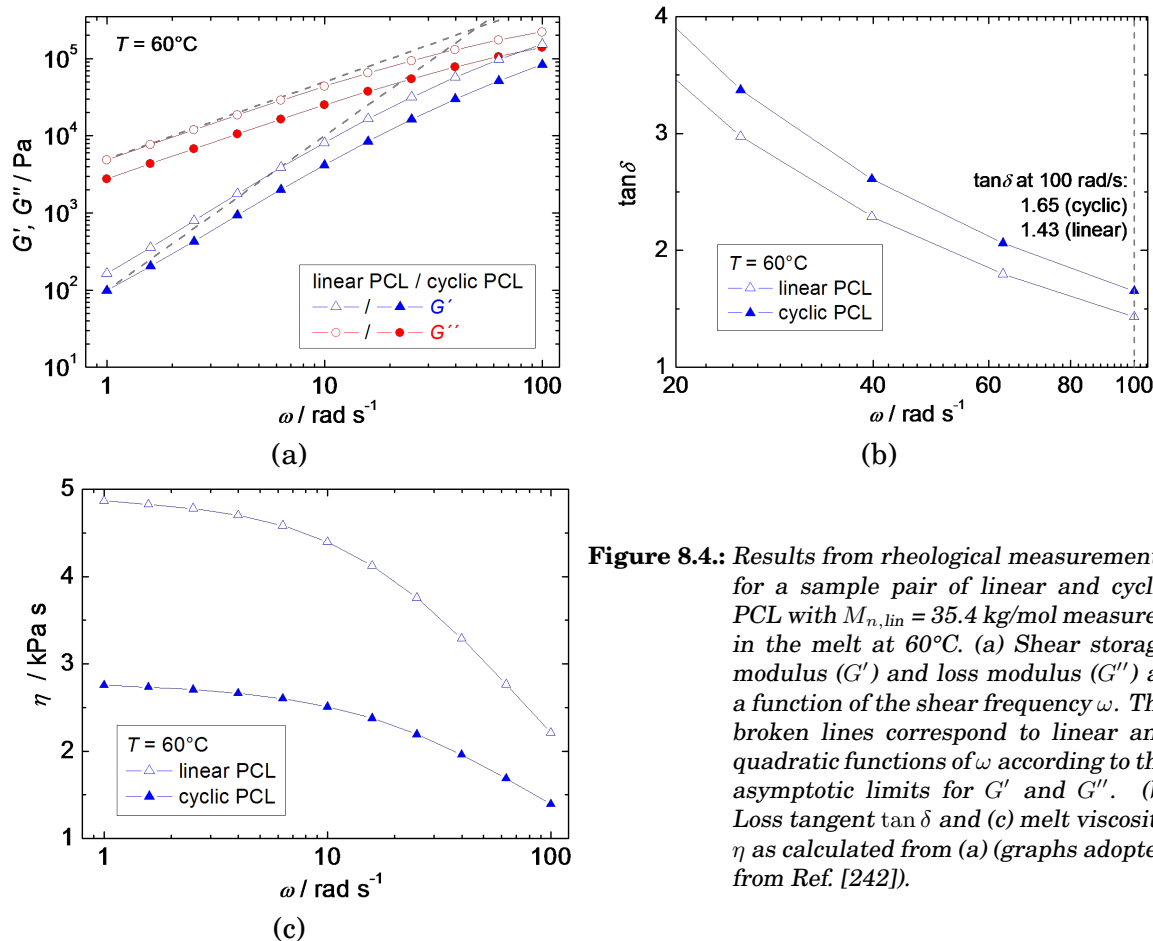


Figure 8.4.: Results from rheological measurements for a sample pair of linear and cyclic PCL with $M_{n,\text{lin}} = 35.4$ kg/mol measured in the melt at 60°C. (a) Shear storage modulus (G') and loss modulus (G'') as a function of the shear frequency ω . The broken lines correspond to linear and quadratic functions of ω according to the asymptotic limits for G' and G'' . (b) Loss tangent $\tan \delta$ and (c) melt viscosity η as calculated from (a) (graphs adopted from Ref. [242]).

Although a cross-over point of G' and G'' could not be reached in the measurements at the highest possible measurement frequency ($\omega = 100$ rad/s),⁵ the values of the loss tangent $\tan \delta = G''/G'$ suggest that a crossover point (i. e. a frequency where $\tan \delta = 1$) exists not only for the linear chains but also for cyclic PCL (see Fig. 8.4 (a) and (b)). Yet, compared to the linear chains this point is shifted to higher frequencies for the cyclics, indicating higher flexibility and/or mobility of the cyclic chains enabling them to follow the fast shear motion in the high frequency range more easily.

For both samples the storage modulus G' deviates from the expected asymptotic power law behavior (see Fig. 8.4 (a)), presumably due to experimental imperfections or a distribution of terminal relaxation times resulting from the polydispersity of the samples. However, the loss modulus G'' approaches terminal flow behavior at low of shear frequencies ω , turning $G'' = \eta \cdot \omega$ into a direct measure for the melt viscosity η . The viscosities of both samples as obtained from the data in Fig. 8.4 (a) are given in Fig. 8.4 (c)

⁵A reduction of temperature in order to shift the crossover point to lower frequencies was not feasible due to crystallization setting in at temperatures below 60°C.

as a function of ω (for numerical values see Table 8.1). The values for the PCL rings are lower than for the linear form by almost a factor of two, confirming a higher fluidity of the melt of rings due a faster mechanical relaxation as compared to the linear chains [275]. Similar trends have been found in theoretical [285] and experimental works, e. g., on PS [278,290,310] and on PB by Roovers [277]. Compared to the values of the linear counterparts the latter reported melt viscosities of the cyclics being reduced by a factor of 10. The smaller factor found here can be ascribed to contaminations of the ring systems with opened linear chains, the extent of which cannot be evaluated definitely. Yet, compared to viscosity data in Refs. [275,311], the results obtained here hint at an impurity level of about 10%.

The melt rheology experiments were repeated for another pair of samples ($M_{n,\text{lin}} = 38.6$ kg/mol) and for both sample pairs at a higher temperature of 80°C (see Table 8.1). All measurements yielded consistent results. In conclusion, the shear measurement data are in good agreement with the findings from Hahn-echo and MQ NMR experiments, where a higher chain mobility was found for cyclic PCL as well.

8.2. Crystallinity and Crystallization

NMR and DSC Crystallinity Measurements. For crystallinity determination by means of low-field ^1H NMR, sample pairs of linear and corresponding cyclic PCL chains were kept at 90°C for about 30 minutes in order to remove melt-memory or self-seeding effects (see Chapter 6) and then crystallized isothermally at $T_c = 48^\circ\text{C}$ all together in an external thermostat for four to five days (depending on the order of the subsequent NMR measurements) before they were directly transferred into the pre-heated spectrometer (48°C). Thus, the crystallization time was extended for the samples investigated at last. However, the absolute increase in crystallinity of about 1% during this waiting period (from the first to the last measurement) is on the order of the measurement uncertainty. FID, MSE and MAPE-filtered MSE signals were recorded at the crystallization temperature for each sample and the sample mass fractions f_c , f_i and f_a of the crystalline, rigid-amorphous and mobile-amorphous phase were determined by MSE signal decomposition as described in Sections 4.2 and 4.1. In order to stabilize the fit, the shape parameters T_{2a}^* and ν_a for the mobile-amorphous-part signal were independently obtained by fits to the MAPE-filtered signal using a modified exponential function (see Section 4.4.1) and fixed in the fit to the MSE signal. Hence, the signal fractions slightly depend on the choice of the filter time and may be subject to an additional systematic error of a few percent, which is the same for all samples investigated (see Section 4.4.1). The signal contributions derived from the fits were corrected for signal loss due to the MSE sequence by means of phase-specific correction factors as described in Section 4.2.⁶ The relative overall uncertainties of the sample mass fractions are estimated to be smaller than 5% for f_c and f_a and smaller than 10% for f_i .

Fig. 8.5 displays a comparison of typical MSE curves for linear and corresponding cyclic PCL chains of the same molecular weight. Here, one can already conclude that more protons reside in the mobile-amorphous regions of the sample consisting of linear chains

⁶The correction factors adopted values from 1.10 to 1.14, 1.01 to 1.03 and 1.05 to 1.13 for the crystalline phase, mobile-amorphous phase and rigid-amorphous interphase, respectively. They were similar to values obtained for other PCL samples at the same temperature.

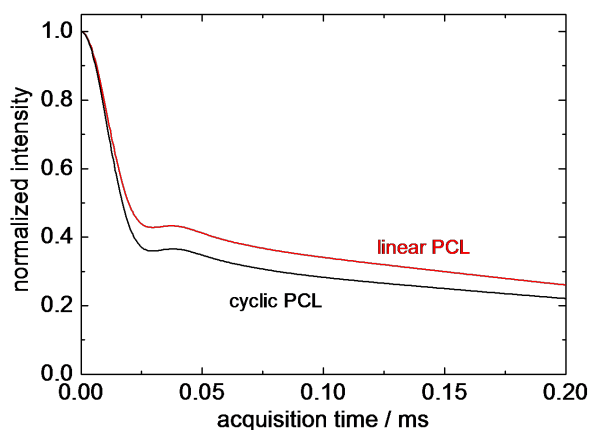


Figure 8.5: MSE signals ($n_{\text{MSE}} = 1$, $\tau_{\varphi} = 2.2 \mu\text{s}$) of cyclic and linear PCL with $M_{n,\text{lin}} = 35.4 \text{ kg/mol}$ at 48°C . The intensities have been corrected for MSE signal loss (graph adopted from Ref. [242]).

compared to the cyclics.

The mass fractions of the investigated samples are shown in Fig. 8.6 (a). The cyclic polymers exhibit mass crystallinities f_c which are higher than for their linear counterparts by several percent ($\sim 54\%$ as compared to $\sim 48\%$), while the mobile-amorphous fractions show the inverted trend, and the rigid-amorphous fractions do not reveal a correlation with the polymer type. As depicted in Fig. 8.6 (b) this trend also continues for a wider range of molecular weights. The data shown there originate from a previous series of experiments, in which, due to sparse information about the dependency of the crystallinity on measurement and crystallization temperature at that time, crystallization and measurement conditions were defined less accurately. Despite this less reproducible temperature pretreatment the crystallinity results are in good agreement with the tendency described above.

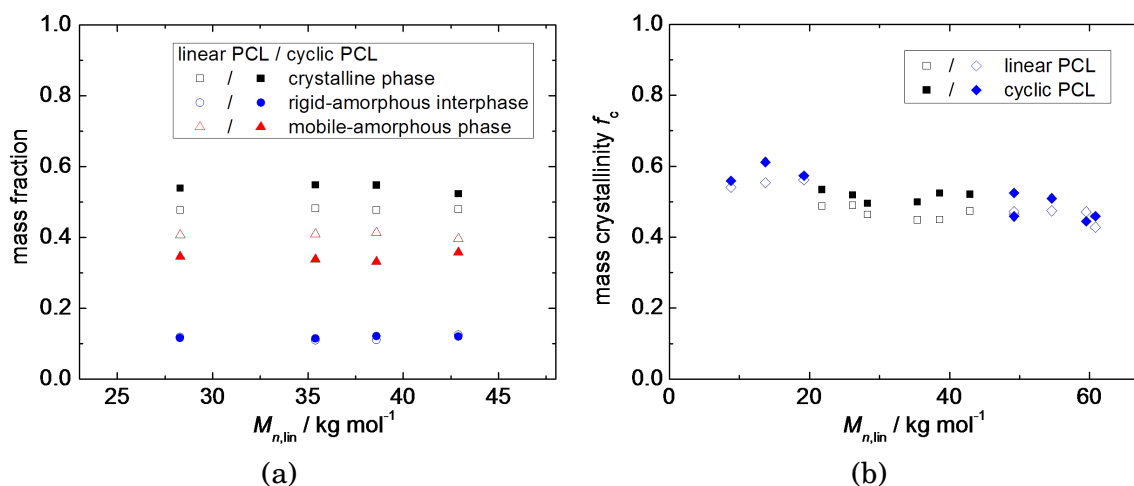


Figure 8.6.: (a) Mass fractions of the crystalline phase, mobile-amorphous phase and rigid-amorphous interphase of cyclic and linear PCL obtained by low-field NMR MSE measurements at 48°C after isothermal crystallization at 48°C for different molecular weights; (b) Mass crystallinities derived from analogous measurements at 30°C after isothermal crystallization at 46°C to 48°C and temporary storage at room temperature. Results originating from an older sample batch are depicted as blue diamond symbols (graphs adopted from Ref. [242]).

To confirm the crystallinity results from low-field NMR, DSC measurements have been performed exemplarily for two sample pairs ($M_{n,\text{lin}} = 42.9 \text{ kg/mol}$ and 28.3 kg/mol). The

DSC temperature program was comparable to the temperature procedure used for the NMR crystallinity measurements described above, consisting of a long isothermal crystallization step at 48°C and a subsequent heating scan (see Appendix A).

The DSC crystallinity was determined as explained in Chapter 6, using $\Delta H_m^0 = 142.4 \text{ J/g}$. To check for consistency one set of cooling and heating scans was conducted before and after the isothermal crystallization step. The corresponding heat flow curves matched well, indicating that a quantitative analysis in terms of crystallinity was admissible. For the reason of practicability the crystallization time for the DSC experiments was restricted to 200 minutes instead of 4 to 5 days as chosen for the NMR measurements. To obtain comparable crystallinity results from both types of experiment, the shortened crystallization time was considered by correcting the DSC crystallinities by means of a factor of 1.12 taking into account the expected 12% of additional increase in crystallinity during secondary crystallization (see Fig. 6.6 in Chapter 6). The crystallinities obtained this way match the NMR data nicely (see Fig. 8.7), confirming the difference in crystallinity between the linear and cyclic polymers.

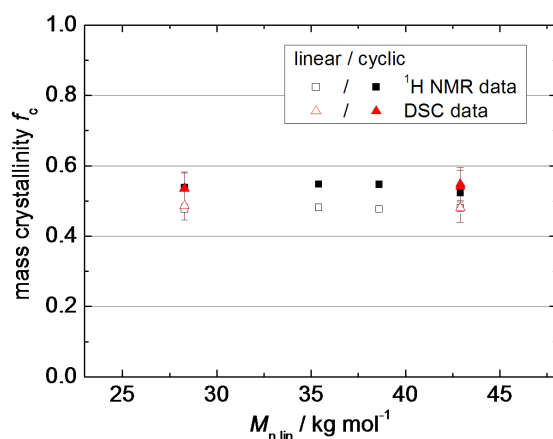


Figure 8.7.: Comparison of crystallinity of linear and corresponding cyclic PCL for different molecular weights as obtained from NMR and DSC measurements (graph adopted from Ref. [242]).

Non-Isothermal Crystallization Investigated by DSC. Non-isothermal DSC measurements are a standard method for the investigation of polymer crystallinity. Yet, literature data of high molecular weight polymer rings, determined from such experiments, are ambiguous. While, e. g., Bielawski et al. found increased crystallization and melting temperatures of PE macrocycles by about 2°C in comparison to the linear analogues (for heating rates of 10 K/min) [237], Lecomte et al. reported a reduced crystallization and melting temperature of cyclic PCL ($M_{n,lin} = 24.0 \text{ kg/mol}$, heating rate 10 K/min) by about 5°C to 7°C as compared to linear chains of the same length [261].

Interpreting data obtained for non-isothermal crystallization is often difficult, as they are influenced simultaneously by effects of nucleation and crystal growth and depend significantly on the chosen temperature program. Using nucleating agents, one can isolate the crystal-growth information from information on nucleation effects by nucleating all samples to the same high amount (see Chapter 6). To obtain reliable DSC results on crystallization kinetics, samples of linear and cyclic PCL of the same molecular weight ($M_{n,lin} = 20.2 \text{ kg/mol}$) were blended with 1.5 wt% of cl-DBS as a nucleating agent (see Chapter 6), following the procedures described by Wangsoub et al. [233].

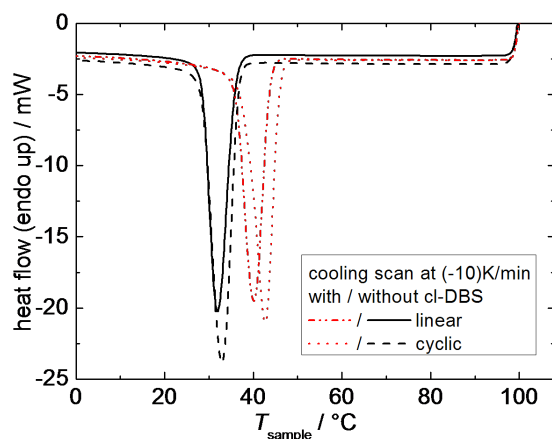


Figure 8.8.: DSC heat-flow curves obtained from a cooling scan at a cooling rate of -10 K/min for a pair of linear and corresponding cyclic PCL ($M_{n,lin} = 20.2$ kg/mol), either pure or blended with *cl*-DBS as a nucleating agent (graph adopted from Ref. [242]).

In Fig. 8.8 heat-flow curves obtained at cooling from the melt are depicted for linear and cyclic PCL with and without nucleating agent. In accordance with the findings in Chapter 6, the crystallization is accelerated in the blended samples as compared to the pure ones, resulting in an increase of the crystallization temperature T_c in the non-isothermal DSC measurement by about 6°C to 9°C .

As opposed to the results for the pure samples, the differences in T_c and in the crystallinity f_c between linear and cyclic PCL are significantly enhanced for the nucleated samples. T_c and f_c of the cyclics are higher by about 2°C and 5% , respectively, than for the corresponding linear form ($T_c \approx 45.6^\circ\text{C}$ as compared to 43.7°C and $f_c \approx 51\%$ as compared to 46%). Since equal nucleation kinetics have been ensured for linear and cyclic PCL by using the nucleating agent, the earlier onset of crystallization for the cyclics (i. e. the higher T_c value) indicates faster crystal growth compared to the linear analogue, which finally results in a higher crystallinity. Faster (isothermal and non-isothermal) crystallization of PCL rings as opposed to the linear form has also been found recently by Córdova et al. for low molecular weights [296] and by Shin et al. for higher molecular weights than the ones used here [297]. However, in the latter publication, equal crystallinities of linear and cyclic polymers have been reported in contrast to our findings.

8.3. Domain Thicknesses

To investigate the influence of chain topology on the domain thicknesses in PCL, spin-diffusion and Saturation-Recovery measurements have been performed exemplarily for a sample pair of linear and corresponding cyclic PCL ($M_{n,lin} = 35.4$ kg/mol) according to the explanations in Section 7.2. The samples were prepared under the same crystallization conditions as described for the NMR crystallinity measurements (see above). All sets of raw data (FID, MSE, spin-diffusion and Saturation-Recovery data) were analyzed as explained in Sections 4.1, 4.2 and 7.2.

The crystalline-phase-selected (DQ-filtered) and mobile-phase-selected (MAPE-filtered) spin-diffusion curves for both samples are shown in Fig. 8.9. There are only minor differences between the signal intensities for linear and cyclic chains from the DQ-filtered experiment (see Fig. 8.9 (a)). At best the crystalline-phase signal decay is somewhat

	P18		P14		P15		P13	
	linear	cyclic	linear	cyclic	linear	cyclic	linear	cyclic
$M_n / \text{kg mol}^{-1}$ ^(a)	28.3	25.2	35.4	32.1	38.6	35.7	42.9	38.5
M_w/M_n ^(a)	1.6	1.6	1.6	1.6	1.8	1.8	2.1	2.1
$\eta_{\omega \rightarrow 0} / \text{Pa}\cdot\text{s}$ (60°C)			4867	2748	6987	3917		
$\eta_{\omega \rightarrow 0} / \text{Pa}\cdot\text{s}$ (80°C)			2371	1288	3355	1879		
T_2 / ms (80°C)	4.3	6.1	4.3	7.2	4.4	9.7	3.9	8.1
$f_{c,\text{NMR}}$ ^(b)	0.48	0.54	0.48	0.55	0.48	0.55	0.48	0.52
$f_{c,\text{DSC}}$ ^(b)	0.48	0.53					0.48	0.54
$T_{m,\text{DSC}} / ^\circ\text{C}$ (Onset) ^(c)	53.7	53.3					54.1	54.2
$T_{c,\text{DSC}} / ^\circ\text{C}$ (Onset) ^(c)	35.0	36.4					36.1	36.8
$d_{a,\text{NMR}} / \text{nm}$ ^(b)			6.6	5.3				

^(a) from GPC (see Appendix A); Despite the equal number of monomers of corresponding linear and cyclic samples, a smaller value of M_n was obtained for cyclic PCL due to smaller hydrodynamic radii.

^(b) after isothermal crystallization

^(c) for non-isothermal crystallization of a non-nucleated sample

Table 8.1.: Representative sample properties for a number of investigated PCL samples as obtained by GPC, rheology, solid-state NMR and DSC.

slower and the interphase maximum intensity is slightly weaker for the cyclics than for the linear chains, hinting at marginally thicker lamellae of the cyclics. The interphase signal curves from the MAPE-filtered experiment exhibit the familiar deviations from the expected shape as a result of non-planar crystallite surfaces (see Section 7.5). Yet, a higher maximum value of the crystallite signal intensity and a faster decay of the mobile-amorphous-phase signal intensity was found in the MAPE-filtered experiment for the cyclics as compared to the linear chains, indicating thinner mobile-amorphous regions of the cyclic polymer system.

The findings on domain-size differences were confirmed quantitatively as described in the following by means of the Initial Rate Approximation and the simultaneous fit of the spin-diffusion and Saturation-Recovery data sets.

Initial Rate Approximation. The Initial Rate Approximation was performed as explained in Section 7.7 with $T_{1,\text{ave,ini}} = (283 \pm 30)$ ms and (570 ± 70) ms used for T_1 correction for the linear and cyclic PCL, respectively. The relative proton spin densities of the individual polymer phases, required for the evaluation of the domain sizes via Eq. 7.6, were calculated from literature data for the total PCL density and the density of the mobile-amorphous phase at the measurement temperature of 48°C [238] according to the explanations in Appendix E. The values used are given in Table E.1.

The spin-diffusion coefficient of the mobile-amorphous phase, $D_a = 0.0295 \text{ nm}^2/\text{ms}$, used for the domain-size evaluation, was derived via linear extrapolation of the values given in Section 7.6 to the measurement temperature. The same value was applied for linear and cyclic PCL, because the chain mobility in the mobile-amorphous phase and hence the dipolar coupling strength within this phase is similar for both types of polymer. This fact becomes apparent when comparing the corresponding mobile-phase T_2 relaxation time constants derived in Hahn-echo experiments, amounting to 0.47 ms and 0.56 ms

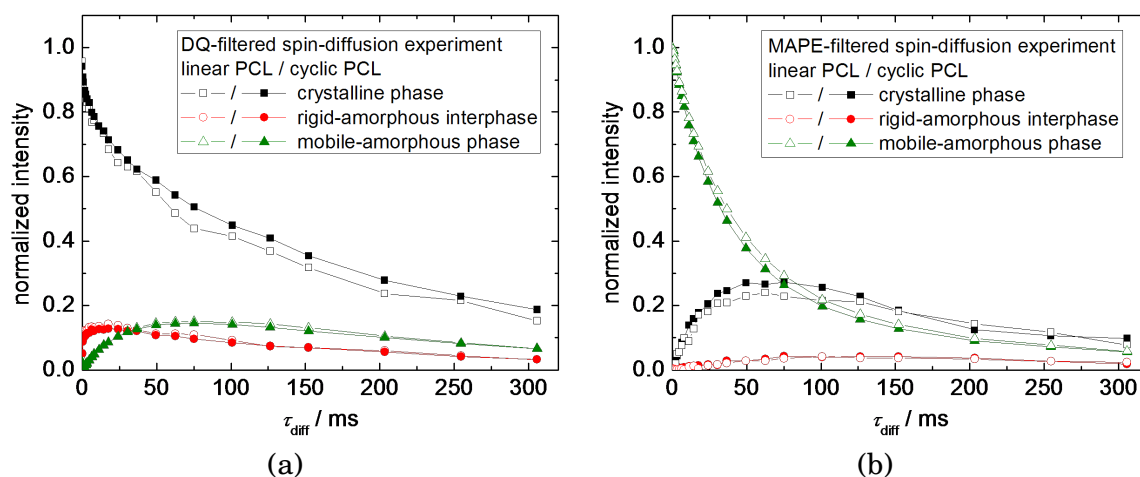


Figure 8.9.: Spin-diffusion curves for linear and corresponding cyclic PCL ($M_{n,\text{lin}} = 35.4 \text{ kg/mol}$) measured at 48°C after isothermal crystallization at 48°C for 4 days in DQ-filtered (a) and MAPE-filtered (b) spin-diffusion experiments.

for the linear and cyclic PCL, respectively. According to the calibration of the mobile-phase spin-diffusion coefficient as a function of the T_2 time constant given by Mellinger et al. [129, 251] the difference between the T_2 values for linear and cyclic chains results in a difference of the corresponding spin-diffusion coefficients of 4.5%. Such a small deviation ranges within the uncertainty margin ($\sim 10\%$) of the coefficients determined in Section 7.6.

The rigid-phase spin-diffusion coefficient, $D_{\text{rig}} = 0.31 \text{ nm}^2/\text{ms}$, was calculated as a weighted mean from the coefficients of the crystalline phase and interphase given in Section 7.6 according to Eq. 7.5. Again, the same value was used for linear and cyclic PCL, based on the assumption of very similar average coupling strengths in the crystallites due to a similar crystallite structure, which is indicated by the very similar second moments M_2 of the proton line shapes, ranging at about 10400 kHz^2 for linear and cyclic PCL over the whole range of molecular weights investigated here.⁷ The similarity of the crystallite structure of linear and cyclic PCL of high molecular weight was in fact confirmed by Shin et al. on the basis of WAXS measurements [297].

According to the findings in Section 7.7 the IRA analysis was performed for the crystalline-phase-selected (DQ-filtered) spin-diffusion experiment using Eq. 7.6. The results are listed in Table 8.2. As supposed above after comparing the spin-diffusion curves qualitatively, the cyclic PCL chains formed thinner mobile-amorphous domains compared to their linear analogues. The size difference amounts to about 1 nm. Yet, no difference was detected for the interphase and crystalline-phase domain thicknesses of the linear and cyclic PCL within the uncertainty ranges.

Simultaneous Fit of Spin-Diffusion and Saturation-Recovery Data. More precise domain-size results were obtained from simultaneous fits of the crystalline-phase-selected (DQ-filtered) spin-diffusion curves and the Saturation-Recovery data as described in Sections 7.3 and 7.6. The starting values for the spin-diffusion coefficients in

⁷ M_2 was calculated from the parameters a and b from fits to the MSE signals via Eq. 4.3 (see Section 4.1).

	$\sqrt{t_0} / \sqrt{\text{ms}}$	d_a / nm	$d_{\text{rig}} / \text{nm}$	d_c / nm	d_i / nm
linear	33.8 ± 1.0	6.6 ± 0.3	9.7 ± 0.4	7.79 ± 0.96	0.96 ± 0.23
cyclic	35.6 ± 1.0	5.5 ± 0.2	10.2 ± 0.4	8.25 ± 0.98	0.97 ± 0.23

Table 8.2.: Results from the Initial Rate Approximation for spin-diffusion data of linear and cyclic PCL ($M_{n,\text{lin}} = 35.4 \text{ kg/mol}$) at 48°C

the fit were chosen to be $D_a = 0.0295 \text{ nm}^2/\text{ms}$, $D_i = 0.19 \text{ nm}^2/\text{ms}$ and $D_c = 0.34 \text{ nm}^2/\text{ms}$ according to the findings in Section 7.6, and the initial T_1 parameter values were set to the apparent $T_{1,\text{ini}}$ time constants of the individual phases, obtained from linear fits to the initial rises of the corresponding Saturation-Recovery curves (see Section 5.1). For the domain thicknesses the results from the IRA analysis (see above) were selected as starting values. In order to obtain reliable domain thicknesses, in the fits the spin-diffusion coefficients were kept fixed at the starting values, leaving the thicknesses and T_1 time constants as free fit parameters.⁸ Fit parameters have been reset, if physically unreasonable combinations of the parameter values arose, such as $D_i > D_c$ or $T_{1i} > T_{1c}$ (see Appendix F.4). Moreover, in order to define an uncertainty level of the thickness results obtained from the fit, the starting values of the spin-diffusion coefficients were varied within the uncertainty ranges given in Section 7.6. Despite partially noisy data the fitting quality was good. A comparison between the measured data and the fit curves is depicted exemplarily in Fig. 8.10 and the results for the fit parameters are given in Table 8.3.

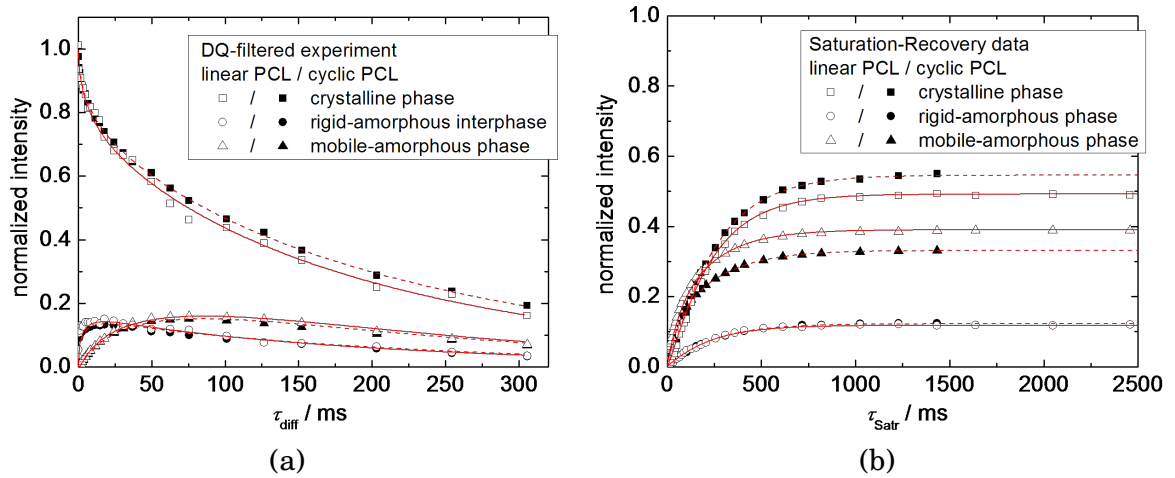


Figure 8.10.: Simultaneous fit to DQ-filtered spin-diffusion and Saturation-Recovery data, measured at 48°C for linear and corresponding cyclic PCL ($M_{n,\text{lin}} = 35.4 \text{ kg/mol}$): (a) spin-diffusion curves for the DQ-filtered experiment, (b) Saturation-Recovery curves. The solid and dashed lines represent the fit curves. Results for the fit parameters are summarized in Table 8.3.

Within the uncertainty margins, the domain thicknesses found here are in good agreement with the results from the IRA analysis (see above), confirming that the mobile-amorphous domains were smaller for the cyclic PCL as compared to the linear analogue by about 1.3 nm. This thickness difference corresponds to the length of about 1.5 PCL

⁸Only at the end of the fitting procedure, the diffusion coefficient values were allowed to adjust freely (at fixed thicknesses) to ensure a further approach to the fit minimum. Yet, the resulting values hardly deviated from the initial values.

repeat units. According to the results from the simultaneous fits of spin-diffusion and Saturation-Recovery data, moreover, the crystal thickness of the cyclics is slightly larger (by about 0.3 nm) than found for the linear PCL. Consequently, as the interphase domain sizes do not show any topology effect, the long period is somewhat smaller (by about 0.8 nm) for the cyclics in comparison to the linear analogue. The latter finding is in contrast to the results of Shin et al. who reported equal crystal thicknesses and long periods of linear and cyclic PCL obtained from SAXS experiments, however, without stating concrete numbers [297].

	mobile-amorphous phase	rigid-amorphous interphase	crystalline phase	total
	linear			
d / nm	6.57 ± 0.09	0.95 ± 0.03	7.77 ± 0.11	16.24 ± 0.26
$D / \text{nm}^2 \text{ ms}^{-1}$	0.0293 ± 0.0004	0.22 ± 0.05	0.38 ± 0.07	
T_1 / ms	115 ± 1	130 ± 10	550 ± 35	
	cyclic			
d / nm	5.28 ± 0.08	0.97 ± 0.03	8.13 ± 0.09	15.35 ± 0.23
$D / \text{nm}^2 \text{ ms}^{-1}$	0.0293 ± 0.0004	0.19 ± 0.03	0.37 ± 0.05	
T_1 / ms	107 ± 6	120 ± 10	760 ± 120	

Table 8.3.: Domain thicknesses d , spin-diffusion coefficients D , longitudinal relaxation time constants T_1 and long period L (last column) as obtained from simultaneous fits of spin-diffusion and Saturation-Recovery data for linear and cyclic PCL ($M_{n,\text{lin}} = 35.4 \text{ kg/mol}$) at 48°C (see text). The uncertainties represent the ranges of fluctuation of the fitting results for slightly different starting parameters.

8.4. Summarizing Remarks

The comparison of PCL chains of linear and cyclic topology yielded the following overall picture (see Fig. 8.11):

- ^1H low-field NMR Hahn-echo and multiple-quantum measurements revealed a lower residual order of the chain segments and a faster loss of orientational memory in the melt of rings when compared to the linear analogues, resulting from less or weaker topological restrictions to chain motion, such as entanglements and/or packing constraints. The enhanced cyclic-chain mobility was also reflected in the lower melt viscosities of the cyclic polymers in comparison to their linear counterparts.
- The higher chain mobility in the melt enabled an easier, i. e. faster crystal growth of the cyclics in comparison to the linear chains, resulting in a higher crystallinity as observed by means of DSC and ^1H low-field NMR MSE measurements during non-isothermal and after isothermal crystallization. Large effects of missing chain ends of the cyclics on the fold-surface energy of the crystals and on the crystallization process can be excluded, as for the high molecular weights used here the chain-end concentration in the fold surface (roughly estimated for an adjacent-reentry scenario and a crystal thickness of 8 nm) does not exceed 6%.

- From the results of the spin-diffusion measurements one can conclude, that the higher crystallinity of the cyclic PCL is based on a reduced size of the mobile-amorphous domains compared to the linear polymer, while the crystal thickness is increased only marginally. This finding is consistent with the lower number of packing restrictions for cyclic chains in the melt, which counteract the crystallization, hence allowing the formation of thinner mobile-amorphous regions.

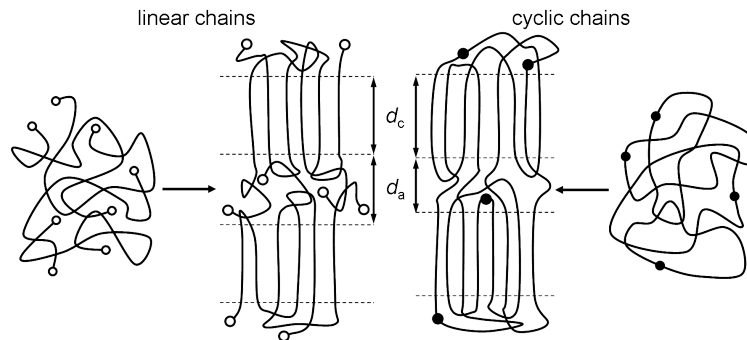


Figure 8.11.: Schematic representation of the semicrystalline structure of linear and cyclic PCL forming from the coiled melt state.

9. Summary

Proton low-field NMR methods are well-suited for investigations of the phase structure of semicrystalline polymers and the chain dynamics within their crystalline and mobile-amorphous regions. The main issue here is the sensitivity of the NMR time-domain signal to the strength of the homonuclear dipolar couplings between the protons in the sample. The reduction of this coupling strength as a result of molecular motions and differences between the coupling strengths in the individual polymer phases are observed due to their characteristic effect on the signal shape and intensity. Both influences have been exploited in this thesis in order to study the semicrystalline polymers PCL and PE.

Crystallinity and Crystal-Growth Investigations. Based on mobility distinctions or rather differences in the anisotropy of fast chain motions between amorphous and crystalline polymer phases, the crystallinity of PCL and PE could be determined reliably by means of FID measurements at temperatures far above the glass transition. The crystallinities obtained by low-field NMR are comparable to values from SAXS and DSC measurements. Since a model fit function has been adapted for a stable fit of the NMR time-domain signals, a fast analysis of the phase composition of the samples is possible. For both polymers, PCL and PE, besides the crystalline-phase and mobile-amorphous-phase signal a third contribution had to be introduced in order to attain a high fitting quality. This contribution is ascribed to the signal of a rigid-amorphous interphase of restricted chain mobility between crystallites and mobile-amorphous regions.

The isothermal crystallization of PCL could be tracked reproducibly by NMR FID (or MSE) measurements. As PCL exhibits a self-seeding or melt-memory phenomenon, the samples had to be molten at a sufficiently high temperature (above $\sim 85^{\circ}\text{C}$) in order to prevent unpredictable effects of surviving self nuclei on the kinetics of a subsequent crystallization. Also impurities influence the crystallization kinetics by accelerating the nucleation step. The crystal-growth rate of different samples is comparable only if they exhibit a similar, high number of external nuclei. Hence, it is recommendable to blend PCL samples with chloro-substituted DBS as a nucleating agent to eliminate the nucleation as the rate-determining step of the crystallization process, when crystal-growth kinetics shall be compared.

Investigations of Dynamics in PE and PCL crystallites. The MSE sequence has an advantage over the FID in that it prevents signal loss during the receiver dead time. When using the MSE for crystallinity determinations, however, phase-specific intensity corrections have to be considered to compensate for the loss due to strong dipolar couplings and technical imperfections of the sequence or molecular dynamics on an intermediate time scale of microseconds to milliseconds. Yet, the systematic signal loss due to such motions enables the application of the MSE sequence to study polymer dynamics within the crystallites.

Here, the MSE sequence was used to explore the time scale of the local 180° helical jumps in PE crystallites. The investigation of this jump process by NMR is difficult as many NMR interactions, such as the geminal proton dipolar couplings, the chemical shifts and ^2H quadrupolar interactions are invariant under the flip motion. However, as shown here, one can exploit the fact that the strength of the dipolar couplings between

protons of a moving chain and protons of the neighboring chains is changed compared to the static case, leading to a systematic reduction of the MSE refocusing efficiency, when chain flips take place on the time scale of the sequence length. Jump rates for the local chain-flip process have been determined quantitatively for three PE samples of different molecular weight and lamellar thickness and different forms of the crystallite chain-fold surface (tight chain folds vs. disordered fold surface). For this purpose, FID signal decomposition has been used and the Anderson-Weiss approach to describe the MSE crystallite signal intensity decay as a function of the MSE sequence length. The jump rates observed here agree well with results from advanced, complex and time-consuming ^{13}C -based high-field NMR experiments. Within the available time and temperature window of the method the differences in phase morphology as well as in molecular weight and lamellar thickness did not influence the chain-flip rate significantly, although a considerable difference in the speed of the longer-range chain transport through the crystallites was reported in literature for samples similar to the ones investigated here. Apparently, this difference is not based on different jump rates of the local flip process. Yet, for the reactor powder samples, exhibiting an adjacent-reentry-like morphology, slightly smaller activation energies were found than for melt-crystallized PE with its disordered fold surfaces.

Following the interpretation of Kaji and Horii the methylene groups in the PCL crystallites should perform rather large-amplitude motions (up to 90°) on an intermediate to slow time scale. However, neither the results of low-field MSE measurements nor the second moment M_2 of the proton line shape as a function of temperature give any hints to intermediate motions within the PCL crystallites. Moreover, findings from high-field NMR DIPSHIFT and CODEX experiments, performed to check the low-field results and to extend the available time scale for the observation of motions, confirmed the absence of intermediate-regime and slow motions. Only fast motions, presumably vibrations, with amplitudes up to about 20° have been proven by means of the DIPSHIFT method. Since jump motions of large amplitudes are not present within the PCL crystallites, chain diffusion through the crystallites and crystal thickening during crystallization or cooling as known for PE are not expected for PCL. The absence of crystal thickening processes was in fact confirmed by SAXS measurements. Hence, a classification of PCL as a crystal-fixed polymer is justified.

Investigations of the Domain Morphology in PCL by Means of Spin-Diffusion Experiments. As shown here exemplarily for PCL, spin-diffusion experiments enable the determination of domain sizes in semicrystalline polymers provided that the spin-diffusion coefficients are known. This method again relies on the differentiation of the individual polymer phases on the basis of different chain mobility and dipolar coupling strengths. It is favorable compared to other techniques as no particular sample pre-treatment is required, such as staining or degassing.

The selection of magnetization in one of the PCL phases has been accomplished by means of the MAPE sequence as a mobile-phase filter and a short DQ filter as a crystalline-phase filter. The filter length of both sequences has been optimized for the application to PCL. However, a perfect excitation of magnetization in only one polymer phase has not been possible due to mobility gradients within the amorphous phase and a lack in filter efficiency of the DQ filter. Using the DQ filter, moreover, it was found

that the magnetization level within the crystalline lamellae after the application of the filter was not equal for all the lamellar stacks as a result of the orientation dependence of the dipolar couplings mediating the filter action and the different orientations of the stacks of lamellae. As opposed to glassy-amorphous polymer systems this uneven magnetization distribution could not be equilibrated at short times, because of the missing contact between the lamellar stacks of different orientations.

The spin-diffusion curves of PCL exhibit specific deviations from curves, which have been simulated under the assumption of one-dimensional spin diffusion via planar interfaces in a system comprising two or three polymer phases, taking into account phase-specific T_1 relaxation. The delayed magnetization transfer compared to the simulation could be explained quantitatively by the existence of lag phases which are evaluated as a part of the magnetization source region but in fact are unpolarized initially. The directly traceable reasons for magnetization transfer lags (i. e. the incomplete polarization of the individual source phases by the filter sequences) do not suffice quantitatively to explain the deviation from the simulated curves. The remaining difference, in particular the too low interphase signal intensity and the too high crystalline-phase signal intensity in the MAPE-filtered spin-diffusion curves, probably arise from corrugated crystallite surfaces causing an enhanced magnetization transfer from the mobile-amorphous domains to the crystallites compared to a scenario with planar crystallite surfaces. As the variations between measured curves from the MAPE-filtered experiment and simulated curves were dramatic, it is strongly recommended to restrict the analysis to data from DQ-filtered spin-diffusion experiments.

For the individual polymer phases in semicrystalline PCL neither calculated nor experimentally derived values for the spin-diffusion coefficients have been reported in literature up to now. However, these values are required for the estimation of domain sizes by means of NMR spin-diffusion experiments. Hence, they have been determined here by fitting measured DQ-filtered spin-diffusion and Saturation-Recovery curves with the help of simulated curves, calculated for one-dimensional spin diffusion via planar surface boundaries in a three-phase polymer system with fixed domain thicknesses derived from SAXS measurements. This way, effective spin-diffusion coefficients were obtained for all three PCL phases for temperatures of about 27°C to 45°C. Using these coefficients, the domain sizes derived by SAXS could be reproduced well by means of the Initial Rate Approximation (IRA) of the DQ-filtered spin-diffusion data, confirming the practicability of the IRA approach.

Influence of Chain Topology on the Semicrystalline Structure of PCL. A variety of low-field NMR techniques complemented by rheological investigations and DSC studies have been applied to linear and macrocyclic PCL chains of the same chain length in order to compare their mobility in the melt, their crystal-growth kinetics and their semicrystalline structure. The melt of PCL rings exhibited a higher chain mobility compared to the linear chains, observed in the form of a lower residual order and a faster loss of orientational memory of the chain segments as a result of less or weaker topological restrictions to chain motion, such as entanglements and/or packing constraints. Due to the enhanced mobility the cyclics crystallized faster and finally reached a higher crystallinity in comparison to the corresponding linear chains. As proven by spin-diffusion measurements using the spin-diffusion coefficients derived for PCL before, this gain in

crystallinity is not caused by thicker lamellae but by thinner mobile-amorphous regions of the cyclic PCL essentially because, compared to the linear chains, less packing constraints counteracted the crystallization.

A. Experimental Details

A.1. Experimental Techniques

^1H Low-Field NMR. The ^1H low-field time-domain measurements were carried out on Bruker minispec mq20 spectrometers with a static magnetic field of about 0.5 T and ^1H Larmor frequencies of 19.9 MHz to 20.0 MHz, equipped with commercial wide temperature range static probes. The spectrometers featured 90° pulse lengths of 1.6 μs to 3.0 μs and receiver dead times of 11 μs to 15 μs .

For the NMR measurements about 0.3 g of sample were packed into 8 mm or 10 mm NMR sample tubes in form of small pieces. The tubes were flame-sealed under vacuum conditions if necessary in order to avoid degradation of the samples (see Appendix B). To keep the sample in the center of the magnet, i. e. in the region of the highest homogeneity of the magnetic field, only the lowermost 6 mm to 8 mm of the tubes were filled with sample. The sample tubes were centered in the middle of the spectrometer coil region by custom-made Teflon spacers.

The sample temperature was regulated by means of a BVT3000 heater with air as the heat-transfer medium for heating and cooling. A cooler was required for temperatures below 300 K. At temperatures below 230 K nitrogen gas was used as a cooling gas instead of air to prevent the condensation and freezing of water (air moisture) inside the cooling hoses. The temperature at the sample position could be set with an uncertainty of about 1 K and a temperature gradient over the sample of 0.5 K. Temperature measurements at the sample position inside the spectrometer have been accomplished by means of an external thermo sensor which was put into a NMR sample tube, filled with a small amount of silicone oil, and placed at the sample position. The temperature at the sample position was checked after each change of the temperature setting of the heater and also regularly between measurements at the same temperature setting.

All time-domain NMR signals were recorded on-resonant and in full-absorption mode receiver setting, analyzing only the real part of the complex time-domain signal. A setup was made in the beginning of a series of measurements for every sample (yet, at least once a day) comprising a nutation experiment for the determination of the 90° and 180° pulse length. Moreover, to ensure that the longitudinal relaxation was complete between the scans in the semicrystalline state of the sample as well as in the melt, an appropriate recycle delay was determined either by variation of this delay or by means of a Saturation-Recovery experiment. For semicrystalline PCL and PE the recycle delay was typically set to 1.5 s and 2 s to 4.8 s, respectively. (Note, that for the Saturation-Recovery measurements a very short delay of 0.1 s was sufficient, because the magnetization was destroyed again before every new scan.) The number of scans was varied between 16 and 512 depending on the NMR sequence used, in order to ensure a sufficiently high signal-to-noise ratio.

High-Field ^{13}C NMR DIPSHIFT Sequence. The DIPSHIFT sequence used is shown in Fig. A.1 adopted from Ref. [173]. A short description of its mode of operation is given in the following. The sequence is performed under Magic-Angle Spinning (MAS) of the sample in order to enable the acquisition of high-resolution ^{13}C spectra. Transverse ^{13}C magnetization is excited by means of Cross Polarization (CP). Subsequently, the

spin system develops under the influence of resonance offsets and ^1H - ^{13}C heteronuclear dipolar couplings during an incremented time t_1 , which is varied between 0 and a full rotor period T_R (see Fig. A.1). During this time the homonuclear proton dipolar coupling is suppressed by means of the frequency-switched Lee-Goldberg (FSLG) decoupling sequence [170,173]. For the rest of the sequence the system develops under heteronuclear decoupling using the SPINAL64 sequence [173]. The 180° pulse on the ^{13}C channel after a complete rotor period T_R serves to generate a Hahn echo at the beginning of the signal acquisition period after $2T_R$, i. e. it cancels resonance offsets. Hence, effectively, the heteronuclear dipolar coupling is the only NMR interaction which influences the spin system during t_1 and contributes to the detected signal [170].

The signal intensity varies with increasing t_1 in a way which is characteristic for the strength of the average ^1H - ^{13}C coupling. Therefore this coupling strength can be derived here [170,173]. It may be reduced by a pre-averaging of the couplings due to fast molecular motions with rates much larger than the static coupling strength and its actual value yields information about the presence of fast motions and their motional amplitude provided that the geometry of the motion is known.

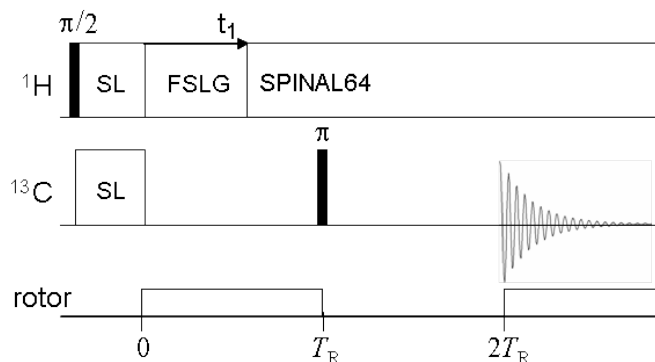


Figure A.1.: Schematic sketch of the DIPSHIFT pulse sequence. The abbreviation SL designates a spin lock for Cross Polarization (CP).

The DIPSHIFT experiments were performed on a Bruker Avance III spectrometer with an Oxford magnet, at ^1H and ^{13}C Larmor frequencies of 400.16 MHz and 100.06 MHz, respectively, equipped with a 4 mm double-resonance probe at a spinning frequency of 5 kHz. The PCL sample was packed into a 4 mm ZrO_2 MAS rotor. The temperature accuracy was ± 1 K. The 90° pulse lengths were $3.5 \mu\text{s}$ for ^1H and $3.1 \mu\text{s}$ (at room temperature) or $3.0 \mu\text{s}$ (at 52°C) for ^{13}C , respectively. For heteronuclear decoupling the SPINAL64 sequence was applied at a ^1H decoupling frequency of 71.5 kHz. For homonuclear decoupling with FSLG an rf field strength $\omega_{\text{eff}} = 87.5$ kHz along the effective field was used. The contact time for ^1H - ^{13}C Cross Polarization was chosen to be 0.3 ms and the repetition delay was set to 2 s. 2048 scans were acquired for each of the 16 t_1 increments.

High-Field ^{13}C NMR CODEX Sequence. The CODEX sequence used is shown in Fig. A.2 adopted from Ref. [173]. Its mode of operation is shortly described in the following. Transverse ^{13}C magnetization is excited using Cross Polarization (CP). After that, during $N/2$ rotor periods (with N being an integer), the spin system develops under the Chemical-Shift Anisotropy (CSA) interaction, which is reintroduced by means of a series of rotor-synchronized 180° pulses applied every half a rotor period (see Fig. A.2) [190]. A 90° store pulse serves to store magnetization in the direction of the magnetic field dur-

ing the mixing time $\tau_{\text{mix}} < T_1$, being an integer multiple of the rotor period T_R . During this mixing time the magnetization does not precess or dephase but it develops under the influence of slow molecular dynamics, if present in the sample [190, 191]. Subsequently, the magnetization is flipped into the transverse plane by means of another 90° pulse and develops again under the reintroduced CSA interaction during $N/2$ rotor periods [190]. The sequence is completed by storage of the magnetization in direction of the magnetic field during a short time $t_z = T_R$ and the acquisition of the exchange signal after a read-out pulse.

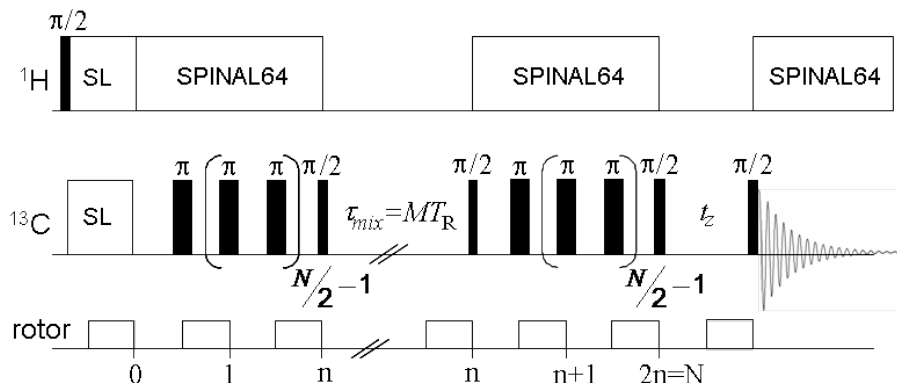


Figure A.2.: Schematic sketch of the CODEX pulse sequence. The abbreviation SL designates a spin lock for Cross Polarization (CP).

When slow segmental reorientations occur during τ_{mix} , i. e. on a time scale of milliseconds to seconds, which change the orientation-dependent CSA interaction of the carbon spins, a dephasing of magnetization takes place, which is not reversed until the beginning of the signal acquisition period and is detected in the form of an intensity loss compared to a situation without molecular motions. The signal intensity as a function of the mixing time τ_{mix} or the duration NT_R of the CSA recoupling periods yields information about the correlation time and amplitude of slow motions, respectively [190, 191]. For the latter the geometry of the motion has to be known.

In order to cancel T_1 relaxation effects during τ_{mix} and T_2 relaxation effects during the CSA recoupling periods, a reference signal is detected using the same sequence but with interchanged durations of τ_{mix} and t_z . Here, $\tau_{\text{mix}} = T_R$ is short, preventing slow dynamics during the mixing time. For normalization the exchange signal intensity is divided by this reference signal intensity [191].

The CODEX experiments were performed on a Bruker Avance II spectrometer with a Jastec magnet at ^1H and ^{13}C Larmor frequencies of 400.16 MHz and 100.06 MHz with a 4 mm double-resonance MAS probe at a spinning frequency of 5 kHz. The sample was packed into a 4 mm ZrO_2 MAS rotor and the temperature accuracy amounted to ± 1 K. The ^1H and ^{13}C 90° pulse lengths were 3.0 μs and 3.7 μs , respectively. The SPINAL64 sequence was applied for heteronuclear ^1H - ^{13}C decoupling during the recoupling and acquisition period with a decoupling frequency of 80 kHz. For ^1H - ^{13}C Cross Polarization the contact time was set to either 0.2 ms or 1.5 ms. The repetition delay was chosen to be 2 s. Exchange and reference spectra were measured for CSA recoupling durations NT_R between 0.4 ms and 3.2 ms with 1024 scans each and a mixing time τ_{mix} of either 100 ms or 200 ms.

Small Angle X-Ray Scattering (SAXS). The Small Angle X-Ray Scattering (SAXS) measurements and data analysis were done by M. Sc. A. Seidlitz at the Institute of Physics (Experimental Polymer Physics group) of the Martin-Luther-Universität Halle with a PCL sample analogous to the one used for the low-field NMR spin-diffusion experiments described in Section 7.2.

The SAXS apparatus contained a Cu-K α X-ray source (wave length $\lambda = 0.154$ nm) with a beam focus of 0.4×12 mm², refocusing X-ray lenses and a Kratky camera including the collimator system. The detection was carried out by means of a scintillation counter placed in a distance of 200 mm from the temperature-controlled sample holder [218].

The SAXS measurements were performed under the same temperature conditions as for the corresponding low-field NMR spin-diffusion and Saturation-Recovery measurements (cf. Section 7.2). For this purpose, the temperature setting of the NMR spectrometer and the SAXS sample holder was adjusted prior to the measurements by comparing the readout of one temperature sensor in both devices.

The scattering intensities measured by SAXS were deconvoluted using a desmearing algorithm to consider the line-shaped beam focus. The SAXS signal amplitude is proportional to the three-dimensional Fourier transform of the electron density in the sample. In case of a lamellar system it can be traced back to a one-dimensional electron density correlation function, the second derivative of which is the interface distance distribution function [218, 312]. Such distribution functions were calculated from the measured data and fitted by means of a simulated function which comprises the thicknesses of the crystalline and amorphous domains and the corresponding distribution widths as fit parameters. The fit enabled the determination of domain sizes also at crystallinities close to 50% [218].

Differential Scanning Calorimetry (DSC). Differential Scanning Calorimetry was carried out by means of a Perkin Elmer DSC7 and a Perkin Elmer Pyris Diamond instrument calibrated with indium and mercury and indium and cyclopentane, respectively. The measurements were conducted by K. Herfurt in the Experimental Polymer Physics group at the Institute of Physics of the Martin-Luther-Universität Halle. Samples of 5 mg to 10 mg were encapsulated in pressure-tight 30 μ l or 50 μ l aluminum pans. Nitrogen was used as purge gas. The data were analyzed by means of the software Pyris Thermal Analysis version 3.81 or version 5.00.02 including a baseline subtraction for all non-isothermally measured DSC curves.

For evaluating the crystallinity after isothermal crystallization, each sample was pretreated non-isothermally by keeping it in the melt at 90°C for 10 minutes, cooling to 0°C at -10 K/min, holding at 0°C for 10 minutes and re-heating to 90°C. After 10 minutes in the melt the sample was rapidly cooled to the crystallization temperature (at -200 K/min or the highest possible cooling rate) and isothermally crystallized for a crystallization time t_c . From the subsequent heating scan to 90°C at 10 K/min heat flow and enthalpy of fusion were determined for the estimation of the crystallinity. Moreover, as a check for consistency, the pretreatment steps were repeated.

In order to investigate the non-isothermal crystallization, the melting and crystallization temperatures (evaluated at the peak onsets) were deduced from heat-flow curves obtained during heating to 100°C (after cooling from the melt (at 100°C) to 0°C and hold-

ing the sample at 0°C for 10 minutes) and a second cooling run to 0°C after annealing at 100°C for 10 minutes. All cooling and heating steps were conducted at 10 K/min.

The glass transition temperatures of the amorphous regions of the semicrystalline PCL samples were measured upon heating to 85°C at 20 K/min after having cooled the sample from the melt to -100°C at 20 K/min and annealing for more than 10 minutes. The glass transition was visible and the glass transition temperatures T_g were determined as the midpoints of the glass transition step. The T_g values did not differ by more than 1 K to 2 K. Within the scatter no significant trend concerning a differentiation between linear and cyclic PCL was observed. Hence, also at higher temperatures (i. e. in the melt) significant deviations of the segmental dynamics between linear and cyclic chains caused by free volume differences are not expected.

Gel Permeation Chromatography (GPC). Gel Permeation Chromatography (GPC) measurements were performed by a staff member of the Division of Macromolecular Science in the Department of Macromolecular Chemistry at the Martin-Luther-Universität Halle at a Viscotek GPCmax VE 2001 apparatus with a Styragel linear column GMH_{HR} with tetrahydrofuran (THF) as a carrier solvent at 1 ml/min at room temperature. The sample concentration was approximately 3 mg/ml.

Polystyrene standards ($M_p = 1050 - 115000$ g/mol) were used for conventional external calibration, using a Waters RI 3580 refractive index detector. The absolute PCL molecular weights were calculated from the apparent ones (for PS standard) using the Mark-Houwink equation [313] and the parameters or formulas given in the literature [314–317].

Rheological Measurements. Rheological measurements were performed by Dr. K. Schröter and Dipl.-Chem. E. Ostas at the Institute of Physics (Experimental Polymer Physics group) of the Martin-Luther-Universität Halle, using a Rheometrics Dynamic Analyzer RDAII with a parallel-plate geometry purchased from TA Instruments. The diameter and the thickness of the samples were 25 mm and around 1.7 mm, respectively. In this case, compliance effects of the instrument are negligible. Shear loss modulus (G'') and storage modulus (G') were determined as a function of the shear frequency ω between 1 rad/s and 100 rad/s. Typically, the strain in the sample was 2%, being well within the linear deformation range. The strain was chosen to keep the measured torque values in a range of about 100 g·cm to 0.2 g·cm, according to the measurement range of the transducer of the instrument. At low frequencies the decreasing modulus values and hence also the torque values limited the usable measurement range of the rheometer.

For sample preparation the PCL powder was pressed under vacuum in a cylindrical mould with the desired diameter and thickness. After 8 h at 90°C the sample was slowly cooled down to room temperature over night under vacuum. The cylindrical polymer sample was placed between the two plates of the rheometer and after heating to 90°C and slight compression it stuck to the surface of the plates. Subsequently, the temperature was lowered to the measurement temperatures of 60°C or 80°C and equilibrated. During these temperature changes the thermal expansion of the tools of the instrument was compensated by a corresponding change of the gap setting. Due to the air and humidity sensitivity of cyclic PCL (see Appendix B) all measurements were conducted

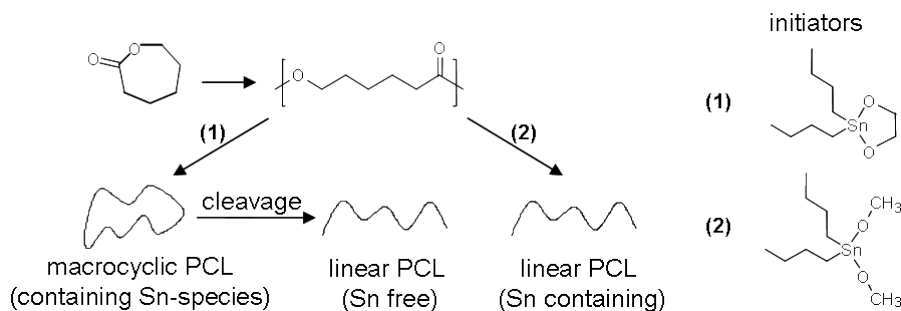


Figure A.3.: Synthetic approach for the preparation of cyclic and linear PCL (graph adapted from Ref. [242]).

under a nitrogen gas flow.

A.2. Samples

PCL Samples. For this work two kinds of PCL systems have been used, i. e. industrially produced PCL on the one hand and linear and cyclic PCL synthesized by Dipl.-Chem. E. Ostas (Macromolecular Chemistry Department, Division of Macromolecular Science, Martin-Luther-Universität Halle) on the laboratory scale on the other hand.

The industrially produced PCL with $M_n \approx 42.5$ kg/mol and $PD \approx 1.5$ ($M_w \approx 63.8$ kg/mol) was purchased from Sigma Aldrich.

The cyclic PCL samples were prepared by E. Ostas by insertion polymerization according to procedures reported by Kricheldorf et al. [301]. For the ring opening polymerization of ϵ -caprolactone an Sn-based cyclic initiator (2,2-dibutyl-1,2-dioxo-2-stannane) ((1) in Fig. A.3) was used, which does not allow for the concatenation of rings. The corresponding linear polymers were obtained directly from the respective cyclic PCLs by cleavage of the Sn-O bond with 1,2-ethane-dithiol to yield bis-hydroxytelechelic PCL [318]. They exhibit the same number of monomers as their cyclic counterparts and are free of tin. Details on the synthesis are given in Refs. [242] and [319].

A number of PCL samples was blended with chloro-substituted dibenzylidene sorbitol (1,3:2,4-di(4-Chlorobenzylidene) Sorbitol) (cl-DBS) synthesized by E. Ostas according to the instructions given in Ref. [233]. For the solution blending of the samples, PCL (98.5 wt%) and cl-DBS (1.5 wt%) were dissolved in heated butanone separately. The solutions were mixed and the mixture was dried afterwards in a rotary evaporator and under high vacuum.

PE Samples. Two types of PE samples were compared in Section 5.2, a commercial high-density (HD) PE and two reactor powders of ultra-high molecular weight.

The commercial HD PE sample was provided by Basell Polyolefine GmbH. It exhibits a weight-averaged molecular weight $M_w \approx 349$ kg/mol and a polydispersity $PD \approx 21.4$ (as measured by GPC). It was crystallized from the melt and exhibits lamellar crystals with disordered fold surfaces (see Fig. 5.10). Because of the high polydispersity the sample contains short chains possibly forming tight folds at crystalline surfaces as well as long

chains which may form entanglements in the amorphous regions. The mass and volume crystallinity of the HD PE amounts to 59 % and 55.4 %, respectively, determined by DSC and Wide Angle X-Ray Scattering (WAXS), respectively. Results from SAXS revealed a long period $L \approx 21$ nm. The lamellar thickness $d_c \approx 13$ nm was estimated using the crystallinity data. The melting temperature was quantified to be 405 K by DSC (heating rate: 20 K/min).

The two PE reactor powder samples were provided by Prof. S. Rastogi (Loughborough University). Information about sample preparation and properties is given in Ref. [199]. Both samples show a rather adjacent-reentry-like morphology (see Fig. 5.10) but differ in molecular weight ($M_w \approx 5000$ kg/mol and 750 kg/mol) and polydispersity ($PD \approx 3$ and 1.8, respectively), derived from rheology. The lamellar thickness of both samples ranges at about 8 nm as estimated by transmission electron microscopy (TEM) [320].

B. PCL Degradation Investigations

B.1. Degradation of Cyclic PCL Chains

For testing the degradation of the cyclic PCL chains resulting from the cleavage of the Sn-O bonds, linear, tin-containing PCL samples were prepared by E. Ostas (Macromolecular Chemistry Department, Division of Macromolecular Science, Martin-Luther-Universität Halle) by means of a dibutyl-tin-dimethoxide initiator ((**2**) in Fig. A.3) The Sn-O bond cleavage separates these chains into two parts of about half the molecular weight. Such a large change in molecular weight causes a significant effect on the GPC retention volume and can be detected more clearly than the small difference between cyclic chains and their linear counterparts, formed by the Sn-O bond cleavage of the cyclics (see also Fig. 8.1).

Two samples of accordingly prepared linear chains, i. e. a test sample and a reference sample, were placed in sealed glass tubes. While the reference sample was kept under an atmosphere of argon, the test sample was studied under ambient conditions (moisture and oxygen). The degradation test was performed by E. Ostas by annealing both samples at 95°C for some hours and by monitoring the molecular weights in regular time intervals by GPC.

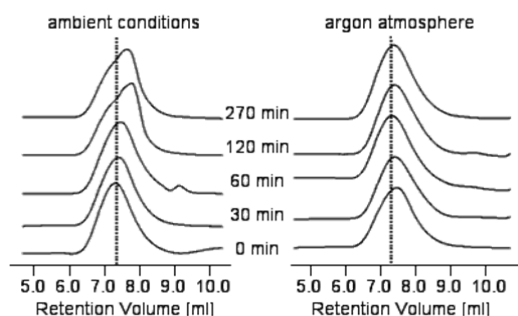


Figure B.1.: GPC traces for a linear tin-containing PCL ($M_n = 16.1$ kg/mol, $M_w/M_n = 1.7$) at 95°C at ambient conditions (moisture and oxygen) and under argon atmosphere. The bottom traces ($t = 0$) reflect the sample state before cleavage. The measurement times during the cleavage experiment are given in the plot (graph adopted from Ref. [242]).

As can be seen in Fig. B.1, heating under ambient conditions afforded the appearance of a second peak at higher retention volume, i. e. lower molecular weight due to cleavage of the Sn-O-bonds. By contrast, the reference sample did not show a significant change in molecular weight and thus no cleavage reactions. Similar degradation results are known for PCL rings synthesized by click chemistry [259]. According to these findings all further measurements were conducted under exclusion of air and moisture. Moreover the samples were stored under vacuum.

B.2. Degradation of Linear PCL Chains

As chain degradation results in a shortening of the chains and hence in an enhancement of the chain mobility and a reduction of the residual dipolar coupling strength, T_2 Hahn-echo measurement probing the residual dipolar coupling strength qualitatively, can be applied to detect degradation effects.

Here, the long-term stability of linear PCL chains was tracked for a period of some months by means of Hahn-echo decay measurements at 80°C performed for two industrially produced PCL samples ($M_n = 42.5$ kg/mol, without tin) stored under different

conditions. Between the measurements the test sample was stored in an evacuated sample tube at 90°C under natural light, whereas the reference sample was stored at room temperature, under vacuum and in a dark environment.

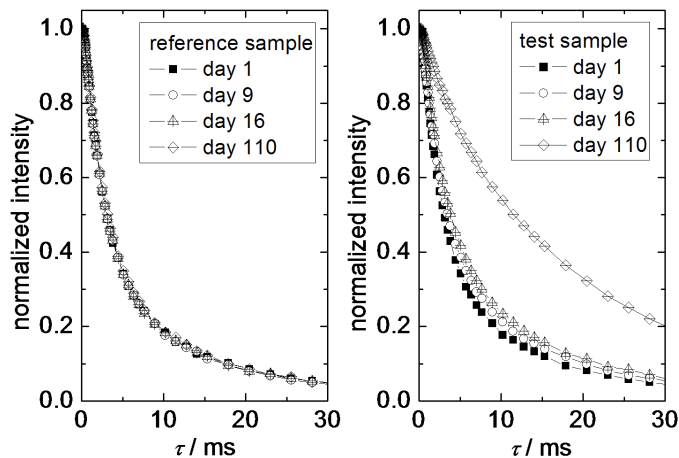


Figure B.2.: Long-term stability test for linear PCL. Hahn-echo decay curves measured at 80°C for 2 industrially produced PCL samples ($M_n = 42.5$ kg/mol): a reference sample (left), stored under vacuum at room temperature in a dark environment, and a test sample (right), stored in an evacuated sample tube at 90°C under natural light.

In Fig. B.2 the Hahn-echo decay curves detected after increasing storage periods are depicted for both samples. The decay time of the reference sample did not change during the test period. Yet, the decay observed for the test sample slowed down significantly with increasing storage time as a result of reduced residual dipolar couplings due to more isotropic chain motions (cf. Section 8.1) of the shorter PCL chains formed by chain degradation. Hence, it may be concluded that PCL chains decompose during (long) annealing periods at high temperatures, presumably by the random cleavage of ester bonds [321]. This finding has to be considered with regard to sample treatment when a specific molecular weight is required.

C. Quantum-Mechanical Basics of NMR

The quantum-mechanical state of a nuclear spin system is described by the wave function $|\psi(t)\rangle$, which contains information about the position, speed and spin state of every particle of the system. The time development of the system is specified by the Schrödinger equation

$$\frac{d}{dt}|\psi(t)\rangle = -\frac{i}{\hbar}\hat{H}|\psi(t)\rangle,$$

where \hat{H} is the Hamiltonian, a Hermitian operator describing the orientation dependence of the interaction energies in the spin system [53]. The corresponding observable is the energy of the system. The energy eigenfunctions of the Hamiltonian are stationary and orthonormal and the eigenvalues, i. e. the energy levels of the spin system, are real values. In the following only the nuclear spin states and the nuclear spin Hamiltonian are considered, assuming that the effects of the rapidly moving electrons are averaged to a mean value, which is stable in time and contributes only a constant portion to the net Hamiltonian [53].

The spin operator and the Zeeman Hamiltonian [17, 53, 54]. The atomic nucleus carries a magnetic dipole moment μ and a spin I . These observables are associated with their quantum-mechanical analogues, the Hermitian operators $\hat{\mu}$ and \hat{I} , which are related to each other via

$$\hat{\mu} = \gamma\hat{I}$$

as in the macroscopic representation. Both operators are vectors with cartesian coordinates $\hat{\mu}_x, \hat{\mu}_y, \hat{\mu}_z$ and $\hat{I}_x, \hat{I}_y, \hat{I}_z$, which are Hermitian, too.

The spin operator \hat{I} , similarly to the orbital angular momentum operator, fulfills the eigenequations

$$\begin{aligned}\hat{I}^2|I, m_I\rangle &= I(I+1)|I, m_I\rangle \text{ and} \\ \hat{I}_z|I, m_I\rangle &= m_I|I, m_I\rangle,\end{aligned}$$

where, $\hat{I}^2 = \hat{I}_x^2 + \hat{I}_y^2 + \hat{I}_z^2$. A detailed description of the orthonormal eigenfunctions $|I, m_I\rangle$ is usually not necessary. From the eigenequations one can learn that the length of the spin vector and one of the components¹ are quantized with the corresponding spin quantum numbers I and m_I . The former can take half-integer numbers (although $I=2$ seems not to occur in nature) and the latter runs from $-I$ to I . The quantum number I is often used to characterize a nucleus, e. g., $I = 1/2$ for so-called spin-1/2 nuclei. Note, that the functions $|I, m_I\rangle$ are no eigenfunctions of the spin operator components \hat{I}_x and \hat{I}_y .

The interaction of the nuclear magnetic dipole moments with a magnetic field of strength B is described by the Zeeman Hamiltonian

$$\hat{H}_0 = -\hbar(\hat{\mu} \cdot \mathbf{B}) = -\hbar\gamma(\hat{I} \cdot \mathbf{B})$$

NMR measurements are usually performed in a strong static magnetic field B_0 , the orientation of which is chosen to be in z direction of the cartesian coordinate system,

¹Here, we chose the z component as it is usually done in literature.

so that

$$\hat{H}_0 = -\gamma B_0 \hbar \hat{I}_z = -\omega_0 \hbar \hat{I}_z .$$

As the Zeeman Hamiltonian is proportional to \hat{I}_z , both operators share the same eigenfunctions $|I, m_I\rangle$, forming the so-called orthogonal Zeeman eigenbasis. The energy eigenvalues of the Hamiltonian can be found from

$$\hat{H}_0 |I, m_I\rangle = -\gamma \hbar B_0 \hat{I}_z |I, m_I\rangle = -\gamma B_0 \hbar m_I |I, m_I\rangle = -\omega_0 \hbar m_I |I, m_I\rangle = E_{I,m} |I, m_I\rangle ,$$

adopting values $E_{I,m} = -\hbar\omega_0 m_I$. Here, we find a splitting of energy levels, the Zeeman splitting, according to the value of the quantum number m_I . The energy gap between the Zeeman energy levels amounts to $\hbar\omega_0 \approx h \cdot 20 \text{ MHz} \approx 1.3 \cdot 10^{-26} \text{ J}$, which is very small compared to the thermal energy at 25°C ($\sim 4.1 \cdot 10^{-21} \text{ J}$).

A nucleus in the magnetic field does not have to be in an eigenstate of \hat{H}_0 and \hat{I}_z . In general it adopts a normalized superposition state, i. e. a linear combination of eigenstates:

$$|\psi\rangle = \sum_j \alpha_j |I_j, m_{I,j}\rangle ,$$

where the prefactors α_j specify the actual spin state [53].

Measurements of the observable of a quantum-mechanical operator (e. g., the energy of the spin system) always yield an eigenvalue of the corresponding operator. However, it is not known a priori which of them, i. e. the observable is not well-defined. The result of a measurement is governed by statistics and one can only calculate a probability to find a certain eigenvalue, when the system is in the state $|\psi\rangle$. (This probability amounts to 100%, when $|\psi\rangle$ is the corresponding eigenstate.) Moreover, the mean result after a high number of measurements, i. e. the expectation value, can be derived. As superposition states are no eigenstates of \hat{I}_z and \hat{H}_0 they do not have well-defined energies (and spin components in z direction) and cannot be depicted in an energy level diagram. Nevertheless they are real states [53].

The polarization axis of a spin denotes the direction in space, along which the spin is well-defined, i. e. the direction of a spin operator component, for which the present spin state is an eigenstate. This component is not necessarily a cartesian one, but a linear combination of them. As every orientation in space is related to such a component of \hat{I} , possessing an arbitrary superposition state as an eigenstate, the polarization axis can take every direction [53].² This axis is the quantum-mechanical analogue of the direction of the spin vector in the macroscopic representation and one can, e. g., show, that it precesses about B_0 by solving the Schrödinger equation (see above) for a spin in a superposition state with the Zeeman Hamiltonian describing the interaction with B_0 [53].

The Spin Density Operator and its Time Development. For the calculation of macroscopic properties of the spin system, one can in principle sum up the individual quantities of all spins in the system. However, this is cumbersome and often not possible

²The often used representation of the spin vector, rotating on the surface of a cone with fixed opening angle, is only a model to explain the quantization of the spin in a descriptive way. It does not reveal any information about the orientation of the spin vector in the magnetic field [53].

at all. For this reason the spin density operator

$$\hat{\rho} = \langle(|\psi\rangle\langle\psi|)\rangle$$

was introduced, which describes the quantum-mechanical state of the whole system as a kind of average spin state and is based on the expectation values of the observables. Here, $|\psi\rangle$ is again the wave function of the spin system and the outer angle brackets denote the average over all members of the spin ensemble [53].

The mean contribution of each individual spin to the macroscopic observable A of an operator \hat{A} is equal to the expectation value

$$\langle\hat{A}\rangle = Tr(\hat{\rho}\hat{A}) . \quad (\text{C.1})$$

Thus, the macroscopic quantity can be evaluated from the corresponding quantum-mechanical operator and the operator $\hat{\rho}$ describing the spin system as a whole.

When writing the density operator in the matrix form, the diagonal elements represent the populations of the eigenstates of \hat{I}_z and the off-diagonal elements are interpreted as coherences between two eigenstates [53].

Every (superposition) spin state comprises certain fractions of the distinct eigenstates. The population of an eigenstate can be understood as the sum of the portions of this eigenstate of all the spins in the system. Populations are positive, real numbers ranging between 0 and 1. Their sum is equal to 1 as a result of the normalization of the spin states. In the macroscopic representation for spins 1/2 the populations are related to the sum of all spin vector components in or opposed to the direction of the magnetic field. Hence, a difference of the eigenstate populations, as present in thermal equilibrium where the populations follow a Boltzmann distribution, results in macroscopic longitudinal magnetization.

Coherences between two eigenstates $|j\rangle$ and $|k\rangle$ are complex numbers which characterize particular states of the spin system. They are specified by the coherence order $o = m_{I,j} - m_{I,k}$, calculated from the quantum numbers of \hat{I}_z . In the thermal equilibrium coherences of order $o \geq 1$ are not available. A coherence of order $o = 1$ is a state of the spin system, where a certain orientation of the spin polarization axes in the transverse plane is preferred, so that transverse magnetization exists. Higher order coherences, i. e. so called multi-quantum coherences, develop under spin interactions, e. g., in dipolarly coupled systems. They are not directly detectable in the form of magnetization. One can imagine such coherences as a correlation of the orientations of spins within a group of interacting spins [53]. In the spin density operator higher order coherences are characterized by distinct products of spin operator components. As an example, the expression $2\hat{I}_{x,j}\hat{I}_{y,k}$ identifies a sum of two coherences with $o = 0$ and $o = 2$, i. e. a zero-quantum and a double-quantum coherence. It describes a situation of pairs of interacting spins j and k , where none of the partners tends to orient in a particular direction, but where the orientation of both partners correlates with each other. When spin j points into $+x$ direction, there is a high probability for spin k to be oriented in $+y$ direction, but still the overall orientation of pairs of spins is isotropic, preventing the build-up of magnetization.

In the thermal equilibrium in the magnetic field and in case of high temperatures,

i. e. when $|\hbar\gamma B_0/kT| \ll 1$ (which is the case for $T \gg 1$ K), the spin density operator is given by

$$\hat{\rho}_{\text{eq}} \sim (1/2)\hat{E} + (1/2)\hat{I}_z\hat{E}.$$

For practical purposes the unity operator \hat{E} is usually skipped as it does not represent detectable transverse magnetization. Also the prefactor is omitted, because it only varies the signal amplitude, which is commonly not of interest. Thus, \hat{I}_z is considered as the equilibrium spin density operator. The measured signal is calculated using Eq. C.1. As an example, for the measured transverse magnetization after a 90° pulse we obtain

$$\langle I_x \rangle = \text{Tr}(\hat{I}_x \hat{\rho}) \sim \text{Tr}(\hat{I}_x \cdot \hat{I}_x) = 1/2.$$

Thus, a signal can be observed in x direction.

The presence of the term \hat{I}_z in the spin density operator indicates longitudinal magnetization M_z according to $M_z \propto \sum_j \mu_{z,j}$ and $\hat{\mu}_{z,j} = \gamma \cdot \hat{I}_{z,j}$. Moreover, terms $\hat{I}_{x,y}$ are related to transverse magnetization.

The time development of the spin density operator is described by the Liouville-van-Neumann equation, a generalized form of the Schrödinger equation, which combines the density operator characterizing the state of spin system and the Hamiltonian specifying the interaction within the system:

$$\frac{d}{dt}\hat{\rho} = -i[\hat{H}, \hat{\rho}] \quad (\text{C.2})$$

If Hamiltonian and density operator commute, the system is time invariant. In case of a time-independent Hamiltonian the expression

$$\hat{\rho}(t) = e^{-i\hat{H}t}\hat{\rho}(0)e^{i\hat{H}t} = \hat{U}(t)\hat{\rho}(0)\hat{U}^{-1}(t)$$

solves the equation. Here, $\hat{U}(t) = e^{-i\hat{H}t}$ denotes the time-development operator or propagator. For a time-dependent Hamiltonian the same solution can be used, if the Hamiltonian can be assumed to be piecewise constant in time:

$$\hat{\rho}(t_1 + t_2 + \dots t_n) = e^{-i\hat{H}_n t_n} \dots e^{-i\hat{H}_2 t_2} e^{-i\hat{H}_1 t_1} \hat{\rho}(0) e^{i\hat{H}_1 t_1} e^{i\hat{H}_2 t_2} \dots e^{i\hat{H}_n t_n}$$

This equation can be applied to calculate the effect of a pulse sequence on the spin system (see Appendices D.1.1, D.1.2 and D.2). Yet, this spin density operator formalism neglects relaxation processes.

Dipolar Couplings and their Effect on the ^1H NMR Signal. The pairwise dipolar spin interactions are considered as a contribution \hat{H}_D to the full Hamiltonian of the spin system

$$\hat{H} = \hat{H}_0 + \hat{H}_D.$$

In its general form H_D reads [17]

$$\hat{H}_D = \frac{\mu_0}{4\pi} \hbar^2 \sum_k \sum_j^{k-1} \gamma_j \gamma_k \frac{1}{r_{jk}^3} \left(\hat{I}_j \cdot \hat{I}_k - \frac{3}{r_{jk}^2} (\hat{I}_j \cdot \mathbf{r}_{jk})(\hat{I}_k \cdot \mathbf{r}_{jk}) \right),$$

with $\hat{I}_{j,k}$ and $\gamma_{j,k}$ denoting spin operators and the magnetogyric ratios of the coupling spins and \mathbf{r}_{jk} being the spin-spin interconnection vector. For two proton spins I_1 and I_2 with magnetogyric ratio γ and the interconnection vector \mathbf{r} we find

$$\hat{H}_D = \frac{\mu_0}{4\pi} \hbar^2 \gamma^2 \frac{1}{r^3} \left(\hat{\mathbf{I}}_1 \cdot \hat{\mathbf{I}}_2 - \frac{3}{r^2} (\hat{\mathbf{I}}_1 \cdot \mathbf{r})(\hat{\mathbf{I}}_2 \cdot \mathbf{r}) \right). \quad (\text{C.3})$$

By inserting the scalar products

$$\begin{aligned} \hat{\mathbf{I}}_1 \cdot \hat{\mathbf{I}}_2 &= \begin{pmatrix} \hat{I}_{1x} \\ \hat{I}_{1y} \\ \hat{I}_{1z} \end{pmatrix} \cdot \begin{pmatrix} \hat{I}_{2x} \\ \hat{I}_{2y} \\ \hat{I}_{2z} \end{pmatrix} = \hat{I}_{1x}\hat{I}_{2x} + \hat{I}_{1y}\hat{I}_{2y} + \hat{I}_{1z}\hat{I}_{2z} \\ \hat{\mathbf{I}}_{1/2} \cdot \hat{\mathbf{r}} &= \begin{pmatrix} \hat{I}_{1x/2x} \\ \hat{I}_{1y/2y} \\ \hat{I}_{1z/2z} \end{pmatrix} \cdot \begin{pmatrix} r \cos \varphi \sin \vartheta \\ r \sin \varphi \sin \vartheta \\ r \cos \vartheta \end{pmatrix} = r \left((\hat{I}_{1x/2x} \cos \varphi + \hat{I}_{1y/2y} \sin \varphi) \sin \vartheta + \hat{I}_{1z/2z} \cos \vartheta \right) \end{aligned}$$

into Eq. C.3 and using the shift operators

$$\begin{aligned} \hat{I}_{1+2+} &= \hat{I}_{1x/2x} + i\hat{I}_{1y/2y} & \text{and} \\ \hat{I}_{1-2-} &= \hat{I}_{1x/2x} - i\hat{I}_{1y/2y} \end{aligned}$$

the interaction Hamiltonian can be expressed as [58, 70]

$$\begin{aligned} \hat{H}_D &= \frac{\mu_0}{4\pi} \hbar^2 \gamma^2 \frac{1}{r^3} \left(\hat{I}_{1x}\hat{I}_{2x} + \hat{I}_{1y}\hat{I}_{2y} + \hat{I}_{1z}\hat{I}_{2z} \right. \\ &\quad \left. - 3 \left(\frac{1}{2}(\hat{I}_{1+}e^{-i\varphi} + \hat{I}_{1-}e^{i\varphi}) \sin \vartheta + \hat{I}_{1z} \cos \vartheta \right) \left(\frac{1}{2}(\hat{I}_{2+}e^{-i\varphi} + \hat{I}_{2-}e^{i\varphi}) \sin \vartheta + \hat{I}_{2z} \cos \vartheta \right) \right) \\ &= \frac{\mu_0}{4\pi} \hbar^2 \gamma^2 \frac{1}{r^3} (A + B + C + D + E + F) \end{aligned}$$

with

$$\begin{aligned} A &= (1 - 3 \cos^2 \vartheta) \hat{I}_{1z} \hat{I}_{2z}, \\ B &= -\frac{1}{4} (1 - 3 \cos^2 \vartheta) \left(\hat{I}_{1+} \hat{I}_{2-} + \hat{I}_{1-} \hat{I}_{2+} \right) = -\frac{1}{2} (1 - 3 \cos^2 \vartheta) \left(\hat{\mathbf{I}}_1 \cdot \hat{\mathbf{I}}_2 - \hat{I}_{1z} \hat{I}_{2z} \right), \\ C &= -\frac{3}{2} e^{-i\varphi} \sin \vartheta \cos \vartheta \left(\hat{I}_{1+} \hat{I}_{2z} + \hat{I}_{1z} \hat{I}_{2+} \right), \\ D &= -\frac{3}{2} e^{i\varphi} \sin \vartheta \cos \vartheta \left(\hat{I}_{1-} \hat{I}_{2z} + \hat{I}_{1z} \hat{I}_{2-} \right), \\ E &= -\frac{3}{4} e^{-2i\varphi} \sin^2 \vartheta \left(\hat{I}_{1+} \hat{I}_{2+} \right) \quad \text{and} \\ F &= -\frac{3}{4} e^{2i\varphi} \sin^2 \vartheta \left(\hat{I}_{1-} \hat{I}_{2-} \right). \end{aligned}$$

Compared to the external static magnetic field the local fields arising from the dipolar couplings are small. As those parts of the perturbing Hamiltonian \hat{H}_D , which do not commute with the Zeeman Hamiltonian \hat{H}_0 , have almost no influence on the energy levels of the spin system and the NMR signal, it is, in most cases, sufficient to retain only the secular (or adiabatic) part of \hat{H}_D , i. e. the commuting part, while the rest is neglected. This proceeding is called high-field truncation or secular approximation.

The time-dependent non-secular interaction terms of \hat{H}_D , are meaningful for relaxation processes [53].

Here, only the expressions A and B commute with the Zeeman Hamiltonian $\hat{H}_0 = -\gamma B_0 (\hat{I}_{1z} + \hat{I}_{2z})$:

$$\begin{aligned} A &: [\hat{I}_{1z} + \hat{I}_{2z}, \hat{I}_{1z}\hat{I}_{2z}] = 0 \\ B &: [\hat{I}_{1z} + \hat{I}_{2z}, \hat{I}_{1x}\hat{I}_{2x} + \hat{I}_{1y}\hat{I}_{2y}] = 0 \\ C &: [\hat{I}_{1z} + \hat{I}_{2z}, \hat{I}_{1+}\hat{I}_{2z} + \hat{I}_{1z}\hat{I}_{2+}] = \hat{I}_{1+}\hat{I}_{2z} + \hat{I}_{1z}\hat{I}_{2+} \neq 0 \\ D &: [\hat{I}_{1z} + \hat{I}_{2z}, \hat{I}_{1-}\hat{I}_{2z} + \hat{I}_{1z}\hat{I}_{2-}] = -\hat{I}_{1-}\hat{I}_{2z} - \hat{I}_{1z}\hat{I}_{2-} \neq 0 \\ E &: [\hat{I}_{1z} + \hat{I}_{2z}, \hat{I}_{1+}\hat{I}_{2+}] = 2\hat{I}_{1+}\hat{I}_{2+} \neq 0 \\ F &: [\hat{I}_{1z} + \hat{I}_{2z}, \hat{I}_{1-}\hat{I}_{2-}] = -2\hat{I}_{1-}\hat{I}_{2-} \neq 0 \end{aligned}$$

Therefore the truncated Hamiltonian only contains term A and B [58]:

$$\begin{aligned} \hat{H}_D &= \frac{\mu_0}{4\pi} \hbar^2 \gamma^2 \frac{1}{r^3} \left((1 - 3 \cos^2 \vartheta) \left(\hat{I}_{1z}\hat{I}_{2z} - \frac{1}{2}\hat{I}_{1x}\hat{I}_{2x} - \frac{1}{2}\hat{I}_{1y}\hat{I}_{2y} \right) \right) \\ &= \omega_D \left(3\hat{I}_{1z}\hat{I}_{2z} - \hat{\mathbf{I}}_1 \cdot \hat{\mathbf{I}}_2 \right) \end{aligned}$$

Here,

$$\omega_D = -\frac{\mu_0}{4\pi} \hbar \frac{\gamma^2}{r^3} \frac{1}{2} (3 \cos^2 \vartheta - 1)$$

designates the dipolar coupling strength. It is approximately a factor of 1000 smaller than the Zeeman splitting.

To describe effects of dipolar couplings on the ^1H NMR signal we consider a system of isolated pairs of spins 1 and 2, with $I_1 = I_2 = 1/2$. A suited set of orthonormal eigenfunctions for the z component of the spin operator $\hat{I}_z = \hat{I}_{1,z} + \hat{I}_{2,z}$ is given by the Zeeman product basis [53]

$$\begin{aligned} |\alpha\alpha\rangle &= |\alpha\rangle \cdot |\alpha\rangle = \left| \frac{1}{2}, \frac{1}{2} \right\rangle \cdot \left| \frac{1}{2}, \frac{1}{2} \right\rangle \\ |\alpha\beta\rangle &= |\alpha\rangle \cdot |\beta\rangle = \left| \frac{1}{2}, \frac{1}{2} \right\rangle \cdot \left| \frac{1}{2}, -\frac{1}{2} \right\rangle \\ |\beta\alpha\rangle &= |\beta\rangle \cdot |\alpha\rangle = \left| \frac{1}{2}, -\frac{1}{2} \right\rangle \cdot \left| \frac{1}{2}, \frac{1}{2} \right\rangle \\ |\beta\beta\rangle &= |\beta\rangle \cdot |\beta\rangle = \left| \frac{1}{2}, -\frac{1}{2} \right\rangle \cdot \left| \frac{1}{2}, -\frac{1}{2} \right\rangle \end{aligned}$$

Here, $|\alpha\rangle = |I = 1/2, m_I = 1/2\rangle$ and $|\beta\rangle = |I = 1/2, m_I = -1/2\rangle$ are the eigenfunctions of \hat{I}_z for an isolated spin with $I = 1/2$. \hat{I}_{1z} and \hat{I}_{2z} act on the first and on the second function in the eigenfunction products, respectively. The product functions are eigenstates of the Zeeman Hamiltonian

$$\hat{H}_0 = \omega_{0,1}\hat{I}_{1z} + \omega_{0,2}\hat{I}_{2z} = \omega_0(\hat{I}_{1z} + \hat{I}_{2z})$$

for two magnetically equivalent nuclei, but not for the complete Hamiltonian of the

system

$$\hat{H} = \hat{H}_0 + \hat{H}_D = -\omega_0(\hat{I}_{1z} + \hat{I}_{2z}) + \omega_D(3\hat{I}_{1z}\hat{I}_{2z} - \hat{\mathbf{I}}_1 \cdot \hat{\mathbf{I}}_2)$$

This is indicated by non-zero off-diagonal elements of the Hamiltonian \hat{H} in the matrix representation in the Zeeman product basis, the values of which depend on ω_D . However, \hat{H} can be diagonalized by means of four corresponding eigenfunctions:

$$\begin{aligned} |T_{-1}\rangle &= |\alpha\alpha\rangle \\ |T_0\rangle &= \frac{1}{\sqrt{2}}(|\alpha\beta\rangle + |\beta\alpha\rangle) \\ |T_{+1}\rangle &= |\beta\beta\rangle \\ |S_0\rangle &= \frac{1}{\sqrt{2}}(|\alpha\beta\rangle - |\beta\alpha\rangle) \end{aligned}$$

The states $|T_{-1,0,1}\rangle$ are named triplet states. Using these functions, the spin operators $\hat{I}_x = \hat{I}_{1x} + \hat{I}_{2x}$, $\hat{I}_y = \hat{I}_{1y} + \hat{I}_{2y}$ and $\hat{I}_z = \hat{I}_{1z} + \hat{I}_{2z}$ fulfill the same eigenequations as given for a system of isolated spins with $I = 1$. For the singlet state $|S_0\rangle$ and the same operators we find the eigenvalues $I = m_I = 0$. Thus, two dipolarly coupled, magnetically equivalent spin-1/2 nuclei behave as two separate spins, one with $I = 1$ (triplet states) and another one with $I = 0$ (singlet state). The latter is usually neglected, as it does not interact with the magnetic field. The energy levels of the triplet states as read from the diagonalized Hamiltonian \hat{H} amount to

$$\begin{aligned} E_{-1} &= \omega_0 + \frac{\omega_D}{2} \\ E_0 &= -\omega_D \\ E_{+1} &= -\omega_0 + \frac{\omega_D}{2} . \end{aligned}$$

In the NMR signal two spectral lines arise at positions ω corresponding to the transition frequencies between these levels

$$\omega = \omega_0 \pm (3/2)\omega_D$$

with a line distance of $3\omega_D$ (see Fig. 3.3).

In a real system molecular motions may cause an averaging of the dipolar couplings and the spin orientations vary from spin pair to spin pair. Thus, the spectral lines appear at

$$\omega = \omega_0 \pm \frac{3}{2} \langle \omega_D \rangle_{t,N} = \omega_0 \pm \frac{3}{2} \left(-\frac{\mu_0}{4\pi} \right) \hbar \gamma^2 \frac{1}{2} \left\langle \left(\frac{3 \cos^2 \vartheta - 1}{r^3} \right) \right\rangle_{t,N}$$

where $\langle \dots \rangle_{t,N}$ designates the time and ensemble average. In a powder sample the spin pairs are oriented isotropically. Depending on the angle ϑ different positions of the line doublet are found in the spectrum (see Fig. 3.3). These doublets superpose each other, thus forming a broad line with a characteristic shape, the so-called Pake pattern [17]. The angle ϑ is not equally distributed in a powder sample, but it follows a distribution function $P(\vartheta) = \sin \vartheta$ [53]. The highest signal intensity is found for $\vartheta = 90^\circ$, as there is a multitude of possible orientations of spin pairs with the interconnection vector perpendicular to B_0 . Yet, only two spin pair orientations fulfill the condition $\vartheta = 0$. Thus, the intensity is low for this case.

The powder average of the NMR time-domain signal (FID)

$$M_x(t) = \langle M_x(\omega_0 + (3/2)\omega_D) + M_x(\omega_0 - (3/2)\omega_D) \rangle_{\vartheta} = \langle e^{i(\omega_0 + (3/2)\omega_D)t} + e^{i(\omega_0 - (3/2)\omega_D)t} \rangle_{\vartheta}$$

is calculated by averaging over all possible spin pair orientations ϑ under consideration of the angular distribution function $\sin \vartheta$. Fourier transformation of this signal yields the Pake pattern (see Fig. 3.3). The FID of a powder sample of dipolarly coupled spins decreases much faster than the one of a non-coupled system as a result of the superposition of different signal contributions with different signal frequencies. This decay induced by dipolar couplings can be refocused due to the fixed relation between the different frequency contributions. By contrast a decay caused by molecular motions is not refocusable as the frequencies change in a random manner.

The frequency distance $\Delta\omega$ between the two horns of the Pake pattern depends on the distance r between the coupled spins (see Fig. 3.3). However, molecular motions on the NMR time scale may lead to averaged, i. e. reduced dipolar couplings and smaller splittings in the Pake pattern. In the limit of fast and isotropic motions the couplings are averaged out completely [53] as

$$\int_0^{\pi} (3 \cos^2 \vartheta - 1) \sin(\vartheta) d\vartheta = \int_{-1}^1 (3x^2 - 1) dx = 0$$

and a single narrow line at the isotropic chemical shift results. Furthermore, in a real sample the Pake Pattern is often 'washed out' leaving spectra with rather Gaussian or Abragam shape.

D. Demonstration of the Effect of Diverse Pulse Sequences

D.1. Average Hamiltonian Theory for Calculating the Mode of Action of Pulse Sequences

Average Hamiltonian Theory was introduced by Haeberlen und Waugh in 1968 [322] and is helpful for understanding the mode of operation of miscellaneous NMR experiments. It can be applied for pulse sequences, in which the strength of the rf pulses averaged over the duration of the sequence is much higher than the strength of the local fields 'sensed' by the nuclear spins, e. g. the dipolar coupling strength and the resonance offset. If this is the case, the effect of the local-field Hamiltonians on the spin system can be calculated approximatively in terms of a simple (zeroth order) Average Hamiltonian [17]. For this purpose the propagator $\hat{U} = e^{-i\hat{H}(t)t}$ of the pulse sequence is examined, which describes the time development of the spin system and depends on the Hamiltonian $\hat{H}(t)$ as a measure of the interactions in and the manipulations of the spin system. The effect of rf pulses in the sequence is considered by changing the coordinate system to a frame which compared to the rotating frame (see NMR textbooks) is tilted about the axis of the pulse irradiation by the pulse angle. In this so-called toggling frame the pulse action vanishes and only internal spin interactions remain, whose effects can be evaluated approximatively [17].

D.1.1. The Magic Sandwich Echo

Here, the effect of the Magic Sandwich Echo (MSE) sequence shall be demonstrated using Average Hamiltonian Theory, first for a sequence containing long burst pulses in the sandwich part [80, 85], and second for the pulsed and mixed version applied in the measurements for this thesis (see Fig. D.1). The considerations will be performed for a system of isolated pairs of spins $I_1 = I_2 = 1/2$, interacting via dipolar couplings.

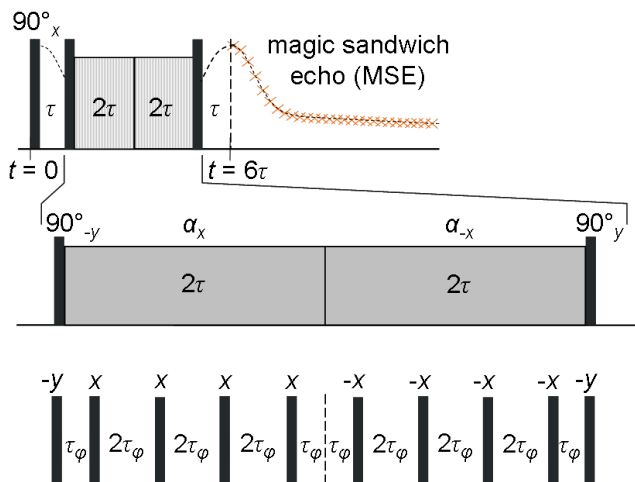


Figure D.1.: Pulse sequence assumed for demonstrating the formation of the Magic Sandwich Echo (MSE). The middle row depicts a 'sandwich part' containing two burst pulses of length 2τ , while the lower row illustrates the pulsed and mixed MSE version consisting of ten 90° pulses (see Section 4.2).

As usual, one assumes that before the application of the pulse sequence the system is in the Boltzmann equilibrium, i. e. in an approximation the spin density operator at time $t = 0$ is given by $\hat{\rho}(0) = \hat{I}_{1z} + \hat{I}_{2z}$ (see Appendix C). The state of the spin system after application of the sequence at time $t = 6\tau$ is described by $\hat{\rho}(6\tau) = \hat{U}(6\tau)\hat{\rho}(0)\hat{U}^{-1}(6\tau)$. The propagator $\hat{U}(6\tau)$ of the sequence can be written as a product of contributions from

all time intervals, during which internal interactions within the spin system take place, and all pulses of the sequence in reversed chronological order. Here, we suppose that the Hamiltonian of the sequence is piecewise constant. The spins of the system shall be subject to pairwise dipolar couplings, described by the truncated dipolar Hamiltonian

$$\hat{H}_D = \omega_D \left(3\hat{I}_{1z}\hat{I}_{2z} - \hat{\mathbf{I}}_1 \cdot \hat{\mathbf{I}}_2 \right)$$

as deduced in Appendix C. The propagator contribution of time intervals t_D in the sequence, during which dipolar couplings are active, is

$$\hat{U}_D = e^{-i\hat{H}_D t_D} .$$

In the following we assume that rf pulses are defined referring to the rotating frame [54]. The action of rf pulses can be specified by the Hamiltonian

$$\hat{H}_P = -\omega_1 \left[(\hat{I}_{1x} \cos \varphi + \hat{I}_{1y} \sin \varphi) + (\hat{I}_{2x} \cos \varphi + \hat{I}_{2y} \sin \varphi) \right]$$

with the pulse phase φ , the nutation frequency ω_1 and the pulse duration t_P [54]. Thus, the corresponding propagator contribution reads

$$\hat{U}_P = \hat{P} = e^{-i\phi((\hat{I}_{1x} \cos \varphi + \hat{I}_{1y} \sin \varphi) + (\hat{I}_{2x} \cos \varphi + \hat{I}_{2y} \sin \varphi))} .$$

Here, $\phi = \omega_1 t_P$ denotes the angle the magnetization is flipped about when applying the rf pulse. (E. g., for a $(\pi/2)_x$ pulse $\phi = \pi/2$ and $\varphi = 0$.)

This form of \hat{P} is based on the assumption that the rf pulses in the sequence exhibit negligible length compared to the intervals between them and that they are strong compared to the dipolar coupling interaction, so that the action of the dipolar couplings during the pulse irradiation can be disregarded. However, this is not possible, when burst pulses are applied. In this case, the propagator has to account for pulse irradiation and dipolar couplings at once:

$$\hat{P} = e^{-i\hat{H}_D t_P - i\phi((\hat{I}_{1x} \cos \varphi + \hat{I}_{1y} \sin \varphi) + (\hat{I}_{2x} \cos \varphi + \hat{I}_{2y} \sin \varphi))} .$$

Now, the propagator \hat{P} for the complete sequence (cf. middle row in Fig. D.1) can be written as

$$\begin{aligned} \hat{U}(6\tau) &= e^{-i\hat{H}_D \tau} e^{-i\frac{\pi}{2}(\hat{I}_{1y} + \hat{I}_{2y})} e^{-i\hat{H}_D 2\tau + i\omega_1 2\tau(\hat{I}_{1x} + \hat{I}_{2x})} \\ &\quad \times e^{-i\hat{H}_D 2\tau - i\omega_1 2\tau(\hat{I}_{1x} + \hat{I}_{2x})} e^{+i\frac{\pi}{2}(\hat{I}_{1y} + \hat{I}_{2y})} e^{-i\hat{H}_D \tau} \\ &\quad \times e^{-i\frac{\pi}{2}(\hat{I}_{1x} + \hat{I}_{2x})} \end{aligned} \quad (\text{D.1})$$

The transition into the toggling frame is performed by inserting unity operators $\hat{E} = \hat{P}_{\pm\alpha}^{-1} \hat{P}_{\pm\alpha}$ at suitable positions in Eq. D.1 [322]. Here, α denotes the pulse irradiation axis. Now, one can take advantage of the exponential relation

$$\hat{P}_{\pm\alpha} e^{-i\hat{H}_D t} \hat{P}_{\pm\alpha}^{-1} = e^{\mp i\phi \hat{I}_\alpha} e^{-i\hat{H}_D t} e^{\pm i\phi \hat{I}_\alpha} = e^{-it(e^{\mp i\phi \hat{I}_\alpha} \hat{H}_D e^{\pm i\phi \hat{I}_\alpha})} = e^{-it\hat{P}_{\pm\alpha} \hat{H}_D \hat{P}_{\pm\alpha}^{-1}} = e^{-i\hat{H}'_D t} \quad (\text{D.2})$$

The product in the exponent can be understood as a rotation of the Hamiltonian \hat{H}_D

about the axis of the pulse irradiation by the flip angle ϕ , which is equivalent to a rotation of the coordinate system about the same axis by $-\phi$. As a result, this rotation yields the same Hamiltonian, but observed from the tilted frame, i. e. the toggling frame Hamiltonian \hat{H}'_D .¹ This procedure is repeated in order to eliminate the effect of the rf pulses, leaving a toggling frame Hamiltonian, which depends on the spin interactions only (cf. Ref. [54]).

By inserting the unity operator $\hat{E} = e^{-i\omega_1 2\tau(\hat{I}_{1x} + \hat{I}_{2x})} e^{i\omega_1 2\tau(\hat{I}_{1x} + \hat{I}_{2x})}$ after the second, third and fourth exponential term in Eq. D.1 one obtains

$$\begin{aligned} \hat{U}(6\tau) &= e^{-i\hat{H}_D\tau} e^{-i\frac{\pi}{2}(\hat{I}_{1y} + \hat{I}_{2y})} e^{-i\omega_1 2\tau(\hat{I}_{1x} + \hat{I}_{2x})} \\ &\quad \times e^{i\omega_1 2\tau(\hat{I}_{1x} + \hat{I}_{2x})} e^{-i\hat{H}_D 2\tau + i\omega_1 2\tau(\hat{I}_{1x} + \hat{I}_{2x})} e^{-i\omega_1 2\tau(\hat{I}_{1x} + \hat{I}_{2x})} \\ &\quad \times e^{i\omega_1 2\tau(\hat{I}_{1x} + \hat{I}_{2x})} e^{-i\hat{H}_D 2\tau - i\omega_1 2\tau(\hat{I}_{1x} + \hat{I}_{2x})} e^{-i\omega_1 2\tau(\hat{I}_{1x} + \hat{I}_{2x})} \\ &\quad \times e^{i\omega_1 2\tau(\hat{I}_{1x} + \hat{I}_{2x})} e^{+i\frac{\pi}{2}(\hat{I}_{1y} + \hat{I}_{2y})} e^{-i\hat{H}_D\tau} e^{-i\frac{\pi}{2}(\hat{I}_{1x} + \hat{I}_{2x})}. \end{aligned} \quad (\text{D.3})$$

Now, the two central product terms arising from the burst pulses can be analyzed further using Eq. D.2:

$$\begin{aligned} e^{i\omega_1 2\tau(\hat{I}_{1x} + \hat{I}_{2x})} e^{-i\hat{H}_D 2\tau \pm i\omega_1 2\tau(\hat{I}_{1x} + \hat{I}_{2x})} e^{-i\omega_1 2\tau(\hat{I}_{1x} + \hat{I}_{2x})} \\ = e^{e^{i\omega_1 2\tau(\hat{I}_{1x} + \hat{I}_{2x})} (-i\hat{H}_D 2\tau \pm i\omega_1 2\tau(\hat{I}_{1x} + \hat{I}_{2x}))} e^{-i\omega_1 2\tau(\hat{I}_{1x} + \hat{I}_{2x})} \end{aligned}$$

where

$$\begin{aligned} e^{i\omega_1 2\tau(\hat{I}_{1x} + \hat{I}_{2x})} (-i\hat{H}_D 2\tau \pm i\omega_1 2\tau(\hat{I}_{1x} + \hat{I}_{2x})) e^{-i\omega_1 2\tau(\hat{I}_{1x} + \hat{I}_{2x})} \\ = -i2\tau e^{i\omega_1 2\tau(\hat{I}_{1x} + \hat{I}_{2x})} \hat{H}_D e^{-i\omega_1 2\tau(\hat{I}_{1x} + \hat{I}_{2x})} \pm i\omega_1 2\tau e^{i\omega_1 2\tau(\hat{I}_{1x} + \hat{I}_{2x})} (\hat{I}_{1x} + \hat{I}_{2x}) e^{-i\omega_1 2\tau(\hat{I}_{1x} + \hat{I}_{2x})} \\ = -i2\tau e^{i\omega_1 2\tau(\hat{I}_{1x} + \hat{I}_{2x})} \hat{H}_D e^{-i\omega_1 2\tau(\hat{I}_{1x} + \hat{I}_{2x})} \pm i\omega_1 2\tau (\hat{I}_{1x} + \hat{I}_{2x}). \end{aligned}$$

By inserting the Hamiltonian \hat{H}_D one finds for the first term in this sum

$$\begin{aligned} -i2\tau e^{i\omega_1 2\tau(\hat{I}_{1x} + \hat{I}_{2x})} \hat{H}_D e^{-i\omega_1 2\tau(\hat{I}_{1x} + \hat{I}_{2x})} \\ = -i2\tau\omega_D \left[e^{i\omega_1 2\tau(\hat{I}_{1x} + \hat{I}_{2x})} \left(3\hat{I}_{1z}\hat{I}_{2z} - \hat{\mathbf{I}}_1 \cdot \hat{\mathbf{I}}_2 \right) e^{-i\omega_1 2\tau(\hat{I}_{1x} + \hat{I}_{2x})} \right] \\ = -i2\tau\omega_D \left[e^{i\omega_1 2\tau(\hat{I}_{1x} + \hat{I}_{2x})} \left(3\hat{I}_{1z}\hat{I}_{2z} \right) e^{-i\omega_1 2\tau(\hat{I}_{1x} + \hat{I}_{2x})} \right. \\ \quad \left. - e^{i\omega_1 2\tau(\hat{I}_{1x} + \hat{I}_{2x})} \left(\hat{\mathbf{I}}_1 \cdot \hat{\mathbf{I}}_2 \right) e^{-i\omega_1 2\tau(\hat{I}_{1x} + \hat{I}_{2x})} \right] \quad (\text{D.4}) \\ = -i2\tau\omega_D \left[3 \left(\hat{I}_{1z} \cos(\omega_1 2\tau) + \hat{I}_{1y} \sin(\omega_1 2\tau) \right) \left(\hat{I}_{2z} \cos(\omega_1 2\tau) + \hat{I}_{2y} \sin(\omega_1 2\tau) \right) \right. \\ \quad \left. - \left(\hat{\mathbf{I}}_1 \cdot \hat{\mathbf{I}}_2 \right) \right] \\ = -i2\tau\omega_D \hat{H}'_D. \end{aligned}$$

Here, we used

$$[\hat{I}_{1x} + \hat{I}_{2x}, \hat{\mathbf{I}}_1 \cdot \hat{\mathbf{I}}_2] = 0$$

¹The coordinate system, which moves according to the action of the pulses, is usually called interaction representation [54]. In case of continuous irradiation the toggling frame rotates continuously and is named doubly-rotating frame.

and exploited the sandwich relation [53]

$$e^{-i\beta\hat{A}}\hat{B}e^{i\beta\hat{A}} = \hat{B}\cos(n\beta) + \hat{C}\sin(n\beta) \quad (\text{D.5})$$

for two operators \hat{A} and \hat{B} , which is valid provided that

$$[\hat{A}, \hat{B}] = in\hat{C} \text{ and } [\hat{A}, \hat{C}] = -in\hat{B}.$$

Thus, we found

$$\begin{aligned} & e^{i\omega_1 2\tau(\hat{I}_{1x} + \hat{I}_{2x})} \left(\hat{I}_{1z} \hat{I}_{2z} \right) e^{-i\omega_1 2\tau(\hat{I}_{1x} + \hat{I}_{2x})} \\ &= e^{i\omega_1 2\tau \hat{I}_{1x}} e^{i\omega_1 2\tau \hat{I}_{2x}} \left(\hat{I}_{1z} \hat{I}_{2z} \right) e^{-i\omega_1 2\tau \hat{I}_{2x}} e^{-i\omega_1 2\tau \hat{I}_{1x}} \\ &= e^{i\omega_1 2\tau \hat{I}_{1x}} \left(\hat{I}_{1z} \hat{I}_{2z} \cos(\omega_1 2\tau) + \hat{I}_{1z} \hat{I}_{2y} \sin(\omega_1 2\tau) \right) e^{-i\omega_1 2\tau \hat{I}_{1x}} \\ &= e^{i\omega_1 2\tau \hat{I}_{1x}} \left(\hat{I}_{1z} \hat{I}_{2z} \cos(\omega_1 2\tau) \right) e^{-i\omega_1 2\tau \hat{I}_{1x}} + e^{i\omega_1 2\tau \hat{I}_{1x}} \left(\hat{I}_{1z} \hat{I}_{2y} \sin(\omega_1 2\tau) \right) e^{-i\omega_1 2\tau \hat{I}_{1x}} \\ &= \cos(\omega_1 2\tau) \left(\hat{I}_{1z} \hat{I}_{2z} \cos(\omega_1 2\tau) + \hat{I}_{1y} \hat{I}_{2z} \sin(\omega_1 2\tau) \right) + \sin(\omega_1 2\tau) \left(\hat{I}_{1z} \hat{I}_{2y} \cos(\omega_1 2\tau) + \hat{I}_{1y} \hat{I}_{2y} \sin(\omega_1 2\tau) \right) \\ &= \left(\hat{I}_{1z} \cos(\omega_1 2\tau) + \hat{I}_{1y} \sin(\omega_1 2\tau) \right) \left(\hat{I}_{2z} \cos(\omega_1 2\tau) + \hat{I}_{2y} \sin(\omega_1 2\tau) \right). \end{aligned}$$

The toggling frame dipolar Hamiltonian \hat{H}'_D in Eq. D.4 can be averaged over the duration of the burst pulses:

$$\begin{aligned} \langle \hat{H}'_D \rangle &= \frac{1}{\omega_1 2\tau} \int_0^{\omega_1 2\tau} \omega_D \left[3 \left(\hat{I}_{1z} \cos(x) + \hat{I}_{1y} \sin(x) \right) \right. \\ &\quad \left. \times \left(\hat{I}_{2z} \cos(x) + \hat{I}_{2y} \sin(x) \right) - \hat{\mathbf{I}}_1 \cdot \hat{\mathbf{I}}_2 \right] dx \\ &= \frac{\omega_D}{\omega_1 2\tau} \left[\int_0^{\omega_1 2\tau} 3\hat{I}_{1z}\hat{I}_{2z} \cos^2(x) dx + \int_0^{\omega_1 2\tau} 3(\hat{I}_{1z}\hat{I}_{2y} + \hat{I}_{1y}\hat{I}_{2z}) \sin(x) \cos(x) dx \right. \\ &\quad \left. + \int_0^{\omega_1 2\tau} 3\hat{I}_{1y}\hat{I}_{2y} \sin^2(x) dx - \int_0^{\omega_1 2\tau} \hat{\mathbf{I}}_1 \cdot \hat{\mathbf{I}}_2 dx \right]. \end{aligned} \quad (\text{D.6})$$

If the flip angle of the burst pulses is a multiple of 2π , i. e. $\omega_1 2\tau = 2\pi n$ or in the limit of very long pulses ($2\tau \rightarrow \infty$), due to the boundedness of the sine and cosine terms in Eq. D.6 solving the integrals results in

$$\begin{aligned} \langle \hat{H}'_D \rangle &= \frac{\omega_D}{2} \left(3\hat{I}_{1z}\hat{I}_{2z} + 3\hat{I}_{1y}\hat{I}_{2y} - 2\hat{\mathbf{I}}_1 \cdot \hat{\mathbf{I}}_2 \right) \\ &= -\frac{\omega_D}{2} \left(3\hat{I}_{1x}\hat{I}_{2x} - \hat{\mathbf{I}}_1 \cdot \hat{\mathbf{I}}_2 \right) \\ &= -\frac{1}{2} \hat{H}_{D,x} \end{aligned} \quad (\text{D.7})$$

by considering the scalar product $\hat{\mathbf{I}}_1 \cdot \hat{\mathbf{I}}_2 = \hat{I}_{1x}\hat{I}_{2x} + \hat{I}_{1y}\hat{I}_{2y} + \hat{I}_{1z}\hat{I}_{2z}$.

Using this effective dipolar Hamiltonian $\langle \hat{H}'_D \rangle$, the propagator of the sequence (Eq. D.3)

amounts to

$$\begin{aligned}\hat{U}(6\tau) &= e^{-i\hat{H}_D\tau} e^{-i\frac{\pi}{2}(\hat{I}_{1y}+\hat{I}_{2y})} e^{-i\omega_1 2\tau(\hat{I}_{1x}+\hat{I}_{2x})} \\ &\quad \times e^{i\frac{1}{2}\hat{H}_{D,x}2\tau+i\omega_1 2\tau(\hat{I}_{1x}+\hat{I}_{2x})} \\ &\quad \times e^{i\frac{1}{2}\hat{H}_{D,x}2\tau-i\omega_1 2\tau(\hat{I}_{1x}+\hat{I}_{2x})} \\ &\quad \times e^{i\omega_1 2\tau(\hat{I}_{1x}+\hat{I}_{2x})} e^{i\frac{\pi}{2}(\hat{I}_{1y}+\hat{I}_{2y})} e^{-i\hat{H}_D\tau} e^{-i\frac{\pi}{2}(\hat{I}_{1x}+\hat{I}_{2x})} .\end{aligned}$$

Because of

$$[\hat{H}_{D,x}, \hat{I}_{1x} + \hat{I}_{2x}] = [3\hat{I}_{1x}\hat{I}_{2x} - \hat{\mathbf{I}}_1 \cdot \hat{\mathbf{I}}_2, \hat{I}_{1x} + \hat{I}_{2x}] = 0$$

the propagator can be simplified to

$$\begin{aligned}\hat{U}(6\tau) &= e^{-i\hat{H}_D\tau} e^{-i\frac{\pi}{2}(\hat{I}_{1y}+\hat{I}_{2y})} e^{-i\omega_1 2\tau(\hat{I}_{1x}+\hat{I}_{2x})} \\ &\quad \times e^{i\frac{1}{2}\hat{H}_{D,x}2\tau} e^{i\omega_1 2\tau(\hat{I}_{1x}+\hat{I}_{2x})} e^{-i\omega_1 2\tau(\hat{I}_{1x}+\hat{I}_{2x})} e^{i\frac{1}{2}\hat{H}_{D,x}2\tau} \\ &\quad \times e^{i\omega_1 2\tau(\hat{I}_{1x}+\hat{I}_{2x})} e^{i\frac{\pi}{2}(\hat{I}_{1y}+\hat{I}_{2y})} e^{-i\hat{H}_D\tau} e^{-i\frac{\pi}{2}(\hat{I}_{1x}+\hat{I}_{2x})} \\ &= e^{-i\hat{H}_D\tau} e^{-i\frac{\pi}{2}(\hat{I}_{1y}+\hat{I}_{2y})} e^{i\hat{H}_{D,x}2\tau} e^{i\frac{\pi}{2}(\hat{I}_{1y}+\hat{I}_{2y})} e^{-i\hat{H}_D\tau} e^{-i\frac{\pi}{2}(\hat{I}_{1x}+\hat{I}_{2x})} .\end{aligned}$$

The rotation

$$e^{-i\frac{\pi}{2}(\hat{I}_{1y}+\hat{I}_{2y})} e^{i\hat{H}_{D,x}2\tau} e^{i\frac{\pi}{2}(\hat{I}_{1y}+\hat{I}_{2y})} = e^{(i2\tau e^{-i\frac{\pi}{2}(\hat{I}_{1y}+\hat{I}_{2y})} \hat{H}_{D,x} e^{i\frac{\pi}{2}(\hat{I}_{1y}+\hat{I}_{2y})})}$$

can be calculated by analyzing the exponent

$$\begin{aligned}i2\tau \left(e^{-i\frac{\pi}{2}(\hat{I}_{1y}+\hat{I}_{2y})} \hat{H}_{D,x} e^{i\frac{\pi}{2}(\hat{I}_{1y}+\hat{I}_{2y})} \right) &= i2\tau\omega_D \left[e^{-i\frac{\pi}{2}(\hat{I}_{1y}+\hat{I}_{2y})} \left(3\hat{I}_{1x}\hat{I}_{2x} - \hat{\mathbf{I}}_1 \cdot \hat{\mathbf{I}}_2 \right) e^{i\frac{\pi}{2}(\hat{I}_{1y}+\hat{I}_{2y})} \right] \\ &= i2\tau 3\omega_D \left[e^{-i\frac{\pi}{2}(\hat{I}_{1y}+\hat{I}_{2y})} \left(\hat{I}_{1x}\hat{I}_{2x} \right) e^{i\frac{\pi}{2}(\hat{I}_{1y}+\hat{I}_{2y})} \right] - i2\tau\omega_D \left[e^{-i\frac{\pi}{2}(\hat{I}_{1y}+\hat{I}_{2y})} \left(\hat{\mathbf{I}}_1 \cdot \hat{\mathbf{I}}_2 \right) e^{i\frac{\pi}{2}(\hat{I}_{1y}+\hat{I}_{2y})} \right] \\ &= i2\tau 3\omega_D \left[e^{-i\frac{\pi}{2}\hat{I}_{1y}} e^{-i\frac{\pi}{2}\hat{I}_{2y}} \left(\hat{I}_{1x}\hat{I}_{2x} \right) e^{i\frac{\pi}{2}\hat{I}_{1y}} e^{i\frac{\pi}{2}\hat{I}_{2y}} \right] - i2\tau\omega_D \left(\hat{\mathbf{I}}_1 \cdot \hat{\mathbf{I}}_2 \right) \\ &= i2\tau \left(3\omega_D \hat{I}_{1z}\hat{I}_{2z} - \hat{\mathbf{I}}_1 \cdot \hat{\mathbf{I}}_2 \right) = i\hat{H}_D 2\tau .\end{aligned}$$

Here, again the sandwich relation (Eq. D.5) was used. Now, the propagator reads

$$\begin{aligned}\hat{U}(6\tau) &= e^{-i\hat{H}_D\tau} e^{i(\frac{1}{2}\hat{H}_D)4\tau} e^{-i\hat{H}_D\tau} e^{-i\frac{\pi}{2}(\hat{I}_{1x}+\hat{I}_{2x})} \\ &= e^{-i\hat{H}_D(\tau-\frac{1}{2}4\tau+\tau)} e^{-i\frac{\pi}{2}(\hat{I}_{1x}+\hat{I}_{2x})} \\ &= e^{-i\frac{\pi}{2}(\hat{I}_{1x}+\hat{I}_{2x})} .\end{aligned}\tag{D.8}$$

From the first line of this expression one can conclude that during the MSE sequence the spin system evolves under the action of the dipolar Hamiltonian \hat{H}_D during the intervals τ before and after the burst pulses (see Fig. D.1), but under $-(\hat{H}_D/2)$ in the intermediate sandwich part of duration 4τ . After 6τ the action of the Hamiltonians is eliminated and an echo of transverse magnetization occurs:

$$\begin{aligned}\rho(6\tau) &= \hat{U}(6\tau)\hat{\rho}(0)\hat{U}^{-1}(6\tau) \\ &= e^{-i\frac{\pi}{2}(\hat{I}_{1x}+\hat{I}_{2x})} \left(\hat{I}_{1z} + \hat{I}_{2z} \right) e^{i\frac{\pi}{2}(\hat{I}_{1x}+\hat{I}_{2x})} \\ &= -\hat{I}_{1y} - \hat{I}_{2y} .\end{aligned}$$

The change in sign of the Hamiltonian in the sandwich part can be interpreted as a time reversal because the state of the spin system is described by the wave function $|\psi(t)\rangle$ with $|\psi(t)\rangle = \hat{U}|\psi(0)\rangle$ and $\hat{U} = e^{i\frac{1}{2}\hat{H}_D 4\tau} = e^{-i\frac{1}{2}\hat{H}_D(-4\tau)}$.

As can be seen in Eq. D.8 the contributions of pulses in the propagator vanish (except from the first $(\pi/2)$ pulse which flips the magnetization into the transversal plane). Therefore, the MSE sequence is a so-called cycle as introduced by Haeberlen and Waugh [322], with the cycle duration $t_c = 6\tau$. Following from Average Hamiltonian theory, the product of n spin interaction contributions in the propagator can in general be written as

$$\hat{U}(t_c) = e^{-i\hat{H}_n t_n} e^{-i\hat{H}_{n-1} t_{n-1}} \dots e^{-i\hat{H}_1 t_1} = e^{-i\langle \hat{H} \rangle t_c},$$

where $\langle \hat{H} \rangle$ has the same effect as all the interaction Hamiltonians of the pulse sequence together [54] and is given by

$$\langle \hat{H} \rangle = \sum_{k=0}^{\infty} \langle \hat{H}^{(k)} \rangle. \quad (\text{D.9})$$

Here, $\langle \hat{H}^{(0)} \rangle$ is the so-called zeroth order Average Hamiltonian. It is a sum of all interaction Hamiltonians acting during the pulse sequence and can usually be easily calculated:

$$\langle \hat{H}^{(0)} \rangle = \frac{1}{t_c} (\hat{H}_1 t_1 + \hat{H}_2 t_2 + \dots + \hat{H}_n t_n). \quad (\text{D.10})$$

In case of the MSE sequence

$$\langle \hat{H}^{(0)} \rangle = \frac{\hat{H}_D \tau - \frac{1}{2} \hat{H}_D 4\tau + \hat{H}_D \tau}{6\tau} = 0,$$

in agreement with Eq. D.8. The further terms contributing to the sum in Eq. D.9 are corrections, which contain commutators of the interaction Hamiltonians \hat{H}_j of the individual time intervals t_j in the sequence [54]. If the commutators of these piecewise interaction Hamiltonians is (almost) zero, the corrections vanish or can be neglected and the zeroth order Average Hamiltonian gives a good description of the spin interactions during the pulse sequence. In general, this is the case for short cycle durations t_c , i. e. $(t_c/T_2) \rightarrow 0$ [322], while for longer sequences the correction terms have non-negligible values.

For the MSE sequence the Average Hamiltonian is zero only approximately. Technical imperfections such as finite pulse durations, phase-switching times between the pulses and imperfect pulse lengths, shapes and phases cause changes of the piecewise interaction Hamiltonians in a way that non-vanishing commutators of these Hamiltonians may occur, which bring about non-zero higher order corrections of the Average Hamiltonian [80]. Such corrections lead to incomplete signal refocusing and an attenuation of the magnetization echo, which is the stronger the more imperfections occur and the longer they persist, i. e. the attenuation grows with increasing sequence length. If the condition $t_c = 6\tau \ll 1/\omega_D$ is not fulfilled the attenuation becomes noticeable. This is the case for too long sequence durations on the one hand and for too strong dipolar couplings on the other hand. The effect is exploited for signal filtering [89, 90]. As shown by Rhim et al. small corrections of the interaction Hamiltonian in the sandwich part of the MSE sequence cause an attenuation proportional to τ^2 [80, 89].

If the MSE pulse sequence is mirror symmetric with respect to 3τ , the first order correc-

tion of the Average Hamiltonian vanishes. Thus, the refocusing is most effective in this case [82]. In practice, a symmetric sequence is also favorable because it refocuses signal which has dephased due to resonance offsets differences and magnetic field inhomogeneities, when the phase of the last sandwich pulse is reversed by 180° , turning it into a $(90^\circ)_{-y}$ pulse (see Fig. D.1.) This version of the pulse sequence is called mixed MSE sequence, as it combines the original Magic Sandwich Echo and a Hahn echo [86]. The refocusing effect can be demonstrated by repeating the calculation from above for a system of isolated spins $I = 1/2$ using an interaction Hamiltonian describing the chemical shift interaction and the resonance offset:

$$\hat{H}_{\text{CS/off}} = \omega_{\text{CS/off}} \hat{I}_z$$

Here, the propagator of the full MSE sequence reads

$$\begin{aligned} \hat{U}(6\tau) &= e^{-i\hat{H}_{\text{CS/off}}\tau} e^{i\frac{\pi}{2}\hat{I}_y} e^{-i\hat{H}_{\text{CS/off}}2\tau + i\omega_1 2\tau \hat{I}_x} \\ &\quad \times e^{-i\hat{H}_{\text{CS/off}}2\tau - i\omega_1 2\tau \hat{I}_x} e^{+i\frac{\pi}{2}\hat{I}_y} e^{-i\hat{H}_{\text{CS/off}}\tau} e^{-i\frac{\pi}{2}\hat{I}_x} . \end{aligned}$$

By proceeding as explained above the toggling frame interaction Hamiltonian $\hat{H}'_{\text{CS/off}}$ during the burst pulses (cf. Eq. D.4) is identified as

$$\hat{H}'_{\text{CS/off}} = \omega_{\text{CS/off}} \left(\hat{I}_z \cos(\omega_1 2\tau) + \hat{I}_y \sin(\omega_1 2\tau) \right) \quad (\text{D.11})$$

and its average $\langle \hat{H}'_{\text{CS/off}} \rangle$ over the duration of the burst pulse irradiation is 0 for $\omega_1 2\tau = 2\pi n$ as well as for long irradiation times 2τ because of the vanishing time average of the sine and cosine function. This finding shows that, effectively, chemical shifts and resonance offsets do not affect the development of the magnetization during the 'sandwich part' of the sequence. However, before and after the burst pulses both effects are active and the propagator can be written as

$$\begin{aligned} \hat{U}(6\tau) &= e^{-i\hat{H}_{\text{CS/off}}\tau} e^{i\frac{\pi}{2}\hat{I}_y} e^{i\omega_1 2\tau \hat{I}_x} e^{-i\omega_1 2\tau \hat{I}_x} e^{+i\frac{\pi}{2}\hat{I}_y} e^{-i\hat{H}_{\text{CS/off}}\tau} e^{-i\frac{\pi}{2}\hat{I}_x} \\ &= e^{-i\hat{H}_{\text{CS/off}}\tau} e^{i\frac{\pi}{2}\hat{I}_y} e^{i\frac{\pi}{2}\hat{I}_y} e^{-i\hat{H}_{\text{CS/off}}\tau} e^{-i\frac{\pi}{2}\hat{I}_x} \\ &= e^{-i\hat{H}_{\text{CS/off}}\tau} e^{i\pi\hat{I}_y} e^{-i\hat{H}_{\text{CS/off}}\tau} e^{-i\frac{\pi}{2}\hat{I}_x} \\ &= e^{-i\hat{H}_{\text{CS/off}}\tau} \left(e^{i\pi\hat{I}_y} e^{-i\hat{H}_{\text{CS/off}}\tau} e^{-i\pi\hat{I}_y} \right) e^{i\pi\hat{I}_y} e^{-i\frac{\pi}{2}\hat{I}_x} . \end{aligned}$$

Here, we use the sandwich relation (Eq. D.5) to derive

$$\begin{aligned} \left(e^{i\pi\hat{I}_y} e^{-i\hat{H}_{\text{CS/off}}\tau} e^{-i\pi\hat{I}_y} \right) &= e^{-i\tau} \left(e^{i\pi\hat{I}_y} \hat{H}_{\text{CS/off}} e^{-i\pi\hat{I}_y} \right) = e^{-i\omega_{\text{CS/off}}\tau} \left(e^{i\pi\hat{I}_y} \hat{I}_z e^{-i\pi\hat{I}_y} \right) = e^{i\omega_{\text{CS/off}}\hat{I}_z\tau} \\ &= e^{i\hat{H}_{\text{CS/off}}\tau} . \end{aligned}$$

Hence, the propagator can be simplified further:

$$\begin{aligned} \hat{U}(6\tau) &= e^{-i\hat{H}_{\text{CS/off}}\tau} e^{+i\hat{H}_{\text{CS/off}}\tau} e^{i\pi\hat{I}_y} e^{-i\frac{\pi}{2}\hat{I}_x} = e^{-i(\hat{H}_{\text{CS/off}} - \hat{H}_{\text{CS/off}})\tau} e^{i\pi\hat{I}_y} e^{-i\frac{\pi}{2}\hat{I}_x} \\ &= e^{i\pi\hat{I}_y} e^{-i\frac{\pi}{2}\hat{I}_x} . \end{aligned}$$

Thus, for equal durations τ of the intervals before and after the 'sandwich part' of the

mixed MSE sequence, the action of the chemical shift or off-resonance Hamiltonian is canceled. For the spin density operator of the system after application of the sequence, we find (again by applying the sandwich relation Eq. D.5)

$$\begin{aligned} \varrho(\hat{6}\tau) &= \hat{U}(6\tau)\hat{\varrho}(0)\hat{U}^{-1}(6\tau) = e^{i\pi\hat{I}_y}e^{-i\frac{\pi}{2}\hat{I}_x}\left(\hat{I}_z\right)e^{i\frac{\pi}{2}\hat{I}_x}e^{-i\pi\hat{I}_y} = e^{i\pi\hat{I}_y}\left(-\hat{I}_y\right)e^{-i\pi\hat{I}_y} \\ &= -\hat{I}_y \end{aligned}$$

so that and the signal is refocused at time 6τ .

The effect of the pulsed and mixed MSE sequence (cf. lower row in Fig. D.1) can be demonstrated along similar lines as described above for a system of isolated pairs of spins $I_1 = I_2 = 1/2$. Here, under the assumption of short 90° pulses dipolar interactions during the pulses can be neglected. We start again with the propagator of the sequence

$$\begin{aligned} \hat{U}(6\tau) &= e^{-i\hat{H}_D\tau}\hat{P}_{-y}e^{-i\hat{H}_D\tau_\varphi}\hat{P}_{-x}e^{-i\hat{H}_D2\tau_\varphi}\hat{P}_{-x}e^{-i\hat{H}_D2\tau_\varphi}\hat{P}_{-x}e^{-i\hat{H}_D2\tau_\varphi}\hat{P}_{-x}e^{-i\hat{H}_D2\tau_\varphi}\hat{P}_{-x}e^{-i\hat{H}_D2\tau_\varphi} \\ &\times \hat{P}_xe^{-i\hat{H}_D2\tau_\varphi}\hat{P}_xe^{-i\hat{H}_D2\tau_\varphi}\hat{P}_xe^{-i\hat{H}_D2\tau_\varphi}\hat{P}_xe^{-i\hat{H}_D\tau_\varphi}\hat{P}_{-y}e^{-i\hat{H}_D\tau}\hat{P}_x. \end{aligned} \quad (\text{D.12})$$

where $\hat{P}_{\pm\alpha}$ denote the propagator contributions $e^{\mp i\frac{\pi}{2}(\hat{I}_{1\alpha}+\hat{I}_{2\alpha})}$ of the 90° pulses. Insertion of

$$\begin{aligned} \hat{E} &= \hat{P}_{-y}^{-1}\hat{P}_{-y} = e^{-i\frac{\pi}{2}(\hat{I}_{1y}+\hat{I}_{2y})}e^{i\frac{\pi}{2}(\hat{I}_{1y}+\hat{I}_{2y})}, \\ \hat{E} &= \hat{P}_{-x}^{-1}\hat{P}_{-x} = e^{-i\frac{\pi}{2}(\hat{I}_{1x}+\hat{I}_{2x})}e^{i\frac{\pi}{2}(\hat{I}_{1x}+\hat{I}_{2x})} \text{ and} \\ \hat{E} &= \hat{P}_x^{-1}\hat{P}_x = e^{i\frac{\pi}{2}(\hat{I}_{1x}+\hat{I}_{2x})}e^{-i\frac{\pi}{2}(\hat{I}_{1x}+\hat{I}_{2x})} \end{aligned}$$

at suitable positions results in

$$\begin{aligned} \hat{U}(6\tau) &= e^{-i\hat{H}_D\tau}\hat{P}_{-y}e^{-i\hat{H}_D\tau_\varphi}\left(\hat{P}_{-y}^{-1}\hat{P}_{-y}\right)\hat{P}_{-x}e^{-i\hat{H}_D2\tau_\varphi}\left(\hat{P}_{-x}^{-1}\hat{P}_{-x}\right) \\ &\times \hat{P}_{-x}e^{-i\hat{H}_D2\tau_\varphi}\left(\hat{P}_{-x}^{-1}\hat{P}_{-x}\right)\hat{P}_{-x}e^{-i\hat{H}_D2\tau_\varphi}\left(\hat{P}_{-x}^{-1}\hat{P}_{-x}\right)\hat{P}_{-x}e^{-i\hat{H}_D2\tau_\varphi}\left(\hat{P}_{-x}^{-1}\hat{P}_{-x}\right) \\ &\times \hat{P}_xe^{-i\hat{H}_D2\tau_\varphi}\left(\hat{P}_x^{-1}\hat{P}_x\right)\hat{P}_xe^{-i\hat{H}_D2\tau_\varphi}\left(\hat{P}_x^{-1}\hat{P}_x\right)\hat{P}_xe^{-i\hat{H}_D2\tau_\varphi}\left(\hat{P}_x^{-1}\hat{P}_x\right) \\ &\times \hat{P}_xe^{-i\hat{H}_D\tau_\varphi}\left(\hat{P}_x^{-1}\hat{P}_x\right)\hat{P}_{-y}e^{-i\hat{H}_D\tau}\left(\hat{P}_{-y}^{-1}\hat{P}_{-y}\right)\hat{P}_x \\ &= e^{-i\hat{H}_D\tau}\left(\hat{P}_{-y}e^{-i\hat{H}_D\tau_\varphi}\hat{P}_{-y}^{-1}\right)\hat{P}_{-y}\left(\hat{P}_{-x}e^{-i\hat{H}_D2\tau_\varphi}\hat{P}_{-x}^{-1}\right)\hat{P}_{-x} \\ &\times \left(\hat{P}_{-x}e^{-i\hat{H}_D2\tau_\varphi}\hat{P}_{-x}^{-1}\right)\hat{P}_{-x}\left(\hat{P}_{-x}e^{-i\hat{H}_D2\tau_\varphi}\hat{P}_{-x}^{-1}\right)\hat{P}_{-x}\left(\hat{P}_{-x}e^{-i\hat{H}_D2\tau_\varphi}\hat{P}_{-x}^{-1}\right)\hat{P}_{-x} \\ &\times \left(\hat{P}_xe^{-i\hat{H}_D2\tau_\varphi}\hat{P}_x^{-1}\right)\hat{P}_x\left(\hat{P}_xe^{-i\hat{H}_D2\tau_\varphi}\hat{P}_x^{-1}\right)\hat{P}_x\left(\hat{P}_xe^{-i\hat{H}_D2\tau_\varphi}\hat{P}_x^{-1}\right)\hat{P}_x \\ &\times \left(\hat{P}_xe^{-i\hat{H}_D\tau_\varphi}\hat{P}_x^{-1}\right)\hat{P}_x\left(\hat{P}_{-y}e^{-i\hat{H}_D\tau}\hat{P}_{-y}^{-1}\right)\hat{P}_{-y}\hat{P}_x. \end{aligned}$$

The rotations $\left(\hat{P}_{\pm\alpha}e^{-i\hat{H}_D\tau}\hat{P}_{\pm\alpha}^{-1}\right)$ can be calculated using the exponential relation D.2 and

the sandwich relaxation D.5:

$$\begin{aligned}
 \left(\hat{P}_{-y}e^{-i\hat{H}_D t}\hat{P}_{-y}^{-1}\right) &= \left(\hat{P}_y e^{-i\hat{H}_D t}\hat{P}_y^{-1}\right) = e^{-it\omega_D(3\hat{I}_{1x}\hat{I}_{2x}-\hat{\mathbf{I}}_1\cdot\hat{\mathbf{I}}_2)} = e^{-i\hat{H}_{D,x}t} \\
 \left(\hat{P}_{-x}e^{-i\hat{H}_D t}\hat{P}_{-x}^{-1}\right) &= \left(\hat{P}_x e^{-i\hat{H}_D t}\hat{P}_x^{-1}\right) = e^{-it\omega_D(3\hat{I}_{1y}\hat{I}_{2y}-\hat{\mathbf{I}}_1\cdot\hat{\mathbf{I}}_2)} = e^{-i\hat{H}_{D,y}t} \\
 \left(\hat{P}_{-y}e^{-i\hat{H}_{D,x}t}\hat{P}_{-y}^{-1}\right) &= \left(\hat{P}_y e^{-i\hat{H}_{D,x}t}\hat{P}_y^{-1}\right) = e^{-it\omega_D(3\hat{I}_{1z}\hat{I}_{2z}-\hat{\mathbf{I}}_1\cdot\hat{\mathbf{I}}_2)} = e^{-i\hat{H}_D t} \\
 \left(\hat{P}_{-x}e^{-i\hat{H}_{D,y}t}\hat{P}_{-x}^{-1}\right) &= \left(\hat{P}_x e^{-i\hat{H}_{D,y}t}\hat{P}_x^{-1}\right) = e^{-it\omega_D(3\hat{I}_{1z}\hat{I}_{2z}-\hat{\mathbf{I}}_1\cdot\hat{\mathbf{I}}_2)} = e^{-i\hat{H}_D t} \\
 \left(\hat{P}_{-y}e^{-i\hat{H}_{D,y}t}\hat{P}_{-y}^{-1}\right) &= \left(\hat{P}_y e^{-i\hat{H}_{D,y}t}\hat{P}_y^{-1}\right) = e^{-it\omega_D(3\hat{I}_{1y}\hat{I}_{2y}-\hat{\mathbf{I}}_1\cdot\hat{\mathbf{I}}_2)} = e^{-i\hat{H}_{D,y}t} \\
 \left(\hat{P}_{-x}e^{-i\hat{H}_{D,x}t}\hat{P}_{-x}^{-1}\right) &= \left(\hat{P}_x e^{-i\hat{H}_{D,x}t}\hat{P}_x^{-1}\right) = e^{-it\omega_D(3\hat{I}_{1x}\hat{I}_{2x}-\hat{\mathbf{I}}_1\cdot\hat{\mathbf{I}}_2)} = e^{-i\hat{H}_{D,x}t}
 \end{aligned}$$

Hence, the propagator reads

$$\begin{aligned}
 \hat{U}(6\tau) &= e^{-i\hat{H}_D \tau} e^{-i\hat{H}_{D,x}\tau\varphi} \hat{P}_{-y} e^{-i\hat{H}_{D,y}2\tau\varphi} \hat{P}_{-x} e^{-i\hat{H}_{D,y}2\tau\varphi} \hat{P}_{-x} e^{-i\hat{H}_{D,y}2\tau\varphi} \hat{P}_{-x} e^{-i\hat{H}_{D,y}2\tau\varphi} \\
 &\quad \times \hat{P}_{-x} e^{-i\hat{H}_{D,y}2\tau\varphi} \hat{P}_x e^{-i\hat{H}_{D,y}2\tau\varphi} \hat{P}_x e^{-i\hat{H}_{D,y}2\tau\varphi} \hat{P}_x e^{-i\hat{H}_{D,y}2\tau\varphi} \hat{P}_x e^{-i\hat{H}_{D,y}2\tau\varphi} \hat{P}_{-y} \hat{P}_x .
 \end{aligned}$$

Compared to Eq. D.12, here, the pulse propagator terms $\hat{P}_{\pm\alpha}$ have been shifted to the right. By continuing with the insertion of unity operators and the evaluation of the rotations, the propagator contributions of spin interactions and pulses finally can be separated:

$$\begin{aligned}
 \hat{U}(6\tau) &= e^{-i\hat{H}_D \tau} e^{-i\hat{H}_{D,x}\tau\varphi} e^{-i\hat{H}_{D,y}2\tau\varphi} e^{-i\hat{H}_{D,x}2\tau\varphi} e^{-i\hat{H}_{D,y}2\tau\varphi} e^{-i\hat{H}_{D,x}2\tau\varphi} \\
 &\quad \times e^{-i\hat{H}_{D,y}2\tau\varphi} e^{-i\hat{H}_{D,x}2\tau\varphi} e^{-i\hat{H}_{D,y}2\tau\varphi} e^{-i\hat{H}_{D,x}\tau\varphi} e^{-i\hat{H}_D \tau} \\
 &\quad \times \hat{P}_{-y} \hat{P}_{-x} \hat{P}_{-x} \hat{P}_{-x} \hat{P}_{-x} \hat{P}_x \hat{P}_x \hat{P}_x \hat{P}_x \hat{P}_{-y} \hat{P}_x .
 \end{aligned}$$

For subsuming the propagator contributions we exploit

$$[\hat{H}_{D,x}, \hat{H}_{D,y}] = 0 \tag{D.13}$$

and

$$\begin{aligned}
 \hat{H}_{D,x} + \hat{H}_{D,y} + \hat{H}_D &= 3\hat{I}_{1x}\hat{I}_{2x} - \hat{\mathbf{I}}_1 \cdot \hat{\mathbf{I}}_2 + 3\hat{I}_{1y}\hat{I}_{2y} - \hat{\mathbf{I}}_1 \cdot \hat{\mathbf{I}}_2 + 3\hat{I}_{1z}\hat{I}_{2z} - \hat{\mathbf{I}}_1 \cdot \hat{\mathbf{I}}_2 \\
 &= 3(\hat{\mathbf{I}}_1 \cdot \hat{\mathbf{I}}_2) - 3(\hat{\mathbf{I}}_1 \cdot \hat{\mathbf{I}}_2) = 0
 \end{aligned} \tag{D.14}$$

The latter relation is called the 'Magic Zero' of homonuclear dipolar couplings [17]. Hence,

$$\begin{aligned}
 \hat{U}(6\tau) &= e^{-i\hat{H}_D \tau} \left[e^{-i\hat{H}_{D,x}8\tau\varphi} e^{-i\hat{H}_{D,y}8\tau\varphi} \right] e^{-i\hat{H}_D \tau} \\
 &\quad \times e^{i\frac{\pi}{2}(\hat{I}_{1y}+\hat{I}_{2y})} e^{i2\pi(\hat{I}_{1x}+\hat{I}_{2x})} e^{-i2\pi(\hat{I}_{1x}+\hat{I}_{2x})} e^{i\frac{\pi}{2}(\hat{I}_{1y}+\hat{I}_{2y})} e^{-i\frac{\pi}{2}(\hat{I}_{1x}+\hat{I}_{2x})} \\
 &= e^{-i\hat{H}_D \tau} e^{i\hat{H}_D 8\tau\varphi} e^{-i\hat{H}_D \tau} e^{i\pi(\hat{I}_{1y}+\hat{I}_{2y})} e^{-i\frac{\pi}{2}(\hat{I}_{1x}+\hat{I}_{2x})} \\
 &= e^{-i(\hat{H}_D)6\tau} e^{i\pi(\hat{I}_{1y}+\hat{I}_{2y})} e^{-i\frac{\pi}{2}(\hat{I}_{1x}+\hat{I}_{2x})}
 \end{aligned}$$

The penultimate expression again demonstrates that the sign of the dipolar interaction Hamiltonian is reversed due to the action of the sandwich pulses. For $2\tau = 8\tau\varphi$ the

interaction terms vanish

$$\begin{aligned}\hat{U}(6\tau) &= e^{-i\hat{H}_D(\tau-8\tau_\varphi+\tau)} e^{i\pi(\hat{I}_{1y}+\hat{I}_{2y})} e^{-i\frac{\pi}{2}(\hat{I}_{1x}+\hat{I}_{2x})} \\ &= e^{-i\hat{H}_D(\tau-2\tau+\tau)} e^{i\pi(\hat{I}_{1y}+\hat{I}_{2y})} e^{-i\frac{\pi}{2}(\hat{I}_{1x}+\hat{I}_{2x})} \\ &= e^{i\pi(\hat{I}_{1y}+\hat{I}_{2y})} e^{-i\frac{\pi}{2}(\hat{I}_{1x}+\hat{I}_{2x})}\end{aligned}$$

and the Average Hamiltonian $\langle \hat{H}_D \rangle$ is 0. (Here, imperfections leading to corrections in the Average Hamiltonian are not taken into account). Thus, after application of the sequence the spin density operator can be written as

$$\begin{aligned}\rho(\hat{6}\tau) &= \hat{U}(6\tau)\hat{\rho}(0)\hat{U}^{-1}(6\tau) \\ &= e^{i\pi(\hat{I}_{1y}+\hat{I}_{2y})} e^{-i\frac{\pi}{2}(\hat{I}_{1x}+\hat{I}_{2x})} \left(\hat{I}_{1z} + \hat{I}_{2z} \right) e^{i\frac{\pi}{2}(\hat{I}_{1x}+\hat{I}_{2x})} e^{-i\pi(\hat{I}_{1y}+\hat{I}_{2y})} \\ &= e^{i\pi(\hat{I}_{1y}+\hat{I}_{2y})} \left(-\hat{I}_{1y} - \hat{I}_{2y} \right) e^{-i\pi(\hat{I}_{1y}+\hat{I}_{2y})} \\ &= -\hat{I}_{1y} - \hat{I}_{2y}\end{aligned}$$

and the Magic Sandwich Echo occurs at time $t = 6\tau$.

D.1.2. The Magic and Polarization Echo

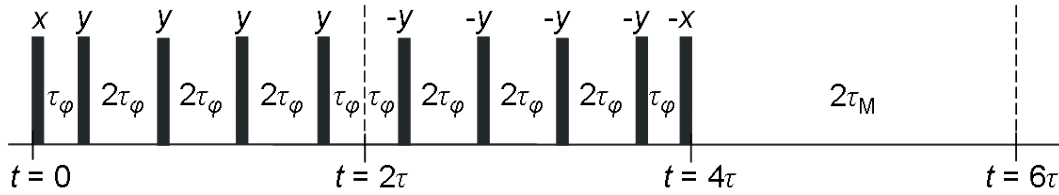


Figure D.2.: Pulse sequence assumed for demonstrating the formation of the Magic and Polarization Echo (MAPE). All pulses are 90° pulses. The delay τ_M is calculated as $\tau_M = 2\tau_{p90} + 4\tau_\varphi$, with τ_{p90} being the 90° pulse length.

The mode of action of the Magic and Polarization Echo sequence can be demonstrated in the same way as explained in Appendix D.1.1 for the pulsed MSE sequence, by evaluating the propagator for a system of isolated pairs of spins $I_1 = I_2 = 1/2$. In case of the sequence shown in Fig. D.2 the propagator is given by

$$\begin{aligned}\hat{U}(6\tau) &= e^{-i\hat{H}_D 2\tau} \hat{P}_{-x} e^{-i\hat{H}_D \tau_\varphi} \hat{P}_{-y} e^{-i\hat{H}_D 2\tau_\varphi} \hat{P}_{-y} e^{-i\hat{H}_D 2\tau_\varphi} \hat{P}_{-y} e^{-i\hat{H}_D 2\tau_\varphi} \hat{P}_{-y} e^{-i\hat{H}_D 2\tau_\varphi} \hat{P}_{-y} e^{-i\hat{H}_D 2\tau_\varphi} \\ &\quad \times \hat{P}_y e^{-i\hat{H}_D 2\tau_\varphi} \hat{P}_y e^{-i\hat{H}_D 2\tau_\varphi} \hat{P}_y e^{-i\hat{H}_D 2\tau_\varphi} \hat{P}_y e^{-i\hat{H}_D \tau_\varphi} \hat{P}_x.\end{aligned}$$

By inserting unity operators and calculating the resulting rotations according to the considerations in Appendix D.1.1 the pulse contributions $\hat{P}_{\pm\alpha}$ and dipolar interaction contributions $e^{-i\hat{H}_D t}$ can be separated:

$$\begin{aligned}\hat{U}(6\tau) &= e^{-i\hat{H}_D 2\tau} e^{-i\hat{H}_{D,y}\tau_\varphi} e^{-i\hat{H}_{D,x}2\tau_\varphi} e^{-i\hat{H}_{D,y}2\tau_\varphi} e^{-i\hat{H}_{D,x}2\tau_\varphi} e^{-i\hat{H}_{D,y}2\tau_\varphi} \\ &\quad \times e^{-i\hat{H}_{D,x}2\tau_\varphi} e^{-i\hat{H}_{D,y}2\tau_\varphi} e^{-i\hat{H}_{D,x}2\tau_\varphi} e^{-i\hat{H}_{D,y}\tau_\varphi} \\ &\quad \times \hat{P}_{-x} \hat{P}_{-y} \hat{P}_{-y} \hat{P}_{-y} \hat{P}_{-y} \hat{P}_y \hat{P}_y \hat{P}_y \hat{P}_y \hat{P}_x.\end{aligned}$$

By means of the relations D.13 and D.14 we find

$$\begin{aligned}
 \hat{U}(6\tau) &= e^{-i\hat{H}_D 2\tau} e^{-i(\hat{H}_{D,y} + \hat{H}_{D,x}) 8\tau_\varphi} \\
 &= e^{-i\hat{H}_D 2\tau} e^{+i\hat{H}_D 8\tau_\varphi} \\
 &= e^{-i\hat{H}_D(2\tau - 8\tau_\varphi)} \\
 &= e^{-i\langle \hat{H}_D \rangle 6\tau}
 \end{aligned}$$

and for $2\tau = 8\tau_\varphi$ this results in

$$\hat{U}(6\tau) = e^{-i\hat{H}_D(2\tau - 2\tau)} = \hat{E},$$

with \hat{E} being the unity operator, rendering $\langle \hat{H}_D \rangle = 0$. (Here again, imperfections leading to corrections in the Average Hamiltonian are not considered.)

The z-magnetization is refocused at time $t = 6\tau$ as demonstrated by writing down the density operator

$$\begin{aligned}
 \varrho(6\tau) &= \hat{U}(6\tau) \hat{\varrho}(0) \hat{U}^{-1}(6\tau) \\
 &= \hat{E} \left(\hat{I}_{1z} + \hat{I}_{2z} \right) \hat{E} \\
 &= \hat{I}_{1z} + \hat{I}_{2z}
 \end{aligned}$$

The filter action of the MAPE sequence, however, is based on higher order corrections of the Average Hamiltonian, brought about by sequence imperfections as described in Appendix D.1.1. Just as in the case of the MSE sequence, these corrections prevent the complete refocusing of magnetization and result in an attenuation of the magnetization echo, if the condition $6\tau \ll 1/\omega_D$ is violated. By adapting the length of the sequence, longitudinal magnetization from regions with strong dipolar couplings can be depleted.

When calculating $\hat{\varrho}(t)$ piecewise after every pulse one observes that the magnetization is refocused already at $t = 4\tau$. However, at this time the (zeroth order) Average Hamiltonian is non-zero and the effect of dipolar couplings has not been reversed yet. Hence, for long MAPE sequences spin diffusion which is mediated by dipolar couplings (see Section 4.3) and may occur during the progression of the sequence, has not been canceled at $t = 4\tau$. However, this is the case at $t = 6\tau$, turning this point in time into a suitable starting point for spin diffusion experiments.

D.2. The Double-Quantum Filter

In order to understand DQ filter action, it is beneficial to calculate the spin density operator piecewise after each pulse and each interval of the pulse sequence. Here, we want to consider the evolution of a system of isolated pairs of spins $I_1 = I_2 = 1/2$, which interact with each other and are subjected to the DQ sequence schematically plotted in Fig. D.3. The spin system is supposed to be in thermal equilibrium in the magnetic field B_0 before application of the pulse sequence. Hence, the spin density operator at time $t = 0$ prior to the first pulse can be written as $\hat{\varrho}(0) = \hat{I}_{1z} + \hat{I}_{2z}$ (see Appendix C). Now, the spin density operator $\hat{\varrho}(t)$ at time t can be estimated using the solution of the

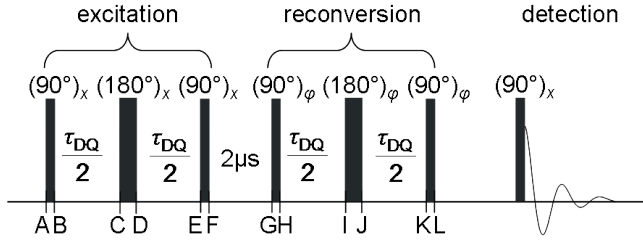


Figure D.3: Pulse sequence scheme assumed for demonstrating the action of the double-quantum (DQ) sequence. The phase φ of the reconversion pulses passes through a 4-step phase cycle with $\varphi = y \bar{x} \bar{y} x$ in subsequent scans and the corresponding receiver phases are $\varphi_{rec} = x \bar{x} x \bar{x}$.

Liouville-van-Neumann equation for a time-independent Hamiltonian (see Appendix C)

$$\hat{\rho}(t) = e^{-i\hat{H}t} \hat{\rho}(0) e^{i\hat{H}t}. \quad (\text{D.15})$$

We assume that the rf pulses are short and strong compared to the coupling interaction, so that we can neglect interactions during pulse irradiation. Hence, for evaluating the development of the spin density operator via Eq. D.15 we have to consider the effect of either the dipolar Hamiltonian [54]

$$\hat{H}_D = \omega_D \left(3\hat{I}_{1z}\hat{I}_{2z} - \hat{\mathbf{I}}_1 \cdot \hat{\mathbf{I}}_2 \right)$$

during intervals in the sequence or the rf-pulse Hamiltonian

$$\hat{H}_P = -\omega_1 \left[(\hat{I}_{1x} \cos \varphi + \hat{I}_{1y} \sin \varphi) + (\hat{I}_{2x} \cos \varphi + \hat{I}_{2y} \sin \varphi) \right]$$

with pulse phase φ , nutation frequency ω_1 and pulse duration t_p . Both Hamiltonians are supposed to be time-independent. However, a descriptive calculation using the product operator formalism is not possible here. Instead tensor operators would have to be used. Hence, for simplicity, instead of the homonuclear dipolar coupling, the J coupling is considered, for which the excitation of double-quantum coherences can be demonstrated easily by means of product operators under the assumption that the coupling is weak compared to the distance of the resonance frequencies of the interacting spins in the spectrum. Here, the interaction Hamiltonian is given by

$$\hat{H}_J = 2\pi J_{1,2} \left(3\hat{I}_{1z}\hat{I}_{2z} \right),$$

with $J_{1,2}$ denoting the strength of the J coupling between spins 1 and 2.

Exploiting the sandwich relation D.5 we can trace the density operator after each step in the pulse sequence. (The distinct time points in the sequence for which the operator is calculated are marked with upper case letters in Fig. D.3). For the excitation period

we find the following evolution of the operator:

$$\begin{aligned}
 A : & \quad \hat{I}_{1z} + \hat{I}_{2z} \\
 & \quad \downarrow (\pi/2)_x \\
 B : & \quad -\hat{I}_{1y} - \hat{I}_{2y} \\
 & \quad \downarrow \hat{H}_J(\tau_{\text{DQ}}/2) \\
 C : & \quad -\left(\hat{I}_{1y} + \hat{I}_{2y}\right) \cos \frac{\pi}{2} J_{1,2} \tau_{\text{DQ}} + \left(2\hat{I}_{1x}\hat{I}_{2z} + 2\hat{I}_{1z}\hat{I}_{2x}\right) \sin \frac{\pi}{2} J_{1,2} \tau_{\text{DQ}} \\
 & \quad \downarrow (\pi)_x \\
 D : & \quad \left(\hat{I}_{1y} + \hat{I}_{2y}\right) \cos \frac{\pi}{2} J_{1,2} \tau_{\text{DQ}} - \left(2\hat{I}_{1x}\hat{I}_{2z} + 2\hat{I}_{1z}\hat{I}_{2x}\right) \sin \frac{\pi}{2} J_{1,2} \tau_{\text{DQ}} \\
 & \quad \downarrow \hat{H}_J(\tau_{\text{DQ}}/2) \\
 E : & \quad \left(\hat{I}_{1y} + \hat{I}_{2y}\right) \cos \pi J_{1,2} \tau_{\text{DQ}} - \left(2\hat{I}_{1x}\hat{I}_{2z} + 2\hat{I}_{1z}\hat{I}_{2x}\right) \sin \pi J_{1,2} \tau_{\text{DQ}} \\
 & \quad \downarrow (\pi/2)_x \\
 F : & \quad \left(\hat{I}_{1z} + \hat{I}_{2z}\right) \cos \pi J_{1,2} \tau_{\text{DQ}} - \left(2\hat{I}_{1x}\hat{I}_{2y} + 2\hat{I}_{1y}\hat{I}_{2x}\right) \sin \pi J_{1,2} \tau_{\text{DQ}} .
 \end{aligned}$$

Nothing changes during the short phase-switching time of 2 μs at which the system is subject to J couplings. Thus, we end up with

$$G : \quad \underbrace{\left(\hat{I}_{1z} + \hat{I}_{2z}\right) \cos \pi J_{1,2} \tau_{\text{DQ}}}_{\text{reference}} - \underbrace{\left(2\hat{I}_{1x}\hat{I}_{2y} + 2\hat{I}_{1y}\hat{I}_{2x}\right) \sin \pi J_{1,2} \tau_{\text{DQ}}}_{\text{DQ coherence}} ,$$

where the second term in the sum describes the portion of the originally longitudinal magnetization, which has been converted into double-quantum coherence (see Appendix C), while the first term depicts the remaining z magnetization and is referred to as the reference part of the spin density operator. In order to demonstrate the evolution in the reconversion part of the sequence both terms are considered separately. Applying

reconversion pulses of phase y the reference term evolves according to

$$\begin{aligned}
 G : & \quad \left(\hat{I}_{1z} + \hat{I}_{2z} \right) \cos \pi J_{1,2} \tau_{\text{DQ}} \\
 & \quad \quad \quad \downarrow (\pi/2)_y \\
 H : & \quad \left(\hat{I}_{1x} + \hat{I}_{2x} \right) \cos \pi J_{1,2} \tau_{\text{DQ}} \\
 & \quad \quad \quad \downarrow \hat{H}_J(\tau_{\text{DQ}}/2) \\
 I : & \quad \left(\hat{I}_{1x} + \hat{I}_{2x} \right) \cos \frac{\pi}{2} J_{1,2} \tau_{\text{DQ}} \cos \pi J_{1,2} \tau_{\text{DQ}} + \left(2\hat{I}_{1y}\hat{I}_{2z} + 2\hat{I}_{1z}\hat{I}_{2y} \right) \sin \frac{\pi}{2} J_{1,2} \tau_{\text{DQ}} \cos \pi J_{1,2} \tau_{\text{DQ}} \\
 & \quad \quad \quad \downarrow (\pi)_y \\
 J : & \quad - \left(\hat{I}_{1x} + \hat{I}_{2x} \right) \cos \frac{\pi}{2} J_{1,2} \tau_{\text{DQ}} \cos \pi J_{1,2} \tau_{\text{DQ}} - \left(2\hat{I}_{1y}\hat{I}_{2z} + 2\hat{I}_{1z}\hat{I}_{2y} \right) \sin \frac{\pi}{2} J_{1,2} \tau_{\text{DQ}} \cos \pi J_{1,2} \tau_{\text{DQ}} \\
 & \quad \quad \quad \downarrow \hat{H}_J(\tau_{\text{DQ}}/2) \\
 K : & \quad - \left(\hat{I}_{1x} + \hat{I}_{2x} \right) \cos \pi J_{1,2} \tau_{\text{DQ}} \cos \pi J_{1,2} \tau_{\text{DQ}} - \left(2\hat{I}_{1y}\hat{I}_{2z} + 2\hat{I}_{1z}\hat{I}_{2y} \right) \sin \pi J_{1,2} \tau_{\text{DQ}} \cos \pi J_{1,2} \tau_{\text{DQ}} \\
 & \quad \quad \quad \downarrow (\pi/2)_y \\
 L : & \quad \left(\hat{I}_{1z} + \hat{I}_{2z} \right) \cos^2 \pi J_{1,2} \tau_{\text{DQ}} - \left(2\hat{I}_{1x}\hat{I}_{2y} + 2\hat{I}_{1y}\hat{I}_{2x} \right) \sin \pi J_{1,2} \tau_{\text{DQ}} \cos \pi J_{1,2} \tau_{\text{DQ}}
 \end{aligned}$$

and the DQ coherence converts into

$$\begin{aligned}
 G : & \quad \left(2\hat{I}_{1x}\hat{I}_{2y} + 2\hat{I}_{1y}\hat{I}_{2x} \right) \sin \pi J_{1,2} \tau_{\text{DQ}} \\
 & \quad \quad \quad \downarrow (\pi/2)_y \\
 H : & \quad - \left(2\hat{I}_{1y}\hat{I}_{2z} + 2\hat{I}_{1z}\hat{I}_{2y} \right) \sin \pi J_{1,2} \tau_{\text{DQ}} \\
 & \quad \quad \quad \downarrow \hat{H}_J(\tau_{\text{DQ}}/2) \\
 I : & \quad \left(\hat{I}_{1x} + \hat{I}_{2x} \right) \sin \frac{\pi}{2} J_{1,2} \tau_{\text{DQ}} \sin \pi J_{1,2} \tau_{\text{DQ}} - \left(2\hat{I}_{1y}\hat{I}_{2z} + 2\hat{I}_{1z}\hat{I}_{2y} \right) \cos \frac{\pi}{2} J_{1,2} \tau_{\text{DQ}} \sin \pi J_{1,2} \tau_{\text{DQ}} \\
 & \quad \quad \quad \downarrow (\pi)_y \\
 J : & \quad - \left(\hat{I}_{1x} + \hat{I}_{2x} \right) \sin \frac{\pi}{2} J_{1,2} \tau_{\text{DQ}} \sin \pi J_{1,2} \tau_{\text{DQ}} + \left(2\hat{I}_{1y}\hat{I}_{2z} + 2\hat{I}_{1z}\hat{I}_{2y} \right) \cos \frac{\pi}{2} J_{1,2} \tau_{\text{DQ}} \sin \pi J_{1,2} \tau_{\text{DQ}} \\
 & \quad \quad \quad \downarrow \hat{H}_J(\tau_{\text{DQ}}/2) \\
 K : & \quad - \left(\hat{I}_{1x} + \hat{I}_{2x} \right) \sin \pi J_{1,2} \tau_{\text{DQ}} \sin \pi J_{1,2} \tau_{\text{DQ}} + \left(2\hat{I}_{1y}\hat{I}_{2z} + 2\hat{I}_{1z}\hat{I}_{2y} \right) \cos \pi J_{1,2} \tau_{\text{DQ}} \sin \pi J_{1,2} \tau_{\text{DQ}} \\
 & \quad \quad \quad \downarrow (\pi/2)_y \\
 L : & \quad \left(\hat{I}_{1z} + \hat{I}_{2z} \right) \sin^2 \pi J_{1,2} \tau_{\text{DQ}} + \left(2\hat{I}_{1x}\hat{I}_{2y} + 2\hat{I}_{1y}\hat{I}_{2x} \right) \sin \pi J_{1,2} \tau_{\text{DQ}} \cos \pi J_{1,2} \tau_{\text{DQ}}
 \end{aligned}$$

Now, the $(\pi/2)_x$ pulse for detection transforms $(\hat{I}_{1z} + \hat{I}_{2z})$ into $(-\hat{I}_{1y} - \hat{I}_{2y})$

and $(2\hat{I}_{1x}\hat{I}_{2y} + 2\hat{I}_{1y}\hat{I}_{2x})$ into $(2\hat{I}_{1x}\hat{I}_{2z} + 2\hat{I}_{1z}\hat{I}_{2x})$. As only transverse magnetization is measurable, the terms containing products of spin operators can be discarded. For the remaining terms the receiver phase must be taken into account. With receiver phase x we finally find the reference signal part

$$(\hat{I}_{1y} + \hat{I}_{2y}) \cos^2(\pi J_{1,2}\tau_{\text{DQ}})$$

and the DQ signal part

$$(\hat{I}_{1y} + \hat{I}_{2y}) \sin^2(\pi J_{1,2}\tau_{\text{DQ}}).$$

Expressions for the remaining reconversion pulse phases and receiver phases are obtained similarly. In summary, we find the following relevant portions of the spin density operator:

reconversion pulse phase	receiver phase	reference signal	DQ signal
y	x	$(\hat{I}_{1y} + \hat{I}_{2y}) \cos^2(\pi J_{1,2}\tau_{\text{DQ}})$	$(\hat{I}_{1y} + \hat{I}_{2y}) \sin^2(\pi J_{1,2}\tau_{\text{DQ}})$
$-x$	$-x$	$-(\hat{I}_{1y} + \hat{I}_{2y}) \cos^2(\pi J_{1,2}\tau_{\text{DQ}})$	$(\hat{I}_{1y} + \hat{I}_{2y}) \sin^2(\pi J_{1,2}\tau_{\text{DQ}})$
$-y$	x	$(\hat{I}_{1y} + \hat{I}_{2y}) \cos^2(\pi J_{1,2}\tau_{\text{DQ}})$	$(\hat{I}_{1y} + \hat{I}_{2y}) \sin^2(\pi J_{1,2}\tau_{\text{DQ}})$
x	$-x$	$-(\hat{I}_{1y} + \hat{I}_{2y}) \cos^2(\pi J_{1,2}\tau_{\text{DQ}})$	$(\hat{I}_{1y} + \hat{I}_{2y}) \sin^2(\pi J_{1,2}\tau_{\text{DQ}})$

After four subsequent scans the reference terms add up to 0 while the summation of the DQ terms yields

$$(\hat{I}_{1y} + \hat{I}_{2y}) 4 \sin^2(\pi J_{1,2}\tau_{\text{DQ}}).$$

Hence, after four (or a multiple of four) scans, only the fraction of originally longitudinal magnetization, which was converted into double-quantum coherence is transformed back into measurable transverse magnetization.

The filter effect of the DQ sequence is based on the fact, that the efficiency of conversion and reconversion depends on the product $J_{1,2}\tau_{\text{DQ}}$, e. g., in the case of isolated spin pairs, on $\sin^2(\pi J_{1,2}\tau_{\text{DQ}})$ (see above). For a short excitation time τ_{DQ} appreciable signal intensity is reached only in case of a high coupling strength $J_{1,2}$. Consequently, magnetization from strongly coupled regions of the sample is selectively excited. At longer τ_{DQ} , signal from sample portions with weaker couplings can be obtained. However then, signal from strongly coupled spin pairs may have already been reduced. Yet, the situation complicates for systems with more than two coupling spins with different coupling strengths [323].

E. PCL Densities

PCL spin densities were obtained based on mass densities ρ_a and ρ_{tot} of amorphous and semicrystalline PCL, respectively, measured by dilatometry over a wide temperature range by Crescenzi et al. [238]. In principle the mass density of the crystalline phase can be calculated using the monomeric mass and the dimensions of the PCL unit cell. These dimensions, however, are temperature dependent and are known from literature only for selected temperatures [49, 51, 52]. Therefore, here, the mass densities for the crystalline phase, interphase (3P model) and the rigid phase, being the sum of the former two (2P model), were estimated at the measurement temperatures by help of the mass fractions f_p from the FID or MSE analysis via

$$\frac{1}{\rho_{\text{tot}}} = \sum_p \frac{f_p}{\rho_p}$$

with $\rho_{\text{tot}} = (1.111 \pm 0.0044) \text{ g/cm}^3$ at 27°C, $(1.098 \pm 0.0044) \text{ g/cm}^3$ at 45°C and $(1.097 \pm 0.0044) \text{ g/cm}^3$ at 45°C [238]. In case of the 3P model the density of the interphase was defined to be the average of the densities of crystalline and amorphous phase. From the mass densities proton spin densities were derived using Eq. 4.8. All densities used are given in Table E.1. The relative spin densities are related to the amorphous-phase spin densities and were used as input parameters to the fit of spin-diffusion and Saturation-Recovery data.

phase p	$T / ^\circ\text{C}$	$\rho / \text{g cm}^{-3}$	$\rho_H / \text{g cm}^{-3}$	$\rho_{H,rel}$
amorphous	27	1.075 ± 0.004	0.0949 ± 0.0004	1.000 ± 0.004
	45	1.062 ± 0.004	0.0938 ± 0.0004	1.000 ± 0.004
	48	1.060 ± 0.004	0.0936 ± 0.0004	1.000 ± 0.004
interphase	27	1.106 ± 0.024	0.0977 ± 0.0021	1.029 ± 0.023
	45	1.096 ± 0.026	0.0968 ± 0.0023	1.032 ± 0.025
	48	1.094 ± 0.026	0.0966 ± 0.0023	1.032 ± 0.025
crystalline	27	1.137 ± 0.044	0.1004 ± 0.0039	1.057 ± 0.041
	45	1.130 ± 0.048	0.0998 ± 0.0042	1.064 ± 0.045
	48	1.129 ± 0.049	0.0997 ± 0.0043	1.065 ± 0.046
rigid	27	1.130 ± 0.061	0.0998 ± 0.0054	1.051 ± 0.057
	45	1.123 ± 0.067	0.0991 ± 0.0059	1.057 ± 0.063
	48	1.122 ± 0.067	0.0991 ± 0.0059	1.058 ± 0.063

Table E.1.: Mass densities ρ and absolute and relative proton spin densities ρ_H and $\rho_{H,rel}$ of the individual phases p in semicrystalline PCL at certain temperatures T . The uncertainties were estimated via error propagation from the reading uncertainty of the literature data for ρ_a and ρ_{tot} of amorphous and semicrystalline PCL and the uncertainty of the measured sample fractions. The small uncertainties of the relative spin densities are negligible for the fits of spin-diffusion and Saturation-Recovery curves as their effect on the simulated data is only marginal.

F. Spin Diffusion

F.1. Description of Magnetization Transfer Between Two Spins 1/2

Based on the following calculation it can be demonstrated easily that a magnetization transfer actually takes place under dipolar interaction [17]. We assume a quantum-mechanical ensemble of two spins 1 and 2 with quantum numbers $I_1 = I_2 = \frac{1}{2}$ which are located at a distance r from each other in a magnetic field being aligned along the direction z of the coordinate system. The state of this system at time t can be described by means of the density operator $\hat{\rho}(t)$. At time $t = 0$ only spin 1 shall exhibit magnetization along z direction: $M_z = -\gamma_1 \hbar \hat{I}_{1z}$. Thus, for $t = 0$ the density operator of the ensemble corresponds to the z component of the spin operator of spin 1: $\hat{\rho}(0) = \hat{I}_{1z}$. The dipolar Hamiltonian \hat{H}_D specifies the pairwise dipolar interaction between the two spins, changing the initial state and mediating spin diffusion. In the case of a weak homonuclear coupling (compared to the Zeeman interaction) it is given by

$$\hat{H}_D = \omega_D(3\hat{I}_{1z}\hat{I}_{2z} - \hat{\mathbf{I}}_1 \cdot \hat{\mathbf{I}}_2)$$

with the spin operators $\hat{\mathbf{I}}_{1,2}$ and their z components $\hat{I}_{1z,2z}$. Via time evolution of the density operator by the help of the propagator $\hat{U}(t) = e^{-i\hat{H}_D t}$ the state of the ensemble at time $t > 0$ can be calculated using a series expansion of the exponential operator [17]:

$$\begin{aligned} \hat{\rho}(t) &= e^{-i\hat{H}_D t} \hat{\rho}(0) e^{+i\hat{H}_D t} \\ &= \hat{\rho}(0) + [-i\hat{H}_D t, \hat{\rho}(0)] + \frac{1}{2!} [-i\hat{H}_D t, [-i\hat{H}_D t, \hat{\rho}(0)]] \\ &\quad + \frac{1}{3!} [-i\hat{H}_D t, [-i\hat{H}_D t, [-i\hat{H}_D t, \hat{\rho}(0)]]] + \dots \\ &= \hat{\rho}(0) - \frac{it}{1!} [\hat{H}_D, \hat{\rho}(0)] + \frac{(it)^2}{2!} [\hat{H}_D, \hat{r}_1] - \frac{(it)^3}{3!} [\hat{H}_D, \hat{r}_2] + \dots, \end{aligned}$$

where the brackets denote the commutator. Inserting the Hamiltonian \hat{H}_D and $\hat{\rho}(0)$ and using the commutators

$$\begin{aligned} [\hat{H}_D, \hat{\rho}(0)] &= i\omega_D(\hat{I}_{1y}\hat{I}_{2x} - \hat{I}_{1x}\hat{I}_{2y}) = \hat{r}_1 \\ [\hat{H}_D, \hat{r}_1] &= \frac{\omega_D^2}{2}(\hat{I}_{1z} - \hat{I}_{2z}) = \hat{r}_2 \\ [\hat{H}_D, \hat{r}_2] &= \omega_D^2 \hat{r}_1 = \hat{r}_3 \\ &\dots \end{aligned}$$

yields

$$\begin{aligned} \hat{\rho}(t) &= e^{-i\hat{H}_D t} \hat{I}_{1z} e^{+i\hat{H}_D t} \\ &= \hat{I}_{1z} - \frac{it}{1!} (i\omega_D(\hat{I}_{1y}\hat{I}_{2x} - \hat{I}_{1x}\hat{I}_{2y})) + \frac{(it)^2}{2!} \left(\frac{\omega_D^2}{2} (\hat{I}_{1z} - \hat{I}_{2z}) \right) \\ &\quad - \frac{(it)^3}{3!} (i\omega_D^3(\hat{I}_{1y}\hat{I}_{2x} - \hat{I}_{1x}\hat{I}_{2y})) + \frac{(it)^4}{4!} \left(\frac{\omega_D^4}{2} (\hat{I}_{1z} - \hat{I}_{2z}) \right) - \dots + \dots \end{aligned}$$

After rearrangement and exploitation of the sum representation of $\cos(\omega_D t)$ and $\sin(\omega_D t)$ one obtains

$$\hat{\varrho}(t) = \frac{1}{2}\hat{I}_{1z}(1 + \cos(\omega_D t)) + \frac{1}{2}\hat{I}_{2z}(1 - \cos \omega_D t) + (\hat{I}_{1y}\hat{I}_{2x} - \hat{I}_{1x}\hat{I}_{2y}) \sin(\omega_D t) .$$

The first two expressions in the sum indicate that, compared to the initial state $\hat{\varrho}(0) = \hat{I}_{1z}$, magnetization has been transferred from spin 1 to spin 2 to a certain extent which depends on the actual dipolar coupling strength ω_D . Additionally, a sine-modulated double-quantum term has developed under dipolar interaction, which cannot be detected as transverse magnetization after a 90° pulse. The cosinusoidal oscillation of detectable magnetization in the two-spin system, expressed in the first two terms of the sum, will be damped in a multi-spin system due to a multitude of mutual couplings yielding a diffusive behavior of the magnetization $M_z(t) \sim \sqrt{t}$, if couplings of different strengths or between spins of differing distances exist [17].

F.2. The Simulation Program for Calculating Spin-Diffusion and Saturation-Recovery Curves

Because solving the one-dimensional spin-diffusion equation 4.11 in consideration of T_1 relaxation (see Section 4.3.2) is possible only numerically, it was transformed into a finite difference equation similar to Eq. 4.10:

$$\begin{aligned} \frac{M(x_i, t_{j+1}) - M(x_i, t_j)}{\Delta t} &= D_p \frac{M(x_{i-1}, t_j) + M(x_{i+1}, t_j) - 2M(x_i, t_j)}{(\Delta x)^2} \\ &+ \frac{1}{T_{1p}}(M_0 - M(x_i, t_j)) \\ M(x_i, t_{j+1}) &= M(x_i, t_j) + \frac{D_p \Delta t}{(\Delta x)^2} (M(x_{i-1}, t_j) + M(x_{i+1}, t_j) - 2M(x_i, t_j)) \\ &+ \frac{\Delta t}{T_{1p}}(M_0 - M(x_i, t_j)) . \end{aligned} \quad (\text{F.1})$$

Here, M denotes the space and time-dependent magnetization. The variables of space x_i and time t_j adopt discrete values with equidistant increments $\Delta x = x_{i+1} - x_i$ and $\Delta t = t_{j+1} - t_j$, respectively. M_0 designates the equilibrium magnetization of the T_1 relaxation process. According to Eq. F.1 the simulation program written by Prof. H. Schneider calculates $M(x_i, t_{j+1})$ stepwise for every domain p . By reason of symmetry, it is sufficient to conduct the computation for half of the repeat unit (see Fig. 7.6 (b)) and to introduce the following periodic symmetry and boundary conditions to take into account the lamellar structure of the system [139, 141]:

- at the symmetry planes s (see Fig. 7.6 (a)), with space coordinate x_s , magnetization is not allowed to change locally: $M(x_s, t) = M(x_{s+1}, t) = M(x_{s-1}, t)$
- at the boundary planes b located at x_b (see Fig. 7.6 (b)) between two phases p_1 and p_2 magnetization must develop continuously: $M_{p_1}(x_b, t) = M_{p_2}(x_b, t)$,
- boundary planes b must not act as magnetization sources or sinks, i. e. the flux of

magnetization has to be continuous there:

$$\varrho_{H,p1} D_{p1} \frac{M_{p1}(x_b, t) - M_{p1}(x_{b-1}, t)}{x_b - x_{b-1}} = \varrho_{H,p2} D_{p2} \frac{M_{p2}(x_{b+1}, t) - M_{p2}(x_b, t)}{x_{b+1} - x_b}$$

The last expression contains the phase-specific proton spin density $\varrho_{H,p}$ (see Section 4.1). The observable in the experiments is the total magnetization $M_p(\tau_{\text{diff}})$ in each phase p . An equivalent parameter $M_p(t_j)$ can be derived from the simulation by summing up the magnetization $M(x_i, t_j)$ of every discrete position x_j in a phase p , multiplied by the corresponding proton spin density $\varrho_{H,p}$. Here, the time coordinate t_j corresponds to the mixing time τ_{diff} in the experimental setup. Depending on the initial values of the magnetization in the individual phases $M_p(0)$ and the equilibrium magnetization M_0 ,¹ the magnetization development in spin-diffusion and Saturation-Recovery experiments can be computed. In order to compare simulated and measured data the magnetization development has to be calculated starting from a given initial distribution and proceeding until the equilibrium distribution is reached. The accuracy of the calculation depends on the choice of the space and time increments Δx and Δt . Following from Eq. F.1 the value of the expression $(D_p \Delta t)/(\Delta x)^2$ must be limited. For convergence a value smaller than 0.5 is necessary. All fits and simulations represented herein were conducted with equal increments $\Delta x = 0.5 \text{ \AA}$ and $\Delta t = 2 \text{ \mu s}$ to achieve comparable results.

F.3. Derivation of the Source Domain Size by means of the Initial Rate Approximation

The analytical solution of the spin-diffusion equation for a scenario of a finite source region from which magnetization is transferred into an infinite sink region can be used to deduce an expression for the source domain size in a two-phase polymer system. In order to explain this idea, the derivation of the IRA equation shall be described here in detail according to the considerations of Clauss et al. [139]. The space coordinate in the one-dimensional scenario is denoted by x and the time by t . In the experimental setup the time coordinate t corresponds to the mixing time τ_{diff} . When magnetization emanates from a point-shaped source at the position $x = r$, the Gaussian function

$$M(x, t) = \frac{M_0}{\sqrt{4\pi Dt}} e^{-\frac{(x-r)^2}{4Dt}} \quad (\text{F.2})$$

for the magnetization $M(x, t)$ is a solution of the spin-diffusion equation 4.11 for a constant spin-diffusion coefficient D and a constant proton spin density ϱ_H over all positions x . Here, M_0 is the initial magnetization at $x = r$.

A finite magnetization source at $-r_0 < x < r_0$ between infinite sinks at $|x| > r_0$ at $t = 0$ can be represented by an infinite number of point-shaped sources uniformly distributed over all positions $-r_0 < x < r_0$. Thus, in this case a superposition of Gaussian functions

¹The value of M_0 is 0 for the calculation of spin-diffusion curves due to the z filter used in the experiments (see Section 4.3.2) and 1 for the calculation of Saturation-Recovery curves.

F.2 at $r = -r_0 \dots r_0$ solves Eq. 4.11:

$$\begin{aligned}
 M(x, t) &= \int_{-r_0}^{r_0} \frac{M_0}{\sqrt{4\pi Dt}} e^{-\frac{(x-r)^2}{4Dt}} dr = -\frac{M_0}{\sqrt{\pi}} \int_{\frac{x+r_0}{\sqrt{4Dt}}}^{\frac{x-r_0}{\sqrt{4Dt}}} e^{-z^2} dz \\
 &= -\frac{M_0}{\sqrt{\pi}} \left(\int_{\frac{x+r_0}{\sqrt{4Dt}}}^0 e^{-z^2} dz + \int_0^{\frac{x-r_0}{\sqrt{4Dt}}} e^{-z^2} dz \right) \\
 &= \frac{M_0}{\sqrt{\pi}} \left(\int_0^{\frac{x+r_0}{\sqrt{4Dt}}} e^{-z^2} dz + \int_0^{-\frac{x-r_0}{\sqrt{4Dt}}} e^{-z^2} dz \right) \\
 &= \frac{M_0}{2} \operatorname{erf} \left(\frac{r_0 + x}{\sqrt{4Dt}} \right) + \frac{M_0}{2} \operatorname{erf} \left(\frac{r_0 - x}{\sqrt{4Dt}} \right), \tag{F.3}
 \end{aligned}$$

where $\operatorname{erf}(x)$ is the error function defined as

$$\operatorname{erf}(x) = \int_0^x \frac{2}{\pi} e^{-z^2} dz .$$

Equation F.3 is symmetric with respect to $x = 0$ and contains one term each for the magnetization transfer via the source-sink interfaces at $x = -r_0$ and at $x = r_0$. At $t = 0$ it results in a box function with $M(x, t = 0) = M_0$ for $|x| < r_0$ and $M(x, t = 0) = 0$ otherwise. With increasing time the magnetization at $x = 0$ and the magnetization gradient near the interfaces decreases until at $t \rightarrow \infty$ a uniform distribution of magnetization is reached for all x with $M(x) \rightarrow 0$. However, as a result of the error function properties at short times $t \ll (r_0^2/4D)$ the first term in Eq. F.3 is approximately constant in time and space for $x > 0$ while the second one yields a constant at positions $x < 0$:

$$M(x > 0, t \ll (r_0^2/4D)) = \frac{M_0}{2} + \frac{M_0}{2} \operatorname{erf} \left(\frac{r_0 - x}{\sqrt{4Dt}} \right) \tag{F.4}$$

$$M(x < 0, t \ll (r_0^2/4D)) = \frac{M_0}{2} \operatorname{erf} \left(\frac{r_0 + x}{\sqrt{4Dt}} \right) + \frac{M_0}{2} \tag{F.5}$$

These expressions equal the solution of Eq. 4.11 for an infinite source either at $x < r_0$ (Eq. F.4) or at $x > -r_0$ (Eq. F.5). (Alternatively, these solutions can also be derived by superposing the solutions for an infinite number of point-shaped sources in the corresponding source regions.) Hence, at short times the magnetization close to an interface develops as if no other interface would exist (cf. Fig. 7.18 (a)). It therefore suffices to consider only the magnetization development near one interface even if many more of the same kind are present. Expressions of the type of Eqs. F.4 or F.5 can therefore also be used to describe the short-time behavior of magnetization in periodic systems of alternating source and sink regions as present in the 2P model.

Now the solution shall be specified for a periodic two-phase polymer system containing source domains A and sink domains B with individual spin-diffusion coefficients D_A and D_B and proton spin densities $\varrho_{H,A}$ and $\varrho_{H,B}$ which are each constant within the respective phase. For this purpose the solutions for each phase have to be adapted to fulfill certain initial and boundary conditions equal to those given in Section F.2. Here, they are presented in a continuous form:

- At $t = 0$ the source domain A contains the full magnetization, i. e.

$$M_A(x, t = 0) = M_0 \text{ and } M_B(x, t = 0) = 0,$$

- at the boundary surface r_0 between source and sink domain the magnetization develops continuously, i. e. $M_A(r_0, t) = M_B(r_0, t)$,
- at the boundary surface r_0 the magnetization flux is continuous, i. e.

$$-D_A \varrho_{H,A} \frac{\partial M_A(r_0, t)}{\partial x} = -D_B \varrho_{H,B} \frac{\partial M_B(r_0, t)}{\partial x}$$

The differences in spin-diffusion coefficients and spin densities of the phases A and B result in changes of the absolute values of the magnetization compared to the expressions F.4 and F.5, while the principal structure of the solution is preserved. Therefore for both phases a generalized ansatz is made:

$$M_A(x, t) = E_A + F_A \operatorname{erf} \left(\frac{x - r_0}{\sqrt{4Dt}} \right) \text{ for domain A at } x < r_0 \text{ and} \quad (\text{F.6})$$

$$M_B(x, t) = E_B + F_B \operatorname{erf} \left(\frac{x - r_0}{\sqrt{4Dt}} \right) \text{ for domain B at } x > r_0. \quad (\text{F.7})$$

Applying the conditions above to these equations and taking into account the properties of the error function

$$\operatorname{erf}(x \rightarrow \pm\infty) = \pm 1$$

$$\operatorname{erf}(0) = 0$$

$$\begin{aligned} \frac{d}{dx} \operatorname{erf}(y(x)) &= \frac{d}{dx} \int_0^{y(x)} \frac{2}{\pi} e^{-z^2} dz = \frac{d}{dx} (F(y(x)) - F(0)) \\ &= \frac{dF(y)}{dy} \frac{dy(x)}{dx} = \frac{2}{\pi} e^{-y(x)^2} \frac{dy(x)}{dx}, \end{aligned}$$

with $F(y)$ being the antiderivative of $\left(\frac{2}{\pi} e^{-y^2}\right)$, one obtains

$$E_A - F_A = M_0,$$

$$E_B + F_B = 0,$$

$$E_A = E_B \text{ and}$$

$$\sqrt{D_A} \varrho_{H,A} F_A = \sqrt{D_B} \varrho_{H,B} F_B.$$

Rearranging these expressions and inserting them into Eq. F.6 and Eq. F.7 yields [139]

$$\begin{aligned} M_A(x, t) &= \frac{M_0 \varrho_{H,A} \sqrt{D_A}}{\varrho_{H,A} \sqrt{D_A} + \varrho_{H,B} \sqrt{D_B}} - \frac{M_0 \varrho_{H,B} \sqrt{D_B}}{\varrho_{H,A} \sqrt{D_A} + \varrho_{H,B} \sqrt{D_B}} \operatorname{erf} \left(\frac{x - r_0}{\sqrt{4D_A t}} \right) \text{ and} \\ M_B(x, t) &= \frac{M_0 \varrho_{H,A} \sqrt{D_A}}{\varrho_{H,A} \sqrt{D_A} + \varrho_{H,B} \sqrt{D_B}} - \frac{M_0 \varrho_{H,A} \sqrt{D_A}}{\varrho_{H,A} \sqrt{D_A} + \varrho_{H,B} \sqrt{D_B}} \operatorname{erf} \left(\frac{x - r_0}{\sqrt{4D_B t}} \right) \\ &= \frac{M_0 \varrho_{H,A} \sqrt{D_A}}{\varrho_{H,A} \sqrt{D_A} + \varrho_{H,B} \sqrt{D_B}} \operatorname{erfc} \left(\frac{x - r_0}{\sqrt{4D_B t}} \right) \end{aligned}$$

with $\operatorname{erfc}(x) = 1 - \operatorname{erf}(x)$. For $D_A = D_B$ and $\varrho_{H,A} = \varrho_{H,B}$ Eq. F.4 results again from both solutions.

The total magnetization $M_B(t)$ of the sink at short times t can be estimated by summing

up the magnetization $M_B(x, t)$ of all spins on cross-sectional areas A_S parallel to the interface between A and B for positions $x > r_0$ in consideration of the spin density:

$$\begin{aligned}
 M_B \left(t \ll \frac{r_0^2}{4D_B} \right) &\approx \varrho_{H,B} \int_{r_0}^{\infty} M_B(x, t) A_S dx \\
 &= \varrho_{H,B} A_S \int_{r_0}^{\infty} \frac{M_0 \varrho_{H,A} \sqrt{D_A}}{\varrho_{H,A} \sqrt{D_A} + \varrho_{H,B} \sqrt{D_B}} \operatorname{erfc} \left(\frac{x - r_0}{\sqrt{4D_B t}} \right) dx \\
 &= \frac{2}{\sqrt{\pi}} \frac{A_S M_0 \varrho_{H,A} \varrho_{H,B} \sqrt{D_A} \sqrt{D_B}}{(\varrho_{H,A} \sqrt{D_A} + \varrho_{H,B} \sqrt{D_B})} \sqrt{t}
 \end{aligned} \tag{F.8}$$

Here, the relation $\int_x^{\infty} \operatorname{erfc}(z) dz = \frac{1}{\sqrt{\pi}} e^{-x^2} - x \operatorname{erfc}(x)$ was used. Correspondingly, for the total magnetization $M_A(t)$ of the source one finds

$$\begin{aligned}
 M_A \left(t \ll \frac{r_0^2}{4D_A} \right) &\approx \varrho_{H,A} \int_0^{r_0} M_A(x, t) A_S dr \\
 M_A(t = 0) &\approx \varrho_{H,A} \int_0^{r_0} M_A(x, t = 0) A_S dr = \varrho_{H,A} M_0 A_S r_0
 \end{aligned} \tag{F.9}$$

As visible in Eq. F.8 for short times the sink magnetization follows a \sqrt{t} dependence. The approximated total intensity $M_B(t \ll \frac{r_0^2}{4D_B})$ reaches the value of the total initial magnetization $M_A(t = 0)$ of the system at a characteristic time t_0 :

$$\begin{aligned}
 M_B \left(t \ll \frac{r_0^2}{4D_B}, \sqrt{t_0} \right) &= M_A(t = 0) \\
 \frac{2}{\sqrt{\pi}} \frac{A_S M_0 \varrho_{H,A} \varrho_{H,B} \sqrt{D_A} \sqrt{D_B}}{\varrho_{H,A} \sqrt{D_A} + \varrho_{H,B} \sqrt{D_B}} \sqrt{t_0} &= r_0 \varrho_{H,A} A_S M_0
 \end{aligned} \tag{F.10}$$

The same relation F.10 can also be derived from the expression for the source magnetization via $M_A \left(t \ll \frac{r_0^2}{4D_A}, \sqrt{t_0} \right) = 0$.

For a given value of $\sqrt{t_0}$, Eq. F.10 can finally be used to determine r_0 which in our scenario corresponds to half of the source domain thickness d_A :

$$d_A = 2r_0 = \frac{4}{\sqrt{\pi}} \frac{\sqrt{D_A} \sqrt{D_B}}{\left(\frac{\varrho_{H,A}}{\varrho_{H,B}} \sqrt{D_{H,A}} + \sqrt{D_B} \right)} \sqrt{t_0}. \tag{F.11}$$

F.4. Effects of PCL Domain-Thickness Distributions on Spin Diffusion

It is known from literature, that domain thicknesses in semicrystalline polymers depend on molecular weight, crystallization temperature T_c (0.5 K) and the thermal history of the sample [10]. The PCL sample investigated by spin-diffusion experiments (see Section 7.2) is polydisperse and slight deviations of T_c could not be avoided. Hence, it seems self-evident that distributions of domain sizes exist here. Actually, this is confirmed by the SAXS results, where broad peaks were detected in the interface-distance distribution function. Interestingly, in PCL the distribution width of the amorphous-phase domain thicknesses is significantly larger than the one obtained for the crystalline lamellae (see Table 7.1). This is presumed to be a feature of crystal-fixed polymers [218].

The fact that domain sizes differ within the phases of a polymer sample seems to be accepted in literature concerning SAXS experiments (see, e. g., Ref. [324]) and has also been addressed in NMR literature [89, 116, 250]. However, only a few works deal with the impact of domain-size distributions on spin-diffusion data in more detail. As the domain thicknesses influence the shape of the spin-diffusion curves, the existence of different thicknesses within the phases may alter the data in a complex way [325]. Therefore it shall be discussed here, whether thickness distributions could have induced the discrepancies between measured data and fit data described in Section 7.3.

Domain-size distributions arise when each polymer domain exhibits a constant thickness over its complete lateral extension while different regions of an individual phase exhibit non-uniform domain sizes (see Fig. F.1 (a)), but also when there are thickness fluctuations within distinct domains resulting in non-planar interfaces between them (see Fig. F.1 (b)). Both scenarios may occur in PCL. The analysis of the SAXS data relies on the former concept, the effects of which shall be investigated in this section, while consequences of the latter are discussed in Section 7.5.

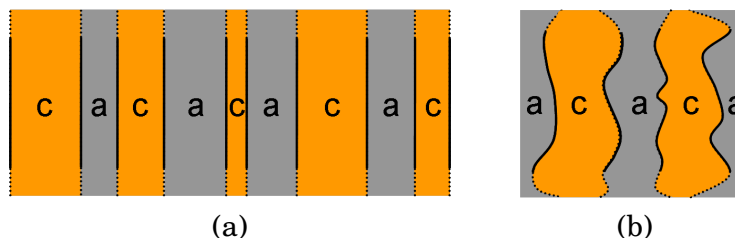


Figure F.1.: Two-phase scenarios showing non-uniform domain thicknesses (see text). The labels *c* and *a* designate the crystalline and amorphous phase, respectively.

The simulation program (see Section 7.3 and Appendix F.2) allows to simulate spin-diffusion curves for non-uniform domain sizes as depicted in Fig. F.1 (a). Here, for each phase p random domain thicknesses are generated which fluctuate around a given mean value $d_{p,\text{ave}}$ following a Gaussian distribution with an adjustable relative distribution width $\sigma_{\text{rel},p} = \sigma_p/d_p$.

Performing simulations for the 2P model with exactly the same program as described here, Mauri et al. have shown that distributions of domain sizes of the rigid and mobile-amorphous phase with relative widths $\sigma_{\text{rel},p}$ up to 0.75 cause only slight changes in the shape of the spin-diffusion curves with root-mean-square deviations *rms* smaller than 3% [8]. From their work they concluded that the domain thicknesses and spin-diffusion coefficients obtained from the fits do not deviate too much from the true values, when relative thickness fluctuations are smaller than $\sigma_{\text{rel},p} \approx 0.2$.

However, according to the SAXS results, in PCL these fluctuations can be larger than 0.2 (see Table 7.1). In order to estimate the effect of thickness distributions for the specific case of PCL, simulations have been performed here for the 2P and the 3P model with realistic parameter values for PCL at 45°C and different domain-size distribution widths ($\sigma_{\text{rel},p} = 0.1, 0.3, 0.5$ and 0.6 for the 2P model and $\sigma_{\text{rel},p} = 0.1$ and 0.5 for the 3P model), on the one hand by assuming domain-size fluctuations in a single phase only and on the other hand by varying the sizes in several or all phases, simultaneously. For every distribution width three different sets of domain thicknesses were tried for the 2P system and only one for the 3P system. When generating the random thicknesses for the individual polymer phases, it was checked that the standard deviation from the

corresponding mean thickness was in accordance with the settled distribution width.

The thickness distributions expectedly induced changes in the shape of the spin-diffusion and Saturation-Recovery curves, which increased with rising distribution width. For domain-size distributions in several polymer phases at the same time the effects of the thickness fluctuations of the single phases added up. The following effects could be detected (see Fig. F.2):

- Changes due to a distribution of mobile-amorphous-phase, crystalline-phase and rigid-phase domain thicknesses followed the same trend and for the same distribution width they also exhibited the same extent.
- The effects of a distribution of interphase domain thicknesses were negligible as the interphase fraction in the simulation model was small.
- The Saturation-Recovery curves exhibited only small changes due to thickness fluctuations in the region of decreasing slope.
- The most striking effect on the shape of the spin-diffusion curves was a decrease of the maximum intensity of the sink-domain signal with increasing distribution width of the domain size of the mobile-amorphous, crystalline or rigid phase, combined with a slight shift of the maximum to shorter mixing times τ_{diff} . At the same time the source domain signal exhibited a slightly retarded decay and/or an increased magnetization level at large mixing times. The latter was predicted by Cheung, who investigated the implications of disorder in polymer morphology on the analytical solution of the spin-diffusion equation [325].

These shape variations were rather small but systematic (see Fig. F.3). The *rms* deviation between simulated spin-diffusion curves calculated for constant domain thicknesses and for a realistic distribution of domain sizes in PCL, derived via

$$rms = \frac{1}{n} \sqrt{\sum_{i=1}^n \frac{(I_{2i} - I_{1i})^2}{(I_{1i})^2}},$$

amounts to 0.4% to 2.4% only and is in the range of the values given by Mauri et al. In the equation n denotes the number of data points in the spin-diffusion curves and I_{1i} and I_{2i} represent the intensities of the two curves which are compared (see Fig. F.3).

To check the consequences of thickness distributions on the parameter values from a fit using a model with constant domain sizes, spin-diffusion and Saturation-Recovery data were simulated assuming realistic distribution widths for the thicknesses of the crystalline and mobile-amorphous domains in PCL at 45°C (cf. Table 7.1): $\sigma_{\text{rel,c}} = 0.11$ and $\sigma_{\text{rel,a}} = 0.52$. The value for the interphase was chosen to be $\sigma_{\text{rel,i}} = 0.11$ as well. Now a simultaneous fit to these data was performed using the 2P or 3P model with the parameter values underlying the simulation used as initial values for the fit. Here, the mean thicknesses from the simulation served as domain size parameter values. The fitting of simulated data which were generated for constant domain sizes worked perfectly well and reproduced the simulation parameters, also when the initial values were changed. Keeping the spin-diffusion coefficients and T_1 values fixed in the fit to data simulated for a distribution of domain sizes, fit curves were obtained which matched the simulated ones acceptably well but brought about too large thickness values for all three polymer phases. The thicknesses d_a and d_c were $\sim 14\%$ higher than defined in the simulation, d_i

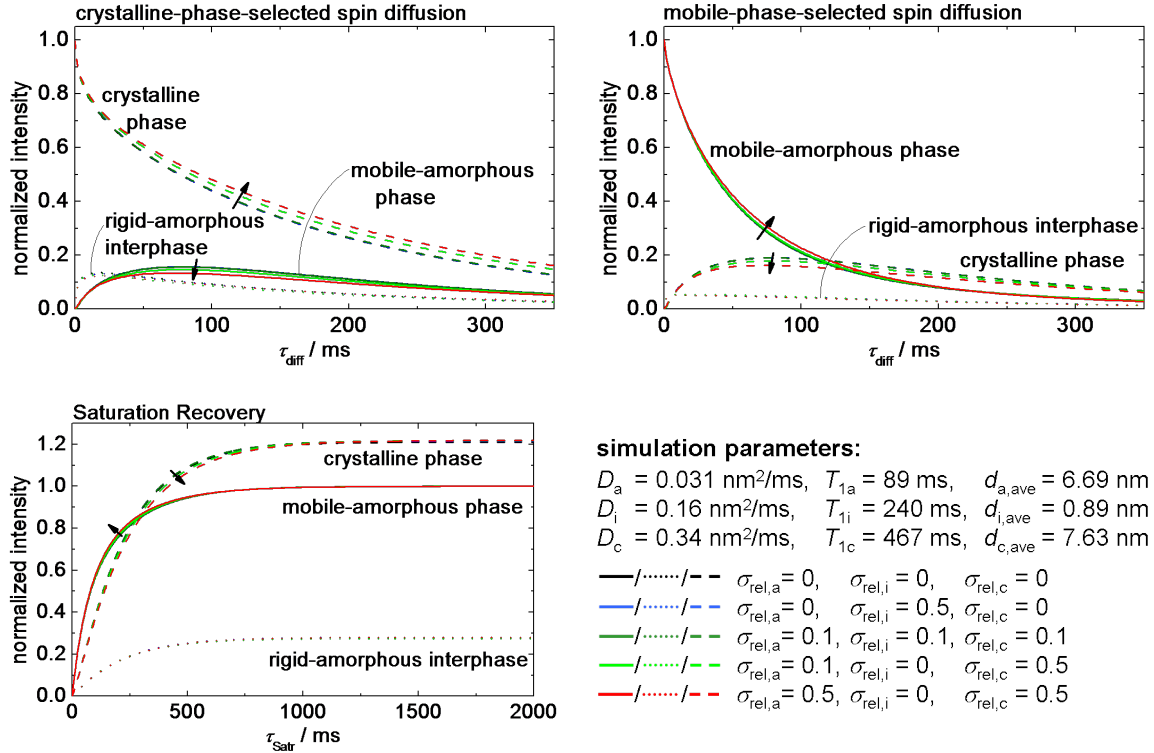


Figure F.2.: Demonstration of the effects of domain-size distributions on simulated data from crystalline-phase-selected (upper left) and mobile-amorphous-phase-selected (upper right) spin-diffusion and Saturation-Recovery (lower left) experiments. The simulations were performed for a 3P model and different combinations of relative thickness distribution widths $\sigma_{\text{rel},a,i,c}$ using the parameters shown in the lower right of the figure and the relative spin densities $\varrho_{H,a} = 1$, $\varrho_{H,i} = 1.034$ and $\varrho_{H,c} = 1.067$. The subscripts *a*, *i* and *c* designate the mobile-amorphous phase, interphase and crystalline phase, respectively. The arrows depict curve variations for increasing distribution widths.

deviated by $\sim 8\%$. These findings agree with the deviation of $\sim 10\%$ stated by Mauri et al. [8]. As for PCL the aim was to derive spin-diffusion coefficients, in a next step the domain sizes were fixed in the fit, while the diffusion coefficients were free parameters. The curves from fit and simulation matched well for the source domain, but the fit could not reproduce the rise of the sink curve completely (see Fig. F.4). However, when fitting noisy experimental data such small differences would not be evident.

Nevertheless, the systematic changes in the curve shape mentioned above induce modifications of the fit parameters compared to the values used for the simulation. The reduced sink-phase intensity is compensated in the fit by a systematic and partly significant variation of the spin-diffusion coefficients. The fit pretended values of D_a which were too low by a factor of 0.67 to 0.77 compared to the true values used in the simulation. Stable fits also yielded too small values of D_{rig} differing from the value of the simulation by the same factor as obtained for D_a . On the other hand, when the initial fit parameters were chosen in an unfavorable way the value of D_{rig} increased dramatically up to implausibly high values larger than $2 \text{ nm}^2/\text{ms}$ but no stable fit was obtained. Such high values of D_{rig} should be discarded when fitting experimental data as they were provoked artificially by the domain-size distributions.

Stable fits using the 3P model were obtained for reduced values of D_a and D_c and in-

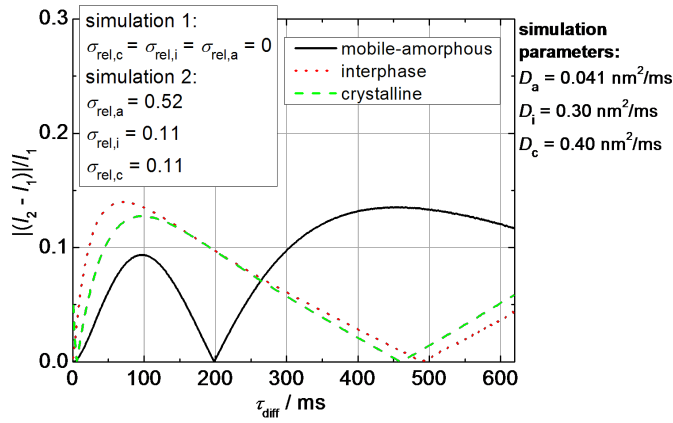


Figure F.3.: Relative difference between the intensities of spin-diffusion curves simulated for constant domain thicknesses (simulation 1 with intensity I_1) and for a realistic distribution of domain sizes (simulation 2 with intensity I_2) for PCL at 45°C. The intensities were calculated using the spin-diffusion coefficients given in the plot. The remaining simulation parameters are the same as in Fig. F.2.

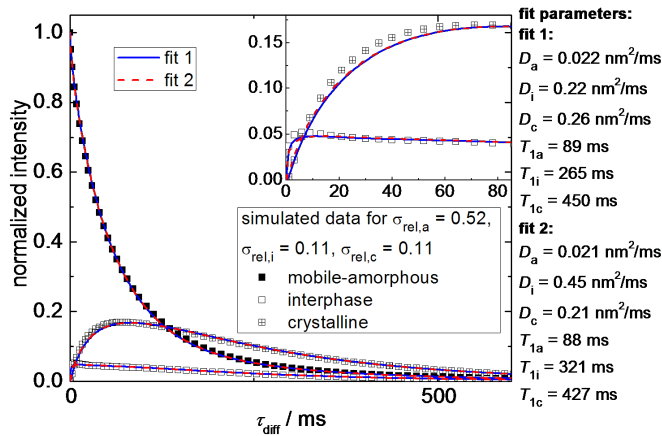


Figure F.4.: Comparison of spin-diffusion data simulated for a realistic distribution of domain sizes (see legend) with two fits to these data, using a fit model which ignores the size distribution. In the fits the domain thicknesses were fixed to the average values applied in the simulation and given in Fig. F.2. The spin densities used are indicated there as well.

creased values of D_i . However, it is not possible to estimate to which extent the values of D_c and D_i deviated from the ones of the simulation, as these parameters strongly depended on each other and both had similar effects on the spin-diffusion curves. A low value of D_c induced a high value of D_i and vice versa. This way, stable fits were possible for large values of $D_c > 0.6 \text{ nm}^2/\text{ms}$ on the one hand and for $D_c < D_i$ on the other hand (see Fig. F.4). The latter seems physically unlikely because, due to less anisotropic chain mobility in the interphase, the dipolar coupling strength and therefore also the spin-diffusion coefficient should be smaller than in the crystallites. The interdependence of all three parameters D_c , D_i and D_a is depicted in Fig. F.5 (b).

Compared to the values of the simulation, the T_1 values did not change appreciably in the fit for the 2P model. Yet, from fits using the 3P model only T_{1a} could be determined precisely. Similar to the interdependence of the diffusion coefficients, also T_{1i} and T_{1c} were coupled, enabling large ranges of possible fit values including $T_{1i} > T_{1c}$. This relation seems doubtful because for the apparent T_1 values derived from the initial rises of the Saturation-Recovery curves the inverted trend was observed (see Fig. 5.3 in Section 5.1).

In fact, interdependencies between the fit results for D_i and D_c as well as T_{1i} and T_{1c} have been found in the fits of measured data for PCL (see Fig. F.5 (a)). As shown here, dubious combinations of fit parameters such as $D_c < D_i$ or $T_{1c} < T_{1i}$ can be discarded as fitting artifacts resulting from neglected domain-size distributions.

In summary, due to the domain-size fluctuations within the polymer phases, stable

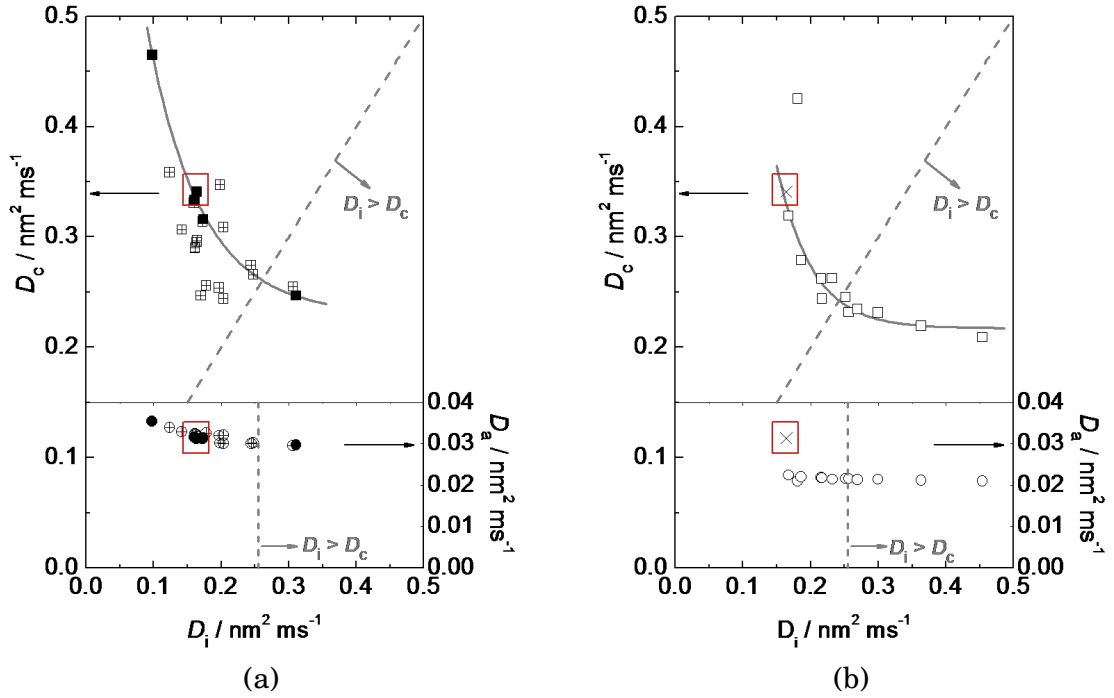


Figure F.5.: Interdependence between the parameter values of the spin-diffusion coefficients D_c , D_a and D_i of crystalline phase, mobile-amorphous phase and interphase. The values were obtained from fits to experimental (a) and simulated (b) data using the program described in Section 7.3 for the 3P model, keeping the domain-size parameters fixed. The simulated data were calculated by means of the same program with parameter values given in Fig. F.2 but taking into account a realistic distribution of domain thicknesses (see text). The solid grey lines are guides to the eye. The red squares mark the set of spin-diffusion coefficients used for the simulation in (b). Crossed symbols in (a) depict values from fits with minor but still acceptable fit quality.

fits to the experimental data will yield average values of mobile-amorphous-phase and crystalline-phase spin-diffusion coefficients, which are lower than actually present in the sample, whereas the coefficient of the interphase will rather be determined too large. The true values cannot be obtained by means of the fit used here. However, a set of such associated apparent values nevertheless permits the determination of correct average domain sizes, which is usually the aim of spin-diffusion experiments. In this sense, neglecting domain-size distributions when fitting PCL spin-diffusion data is justified despite of a large distribution width of the mobile-amorphous-phase domain sizes.

For the experimental spin-diffusion curves in the 2P model a shift of the initial rise and decay was found for the sink and source signal intensity as compared to the simulation (see Sections 7.3 and 7.4). Yet, as shown here, domain-size distributions do not change the initial rise or decay time appreciably and thus cannot be a reason for such a delayed magnetization development. Also the unexpected shape of the measured interphase signal in the MAPE experiments is not caused by thickness fluctuations, as these influence the interphase signal only marginally. Furthermore, the maximum sink-curve signal intensities from MAPE-filtered and DQ-filtered experiments both decrease to the same extent due to realistic domain-size distributions in PCL (cf. Fig. F.2). The attempt to fit both sets of data with one set of spin-diffusion coefficients thus fails also when domain-size distributions are taken into account.

Bibliography

- [1] Pfeifer, H. (1999) A short history of nuclear magnetic resonance spectroscopy and of its early years in Germany. *Magn. Reson. Chem.*, **37**, S154–S159.
- [2] Ernst, R. R. (2010) Zurich's Contributions to 50 Years Development of Bruker. *Angew. Chem., Int. Ed.*, **49**, 8310–8315.
- [3] Nelson, F. A. and Weaver, H. E. (1964) Nuclear Magnetic Resonance Spectroscopy in Superconducting Magnetic Fields. *Science*, **146**, 223–232.
- [4] Lewandowski, J. R., Dumez, J.-N., Akbey, U., Lange, S., Emsley, L., and Oschkinat, H. (2011) Enhanced Resolution and Coherence Lifetimes in the Solid-State NMR Spectroscopy of Perdeuterated Proteins under Ultrafast Magic-Angle Spinning. *J. Phys. Chem. Lett.*, **2**, 2205–2211.
- [5] Samoson, A., Tuherm, T., Past, J., Reinhold, A., Anupöld, T., and Heinmaa, I. (2004) New Horizons for Magic-Angle Spinning NMR. *Topics in Current Chemistry*, Springer-Verlag Berlin Heidelberg.
- [6] Nishiyama, Y., Endo, Y., Nemoto, T., Utsumi, H., Yamauchi, K., Hioka, K., and Asakura, T. (2011) Very fast magic angle spinning ^1H - ^{14}N 2D solid-state NMR: Sub-micro-liter sample data collection in a few minutes. *J. Magn. Reson.*, **208**, 44–48.
- [7] Brown, S. P. (2012) Applications of high-resolution ^1H solid-state NMR. *Solid State Nucl. Magn. Reson.*, **41**, 1–27.
- [8] Mauri, M., Thomann, Y., Schneider, H., and Saalwächter, K. (2008) Spin-diffusion NMR at low field for the study of multiphase solids. *Solid State Nucl. Magn. Reson.*, **34**, 125–141.
- [9] Mandelkern, L. (1990) The Structure of Crystalline Polymers. *Acc. Chem. Res.*, **23**, 380–386.
- [10] Strobl, G. (2007) *The physics of polymers: concepts for understanding their structures and behavior*. Springer, 3., rev. and expanded edn.
- [11] Iwata, K. (2002) Role of entanglement in crystalline polymers 1. Basic theory. *Polymer*, **43**, 6609–6626.
- [12] Kitamaru, R., Horii, F., and Murayama, K. (1986) Phase Structure of Lamellar Crystalline Polyethylene by Solid-state High-Resolution ^{13}C NMR: Detection of the Crystalline-Amorphous Interphase. *Macromolecules*, **19**, 636–643.
- [13] Mandelkern, L., Alamo, R. G., and Kennedy, M. A. (1990) Interphase Thickness of Linear Polyethylene. *Macromolecules*, **23**, 4721–4723.
- [14] Cheng, J. L., Fone, M., Reddy, V. N., Schwartz, K. B., Fisher, H. P., and Wunderlich, B. (1994) Identification and quantitative analysis of the intermediate phase in a linear high-density polyethylene. *J. Polym. Sci., Part B: Polym. Phys.*, **32**, 2683–2693.
- [15] Schick, C., Wurm, A., Merzlyakov, M., Minakov, A., and Marand, H. (2001) Crystallization and melting of polycarbonate studied by temperature-modulated DSC (TMDSC). *J. Therm. Anal. Calorim.*, **64**, 549–555.
- [16] Flory, P. J. (1962) On the morphology of the crystalline state in polymers. *J. Am.*

- Chem. Soc.*, **84**, 2857–2867.
- [17] Schmidt-Rohr, K. and Spiess, H. W. (1994) *Multidimensional Solid-State NMR and Polymers*. Academic Press.
- [18] Schick, C., Dobbertin, J., Potter, M., Dehne, H., Hensel, A., Wurm, A., Ghoneim, A. M., and Weyer, S. (1997) Separation of components of different molecular mobility by calorimetry, dynamic mechanical and dielectric spectroscopy. *J. Thermal Anal.*, **49**, 499–511, Proceedings of the 11th International Congress on Thermal Analysis and Calorimetry.
- [19] Schick, C., Wurm, A., and Mohamed, A. (2001) Vitrification and devitrification of the rigid amorphous fraction of semicrystalline polymers revealed from frequency-dependent heat capacity. *Colloid Polym. Sci.*, **279**, 800–806.
- [20] Armitstead, K., Goldbeck-Wood, G., and Keller, A. (1992) Polymer crystallization theories. *Adv. Polym. Sci.*, **100**, 221–312.
- [21] Lauritzen, J. I. and Hoffman, J. D. (1960) Theory of formation of polymer crystals with folded chains in dilute solution. *J. Res. Natl. Bur. Stand., Sect. A: Phys. Chem.*, **64**, 73–102.
- [22] Hoffman, J. and Miller, R. (1997) Kinetics of crystallization from the melt and chain folding in polyethylene fractions revisited: Theory and experiment. *Polymer*, **38**, 3151–3212.
- [23] Strobl, G. (2000) From the melt via mesomorphic and granular crystalline layers to lamellar crystallites: A major route followed in polymer crystallization? *Eur. Phys. J. E*, **3**, 165–183.
- [24] Sadler, D. M. (1987) New explanation for chain folding in polymers. *Nature*, **326**, 174–177.
- [25] Konishi, T., Sakatsuji, W., Fukao, K., and Miyamoto, Y. (2011) Polymer crystallization mechanism through a mesomorphic state. *Phys. Rev. B*, **84**, 132102.
- [26] Muthukumar, M. (2007) Shifting paradigms in polymer crystallization. *Lect. Notes Phys.*, **714**, 1–18.
- [27] Olmsted, P. D., Poon, W. C. K., McLeish, T. C. B., Terrill, N. J., and Ryan, A. J. (1998) Spinodal-assisted crystallization in polymer melts. *Phys. Rev. Lett.*, **81**, 373–376.
- [28] Robelin-Souffaché, E. and Rault, J. (1989) Origin of the long period and crystallinity in quenched semicrystalline polymers. 1. *Macromolecules*, **22**, 3581–3594.
- [29] Ou-Yang, W.-C., Li, L.-J., Chen, H.-L., and Hwang, J. C. (1997) Bulk crystallization Behavior of Poly(ϵ -caprolactone) with a Wide Range of Molecular Weight. *Polym. J.*, **29**, 889–893.
- [30] Jenkins, M. J. and Harrison, K. L. (2006) The effect of molecular weight on the crystallization kinetics of polycaprolactone. *Polym. Adv. Technol.*, **17**, 474–478.
- [31] Bu, H. S., Gu, F. M., Bao, L. R., and Chen, M. (1998) Influence of entanglements on crystallization of macromolecules. *Macromolecules*, **31**, 7108–7110.
- [32] Psarski, M., Piorkowska, E., and Galeski, A. (2000) Crystallization of polyethylene from melt with lowered chain entanglements. *Macromolecules*, **33**, 916–932.

- [33] Umemoto, S. and Okui, N. (2002) Master curve of crystal growth rate and its corresponding state in polymeric materials. *Polymer*, **43**, 1423–1427.
- [34] Hu, W., Frenkel, D., and Mathot, V. B. F. (2003) Intramolecular nucleation model for polymer crystallization. *Macromolecules*, **36**, 8178–8183.
- [35] Xiao, Z. G., Sun, Q., Xue, G., Yuan, Z. R., Dai, Q. P., and Hu, Y. L. (2003) Thermal behavior of isotactic polypropylene freeze-extracted from solutions with varying concentrations. *Eur. Polym. J.*, **39**, 927–931.
- [36] Mandelkern, L. (2004) Crystallization kinetics of homopolymers: overall crystallization: a review. *Biophys. Chem.*, **112**, 109–116.
- [37] Hikosaka, M., Watanabe, K., Okada, K., and Yamazaki, S. (2005) Topological mechanism of polymer nucleation and growth - The role of chain sliding diffusion and entanglement. *Interphases and mesophases in polymer crystallization III*, vol. 191 of *Advances in Polymer Science*, pp. 137–186.
- [38] Lippits, D. R., Rastogi, S., Hohne, G. W. H., Mezari, B., and Magusin, P. C. M. M. (2007) Heterogeneous distribution of entanglements in the polymer melt and its influence on crystallization. *Macromolecules*, **40**, 1004–1010.
- [39] Traficante, D. (1996) Relaxation: An introduction. Grant, D. M. and Harris, R. K. (eds.), *Encyclopedia of Nuclear Magnetic Resonance*, John Wiley & Sons Ltd.
- [40] Saalwächter, K. (2007) Proton multiple-quantum NMR for the study of chain dynamics and structural constraints in polymeric soft materials. *Prog. Nucl. Magn. Reson. Spectrosc.*, **51**, 1–35.
- [41] Vaca Chávez, F. and Saalwächter, K. (2011) Time-Domain NMR Observation of Entangled Polymer Dynamics: Universal Behavior of Flexible Homopolymers and Applicability of the Tube Model. *Macromolecules*, **44**, 1549–1559.
- [42] Boyd, R. H. (1985) Relaxation processes in crystalline polymers: experimental behavior - a review. *Polymer*, **26**, 323–347.
- [43] Rault, J. (1997) The α c Transition in Semicrystalline Polymers: A New Look at Crystallization Deformation and Aging Process. *J. M. S. - Rev. Macromol. Chem. Phys.*, **C37**, 335–387.
- [44] Hu, W.-G. and Schmidt-Rohr, K. (1999) Polymer ultradrawability: the crucial role of α -relaxation chain mobility in the crystallites. *Acta Polym.*, **50**, 271–285.
- [45] Syi, J.-L. and Mansfield, M. L. (1988) Soliton model of the crystalline α relaxation. *Polymer*, **29**, 987–997.
- [46] Mark, J. E. (ed.) (2007) *Physical Properties of Polymers Handbook*. Springer, 2nd edn.
- [47] Woodruff, M. A. and Hutmacher, D. W. (2010) The return of a forgotten polymer - polycaprolactone in the 21st century. *Prog. Polym. Sci.*, **35**, 1217–1256.
- [48] Röthemeyer, F. and Sommer, F. (2006) *Kautschuktechnologie*. Carl Hanser Verlag, 2nd ed. edn.
- [49] Bittiger, H., Marchessault, R. H., and Niegisch, W. D. (1970) Crystal Structure of Poly- ϵ -caprolactone. *Acta Crystallogr., Sect. B: Struct. Crystallogr. Cryst. Chem.*, **B 26**, 1923–1927.

- [50] Bunn, C. W. and Alcock, T. C. (1945) The texture of polyethylene. *Trans. Faraday Soc.*, **41**, 317–325.
- [51] Chatani, Y., Okita, Y., Tadokoro, H., and Yamashita, Y. (1970) Structural Studies of Polyesters. III. Crystal Structure of Poly- ϵ -caprolactone. *Polym. J.*, **1**, 555–562.
- [52] Hu, H. L. and Dorset, D. L. (1990) Crystal structure of poly(ϵ -caprolactone). *Macromolecules*, **23**, 4604–4607.
- [53] Levitt, M. H. (2008) *Spin Dynamics - Basics of Nuclear Magnetic Resonance*. John Wiley & Sons, Ltd., 2nd edn.
- [54] Duer, M. J. (2002) *Solid-state NMR spectroscopy - principles and applications*. Blackwell Science.
- [55] Fukushima, E. and Roeder, S. B. (1981) *Experimental Pulse NMR: A Nuts and Bolts Approach*. Addison-Wesley Publishing Company.
- [56] Beckmann, P. A. (1988) Spectral densities and nuclear spin relaxation in solids. *Phys. Rep.*, **171**, 85–128.
- [57] Goldman, M. (1970) *Spin Temperature and Nuclear Magnetic Resonance in Solids*. The International Series of Monographs on Physics, Oxford Univ. Press.
- [58] Van Vleck, J. H. (1948) The dipolar broadening of magnetic resonance lines in crystals. *Phys. Rev.*, **74**, 1168–1183.
- [59] Wilson, C. W. and Pake, G. E. (1953) Nuclear magnetic resonance determination of degree of crystallinity in two polymers. *J. Polym. Sci.*, **10**, 503–505.
- [60] Fuschillo, N., Rhian, E., and Sauer, J. A. (1957) Nuclear Magnetic Resonance and Crystallinity in Polyethylene. *J. Polym. Sci.*, **25**, 381–384.
- [61] Slichter, W. P. and McCall, D. W. (1957) Note on the degree of crystallinity in polymers as found by nuclear magnetic resonance. *J. Polym. Sci.*, **25**, 230–234.
- [62] Bridges, B. J., Charlesby, A., and Folland, R. (1979) Pulsed n.m.r. studies of the crystallization kinetics of polyethylene from the melt and solution. *Proc. R. Soc. Lond. A*, **367**, 343–351.
- [63] Fedotov, V. D. and Schneider, H. (1989) Structure and Dynamics of Bulk Polymers by NMR-Methods. Diehl, P., Fluck, E., Günther, H., Kosfeld, R., and Seelig, J. (eds.), *Structure and Dynamics of Bulk Polymers by NMR-Methods*, vol. 21 of *NMR Basic Principles and Progress*, Springer Verlag Berlin Heidelberg New York.
- [64] Kosfeld, R. and v. Mylius, U. (1971) Linienbreiten- und Relaxationsphänomene bei der NMR-Festkörperspektroskopie. Diehl, P., Fluck, E., and Kosfeld, R. (eds.), *Natural and Synthetic High Polymers*, vol. 4 of *NMR Basic Principles and Progress*, Springer Verlag Berlin Heidelberg New York.
- [65] Slichter, W. (1971) NMR Studies of Solid Polymers. Diehl, P., Fluck, E., and Kosfeld, R. (eds.), *Natural and Synthetic High Polymers*, vol. 4 of *NMR Basic Principles and Progress*, Springer Verlag Berlin, Heidelberg, New York.
- [66] Derbyshire, W., van den Bosch, M., van Dusschoten, D., MacNaughtan, W., Farhat, I. A., Hemminga, M. A., and Mitchell, J. R. (2004) Fitting of the beat pattern observed in NMR free-induction decay signals of concentrated carbohydrate-water solutions. *J. Magn. Reson.*, **168**, 278–283.

- [67] Hansen, E. W., Kristiansen, P. E., and Pedersen, B. (1998) Crystallinity of polyethylene derived from solid-state proton NMR free induction decay. *J. Phys. Chem. B*, **102**, 5444–5450.
- [68] Hertlein, C., Saalwächter, K., and Strobl, G. (2006) Low-field NMR studies of polymer crystallization kinetics: Changes in the melt dynamics. *Polymer*, **47**, 7216–7221.
- [69] Lowe, I. J. and Norberg, R. E. (1957) Free-induction decays in solids. *Phys. Rev.*, **107**, 46–61.
- [70] Abragam, A. (1961) *The Principles of Nuclear Magnetism*. Oxford Univ. Press.
- [71] Brereton, M. G. (1991) An exact expression for the transverse nuclear magnetic resonance relaxation of a dynamic scale invariant polymer chain governed by a single relaxation time. *J. Chem. Phys.*, **94**, 2136–2142.
- [72] Dadayli, D., Harris, R. K., Kenwright, A. M., Say, B. J., and Sünnetcioglu, M. M. (1994) Solid-state ^1H n.m.r. studies of polypropylene. *Polymer*, **35**, 4083–4087.
- [73] Maus, A., Hertlein, C., and Saalwächter, K. (2006) A robust proton NMR method to investigate hard/soft ratios, crystallinity, and component mobility in polymers. *Macromol. Chem. Phys.*, **207**, 1150–1158.
- [74] Bergmann, K. and Nawotki, K. (1967) Eine neue Interpretation der Breitlinien-Kernresonanzspektren von linearem Polyäthylen. *Kolloid-Z. u. Z. Polymere*, **219**, 132–144.
- [75] Kitamaru, R., Horii, F., and Hyon, S. H. (1977) Proton magnetic resonance studies of the phase structure of bulk-crystallized linear polyethylene. *J. Polym. Sci., Part B: Polym. Phys.*, **15**, 821–836.
- [76] Eckman, R. R., Henrichs, P. M., and Peacock, A. J. (1997) Study of polyethylene by solid state NMR relaxation and spin diffusion. *Macromolecules*, **30**, 2474–2481.
- [77] Lili, Z., Chen, Q., and Hansen, E. W. (2005) Morphology and phase characteristics of high-density polyethylene probed by NMR spin diffusion and second moment analysis. *Macromol. Chem. Phys.*, **206**, 246–257.
- [78] Hedesiu, C., Demco, D. E., Kleppinger, R., Buda, A. A., Blümich, B., Remerie, K., and Litvinov, V. M. (2007) The effect of temperature and annealing on the phase composition, molecular mobility and the thickness of domains in high-density polyethylene. *Polymer*, **48**, 763–777.
- [79] Isasi, J. R., Mandelkern, L., Galante, M. J., and Alamo, R. G. (1999) The degree of crystallinity of monoclinic isotactic poly(propylene). *J. Polym. Sci., Part B: Polym. Phys.*, **37**, 323–334.
- [80] Rhim, W.-K., Pines, A., and Waugh, J. S. (1971) Time-Reversal Experiments in Dipolar-Coupled Spin Systems. *Phys. Rev. B*, **3**, 684–696.
- [81] Rhim, W.-K., Pines, A., and Waugh, J. S. (1970) Violation of the Spin Temperature Hypothesis. *Phys. Rev. Lett.*, **25**, 218–220.
- [82] Pines, A., Rhim, W.-K., and Waugh, J. S. (1972) Homogeneous and Inhomogeneous Nuclear Spin Echos in Solids. *J. Magn. Reson.*, **6**, 457.
- [83] Hafner, S., Demco, D. E., and Kimmich, R. (1996) Magic echoes and NMR imaging of solids. *Solid State Nucl. Magn. Reson.*, **6**, 275–293.

- [84] Schneider, H. and Schmiedel, H. (1969) Negative time development of a nuclear spin system. *Phys. Lett. A*, **A 30**, 298–299.
- [85] Matsui, S. (1991) Solid-state NMR imaging by magic sandwich echoes. *Chem. Phys. Lett.*, **179**, 187–190.
- [86] Fechete, R., Demco, D. E., and Blümich, B. (2003) Chain orientation and slow dynamics in elastomers by mixed magic-Hahn echo decays. *J. Chem. Phys.*, **118**, 2411–2421.
- [87] Sergeev, N. A., Ryabushkin, D. S., and Moskvich, Y. N. (1985) Magic echo and slow motions in solids. *Phys. Lett. A*, **109**, 338–340.
- [88] Barth, P., Hafner, S., and Kuhn, W. (1994) Magic-echo phase-encoding solid imaging of rubber materials below the glass transition temperature. *J. Magn. Reson. A*, **110**, 198–201.
- [89] Demco, D. E., Johansson, A., and Tegenfeldt, J. (1995) Proton spin diffusion for spatial heterogeneity and morphology investigations of polymers. *Solid State Nucl. Magn. Reson.*, **4**, 13–38.
- [90] Papon, A., Saalwächter, K., Schäler, K., Guy, L., Lequeux, F., and Montes, H. (2011) Low-Field NMR Investigations of Nanocomposites: Polymer Dynamics and Network Effects. *Macromolecules*, **44**, 913–922.
- [91] Takegoshi, K. and McDowell, C. A. (1985) A Magic Echo Pulse Sequence for the High-Resolution NMR-Spectra of Abundant Spins in Solids. *Chem. Phys. Lett.*, **116**, 100–104.
- [92] Weigand, F., Demco, D. E., Blümich, B., and Spiess, H. W. (1996) Spectral parameters for quantitative mobility contrast in NMR imaging of solid polymers. *Solid State Nucl. Magn. Reson.*, **6**, 357–365.
- [93] Wang, X. W. and White, J. L. (2002) Intramonomer polarization transfer: Calibrating spin diffusion coefficients in mobile polyolefins and their blends. *Macromolecules*, **35**, 3795–3798.
- [94] Kretschmer, A., Drake, R., Neidhoefer, M., and Wilhelm, M. (2002) Quantification of composition and domain sizes of industrial poly (phthalamide)/Poly(dimethylsiloxane) block copolymers using different ^1H solid state NMR methods. *Solid State Nucl. Magn. Reson.*, **22**, 204–217.
- [95] Buda, A., Demco, D. E., Bertmer, M., Blümich, B., Litvinov, V. M., and Penning, J. P. (2003) General Analytical Description of Spin-Diffusion for a Three-Domain Morphology. Application to Melt-Spun Nylon 6 Fibers. *J. Phys. Chem. B*, **107**, 5357–5370.
- [96] Werkhoven, T. M., Mulder, F. M., Zune, C., Jérôme, R., and de Groot, H. J. M. (2003) Determination of polyisoprene-block-poly(methyl methacrylate) domain sizes using ^1H spin diffusion. *Macromol. Chem. Phys.*, **204**, 46–51.
- [97] Buda, A., Demco, D. E., Blümich, B., Litvinov, V. M., and Penning, J. P. (2004) Complex Morphology of Melt-Spun Nylon-6 Fibres Investigated by ^1H Double-Quantum-Filtered NMR Spin-Diffusion Experiments. *ChemPhysChem*, **5**, 876–883.
- [98] Gaborieau, M., Graf, R., and Spiess, H. W. (2005) Versatility of the dipolar filter

- selection: From ^1H nuclear spin diffusion experiment to the measurement of nuclear Overhauser effect in homopolymer melts. *Solid State Nucl. Magn. Reson.*, **28**, 160–172.
- [99] Cherry, B. R., Fujimoto, C. H., Cornelius, C. J., and Alam, T. M. (2005) Investigation of domain size in polymer membranes using double-quantum-filtered spin diffusion magic angle spinning NMR. *Macromolecules*, **38**, 1201–1206.
- [100] Jia, X., Wang, X. W., Tonelli, A. E., and White, J. L. (2005) Two-dimensional spin-diffusion NMR reveals differential mixing in biodegradable polymer blends. *Macromolecules*, **38**, 2775–2780.
- [101] Voda, M. A., Demco, D. E., Voda, A., Schaubert, T., Adler, M., Dabisch, T., Adams, A., Baias, M., and Blümich, B. (2006) Morphology of thermoplastic polyurethanes by ^1H spin-diffusion NMR. *Macromolecules*, **39**, 4802–4810.
- [102] Chen, Q. and Schmidt-Rohr, K. (2006) Measurement of the local ^1H spin-diffusion coefficient in polymers. *Solid State Nucl. Magn. Reson.*, **29**, 142–152.
- [103] Saalwächter, K., Thomann, Y., Hasenhindl, A., and Schneider, H. (2008) Direct Observation of Interphase Composition in Block Copolymers. *Macromolecules*, **41**, 9187–9191.
- [104] Thomann, Y., Thomann, R., Hasenhindl, A., Mülhaupt, R., Heck, B., Knoll, K., Steininger, H., and Saalwächter, K. (2009) Gradient Interfaces in SBS and SBS/PS Blends and Their Influence on Morphology Development and Material Properties. *Macromolecules*, **42**, 5684–5699.
- [105] Zhu, H., Graf, R., Hou, G., Zhao, Y., Wang, D., and Spiess, H. W. (2010) Solid-State NMR Characterization of the Multiphase Structure of Polypropylene In-reactor Alloy. *Macromol. Chem. Phys.*, **211**, 1157–1166.
- [106] Cai, W. Z., Schmidt-Rohr, K., Egger, N., Gerharz, B., and Spiess, H. W. (1993) A solid-state n.m.r study of microphase structure and segmental dynamics of poly(styrene-*b*-methylphenylsiloxane) diblock copolymers. *Polymer*, **34**, 267–276.
- [107] Cho, G. and Natansohn, A. (1994) Spin diffusion in a triblock thermoplastic elastomer. *Can. J. Chem.*, **72**, 2255–2259.
- [108] Wang, J. H., Jack, K. S., and Natansohn, A. L. (1997) Spin diffusion and spin-lattice relaxation in multiphase polymers. *J. Chem. Phys.*, **107**, 1016–1020.
- [109] Jack, K. S., Wang, J. H., Natansohn, A., and Register, R. A. (1998) Characterization of the microdomain structure in polystyrene-polyisoprene block copolymers by ^1H spin diffusion and small-angle X-ray scattering methods. *Macromolecules*, **31**, 3282–3291.
- [110] De Paul, S. M., Zwanziger, J. W., Ulrich, R., Wiesner, U., and Spiess, H. W. (1999) Structure, mobility, and interface characterization of self-organized organic-inorganic hybrid materials by solid-state NMR. *J. Am. Chem. Soc.*, **121**, 5727–5736.
- [111] Neagu, C., Puskas, J. E., Singh, M. A., and Natansohn, A. (2000) Domain sizes determination for styrene-isobutylene block copolymer systems using solid-state NMR spectroscopy. *Macromolecules*, **33**, 5976–5981.
- [112] Yu, H. S., Natansohn, A., Singh, M. A., and Torriani, I. (2001) Solid-state NMR

- and small-angle X-ray scattering study of microphase structure of amorphous and semicrystalline poly(styrene-ethylene oxide) diblock copolymers. *Macromolecules*, **34**, 1258–1266.
- [113] Assink, R. A. (1978) Nuclear Spin Diffusion between Polyurethane Microphases. *Macromolecules*, **11**, 1233–1237.
- [114] Cho, G., Natansohn, A., Ho, T., and Wynne, K. J. (1996) Phase Structure of Poly(dimethylsiloxane-urea-urethane)-Segmented Copolymers as Observed by Solid-State Nuclear Magnetic Resonance Spectra. *Macromolecules*, **29**, 2563–2569.
- [115] Cheung, T. T. P., Gerstein, B. C., Ryan, L. M., Taylor, R. E., and Dybowski, D. R. (1980) High resolution ^1H solid state NMR studies of polyethyleneterephthalate. *J. Chem. Phys.*, **73**, 6059–6067.
- [116] Cheung, T. T. P. and Gerstein, B. C. (1981) ^1H nuclear magnetic resonance studies of domain structures in polymers. *J. Appl. Phys.*, **52**, 5517–5528.
- [117] Cheung, T. T. P. (1982) Modulation of proton NMR free induction decay by spin diffusion. *J. Chem. Phys.*, **76**, 1248–1254.
- [118] Cudby, M. E. A., Packer, K. J., and Hendra, P. J. (1984) Proton n.m.r. spin-lattice relaxation in the rotating frame and the thickness of the crystalline lamellae in some polyethylenes. *Polym. Comm.*, **25**, 303–305.
- [119] Havens, J. R. and VanderHart, D. L. (1985) Morphology of Poly(ethylene terephthalate) Fibers As Studied by Multiple-Pulse ^1H NMR. *Macromolecules*, **18**, 1663–1676.
- [120] Spiegel, S., Schmidt-Rohr, K., Boeffel, C., and Spiess, H. W. (1993) ^1H spin diffusion coefficients of highly mobile polymers. *Polymer*, **34**, 4566–4569.
- [121] Caravatti, P., Neuenschwander, P., and Ernst, R. R. (1985) Characterization of Heterogeneous Polymer Blends by Two-Dimensional Proton Spin Diffusion Spectroscopy. *Macromolecules*, **18**, 119–122.
- [122] Caravatti, P., Neuenschwander, P., and Ernst, R. R. (1986) Characterization of Polymer Blends by Selective Proton Spin-Diffusion Nuclear Magnetic Resonance Measurements. *Macromolecules*, **19**, 1889–1895.
- [123] Schmidt-Rohr, K., Clauss, J., Blümich, B., and Spiess, H. W. (1990) Miscibility of polymer blends investigated by ^1H spin diffusion and ^{13}C NMR detection. *Magn. Reson. Chem.*, **28**, S3–S9.
- [124] Cho, G. and Natansohn, A. (1997) Investigation of Phase Structure of Blends of Poly[(N-ethylcarbazol-3-yl)methyl methacrylate] and Poly{2-[(3,5-Dinitrobenzoyl)oxy]ethyl methacrylate} Using ^1H CRAMPS NMR. *Chem. Mater.*, **9**, 148–154.
- [125] Jia, X., Wolak, J., Wang, X. W., and White, J. L. (2003) Independent Calibration of ^1H Spin-Diffusion Coefficients in Amorphous Polymers by Intramolecular Polarization Transfer. *Macromolecules*, **36**, 712–718.
- [126] Nzudie, D. T., Delmotte, L., and Riess, G. (1994) Polybutadiene-poly(methyl methacrylate) core-shell latexes studied by high-resolution solid-state ^{13}C NMR and DSC: Influence of the surface coverage of the polybutadiene seed latex and

- the latex composition on the interphase formation. *Macromol. Chem. Phys.*, **195**, 2723–2737.
- [127] Landfester, K. and Spiess, H. W. (1998) Characterization of interphases in core-shell latexes by solid-state NMR. *Acta Polym.*, **49**, 451–464.
- [128] Mellinger, F., Wilhelm, M., Spiess, H. W., Baumstark, R., and Haunschild, A. (1999) Quantitative measurement of core coverage in core-shell particles by solid-state ^1H NMR spin-diffusion experiments. *Macromol. Chem. Phys.*, **200**, 719–730.
- [129] Mellinger, F., Wilhelm, M., Belik, P., Schwind, H., and Spiess, H. W. (1999) Quantitative determination of dynamic heterogeneities in core-shell latices by ^1H solid-state NMR. *Macromol. Chem. Phys.*, **200**, 2454–2460.
- [130] Mellinger, F., Wilhelm, M., Landfester, K., Spiess, H. W., Haunschild, A., and Packusch, J. (1998) Structure of water-containing latexes: Remagnetization effects during solid-state NMR spin-diffusion experiments. *Acta Polym.*, **49**, 108–115.
- [131] Brus, J. and Dybal, J. (2000) Solid-state NMR study of structure, size and dynamics of domains in hybrid siloxane networks. *Polymer*, **41**, 5269–5282.
- [132] Domjan, A., Erdödi, G., Wilhelm, M., Neidhöfer, M., Landfester, K., Ivan, B., and Spiess, H. W. (2003) Structural Studies of Nanophase-Separated Poly(2-hydroxyethyl methacrylate)-*l*-polyisobutylene Amphiphilic Conetworks by Solid-State NMR and Small-Angle X-ray Scattering. *Macromolecules*, **36**, 9107–9114.
- [133] Kumashiro, K. K., Schmidt-Rohr, K., Murphy, O. J., Ouellette, K. L., Cramer, W. A., and Thompson, L. K. (1998) A Novel Tool for Probing Membrane Protein Structure: Solid-State NMR with Proton Spin Diffusion and X-Nucleus Detection. *J. Am. Chem. Soc.*, **120**, 5043–5051.
- [134] Huster, D., Yao, X. L., and Hong, M. (2002) Membrane Protein Topology Probed by ^1H Spin Diffusion from Lipids Using Solid-State NMR Spectroscopy. *J. Am. Chem. Soc.*, **124**, 874–883.
- [135] Roos, M., Micke, P., and Hempel, G. (2012) Monitoring nuclear spin-flip processes and measuring spin-diffusion constants via hole burning into the magnetization. *Chem. Phys. Lett.*, **536**, 147–154.
- [136] Bloembergen, N. (1949) On the interaction of nuclear spins in a crystalline lattice. *Physica*, **15**, 386–426.
- [137] Lowe, I. J. and Gade, S. (1967) Density-matrix derivation of the spin-diffusion equation. *Phys. Rev.*, **156**, 817–825.
- [138] VanderHart, D. L. (1987) Natural-Abundance ^{13}C - ^{13}C Spin Exchange in Rigid Crystalline Organic Solids. *J. Magn. Reson.*, **72**, 13–47.
- [139] Clauss, J., Schmidt-Rohr, K., and Spiess, H. W. (1993) Determination of Domain Sizes in Heterogeneous Polymers by Solid-State NMR. *Acta Polym.*, **44**, 1–17.
- [140] Schmidt-Rohr, K. and Spiess, H. W. (1991) Chain Diffusion between Crystalline and Amorphous Regions in Polyethylene Detected by 2D Exchange ^{13}C NMR. *Macromolecules*, **24**, 5288–5293.
- [141] Packer, K. J., Pope, J. M., Yeung, R. R., and Cudby, M. E. A. (1984) The Effects of Morphology on ^1H NMR Spectra and Relaxation in Semicrystalline Polyolefins. *J.*

- Polym. Sci., Part B: Polym. Phys.*, **22**, 589–616.
- [142] Booth, A. and Packer, K. (1987) Magnetic spin lattice relaxation in the presence of spin-diffusion. *Mol. Phys.*, **62**, 811–828.
- [143] Wang, J. H. (1996) On the determination of domain sizes in polymers by spin diffusion. *J. Chem. Phys.*, **104**, 4850–4858.
- [144] Buda, A., Demco, D. E., Bertmer, M., Blümich, B., Reining, B., Keul, H., and Höcker, H. (2003) Domain sizes in heterogeneous polymers by spin diffusion using single-quantum and double-quantum dipolar filters. *Solid State Nucl. Magn. Reson.*, **24**, 39–67.
- [145] Kenwright, A. M., Packer, K. J., and Say, B. J. (1986) Numerical Simulations of the Effects of Spin-Diffusion on NMR Spin-Lattice Relaxation in Semicrystalline Polymers. *J. Magn. Reson.*, **69**, 426–439.
- [146] Kenwright, A. M. and Packer, K. J. (1990) On T_1 cancellation schemes in Goldman-Shen-type experiments. *Chem. Phys. Lett.*, **173**, 471–475.
- [147] Kenwright, A. M. and Say, B. J. (1996) Analysis of spin-diffusion measurements by iterative optimisation of numerical models. *Solid State Nucl. Magn. Reson.*, **7**, 85–93.
- [148] Hahn, E. L. (1950) Spin Echoes. *Phys. Rev.*, **80**, 580–594.
- [149] Goldman, M. and Shen, L. (1966) Spin-spin relaxation in LaF_3 . *Phys. Rev.*, **144**, 321–331.
- [150] Packer, K. J. and Pope, J. M. (1983) The Distortion of NMR Spectra by Multiple Quantum Coherence Effects Resulting from Goldman-Shen and Related Pulse Sequences Applied to Heterogeneous Solids. *J. Magn. Reson.*, **55**, 378–385.
- [151] Idiyatullin, D. S., Khozina, E. V., and Smirnov, V. S. (1996) Studies of domain morphology in segmented polyurethanes by pulsed NMR. *Solid State Nucl. Magn. Reson.*, **7**, 17–26.
- [152] Kimura, T., Neki, K., Tamura, N., Horii, F., Nakagawa, M., and Odani, H. (1992) High-resolution solid-state ^{13}C nuclear magnetic resonance study of the combined process of ^1H spin diffusion and ^1H spin-lattice relaxation in semicrystalline polymers. *Polymer*, **33**, 493–497.
- [153] Egger, N., Schmidt-Rohr, K., Blümich, B., Domke, W. D., and Stapp, B. (1992) Solid-State NMR Investigation of Cationic Polymerized Epoxy Resins. *J. Appl. Polym. Sci.*, **44**, 289–295.
- [154] Graf, R., Demco, D. E., Gottwald, J., Hafner, S., and Spiess, H. W. (1997) Dipolar couplings and internuclear distances by double-quantum nuclear magnetic resonance spectroscopy of solids. *J. Chem. Phys.*, **106**, 885–895.
- [155] Ba, Y. and Ripmeester, J. A. (1998) Multiple quantum filtering and spin exchange in solid state nuclear magnetic resonance. *J. Chem. Phys.*, **108**, 8589–8594.
- [156] Meyer, H. W., Schneider, H., and Saalwächter, K. (2012) Proton NMR spin-diffusion studies of PS-PB block copolymers at low field: two- vs three-phase model and recalibration of spin-diffusion coefficients. *Polym. J.*, **44**, 748–756.
- [157] Munowitz, M. and Pines, A. (1987) Principles and Applications of Multiple-Quantum NMR. *Adv. Chem. Phys.*, **66**, 1.

- [158] Orza, R. A., Magusin, P. C. M. M., Litvinov, V. M., van Duin, M., and Michels, M. A. J. (2007) Solid-State ^1H NMR Study on Chemical Cross-Links, Chain Entanglements, and Network Heterogeneity in Peroxide-Cured EPDM Rubbers. *Macromolecules*, **40**, 8999–9008.
- [159] Roos, M. (2012) *Nano-scale Roughness of Phase Boundaries in Heterogeneous Polymers As Studied by Spin-Diffusion NMR*. Master's thesis, Institut für Physik, Naturwissenschaftliche Fakultät II, Martin-Luther-Universität Halle-Wittenberg.
- [160] Mello, N. C., Bonagamba, T. J., Panepucci, H., Dahmouche, K., Judeinstein, P., and Aegerter, M. A. (2000) NMR Study of Ion-Conducting Organic-Inorganic Nanocomposites Poly(ethylene glycol)-Silica- LiClO_4 . *Macromolecules*, **33**, 1280–1288.
- [161] Kaji, H. and Horii, F. (1997) One- and two-dimensional solid-state ^{13}C NMR analyses of the solid structure and molecular motion of poly(ϵ -caprolactone) isothermally crystallized from the melt. *Macromolecules*, **30**, 5791–5798.
- [162] Ito, M., Kubo, M., Tsuruta, A., and Tanaka, K. (1978) The relationship between chemical structure and viscoelastic properties of linear aliphatic polyesters. *J. Polym. Sci., Part B: Polym. Phys.*, **16**, 1435–1446.
- [163] Men, Y., Rieger, J., Endeler, H. F., and Lilge, D. (2003) Mechanical α -Process in Polyethylene. *Macromolecules*, **36**, 4689–4691.
- [164] McCall, D. W. (1971) Nuclear Magnetic Resonance Studies of Molecular Relaxation Mechanisms in Polymers. *Acc. Chem. Res.*, **4**, 223–232.
- [165] Packer, K. J., Poplett, I. J. F., and Taylor, M. J. (1988) ^1H nuclear magnetic resonance and spin-lattice relaxation in solid, high-density polyethylene. *J. Chem. Soc., Faraday Trans. I*, **84**, 3851–3863.
- [166] Vanderschueren, J., Ladang, M., and Heuschen, J. M. (1980) Thermally stimulated depolarization of phase-separated polymer systems. *Macromolecules*, **13**, 973–977.
- [167] Grimau, M., Laredo, E., Perez, M. C. Y., and Bello, A. (2001) Study of dielectric relaxation modes in poly(ϵ -caprolactone): Molecular weight, water sorption, and merging effects. *J. Chem. Phys.*, **114**, 6417–6425.
- [168] Bello, A., Laredo, E., and Grimau, M. (2007) Comparison of analysis of dielectric spectra of PCL in the ϵ^* and the M^* formalism. *J. Non-Cryst. Solids*, **353**, 4283–4287, 4th Conference of the International-Dielectric-Society/9th International Conference on Dielectric and Related Phenomena, Poznan, Poland, Sep 03-07, 2006.
- [169] Semba, T., Kitagawa, K., Ishiaku, U. S., and Hamada, H. (2006) The effect of crosslinking on the mechanical properties of polylactic acid/polycaprolactone blends. *J. Appl. Polym. Sci.*, **101**, 1816–1825.
- [170] deAzevedo, E. R., Saalwächter, K., Pascui, O., de Souza, A. A., Bonagamba, T. J., and Reichert, D. (2008) Intermediate motions as studied by solid-state separated local field NMR experiment. *J. Chem. Phys.*, **128**, 104505.
- [171] Opella, S. J. and Waugh, J. S. (1977) Two-dimensional ^{13}C NMR of highly oriented

- polyethylene. *J. Chem. Phys.*, **66**, 4919–4924.
- [172] Munowitz, M., Griffin, R. G., Bodenhausen, G., and Huang, T. H. (1981) Two-Dimensional Rotational Spin-Echo Nuclear Magnetic Resonance in Solids: Correlation of Chemical Shift and Dipolar Interaction. *J. Am. Chem. Soc.*, **103**, 2529–2533.
- [173] Hackel, C., Zinkevich, T., Belton, P., Achilles, A., Reichert, D., and Krushelnitsky, A. (2012) The trehalose coating effect on the internal protein dynamics. *Phys. Chem. Chem. Phys.*, **14**, 2727–2734.
- [174] Kricheldorf, H. R., Berl, M., and Scharnagl, N. (1988) Poly(lactones). 9. Polymerization Mechanism of Metal Alkoxide initiated Polymerizations of Lactide and Various Lactones. *Macromolecules*, **21**, 286–293.
- [175] Wurm, A., Zhuravlev, E., Eckstein, K., Jehnichen, D., Pospiech, D., Androsch, R., Wunderlich, B., and Schick, C. (2012) Crystallization and Homogeneous Nucleation Kinetics of Poly(ϵ -caprolactone) (PCL) with Different Molar Masses. *Macromolecules*, **45**, 3816–3828.
- [176] Herzfeld, J. and Berger, A. E. (1980) Sideband Intensities in NMR Spectra of Samples Spinning at the Magic Angle. *J. Chem. Phys.*, **73**, 6021.
- [177] Balasubramanian, K., Krishnan, R. S., and Iitaka, Y. (1962) Raman Spectrum of γ -Glycine. *Bull. Chem. Soc. Jpn.*, **35**, 1303–1305.
- [178] Gupta, V. D. and Singh, R. D. (1970) Low frequency spectra of glycine. *Chem. Phys. Lett.*, **5**, 218–220.
- [179] Wendoloski, J. J., Gardner, K. H., Hirschinger, J., Miura, H., and English, A. D. (1990) Molecular Dynamics in Ordered Structures - Computer Simulation and Experimental Results for Nylon-66 Crystals. *Science*, **247**, 431–436.
- [180] Hirschinger, J., Miura, H., Gardner, K. H., and English, A. D. (1990) Segmental Dynamics in the Crystalline Phase of Nylon-66 - Solid-State ^2H NMR. *Macromolecules*, **23**, 2153–2169.
- [181] Wei, Y., Graf, R., Sworen, J. C., Cheng, C.-Y., Bowers, C. R., Wagener, K. B., and Spiess, H. W. (2009) Local and Collective Motions in Precise Polyolefins with Alkyl Branches: A Combination of ^2H and ^{13}C Solid-State NMR Spectroscopy. *Angew. Chem., Int. Ed.*, **48**, 4617–4620.
- [182] Cobo, M. F., Achilles, A., Reichert, D., deAzevedo, E. R., and Saalwächter, K. (2012) Recoupled separated-local-field experiments and applications to study intermediate-regime molecular motions. *J. Magn. Reson.*, **221**, 85–96.
- [183] Olf, H. G. and Peterlin, A. (1970) NMR Study of Molecular Motion in Oriented Long-Chain Alkanes. I. Theoretical Part. *J. Polym. Sci., Part A-2: Polym. Phys.*, **8**, 753–770.
- [184] Ball, R. C., Callaghan, P. T., and Samulski, E. T. (1997) A simplified approach to the interpretation of nuclear spin correlations in entangled polymeric liquids. *J. Chem. Phys.*, **106**, 7352–7361.
- [185] Olf, H. G. and Peterlin, A. (1967) NMR Study of Molecular Motion in Polyethylene. *Kolloid-Z. u. Z. Polymere*, **215**, 97–111.
- [186] Olf, H. G. and Peterlin, A. (1970) NMR Study of Molecular Motion in Oriented

- Long-Chain Alkanes. II. Oriented Mats of Polyethylene Single Crystals. *J. Polym. Sci., Part A-2: Polym. Phys.*, **8**, 771–789.
- [187] Strobl, G. R., Trzebiatowski, T., and Ewen, B. (1978) Analyse der Temperaturabhängigkeit der dielektrischen α -Relaxation am Modell eines Paraffin-Keton-Mischkristalls. *Prog. Coll. Polym. Sci.*, **64**, 219–225.
- [188] Hentschel, D., Sillescu, H., and Spiess, H. W. (1979) Molecular Motion in Solid Polyethylene as Studied by ^2D Wide Line NMR Spectroscopy. *Makromol. Chem.*, **180**, 241–249.
- [189] Duncan, T. M. (1990) *A Compilation of Chemical Shift Anisotropies*. The Farragut Press.
- [190] deAzevedo, E. R., Hu, W.-G., Bonagamba, T. J., and Schmidt-Rohr, K. (1999) Centerband-Only Detection of Exchange: Efficient Analysis of Dynamics in Solids by NMR. *J. Am. Chem. Soc.*, **121**, 8411–8412.
- [191] deAzevedo, E. R., Hu, W.-G., Bonagamba, T. J., and Schmidt-Rohr, K. (2000) Principles of centerband-only detection of exchange in solid-state nuclear magnetic resonance, and extension to four-time centerband-only detection of exchange. *J. Chem. Phys.*, **112**, 8988–9001.
- [192] Hackel, C., Franz, C., Achilles, A., Saalwächter, K., and Reichert, D. (2009) Signal loss in 1D magic-angle spinning exchange NMR (CODEX): radio-frequency limitations and intermediate motions. *Phys. Chem. Chem. Phys.*, **11**, 7022–7030.
- [193] Miyoshi, T., Pascui, O., and Reichert, D. (2002) Helical jump motions in isotactic poly(4-methyl-1-pentene) crystallites revealed by 1D MAS exchange NMR spectroscopy. *Macromolecules*, **35**, 7178–7181.
- [194] Reichert, D., private communication.
- [195] Albrecht, T. and Strobl, G. (1995) Temperature-dependent crystalline-amorphous structures in linear polyethylene - surface melting and the thickness of amorphous layers. *Macromolecules*, **28**, 5827–5833.
- [196] Ward, I. M. and Wilding, M. A. (1984) Creep Behavior of Ultrahigh-Modulus Polyethylene: Influence of Draw Ratio and Polymer Composition. *J. Polym. Sci. B Polym. Phys.*, **22**, 561–575.
- [197] Yao, Y.-F., Graf, R., Spiess, H. W., Lippits, D. R., and Rastogi, S. (2007) Morphological differences in semicrystalline polymers: Implications for local dynamics and chain diffusion. *Phys. Rev. E*, **76**, 060801(R).
- [198] Yao, Y.-F., Graf, R., Spiess, H. W., and Rastogi, S. (2008) Restricted segmental mobility can facilitate medium-range chain diffusion: A NMR study of morphological influence on chain dynamics of polyethylene. *Macromolecules*, **41**, 2514–2519.
- [199] Pandey, A., Champouret, Y., and Rastogi, S. (2011) Heterogeneity in the Distribution of Entanglement Density during Polymerization in Disentangled Ultrahigh Molecular Weight Polyethylene. *Macromolecules*, **44**, 4952–4960.
- [200] Hu, W.-G., Boeffel, C., and Schmidt-Rohr, K. (1999) Chain Flips in Polyethylene Crystallites and Fibers Characterized by Dipolar ^{13}C NMR. *Macromolecules*, **32**, 1611–1619.
- [201] Bärenwald, R., Champouret, Y., Saalwächter, K., and Schäler, K. (2012)

- Determination of Chain Flip Rates in Poly(ethylene) Crystallites by Solid-State Low-Field ^1H NMR for Two Different Sample Morphologies. *J. Phys. Chem. B*, **116**, 13089–13097, <http://pubs.acs.org/articlesonrequest/AOR-QkWmmzKEwE8mhxaMuEp>.
- [202] Kimmich, R. (1997) *NMR Tomography, Diffusometry, Relaxometry*. Springer.
- [203] Sturniolo, S. and Saalwächter, K. (2011) Breakdown in the efficiency factor of the mixed Magic Sandwich Echo: A novel NMR probe for slow motions. *Chem. Phys. Lett.*, **516**, 106–110.
- [204] Schnell, I., Watts, A., and Spiess, H. W. (2001) Double-Quantum Double-Quantum MAS Exchange NMR Spectroscopy: Dipolar-Coupled Spin Pairs as Probes for Slow Molecular Dynamics. *J. Magn. Reson.*, **149**, 90–102.
- [205] Wurm, A., Soliman, R., and Schick, C. (2003) Early stages of polymer crystallization - a dielectric study. *Polymer*, **44**, 7467–7476.
- [206] Hsiao, B. (1993) Some comments on modeling of two-stage crystallization kinetics. *J. Polym. Sci., Part B: Polym. Phys.*, **31**, 237–240.
- [207] Li, J., Li, W., Cheng, H., Zhang, L., Li, Y., and Han, C. C. (2012) Early stages of nucleation and growth in melt crystallized polyethylene. *Polymer*, **53**, 2315–2319.
- [208] Feio, G. and Cohen-Addad, J. P. (1988) NMR Approach to the Kinetics of Polymer Crystallization. 1. Cis-1,4-Polybutadiene. *J. Polym. Sci., Part B: Polym. Phys.*, **26**, 389–412.
- [209] Piorkowska, E., Galeski, A., and Haudin, J.-M. (2006) Critical assessment of overall crystallization kinetics theories and predictions. *Prog. Polym. Sci.*, **31**, 549–575.
- [210] Strobl, G. (2006) Crystallization and melting of bulk polymers: New observations, conclusions and a thermodynamic scheme. *Prog. Polym. Sci.*, **31**, 398–442.
- [211] Goulet, L. and Prud'homme, R. E. (1990) Crystallization kinetics and melting of caprolactone random copolymers. *J. Polym. Sci., Part B: Polym. Phys.*, **28**, 2329–2352.
- [212] De Juana, R. and Cortázar, M. (1993) Study of the Melting and Crystallization Behavior of Binary Poly(ϵ -caprolactone)/Poly(hydroxy ether of Bisphenol A) Blends. *Macromolecules*, **26**, 1170–1176.
- [213] Skoglund, P. and Fransson, A. (1996) Continuous cooling and isothermal crystallization of polycaprolactone. *J. Appl. Polym. Sci.*, **61**, 2455–2465.
- [214] Chiu, F.-C., Fu, Q., and Hsieh, E. T. (1999) Molecular Weight Dependence of Melt Crystallization Behavior and Crystal Morphology of Low Molecular Weight Linear Polyethylene Fractions. *J. Polym. Res.*, **6**, 219–229.
- [215] Lorenzo, A. T., Arnal, M. L., Albuerne, J., and Müller, A. J. (2007) DSC isothermal polymer crystallization kinetics measurements and the use of the Avrami equation to fit the data: Guidelines to avoid common problems. *Polym. Test.*, **26**, 222–231.
- [216] Wurm, A., Merzlyakov, M., and Schick, C. (1999) Isothermal crystallisation of PCL studied by temperature modulated dynamic mechanical and TMDSC analysis. *J. Therm. Anal. Calorim.*, **56**, 1155–1161.

- [217] Rybnikar, F. (1963) Mechanism of secondary crystallization in polymers. *J. Polym. Sci., Part A: Polym. Chem.*, **1**, 2031–2038.
- [218] Seidlitz, A. (2011) *Die teilkristalline Struktur in Poly- ϵ -Caprolacton – Quantitative Untersuchungen mit Hilfe der Röntgenkleinwinkelstreuung*. Master's thesis, Institut für Physik, Naturwissenschaftliche Fakultät II, Martin-Luther-Universität Halle-Wittenberg.
- [219] Heck, B., Hugel, T., Iijima, M., and Strobl, G. (2000) Steps in the formation of the partially crystalline state. *Polymer*, **41**, 8839–8848, International Symposium on Semicrystalline Polymers in Memory of Andrew Keller held at the American-Chemical-Society National Meeting, New Orleans, Louisiana, Aug 23-26, 1999.
- [220] Heck, B., Hugel, T., Iijima, M., Sadiku, E., and Strobl, G. (1999) Steps in the transition of an entangled polymer melt to the partially crystalline state. *New J. Phys.*, **1**, 17.
- [221] Kohn, P. and Strobl, G. (2004) Continuous changes in the inner order of the crystalline lamellae during isothermal crystallization of poly(ϵ -caprolactone). *Macromolecules*, **37**, 6823–6826.
- [222] Men, Y. and Strobl, G. (2003) Critical strains in poly(ϵ -caprolactone) and blends with poly(vinyl methyl ether) and poly(styrene-co-acrylonitrile). *Macromolecules*, **36**, 1889–1898.
- [223] Wurm, A. and Schick, C. (2002) Development of thermal stability of polymer crystals during isothermal crystallisation. *e-Polymers*, **024**, 1–15.
- [224] Lorenzo, A. T., Arnal, M. L., Sánchez, J. J., and Müller, A. J. (2006) Effect of Annealing Time on the Self-Nucleation Behavior of Semicrystalline Polymers. *J. Polym. Sci. B. Polym. Phys.*, **44**, 1738–1750.
- [225] Blundell, D. J. and Keller, A. (1968) Nature of self-seeding polyethylene crystal nuclei. *J. Macromol. Sci., Part B: Phys.*, **2**, 301–336.
- [226] Yamazaki, S., Hikosaka, M., Toda, A., Wataoka, I., and Gu, F. M. (2002) Role of entanglement in nucleation and 'melt relaxation' of polyethylene. *Polymer*, **43**, 6585–6593.
- [227] Maus, A., Hempel, E., Thurn-Albrecht, T., and Saalwächter, K. (2007) Memory effect in isothermal crystallization of syndiotactic polypropylene — role of melt structure and dynamics? *Eur. Phys. J. E*, **23**, 91–101.
- [228] Xu, J. J., Ma, Y., Hu, W., Rehahn, M., and Reiter, G. (2009) Cloning polymer single crystals through self-seeding. *Nat. Mater.*, **8**, 348–353.
- [229] Zhang, Y.-S., Zhong, L.-W., Yang, S., Liang, D.-H., and Chen, E.-Q. (2012) Memory effect on solution crystallization of high molecular weight poly(ethylene oxide). *Polymer*, **53**, 3621 – 3628.
- [230] Bu, H. S., Gu, F. M., Chen, M., Bao, L. R., and Cao, J. (2000) Crystallization and melting behavior of nanopolymeric particles containing single or a few chains. *J. Macromol. Sci., Part B: Phys.*, **39**, 93–108.
- [231] Yu, X., Kong, B., and Yang, X. (2008) Molecular dynamics study on the crystallization of a cluster of polymer chains depending on the initial entanglement structure. *Macromolecules*, **41**, 6733–6740.

- [232] Wangsoub, S., Olley, R. H., and Mitchell, G. R. (2005) Directed crystallisation of poly(ϵ -caprolactone) using a low-molar-mass self-assembled template. *Macromol. Chem. Phys.*, **206**, 1826–1839.
- [233] Wangsoub, S., Davis, F. J., Mitchell, G. R., and Olley, R. H. (2008) Enhanced Templating in the Crystallisation of Poly(ϵ -caprolactone) Using 1,3:2,4-di(4-Chlorobenzylidene) Sorbitol. *Macromol. Rapid Commun.*, **29**, 1861–1865.
- [234] Mercurio, D. J. and Spontak, R. J. (2001) Morphological characteristics of 1,3:2,4-dibenzylidene sorbitol/poly(propylene glycol)organogels. *J. Phys. Chem. B*, **105**, 2091–2098.
- [235] Qiang, Y. (2011) *Influence of Molecular Weight and Nucleating Agent (DBS) on Crystallization Kinetics and Semicrystalline Structure of PCL*. Master's thesis, Institut für Physik/Chemie, Naturwissenschaftliche Fakultät II, Martin-Luther-Universität Halle-Wittenberg.
- [236] Siripitayananon, J., Wangsoub, S., Olley, R. H., and Mitchell, G. R. (2004) The use of a low-molar-mass self-assembled template to direct the crystallisation of poly(ϵ -caprolactone). *Macromol. Rapid Commun.*, **25**, 1365–1370.
- [237] Bielawski, C. W., Benitez, D., and Grubbs, R. H. (2002) An "endless" route to cyclic polymers. *Science*, **297**, 2041–2044.
- [238] Crescenzi, V., Manzini, G., Calzolar, G., and Borri, C. (1972) Thermodynamics of fusion of poly- β -propiolactone and poly- ϵ -caprolactone. Comparative analysis of melting of aliphatic polylactone and polyester chains. *Eur. Polym. J.*, **8**, 449–463.
- [239] Khambatta, F. B., Warner, F., Russell, T., and Stein, R. S. (1976) Small-angle X-ray and light-scattering studies of morphology of blends of poly(ϵ -caprolactone) with Polyvinyl-chloride. *J. Polym. Sci., Part B: Polym. Phys.*, **14**, 1391–1424.
- [240] Pyda, M. (2010), Athas data bank. <http://athas.prz.edu.pl/>.
- [241] Schick, C. (2009) Differential scanning calorimetry (DSC) of semicrystalline polymers. *Anal. Bioanal. Chem.*, **395**, 1589–1611.
- [242] Schäler, K., Ostas, E., Schröter, K., Thurn-Albrecht, T., Binder, W. H., and Saalwächter, K. (2011) Influence of Chain Topology on Polymer Dynamics and Crystallization. Investigation of Linear and Cyclic Poly(ϵ -caprolactone)s by ^1H Solid-State NMR Methods. *Macromolecules*, **44**, 2743–2754.
- [243] Clayden, N. J. (1994) Lamellar Thickness of Crystallizable Ethene Runs induction Ethene-Propene Copolymers by Solid State NMR. *J. Polym. Sci., Part B: Polym. Phys.*, **32**, 2321–2327.
- [244] Jack, K. S., Natansohn, A., Wang, J., Favis, B. D., and Cigana, P. (1998) Determination of domain sizes in compatibilized polystyrene (ethylene-propylene rubber) blends by measurements of ^1H spin diffusion. *Chem. Mater.*, **10**, 1301–1308.
- [245] Hu, W.-G. and Schmidt-Rohr, K. (2000) Characterization of ultradrawn polyethylene fibers by NMR: crystallinity, domain sizes and a highly mobile second amorphous phase. *Polymer*, **41**, 2979–2987.
- [246] Meurer, B. and Weill, G. (2008) Measurement of spin diffusion coefficients in glassy polymers: Failure of a simple scaling law. *Macromol. Chem. Phys.*, **209**, 212–219.

- [247] Yu, H., Wang, J., Natansohn, A., and Singh, M. A. (1999) Microphase structures of poly(styrene-*b*-ethylene/propylene) diblock copolymers investigated by solid-state NMR and small-angle X-ray scattering techniques. *Macromolecules*, **32**, 4365–4374.
- [248] Cheung, T. T. P. (1981) Spin diffusion in NMR in solids. *Phys. Rev. B*, **23**, 1404–1418.
- [249] Meurer, B. and Weill, G. (2002) A Tilted Rotatory Frame Method for the Measurement of Nuclear Spin Diffusion Coefficients in Solids Doped with Paramagnetic Centers: Mn-doped CaF₂. *Appl. Magn. Reson.*, **23**, 133–147.
- [250] Vanderhart, D. L. and Fadden, G. B. (1996) Some perspectives on the interpretation of proton NMR spin diffusion data in terms of polymer morphologies. *Solid State Nucl. Magn. Reson.*, **7**, 45–66.
- [251] Mellinger, F., Wilhelm, M., and Spiess, H. W. (1999) Calibration of ¹H NMR spin diffusion coefficients for mobile polymers through transverse relaxation measurements. *Macromolecules*, **32**, 4686–4691.
- [252] Jia, Z., Zhang, L., Chen, Q., and Hansen, E. W. (2008) Proton Spin Diffusion in Polyethylene as a Function of Magic-Angle Spinning Rate. A Phenomenological Approach. *J. Phys. Chem. A*, **112**, 1228–1233.
- [253] Cho, T.-Y., Stille, W., and Strobl, G. (2007) Zero growth temperature and growth kinetics of crystallizing poly(epsilon-caprolactone). *Colloid Polym. Sci.*, **285**, 931–934.
- [254] Brämer, R. (1972) Eindimensionale Röntgenkleinwinkelstreuformeln parakristalliner Lamellenclusterstrukturen. *Kolloid-Z. u. Z. Polymere*, **250**, 1034–1038.
- [255] Hoffman, J. D., Lauritzen, J. I., Passaglia, E., Ross, G. S., Frolen, L. J., and Weeks, J. J. (1969) Kinetics of Polymer Crystallization from Solution and the Melt. *Kolloid-Z. u. Z. Polymere*, **231**, 564–592.
- [256] Doye, J. P. K. and Frenkel, D. (1998) Mechanism of thickness determination in polymer crystals. *Phys. Rev. Lett.*, **81**, 2160–2163.
- [257] Yang, I.-K. and Liu, C. Y. (2010) Real-Time SAXS and WAXS Study of the Multiple Melting Behavior of Poly(epsilon-caprolactone). *J. Polym. Sci., Part B: Polym. Phys.*, **48**, 1777–1785.
- [258] Roos, M. (2010) Untersuchung der lokalen und makroskopischen Spin-Diffusion in Flüssigkristallen und Polymeren. Martin-Luther-Universität Halle, Institut für Physik, Bachelor thesis.
- [259] Hoskins, J. N. and Grayson, S. M. (2009) Synthesis and Degradation Behavior of Cyclic Poly(epsilon-caprolactone). *Macromolecules*, **42**, 6406–6413.
- [260] Choi, J., Chun, S.-W., and Kwak, S.-Y. (2007) Influence of hyperbranched against linear architecture on crystallization behavior of poly(epsilon-caprolactone)s in binary blends with poly(vinyl chloride). *J. Polym. Sci., Part B: Polym. Phys.*, **45**, 577–589.
- [261] Li, H., Jérôme, R., and Lecomte, P. (2006) Synthesis of tadpole-shaped copolyesters based on living macrocyclic poly(epsilon-caprolactone). *Polymer*, **47**, 8406–8413.
- [262] Nunez, E., Vancso, G. J., and Gedde, U. W. (2008) Morphology, crystallization, and

- melting of single crystals and thin films of star-branched polyesters with poly(ϵ -caprolactone) arms as revealed by atomic force microscopy. *J. Macromol. Sci., Part B: Phys.*, **47**, 589–607.
- [263] Men, Y. F., Rieger, J., and Strobl, G. (2003) Role of the entangled amorphous network in tensile deformation of semicrystalline polymers. *Phys. Rev. Lett.*, **91**.
- [264] Heck, B., Sadiku, E. R., and Strobl, G. R. (2001) SAXS and DSC studies of the crystallization and melting phenomena of poly(ϵ -caprolactone). *Macromol. Symp.*, **165**, 99–113.
- [265] Roovers, J. (1985) Dilute-Solution Properties of Ring Polystyrenes. *J. Polym. Sci., Part B: Polym. Phys.*, **23**, 1117–1126.
- [266] Müller, M., Wittmer, J. P., and Cates, M. E. (1996) Topological effects in ring polymers: A computer simulation study. *Phys. Rev. E*, **53**, 5063–5074.
- [267] Müller, M., Wittmer, J. P., and Cates, M. E. (2000) Topological effects in ring polymers. II. Influence of persistence length. *Phys. Rev. E*, **61**, 4078–4089.
- [268] Gagliardi, S., Arrighi, V., Dagger, A., and Semlyen, A. J. (2002) Conformation of cyclic and linear polydimethylsiloxane in the melt: a small-angle neutron-scattering study. *Appl. Phys. A: Mater. Sci. Process.*, **74**, S469–S471, International Conference on Neutron Scattering, Munich, Germany, sep 09-13, 2001.
- [269] Arrighi, V., Gagliardi, S., Dagger, A. C., Semlyen, J. A., Higgins, J. S., and Shenton, M. J. (2004) Conformation of cyclics and linear chain polymers in bulk by SANS. *Macromolecules*, **37**, 8057–8065.
- [270] Hur, K., Winkler, R. G., and Yoon, D. Y. (2006) Comparison of ring and linear polyethylene from molecular dynamics simulations. *Macromolecules*, **39**, 3975–3977.
- [271] Fu, C., Ouyang, W., Sun, Z., and Ana, L. (2007) Influence of molecular topology on the static and dynamic properties of single polymer chain in solution. *J. Chem. Phys.*, **127**.
- [272] Suzuki, J., Takano, A., and Matsushita, Y. (2008) Topological effect in ring polymers investigated with Monte Carlo simulation. *J. Chem. Phys.*, **129**.
- [273] Halverson, J. D., Lee, W. B., Grest, G. S., Grosberg, A. Y., and Kremer, K. (2011) Molecular dynamics simulation study of nonconcatenated ring polymers in a melt. I. Statics. *J. Chem. Phys.*, **134**.
- [274] Obukhov, S. P., Rubinstein, M., and Duke, T. (1994) Dynamics of a Ring Polymer in a Gel. *Phys. Rev. Lett.*, **73**, 1263–1266.
- [275] Kapnistos, M., Lang, M., Vlassopoulos, D., Pyckhout-Hintzen, W., Richter, D., Cho, D., Chang, T., and Rubinstein, M. (2008) Unexpected power-law stress relaxation of entangled ring polymers. *Nat. Mater.*, **7**, 997–1002.
- [276] McLeish, T. (2002) Polymers without beginning or end. *Science*, **297**, 2005–2006.
- [277] Roovers, J. (1988) Viscoelastic properties of polybutadiene rings. *Macromolecules*, **21**, 1517–1521.
- [278] McKenna, G. B., Hostetter, B. J., Hadjichristidis, N., Fetters, L. J., and Plazek, D. J. (1989) A Study of the Linear Viscoelastic Properties of Cyclic Polystyrenes Using Creep and Recovery Measurements. *Macromolecules*, **22**, 1834–1852.

- [279] Cosgrove, T., Griffiths, P. C., Hollingshurst, J., Richards, R. D. C., and Semlyen, J. A. (1992) Self-Diffusion and Spin-Spin Relaxation in Cyclic And Linear Polydimethylsiloxane Melts. *Macromolecules*, **25**, 6761–6764.
- [280] Habuchi, S., Satoh, N., Yamamoto, T., Tezuka, Y., and Vacha, M. (2010) Multimode Diffusion of Ring Polymer Molecules Revealed by a Single-Molecule Study. *Angew. Chem., Int. Ed.*, **49**, 1418–1421.
- [281] Ungar, G. and Zeng, K. B. (2001) Learning polymer crystallization with the aid of linear, branched and cyclic model compounds. *Chem. Rev.*, **101**, 4157–4188.
- [282] Cooke, J., Viras, K., Yu, G. E., Sun, T., Yonemitsu, T., Ryan, A. J., Price, C., and Booth, C. (1998) Large cyclic poly(oxyethylene)s: Chain folding in the crystalline state studied by Raman spectroscopy, X-ray scattering, and differential scanning calorimetry. *Macromolecules*, **31**, 3030–3039.
- [283] Sakaue, T. (2011) Ring Polymers in Melts and Solutions: Scaling and Crossover. *Phys. Rev. Lett.*, **106**.
- [284] Iyer, B. V. S., Lele, A. K., and Shanbhag, S. (2007) What is the size of a ring polymer in a ring-linear blend? *Macromolecules*, **40**, 5995–6000.
- [285] Halverson, J. D., Lee, W. B., Grest, G. S., Grosberg, A. Y., and Kremer, K. (2011) Molecular dynamics simulation study of nonconcatenated ring polymers in a melt. II. Dynamics. *J. Chem. Phys.*, **134**.
- [286] Hur, K., Jeong, C., Winkler, R. G., Lacevic, N., Gee, R. H., and Yoon, D. Y. (2011) Chain Dynamics of Ring and Linear Polyethylene Melts from Molecular Dynamics Simulations. *Macromolecules*, **44**, 2311–2315.
- [287] Dodgson, K. and Semlyen, J. A. (1977) Studies of cyclic and linear poly(dimethyl siloxanes).1. Limiting viscosity number and molecular weight relationships. *Polymer*, **18**, 1265–1268.
- [288] Higgins, J. S., Dodgson, K., and Semlyen, J. A. (1979) Studies of linear and cyclic poly(dimethyl siloxanes).3. Neutron-Scattering Measurements of the dimensions of ring and chain polymers. *Polymer*, **20**, 553–558.
- [289] Dodgson, K., Bannister, D. J., and Semlyen, J. A. (1980) Studies of cyclic and linear poly(dimethylsiloxanes) .4. bulk viscosities. *Polymer*, **21**, 663–667.
- [290] Semlyen, J. A. (1981) Cyclic Polymers. *Pure Appl. Chem.*, **53**, 1797–1804.
- [291] Higgins, J. S., Ma, K., Nicholson, L. K., Hayter, J. B., Dodgson, K., and Semlyen, J. A. (1983) Studies of cyclic and linear poly(dimethyl siloxanes).12. Observation of diffusion behavior by quasielastic neutron-scattering. *Polymer*, **24**, 793–799.
- [292] Clarson, S. J., Dodgson, K., and Semlyen, J. A. (1985) Studies of cyclic and linear poly(dimethyl siloxanes).19. Glass-transition temperatures and crystallization behavior. *Polymer*, **26**, 930–934.
- [293] Orrah, D. J., Semlyen, J. A., and Rossmurphy, S. B. (1988) Studies of cyclic and linear poly(dimethylsiloxanes). 27. bulk viscosities above the critical molar mass for entanglement. *Polymer*, **29**, 1452–1454.
- [294] Cosgrove, T., Turner, M. J., Griffiths, P. C., Hollingshurst, J., Shenton, M. J., and Semlyen, J. A. (1996) Self-diffusion and spin-spin relaxation in blends of linear and cyclic polydimethylsiloxane melts. *Polymer*, **37**, 1535–1540.

- [295] Choi, J. and Kwak, S. Y. (2004) Architectural effects of poly(ϵ -caprolactone)s on the crystallization kinetics. *Macromolecules*, **37**, 3745–3754.
- [296] Cordova, M. E., Lorenzo, A. T., Müller, A. J., Hoskins, J. N., and Grayson, S. M. (2011) A comparative study on the crystallization behavior of analogous linear and cyclic poly(ϵ -caprolactones). *Macromolecules*, **44**, 1742–1746.
- [297] Shin, E. J., Jeong, W., Brown, H. A., Koo, B. J., Hedrick, J. L., and Waymouth, R. M. (2011) Crystallization of cyclic polymers: Synthesis and crystallization behavior of high molecular weight cyclic poly(ϵ -caprolactone)s. *Macromolecules*, **44**, 2773–2779.
- [298] Gimenez, J., Cassagnau, P., and Michel, A. (2000) Bulk polymerization of ϵ -caprolactone: Rheological predictive laws. *J. Rheol.*, **44**, 527–547.
- [299] Izuka, A., Winter, H. H., and Hashimoto, T. (1992) Molecular-weight dependence of viscoelasticity of polycaprolactone critical gels. *Macromolecules*, **25**, 2422–2428.
- [300] Acierno, S., Di Maio, E., Iannace, S., and Grizzuti, N. (2006) Structure development during crystallization of polycaprolactone. *Rheol. Acta*, **45**, 387–392.
- [301] Kricheldorf, H. R. and Eggerstedt, S. (1998) New polymer syntheses. 100. Multi-block copolyesters by combined macrocyclic polymerization and silicon-mediated polycondensation. *Macromolecules*, **31**, 6403–6408.
- [302] Kricheldorf, H. R. (2010) Cyclic polymers: Synthetic strategies and physical properties. *J. Polym. Sci., Part A: Polym. Chem.*, **48**, 251–284.
- [303] Cohen-Addad, J. P. (1974) Effect of the anisotropic chain motion in molten polymers: The solidlike contribution of the nonzero average dipolar coupling to NMR signals. Theoretical description. *J. Chem. Phys.*, **60**, 2440–2453.
- [304] Klein, P. G. and Ries, M. E. (2003) The dynamics and physical structure of polymers above the glass transition - transverse relaxation studies of linear chains, star polymers and networks. *Progr. NMR Spectrosc.*, **42**, 31–52.
- [305] Saalwächter, K. (2005) Artifacts in transverse proton NMR relaxation studies of elastomers. *Macromolecules*, **38**, 1508–1512.
- [306] Vaca Chávez, F. and Saalwächter, K. (2010) NMR Observation of Entangled Polymer Dynamics: Tube Model Predictions and Constraint Release. *Phys. Rev. Lett.*, **104**, 198305–1–198305–4.
- [307] Vaca Chávez, F. and Saalwächter, K. (2011) Time-Domain NMR Observation of Entangled Polymer Dynamics: Analytical Theory of Signal Functions. *Macromolecules*, **44**, 1560–1569.
- [308] Herrmann, A., Novikov, V. N., and Rössler, E. A. (2009) Dipolar and Bond Vector Correlation Function of Linear Polymers Revealed by Field Cycling ^1H NMR: Crossover from Rouse to Entanglement Regime. *Macromolecules*, **42**, 2063–2068.
- [309] Herrera, D., Zamora, J. C., Bello, A., Grimau, M., Laredo, E., Müller, A. J., and Lodge, T. P. (2005) Miscibility and crystallization in polycarbonate/poly(ϵ -caprolactone) blends: Application of the self-concentration model. *Macromolecules*, **38**, 5109–5117.
- [310] McKenna, G. B., Hadziioannou, G., Lutz, P., Hild, G., Strazielle, C., Straupe, C., Rempp, P., and Kovasc, A. J. (1987) Dilute-solution characterization of cyclic

- polystyrene molecules and their zero-shear viscosity in the melt. *Macromolecules*, **20**, 498–512.
- [311] Halverson, J. D., Grest, G. S., Grosberg, A. Y., and Kremer, K. (2012) Rheology of Ring Polymer Melts: From Linear Contaminants to Ring-Linear Blends. *Phys. Rev. Lett.*, **108**.
- [312] Ruland, W. (1977) The evaluation of the small-angle scattering of lamellar two-phase systems by means of interface distribution functions. *Colloid Polym. Sci.*, **255**, 417–427.
- [313] Coll, H. and Gilding, D. K. (1970) Universal Calibration in GPC: A Study of Polystyrene, Poly- α -Methylstyrene, and Polypropylene. *J. Polym. Sci., Part A-2: Polym. Phys.*, **8**, 89–103.
- [314] Schindler, A., Hibionada, Y. M., and Pitt, C. G. (1982) Aliphatic Polyesters. III. Molecular Weight and Molecular Weight Distribution in Alcohol-Initiated Polymerizations of ϵ -Caprolactone. *J. Polym. Sci., Part A: Polym. Chem.*, **20**, 319–326.
- [315] Dubois, P., Barakat, I., Jérôme, R., and Teyssié, P. (1993) Macromolecular Engineering of Polylactones and Polylactides. 12. Study of the Depolymerization Reactions of Poly(ϵ -caprolactone) with Functional Aluminum Alkoxide End Groups. *Macromolecules*, **26**, 4407–4412.
- [316] Gordin, C., Delaite, C., Medlej, H., Josien-Lefebvre, D., Hariri, K., and Rusu, M. (2009) Synthesis of ABC miktoarm star block copolymers from a new heterotri-functional initiator by combination of ATRP and ROP. *Polym. Bull.*, **63**, 789–801.
- [317] Atanase, L. I., Glaied, O., and Riess, G. (2011) Crystallization kinetics of PCL tagged with well-defined positional triazole defects generated by click chemistry. *Polymer*, **52**, 3074–3081.
- [318] Kricheldorf, H. R. and Lee, S. R. (1995) Polylactones. 35. Macrocyclic and stereoselective polymerization of beta-D,L-butyrolactone with cyclic dibutyltin initiators. *Macromolecules*, **28**, 6718–6725.
- [319] Ostas, E. (2008) Macrocyclic and Linear Poly(ϵ -caprolactone): Investigation of the Crystallization Behavior. Martin-Luther-Universität Halle, Institut für Chemie, Diploma Thesis.
- [320] Bärenwald, R. (2012) *Untersuchung der Kettendynamik in Polyethylen-Kristalliten mit Hilfe von Festkörper-NMR*. Master's thesis, Institut für Physik/Chemie, Naturwissenschaftliche Fakultät II, Martin-Luther-Universität Halle-Wittenberg.
- [321] Rutkowska, M., Jastrzebska, M., and Janik, H. (1998) Biodegradation of polycaprolactone in sea water. *React. Funct. Polym.*, **38**, 27–30, International Conference on Applied Physical Chemistry, Warsaw, Poland, Nov 13-16, 1996.
- [322] Haeberlen, U. and Waugh, J. S. (1968) Coherent Averaging Effects in Magnetic Resonance. *Phys. Rev.*, **175**, 453–467.
- [323] Roy, A. K. and Gleason, K. K. (1996) Analytical Solutions for Multiple-Quantum-Coherence Dynamics among Two or Three Dipolar-Coupled Spin-1/2 Nuclei. *J. Magn. Reson. A*, **120**, 139–147.
- [324] Sakurai, S., Okamoto, S., Kawamura, T., and Hashimoto, T. (1991) Small-Angle X-

ray-Scattering Study of Lamellar Micromdomains in a Block Copolymer. *J. Appl. Crystallogr.*, **24**, 679–684, 8th International Conf. on Small Angle Scattering, Univ. Louvain, Louvain, Belgium, Aug. 06-09, 1990.

- [325] Cheung, T. T. P. (1999) Effects of disorder in polymer morphology on spin diffusion. *J. Phys. Chem. B*, **103**, 9423–9431.

Danksagung

Für die freundliche Unterstützung, die ich von den Mitarbeitern der Fachgruppen NMR und Biophysik der Martin-Luther-Universität in den letzten Jahren erfahren habe, möchte ich mich an dieser Stelle herzlich bedanken.

Diese Dissertation entstand auf Initiative von Prof. Kay Saalwächter, dem ich für die fachliche Unterstützung und die vielen aufschlussreichen Diskussionen danke.

Viele Mitarbeiter der Fachbereiche Physik und Chemie haben mit ihrem Einsatz zum Gelingen meiner Arbeit beigetragen. In diesem Zusammenhang möchte ich mich vielmals bei Elena Ostas für die Bereitstellung der PCL-Proben bedanken sowie für ihre unverzichtbare Hilfe beim Umgang mit Chemikalien und Chemielaborgerätschaften.

Ein weiterer herzlicher Dank geht an Anne Seidlitz, Katrin Herfurt und Dr. Klaus Schröter für die zuverlässige Durchführung der SAXS-, DSC- und Rheologie-Messungen und die Analyse der Rohdaten, sowie an Prof. Thurn-Albrecht für diverse hilfreiche Diskussionen zur Planung und Ausführung dieser Messungen.

Außerdem danke ich ganz herzlich meinen langjährigen „Büromitbewohnerinnen“ Anja Achilles und Christiane Hackel für ihre Hilfe bei den DIPSHIFT- und CODEX-Messungen und ihre wertvollen Hinweise zu deren Auswertung. Vielmals bedanken möchte ich mich weiterhin bei Prof. Horst Schneider für die Einweisung in das Simulationsprogramm und die freundlichen und hilfreichen Erklärungen zu dessen Funktionsweise. Matthias Roos sei an dieser Stelle für die Bereitstellung der PS-PB-Spindiffusionsdaten gedankt. Ein großes Dankeschön geht auch an Ruth Bärenwald für die tolle Zusammenarbeit im PE-Helixsprung-Projekt und die vielen gewinnbringenden Diskussionen.

Nicht zuletzt danke ich Pierre Seiboth für seine stete Hilfe bei technischen Problemen aller Art und bei Detlef Reichert, der immer ein offenes Ohr für Sorgen und Nöte hatte und von dessen langjähriger Erfahrung (nicht nur) auf dem Gebiet der NMR ich profitiert habe. Vielen Dank auch an den Rest der Arbeitsgruppe für die gute Zusammenarbeit, für Hilfe aller Art und für die schönen Grill- und Filmabende.

Ein besonderes Dankeschön möchte ich an Anja Achilles, Tanja Zinkevich und Christiane Hackel, die momentane und ehemalige Besetzung von Raum 107, richten, für die angenehme, entspannte Arbeitsatmosphäre, die vielen anregenden Gespräche, ihre Bereitschaft zur Diskussion auch der dümmsten fachlichen Probleme und ihre Unterstützung bei der Bewältigung der kleinen und größeren Probleme des Büro- und Laboralltags und des Lebens im Allgemeinen. Ich danke ihnen sowie Anke und Jumna außerdem für die vielen schönen, zusammen verbrachten Stunden und die außeruniversitäre Zerstreuung.

Ein weiterer, ganz herzlicher Dank gilt Familie Achilles für die tatkräftige Unterstützung beim Finden der richtigen Formulierungen, beim Aufstöbern von Rechtschreibfehlern und bei der Fertigstellung dieser Arbeit.

Zu guter Letzt geht das allergrößte Dankeschön an meine Familie und an Valentin, die mir immer mit Rat und Tat zur Seite stehen. Ohne ihre Unterstützung und Bestärkung wäre alles viel schwieriger gewesen.

Eidesstattliche Erklärung

Hiermit versichere ich, dass ich die vorliegende Arbeit selbständig und ohne fremde Hilfe verfasst und dabei nur die von mir angegebenen Quellen und Hilfsmittel benutzt habe. Die den benutzten Werken wörtlich oder inhaltlich entnommenen Stellen habe ich als solche kenntlich gemacht.

Die vorliegende Dissertation habe ich weder in der gegenwärtigen noch in einer anderen Fassung einer anderen wissenschaftlichen Einrichtung vorgelegt. Weiterhin bestätige ich hiermit, keine anderweitigen Promotionsversuche unternommen zu haben.

Halle/Saale, den 06. 11. 2012

Kerstin Schäler

Lebenslauf

Persönliche Daten

Name: Kerstin Schäler
Geburtsdatum: 20. April 1983
Geburtsort: Zwenkau
Staatsangehörigkeit: deutsch
Familienstand: ledig

Schulausbildung

1989 - 1993: Grundschule „Hans Christian Andersen“ in Halle (Saale)
1993 - 2002: Thomas-Müntzer-Gymnasium in Halle (Saale)

Studium

10/2002 - 11/2007: Studium der Medizinischen Physik an der
Martin-Luther-Universität Halle-Wittenberg
11/2006 - 11/2007: Diplomarbeit in der Physikalisch-Technischen
Bundesanstalt (PTB) in Braunschweig, Arbeitsgruppe
Neutronenmetrologie
seit 12/2007: Promotion an der Martin-Luther-Universität
Halle-Wittenberg, Institut für Physik, Fachgruppe NMR

Halle/Saale, den 06. 11. 2012

Kerstin Schäler

Publikationsliste

- [1] Röttger, S., Schäler, K., Behrens, R., Nolte, R., and Wissmann, F. (2007) The neutron component of two high-energy photon reference fields. *Radiat. Prot. Dosim.*, **126**, 404-407, doi: 10.1093/rpd/ncm083.
- [2] Röttger, S., Schäler, K., and Nolte, R. (2010) A new simulated neutron workplace field at PIAF. *Radiat. Meas.*, **45**, 1154-1158, doi: 10.1016/j.radmeas.2010.06.037.
- [3] Schäler, K., Ostas, E., Schröter, K., Thurn-Albrecht, T., Binder, W. H., and Saalwächter, K. (2011) Influence of Chain Topology on Polymer Dynamics and Crystallization. Investigation of Linear and Cyclic Poly(ϵ -caprolactone)s by ^1H Solid-State NMR Methods. *Macromolecules*, **44**, 2743-2754, doi: 10.1021/ma102838c.
- [4] Papon, A., Saalwächter, K., Schäler, K., Guy, L., Lequeux, F., and Montes, H. (2011) Low-Field NMR Investigations of Nanocomposites: Polymer Dynamics and Network Effects, *Macromolecules*, **44**, 913-922, doi: 10.1021/ma102486x.
- [5] Bärenwald, R., Champouret, Y., Saalwächter, K., and Schäler, K. (2012) Determination of Chain Flip Rates in Poly(ethylene) Crystallites by Solid-State Low-Field ^1H NMR for Two Different Sample Morphologies. *J. Phys. Chem. B*, **116**, 13089-13097, doi: 10.1021/jp3061625.